LEAD-ACID BATTERY TECHNOLOGIES

Fundamentals, Materials, and Applications

ELECTROCHEMICAL ENERGY STORAGE AND CONVERSION

Series Editor: Jiujun Zhang
National Research Council Institute for Fuel Cell Innovation
Vancouver, British Columbia, Canada

Published Titles

Electrochemical Supercapacitors for Energy Storage and Delivery: Fundamentals and Applications
Aiping Yu, Victor Chabot, and Jiujun Zhang

Proton Exchange Membrane Fuel Cells
Zhigang Qi

Graphene: Energy Storage and Conversion Applications
Zhaoping Liu and Xufeng Zhou

Electrochemical Polymer Electrolyte Membranes
Yan-Jie Wang, David P. Wilkinson, and Jiujun Zhang

Lithium-Ion Batteries: Fundamentals and Applications
Yuping Wu

Lead-Acid Battery Technologies: Fundamentals, Materials, and Applications
Joey Jung, Lei Zhang, and Jiujun Zhang

Forthcoming Titles

Solar Energy Conversion and Storage: Photochemical Modes
Suresh C. Ameta and Rakshit Ameta

Electrochemical Energy: Advanced Materials and Technologies
Pei Kang Shen, Chao-Yang Wang, San Ping Jiang, Xueliang Sun, and Jiujun Zhang

Solid Oxide Fuel Cells: From Fundamental Principles to Complete Systems
Radenka Maric

LEAD-ACID BATTERY TECHNOLOGIES

Fundamentals, Materials, and Applications

Edited by
Joey Jung • Lei Zhang
Jiujun Zhang

CRC Press
Taylor & Francis Group
Boca Raton London New York

CRC Press is an imprint of the
Taylor & Francis Group, an **informa** business

CRC Press
Taylor & Francis Group
6000 Broken Sound Parkway NW, Suite 300
Boca Raton, FL 33487-2742

Version Date: 20150529

International Standard Book Number-13: 978-1-4665-9223-0 (eBook - PDF)

Contents

Series Preface

The goal of the *Electrochemical Energy Storage and Conversion* book series is to provide comprehensive coverage of the field, with titles focusing on fundamentals, technologies, applications, and the latest developments, including secondary (or rechargeable) batteries, fuel cells, supercapacitors, CO_2 electroreduction to produce low-carbon fuels, electrolysis for hydrogen generation/storage, and photoelectrochemistry for water splitting to produce hydrogen, among others. Each book in this series is self-contained, written by scientists and engineers with strong academic and industrial expertise who are at the top of their fields and on the cutting edge of technology. With a broad view of various electrochemical energy conversion and storage devices, this unique book series provides essential reads for university students, scientists, and engineers, and allows them to easily locate the latest information on electrochemical technology, fundamentals, and applications.

Jiujun Zhang
National Research Council of Canada
Richmond, British Columbia

Preface

Currently, energy storage and conversion have become one of the most important topics in ongoing research and development aimed at achieving a clean and sustainable world. Electrochemical energy technologies such as batteries, fuel cells, and electrochemical supercapacitors have been recognized as the most important part of the various energy storage and conversion technologies. Among electrochemical energy technologies, lead-acid rechargeable battery technology is the most popular, mature, reliable, safe, and cost-effective electrochemical technology with much wider applications than other electrochemical devices, although it still has several challenges such as relatively low specific energy density, insufficient cycle life, and possible environmental impacts from the manufacturing process (lead dust). Recently, the technology has found rapidly increasing applications in emerging technologies, in particular, in ground transportation applications including electric bicycles, low-speed electric vehicles, and microhybrid vehicles. Recent materials advancements have produced substantial improvements in lead-acid battery performance characteristics, especially energy density. These improvements have come about by enhancing battery utilization or adapting lighter materials, bringing attention to the relevance of lead-acid battery technology in a wider range of applications. For example, in the development of electric vehicles, with the realization of lithium-ion batteries due to the high cost and safety concerns, lead-acid rechargeable batteries have been reconsidered as a feasible technology as long as their energy density can be further increased.

This book is primarily intended to present an overview of lead-acid rechargeable batteries, including fundamentals, applications, and their advancements as energy storage devices in recent years. In particular, the fundamental sciences involved in their operation and the technological developments in materials science and engineering for materials fabrication are summarized in this book. An in-depth analysis of their integration with other primary power systems and their benefits toward current applications is provided. In addition, several other advanced lead-acid rechargeable battery technologies are described in this book. A group of top lead-acid battery scientists and engineers with not only excellent academic records, but also strong industrial expertise, have contributed chapters, sharing their knowledge, information, and insights on recent advances in fundamental theories, experimental methodologies, and research achievements in lead-acid battery technology.

We believe that this book will be a resource that benefits researchers, students, industrial professionals, and manufacturers by providing a systematic overview of the materials, system design, and related issues for the development of lead-acid rechargeable battery technology. The information in this book will be very helpful to readers as they select existing materials/technologies and develop new materials/technologies to improve the performance of lead-acid rechargeable batteries.

We acknowledge and express our sincere thanks for the contributions of all those involved in preparing and developing the chapters of this book. We also express our

appreciation to CRC Press for inviting us to lead this book project, and we thank Allison Shatkin for her guidance and support in smoothing the book preparation process. We acknowledge with deep appreciation Wirtz Manufacturing Company Inc. and Mac Engineering Inc. for their strong support.

If there are any technical errors in the book, we would deeply appreciate readers constructive comments for further improvement.

Joey Jung
Lei Zhang
Jiujun Zhang

Editors

Joey Jung is the founder and president of EVT Power Inc., a company focusing on lithium-ion and lead-acid battery current collector development, and the operations manager of Kemetco Research Inc., a company that provides service in the field of specialty analytical chemistry, chemical processes, and extractive metallurgy. Jung, a registered professional engineer, earned his MASc degree from the University of British Columbia in 2000. From 2000 to 2004, he was a research officer specializing in battery and fuel cell technology for BC Research Inc. From 2004 to 2007, he served as the vice president and CTO of Power Technology Inc, a public company specializing in advanced lead-acid battery development, and as the principal scientist at MagPower Systems Inc., a company engaged in developing metal-air fuel cells. Jung has more than 15 years of R&D experience in applied electrochemistry and electrochemical engineering, including lead-acid battery R&D, lithium-ion battery R&D, fuel cell R&D, rechargeable metal-air battery and metal-air fuel cells, electroplating/electrowinning R&D, catalyst development for electrochemical production of sodium chlorate, electrochemical production of lithium chlorate, electroreduction of carbon dioxide R&D, and development of a process to recycle waste polyurethane to polyols. He has published many papers and authored a book chapter on lead-acid battery technology. He holds 11 U.S. patents/patent applications in the fields of lead-acid batteries, lithium-ion batteries, and fuel cells.

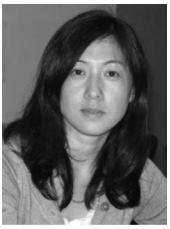

Lei Zhang is a research council officer at the National Research Council of Canada. She earned her BSc in materials science and engineering from Wuhan University of Technology in 1990, her first MSc in materials chemistry from Wuhan University in 1993, and her second MSc in physical chemistry from Simon Fraser University in Canada 2000. After completing her second MSc, Zhang took a position as a research scientist at Membrane Reactor Technologies Inc. in Vancouver, British Columbia, Canada, for 3 years. In 2004 Zhang joined NRC as a research council officer, where she undertook various national and industrial projects as a project manager. Zhang's main research interests include PEM fuel cell electrocatalysis, catalyst layer/electrode structure, metal-air batteries, supercapacitors, and molecular sieve membranes. Zhang has coauthored more than 100 refereed journal papers with more than 5000 citations, 30 conference and invited keynote presentations, 1 book chapter, 2 books, and 40 industrial technical reports. She holds three U.S. patent applications. Zhang is an adjunct professor of the Federal University of Maranhao, Brazil, and Zhengzhou University, China. She is also a member of the NSERC Industrial R&D Fellowships College of Reviewers, Canada (2012–present) and an international advisory member of the Seventh IUPAC International Conference on Novel Materials and Their Synthesis (NMS-VII).

Jiujun Zhang is a principal research officer at the National Research Council of Canada and a fellow of the International Society of Electrochemistry (ISE). His technical expertise areas are electrochemistry, photoelectrochemistry, spectroelectrochemistry, electrocatalysis, fuel cells (PEMFC, SOFC, and DMFC), batteries, and supercapacitors. Dr. Zhang earned his BS and MSc degrees in electrochemistry from Peking University in 1982 and 1985, respectively, and his PhD in electrochemistry from Wuhan University in 1988. Starting in 1990, he carried out three terms of postdoctoral research at the California Institute of Technology, York University, and the University of British Columbia. Dr. Zhang holds more than 10 adjunct professorships, including one at the University of Waterloo, one at the University of British Columbia, and one at Peking University. Dr. Zhang has approximately 400 publications with more than 12,000 citations, including 230 refereed journal papers, 13 edited/coauthored books, 32 book chapters, 110 conference oral and keynote/invited presentations, and more than 10 U.S./EU/WO/JP/CA patents. He has produced in excess of 90 industrial technical reports. Dr. Zhang serves as the editor or editorial board member for several international journals as well as editor for the CRC Press book series on electrochemical energy storage and conversion.

Contributors

Isidor Buchmann
Cadex Electronics Inc.
Richmond, British Columbia, Canada

Hongyu Chen
South China Normal University
Guangzhou, China

Mikaël Cugnet
Université Grenoble Alpes
INES, F-73375
Le Bourget du Lac, France

and

CEA, LITEN, F-38054
Grenoble, France

Joey Jung
EVT Power Inc.
and
Kemetco Research Inc.
Richmond, British Columbia, Canada

Zhongqi Li
South China Normal University
Guangzhou, China

Bor Yann Liaw
Hawaii Natural Energy Institute
University of Hawaii at Manoa
Honolulu, Hawaii

Vladimir Neburchilov
National Research Council
Vancouver, British Columbia, Canada

R. David Prengaman
RSR Technologies, Inc.
Dallas, Texas

J. Kevin Whear
Daramic LLC
Charlotte, North Carolina

Jiujun Zhang
National Research Council
Vancouver, British Columbia, Canada

Yufeng Zhang
South China Normal University
Guangzhou, China

1 Fundamentals of Lead-Acid Rechargeable Batteries

Joey Jung

CONTENTS

1.1 HISTORY

The lead-acid battery was the first secondary (rechargeable) battery to be developed. Since French physicist Gaston Planté invented the lead-acid battery in 1859, its 155 years of development have resulted in numerous applications, for example, as starting batteries, backup power batteries, telecommunication batteries, and traction

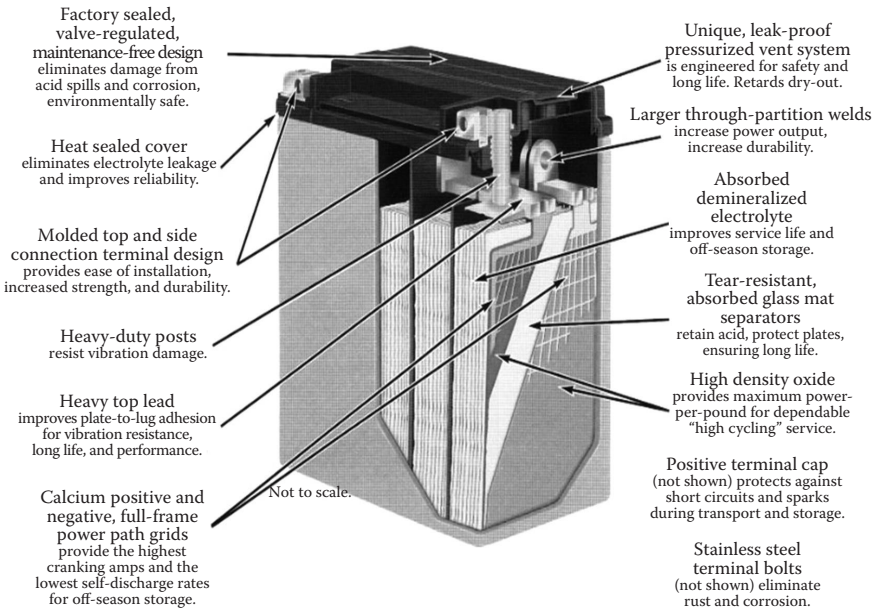

FIGURE 1.1 Cut-away of lead-acid battery. (From East Penn Manufacturing Co.)

batteries. Lead-acid battery sales represent approximately 70% of the secondary battery market in the world. Figure 1.1 shows a cut-away of a lead-acid battery [1].

Despite the recent rapid development of secondary lithium ion/lithium polymer batteries, advanced technology development, designs, and fabrication processes are still being developed and introduced into the lead-acid battery industry. Table 1.1 shows the major advantages and disadvantages of lead-acid batteries.

1.1.1 Major Milestones in Lead-Acid Battery Development

Table 1.2 lists the major technology developments in the lead-acid battery industry since the battery's invention in 1859.

1.2 ECONOMICS OF AND MARKET FOR LEAD-ACID BATTERIES

Lead-acid battery chemistry has been applied to a variety of capacities, sizes, and designs. Despite other battery chemistry technologies that have been marketed, lead-acid chemistry remains the technology of choice for automotive and many other applications. Lead-acid chemistry has proven to be robust, tolerant to abuse, low cost, and well understood. It is widely used in the industrial, portable, and transportation sectors.

Since 2002, lead-acid batteries have been widely used to power electric scooters, electric bicycles, and even electric vehicles. The worldwide lead-acid battery market was an approximately USD 60.3 billion industry in 2010. Its demand is projected to

TABLE 1.1
Advantages and Disadvantages of Lead Acid Batteries

Advantages	Disadvantages
Low-cost secondary battery.	Relatively low cycle life (approximately 500 deep cycles).
Recyclable.	Low energy density (typically 30 to 40 Wh/kg).
Available in maintenance-free version.	Long-term storage in a discharged condition can lead to sulfation of battery electrode and cause irreversible damage.
Easy to manufacture; high-volume production.	Grid contains antimony and arsenic, which are health hazards.
Good recharge efficiency (>70%).	Small size batteries (<500 mAh, AA-size battery) are difficult to make.
Available in a variety of capacities, sizes, and designs.	Short circuit will cause irreversible battery damage.
Good high-rate performance.	
Moderately good operating temperature range (–40°C to 60°C).	
Good single-cell voltage (open circuit voltage >2 V).	
Easy state of discharge–charge indication.	

increase to approximately USD 103.8 billion by 2020. Major market information for lead-acid batteries is provided in the following.

1.2.1 Automotive

1.2.1.1 SLI Batteries

For starting, lighting, and ignition (SLI) batteries, the estimated annual world market in 2010 was USD 38.2 billion. Demand is expected to grow moderately due to the high degree of maturity of SLI batteries in most developed nations and price competition among major suppliers. The development of hybrid and electric vehicles also could provide significant opportunities in this market in the future. Figure 1.2 shows the estimated market growth to 2020.

This sector requires batteries with rapid charge and discharge capabilities, high power output for acceleration, a long-lasting life, minimal maintenance, and low cost. They must also be safe. Major applications include light traction, marine, hybrid electric vehicles (HEVs), plug-in hybrid electric vehicles (PHEVs), electric vehicles (EVs), and neighborhood electric vehicles (NEVs), such as bicycles, motorcycles, buses, and trams.

The key battery performance parameters in this market are cold cranking amps (CCAs) and reserve capacity (RC). For a 12-V SLI battery, CCA is defined as the number of amps a lead-acid battery at 0°F can deliver for 30 sec while maintaining at least 7.2 V. The RC is defined as the amount of time (in minutes) that a battery can deliver 25 A at 80°F while maintaining terminal voltage of at least 10.5 V.

TABLE 1.2
Development History of Lead-Acid Battery

Year	Inventor	Lead-Acid Battery Development
1859	Planté	First practical lead-acid battery, corroded lead foils to form active material
1881	Faure	Pasted lead foils with lead oxide mixed with sulfuric acid paste for positive electrode
1881	Sellon	Lead antimony alloy grid
1881	Volckmar	Perforated lead plates to provide pockets for support of oxide
1882	Brush	Mechanically bonded lead oxide to lead plates
1882	Gladstone and Tribs	Double sulfate theory of reaction in lead-acid battery; $Pb + PbO_2 + 2H_2SO_4 \leftrightarrow 2PbSO_4 + 2H_2O$
1883	Tudor	Pasted mixture of lead oxide on grid pretreated by Planté method
1886	Lucas	Formed lead plates in solutions of chlorates and perchlorates
1890	Phillipart	Early tubular construction; individual rings
1890	Woodward	Early tubular construction
1910	Smith	Slotted rubber tube; Exide tubular construction
1920		Research begins for materials such as expanders and oxides and for manufacturing equipment and techniques
1935	Haring and Thomas	Experimental proof of double sulfate theory
1956	Bode and Voss	Clarification of two forms of lead dioxide (alpha and beta)
1960	Ruetschi and Chan	Clarification of two forms of lead dioxide (alpha and beta)
1970s	McClelland and Devit	Commercial spiral-wound sealed lead-acid battery; expanded metal grid technology; glass fiber separator; heat-sealed plastic case to cover assemblies
1980s		Sealed valve-regulated batteries
1990s		Electric vehicle battery; bipolar battery
2001	Gyenge and Jung	Lead-tin alloy–coated carbon substrate current collectors for lead-acid battery
2002	Kelly	Bare carbon foam current collector for negative current collector for lead-acid battery
2004		Super capacitor negative electrode for lead-acid battery
2009	Jung	Multiconductive polymer or carbon foam substrate current collectors for lead-acid battery

1.2.1.2 Deep-Cycle Batteries

Lead-acid batteries have been widely used in electric bicycles (E-bikes), especially in China. The Chinese government estimated that there were approximately 80 million E-bikes in China in 2010, where 95% of the E-bikes are powered by lead-acid batteries. The market size for E-bike batteries in 2010 for North America (NA), Europe, the Middle East, and Africa (EMEA), Asia-Pacific (AP) and Rest of World (ROW) was USD 13.6 billion and is expected to grow to USD 24.2 billion by 2020, as shown in Figure 1.3.

The key battery performance parameters for E-bike batteries are cost, cycle life, and weight. E-bike battery manufacturers currently warranty new replacement

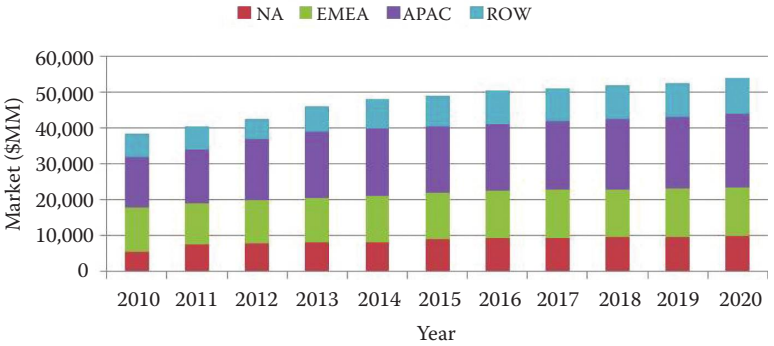

FIGURE 1.2 SLI battery market projection.

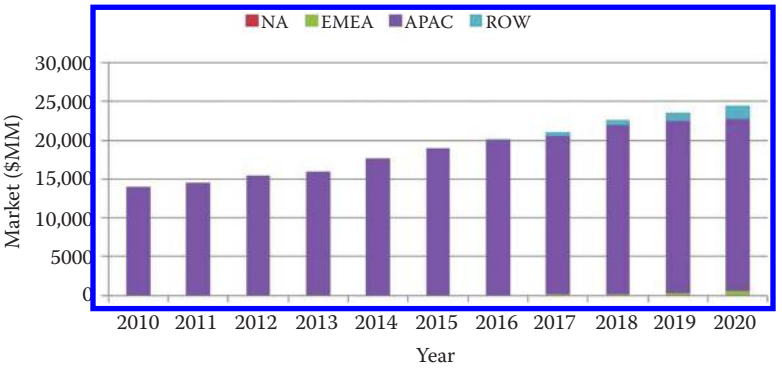

FIGURE 1.3 E-bike battery market projection.

batteries for 8 months and refurbished batteries for 9 to 15 months. E-bike batteries weigh between 12 and 26 kg, the high end of which can be problematic in locations where population-dense, high-rise buildings are popular.

1.2.1.3 Micro-Hybrid Batteries

Micro-hybrid battery technology shuts down an automobile's engine at stoplights and then starts it up again when the driver releases the brake. Micro-hybrid technology makes use of an extra 12-V battery to run the car's accessories (especially air conditioning) when the engine is shut off.

By 2015, estimates are that micro-hybrid start–stop systems will be installed on nearly 20 million cars annually. Urban cars in Europe spend as much as a third of their time on the road not moving. Asian markets, with huge congestion problems, are likely to gain the most from the technology. In contrast, U.S.-style highway driving does not benefit all that much from this technology, which is one of the reasons for its slow adoption in the United States.

The prospects for micro-hybrid batteries are particularly bright in Europe and China. China is projected to produce 15 million cars annually by 2020, with half of

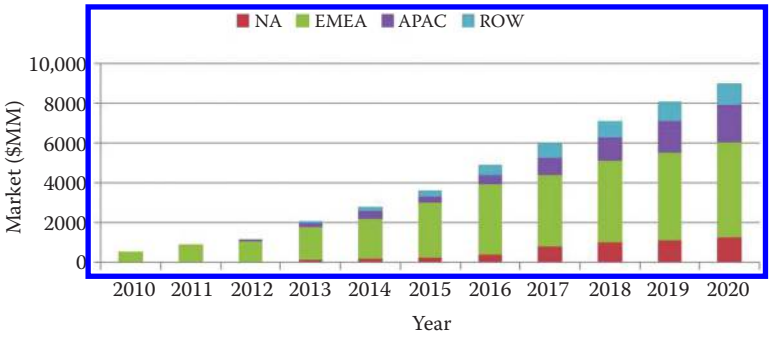

FIGURE 1.4 Micro-hybrid battery market projection.

them using some form of electric drive, and three-quarters of those EV-enabled cars could be micro-hybrids.

The micro-hybrid battery market was estimated at USD 560 million in 2010. Demand is estimated to grow to USD 9.02 billion in 2020, as shown in Figure 1.4. The key performance parameters are dynamic charge acceptance and cycle life. HEV applications require good charge acceptance in a dynamic discharge–charge microcycling operation. The main charge is more throughput, but only at shallow cycling depths (e.g., <1%). A very long stop with high loads might be 2%. A 10× dynamic charge acceptance is the goal against standard SLIs. The cycle life for batteries used in the micro-hybrid market is required to have 5000 SLI cycles and over 10,000 cycles at 60% partial of charge (PSOC) without conditioning.

1.2.2 Industrial

1.2.2.1 MLA Batteries

Increased investment in new manufacturing facilities or upgrading of existing facilities is driving substantial demand for motive lead-acid (MLA) batteries. The worldwide annual market was USD 3.34 billion in 2010 and is expected to grow to USD 4.54 billion in 2020, as shown in Figure 1.5. The industrial MLA batteries form a

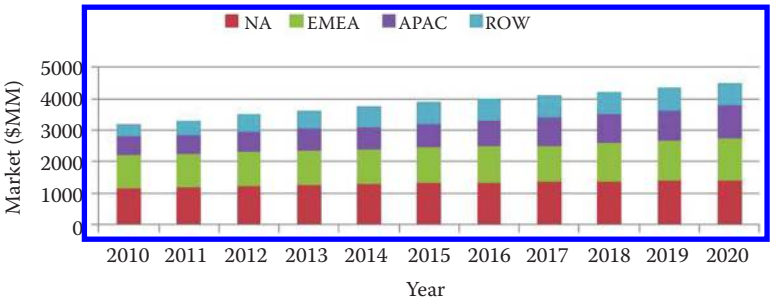

FIGURE 1.5 Motive industrial battery market projection.

critical part of heavy-duty equipment, mining and railroad equipment, pallet jacks, fork lift trucks, floor cleaners, automated guided vehicles (AGVs), and towing vehicles, as well as wheelchairs and golf carts. Globally, Asia is emerging as a particularly attractive market due to rising demand and the low costs of production in the region.

The key required battery performance parameter is the lifetime of the battery. Industrial MLA batteries often endure 100% depth of discharge (DOD) thus 100% DOD testing is the industry standard because that is the quickest way to test. The typical benchmark lifetimes are in the range of 500 to 600 cycles.

Designed for applications where the batteries are regularly discharged, MLAs require rapid charge capabilities, high energy and power output, a long cycle life, and minimal maintenance.

1.2.2.2 Stationary Batteries

Stationary power systems support various critical applications including preventing unscheduled outages, extending the life of sensitive electronic equipment, reducing maintenance costs, and increasing the predictability of equipment failures. The widespread use of lead-acid batteries as standby power sources for several critical applications for more than a century has earned them the trust of end users. Today, stationary lead-acid (SLA) batteries have become vital components in every industrial application and had an estimated USD 3.99 billion market in 2010. Figure 1.6 shows the market is projected to grow to USD 7.85 billion in 2020. A realization of the need for backup power to sustain the running of critical businesses has resulted in constant market revenue for these batteries. The technology has been the forerunner in the field of energy storage, thereby increasing the dependence on backup power for both critical and semicritical end-user applications.

The key battery parameters for this market are lifetime and footprint. The expected lifetime of industrial SLA batteries is 5 to 20 years with corresponding warranties. Uninterruptible power supply (UPS) and telecommunication batteries often have limited cycling. The footprint is also important because battery manufacturers desire a smaller footprint for this type of battery. Some stationary batteries are designed to cycle rather than ‘‘float.’’ Applications of cycling stationary batteries include load-leveling, utility peak-power shaving, and photovoltaic energy-storage systems.

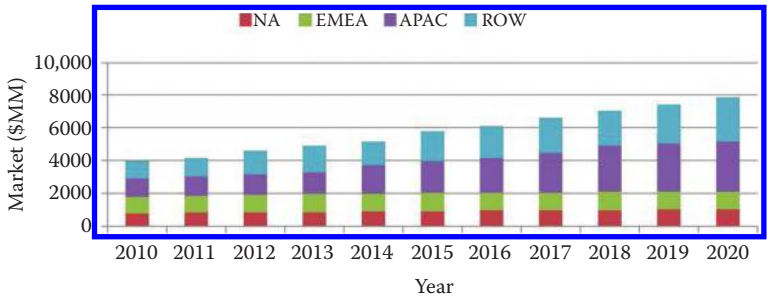

FIGURE 1.6 Stationary industrial battery market projection.

1.2.2.3 Emerging Grid Applications

The calls made by governments in recent years for development of alternative/renewable energy power sources such as solar and offshore/onshore wind power has created a huge demand for stationary batteries. The electricity generated by these technologies is intermittent by nature, and it is available only when the sun shines or the wind blows. Therefore, these alternative energy sources require dedicated equipment that can stabilize voltages by eliminating irregularities in the systems and provide an efficient and reliable storage source to store the generated electrical power and backup.

Improved energy storage is a key requirement for the deployment of the much-touted "smart grid." There are many reasons for this. One is that the efficient integration of solar and (especially) wind power into the grid requires buffering, since these renewable energy sources produce energy best only at certain times. Another reason is that smart grids are intended to be highly resilient, so the ability to store energy for times of peak demand and network outages is critical to building this type of new infrastructure.

Figure 1.7 indicates that the battery market size for emerging grid applications was around USD 22.7 million in 2010. The market is anticipated to grow to USD 882 million in 2020.

The key battery performance requirements are lifetime and cost. Currently, a traditional lead-acid battery can deliver 1500 to 2000 cycles at 90% DOD, which is considered insufficient because a lithium ion battery can deliver up to 8000 cycles. The cost of the batteries for emerging grid applications is also important because peak-shaving and load-leveling applications are not enormously profitable for utilities. It is believed that the battery cost has to be roughly USD 200/kWh to enable widespread adoption.

1.2.2.4 Distributed Renewable Batteries

The integration of distributed renewable generation sources into the electricity grid poses a number of challenges for the industry. Utilities will be faced with issues of enabling high penetration of distributed generation onto both existing and future distribution systems. The battery for this application serves primarily off-grid photovoltaic (PV) installations. Figure 1.8 indicates that the worldwide battery market size for this application was USD 599 million in 2010 and is expected to grow to USD 2.6 billion in 2020.

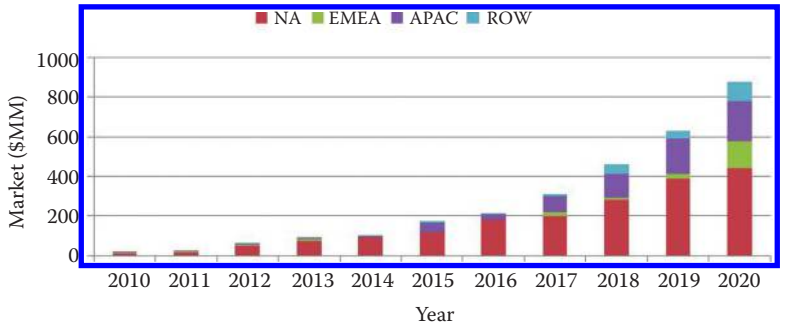

FIGURE 1.7 Emerging grid battery market projection.

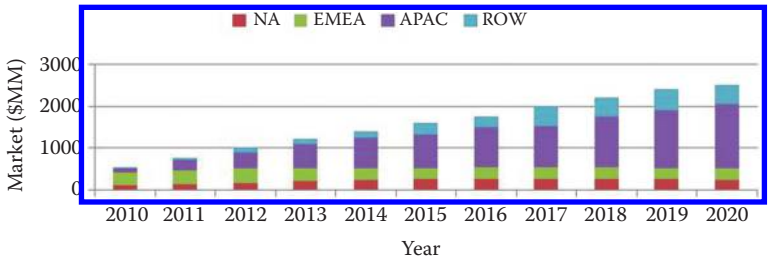

FIGURE 1.8 Distributed renewable battery market projection.

The key battery performance requirement is lifetime at deep discharge and cost. The lifetime for the battery is 100-h systems at 20% DOD for 5 to 6 years, which is approximately 1500 cycles.

1.3 CHEMISTRY/ELECTROCHEMISTRY

The electrochemistry of lead-acid batteries in the charge stage consists of a lead dioxide (PbO_2) positive electrode and lead (Pb) negative electrode in a concentrated (37 wt%, specific gravity of 1.28) sulfuric acid (H_2SO_4) electrolyte. In the discharge stage, the lead dioxide positive electrode and the lead negative electrode will convert to lead sulfate ($PbSO_4$) and consume the sulfate ions, which reduces the specific gravity of the electrolyte such that it is closer to that of water. The positive electrode is the major factor influencing the performance and cycle life of a lead-acid battery. The negative electrode determines the cold-temperature performance.

The electrochemical reactions of lead-acid batteries are as follows.

Positive electrode (anode):

$$PbO_{2(s)} + 4H^+ + 2e^- \underset{\text{Charge}}{\overset{\text{Discharge}}{\rightleftharpoons}} Pb^{2+} + 2H_2O \quad E = +1.7\,\text{V} \tag{1.1}$$

$$Pb^{2+}_{(aq)} + SO^{2-}_{4(aq)} \underset{\text{Charge}}{\overset{\text{Discharge}}{\rightleftharpoons}} PbSO_{4(s)} \tag{1.2}$$

Negative electrode (cathode):

$$Pb_{(s)} \underset{\text{Charge}}{\overset{\text{Discharge}}{\rightleftharpoons}} Pb^{2+}_{(aq)} + 2e^- \quad E = -0.3\,\text{V} \tag{1.3}$$

$$Pb^{2+}_{(aq)} + SO^{2-}_{4(aq)} \underset{\text{Charge}}{\overset{\text{Discharge}}{\rightleftharpoons}} PbSO_{4(s)} \tag{1.4}$$

Overall reaction:

$$Pb + PbO_2 + 2H_2SO_4 \underset{\text{Charge}}{\overset{\text{Discharge}}{\rightleftharpoons}} 2PbSO_4 + 2H_2O \quad E = 2.0\,\text{V} \tag{1.5}$$

The cell electromotive force (E) is determined by the difference between the equilibrium potentials of the $PbSO_4$/Pb and PbO_2/$PbSO_4$ electrolytes, $E_{PbSO_4/Pb}$ and $E_{PbO_2/PbSO_4}$, respectively.

$$\Delta E_e = E_{PbO_2/PbSO_4} - E_{PbSO_4/Pb} \tag{1.6}$$

$$\Delta E_e = \Delta E_e^o + \frac{2RT}{nF} \log \frac{a_{H_2SO_4}}{a_{H_2O}} \tag{1.7}$$

The electromotive force of the cell with no ion transfer (ΔE^o) is 2.040 V and it is determined on the basis of Gibbs free energies of the products and reagents participating in the reaction. The concentration of H_2SO_4 and the temperature of the cell will also impact the cell electromotive force. The open cell potential for lead-acid batteries is 2.10 to 2.13 V and the nominal voltage of a single practical lead-acid battery is 2 V.

In the charged stage, the lead dioxide on the positive electrode consists of two forms, α-PbO_2 (orthorhombic) and β-PbO_2 (tetragonal). Both forms of PbO_2 have different impacts on battery performance, as listed in Table 1.3 (Handbook of Batteries, Ref. 9).

TABLE 1.3
Physical and Chemical Properties of Pb and PbO_2

Property	Pb	α-PbO_2	β-PbO_2
Molecular weight (g/mol)	207.2	239.19	239.19
Composition		$PbO_{1.94–2.03}$	$PbO_{1.87–2.03}$
Crystalline form	Face centered cubic	Orthorhombic (larger, more compact)	Tetragonal (rutile)
Lattice parameters (nm)	a = 0.4949	a = 0.4977 b = 0.5948 c = 0.5444	a = 0.491–0.497 c = 0.337–0.340
X-ray density (g/cm^3)	11.34	9.80	~9.80
Practical density at 20°C (g/cm^3)	11.34	9.1–9.4	9.1–9.4
Heat capacity (cal/deg.mol)	6.80	14.87	14.87
Specific heat (cal/g)	0.0306	0.062	0.062
Electrical resistivity at 20°C (μΩ/cm)	20	~1.709	~1.692
Electrochemical potential (V) at 4.4 M H_2SO_4	0.356	~1.709	~1.692
Melting temperature (°C)	327.4		
Electrochemical potential in 4.4 M H_2SO_4		1.709 V	1.692 V
Electrochemical activity		Less	Better
Capacity per unit weight		Less	Better
Cycle life impact		Better	Less

The lead dioxide is formed by curing and forming a mix of chemicals including lead, lead oxide, sulfuric acid, and water. The ratios of these chemicals and their curing conditions, such as temperature, humidity, and duration, have a significant influence on the crystalline morphology and pore structure of the converted chemicals, which consists of lead sulfate, lead oxide, and a small amount of lead (<5%). During formation, the cured materials will electrochemically form lead dioxide, which contains a ration of α-PbO_2 and β-PbO_2. Both forms of PbO_2 are not stoichiometric. The composition, represented by PbO_x, has an x value that varies between 1.85 and 2.05.

1.4 REACTION THERMODYNAMICS AND KINETICS

1.4.1 Self-Discharge Process in a Lead-Acid Battery

The self-discharge process in a lead-acid battery is initiated by the mixed potentials of the negative and positive electrodes, $E_M^{n.e}$ and $E_M^{p.e}$, at open circuit. The open-circuit potential of the electrodes is determined by the two partial reactions on each negative and positive electrode.

For a negative electrode, the equilibrium potential of the $PbSO_4$/Pb is 0.35 V, which is more negative than the equilibrium potential of the H^+/H_2. This potential difference causes the following reactions to proceed on the negative electrode with no electron or ion transfer to the positive electrode:

$$Pb + H_2SO_4 \rightarrow PbSO_4 + 2H^+ + 2e^- \tag{1.8}$$

$$2H^+ + 2e^- \rightarrow H_2 \tag{1.9}$$

On open circuit, when no current flows through the electrode, the active material reacts with sulfuric acid, which leads to the evolution of H_2. When pressure builds up, the H_2 escapes the cell through the release valve; hence, the negative electrode undergoes an irreversible self-discharge reaction.

For the positive electrode, the equilibrium potential of the $PbO_2/PbSO_4$ electrode is 0.6 V more positive than that of the oxygen H_2O/O_2 electrode. The potential difference causes the following reactions to occur:

$$PbO_2 + PbSO_4 + 2H^+ + 2e^- \rightarrow PbSO_4 + H_2O \tag{1.10}$$

$$H_2O \rightarrow 1/2O_2 + 2H^+ + 2e^- \tag{1.11}$$

Here again when no current passes through the electrode, PbO_2 active material will self-discharge to form $PbSO_4$ and evolved O_2.

At self-discharge, the partial currents of the two coupled reactions from each electrode become equal:

$$i^o_{PbSO_4/Pb} = i^o_{H^+/H_2} \quad E_M^{n.e} \tag{1.12}$$

$$i^{o}_{PbO_2/PbSO_4} = i^{o}_{H_2O/O_2} \quad E^{p.e}_{M} \tag{1.13}$$

As a result of the self-discharge process, the voltage of a lead-acid cell at open circuit is practically equal to the difference between the potentials of the negative and positive electrodes. The currents of the self-discharge reactions are very low due to the high overvoltage of H_2 and O_2. Consequently, the differences between the thermodynamically determined values for the equilibrium potentials of $PbSO_4$/Pb and PbO_2/$PbSO_4$ electrodes and the open-circuit potentials are very small. As such, the potential difference at open circuit of the lead-acid cell can be assumed to be the electromotive force (emf) of the lead-acid battery.

The rates of the self-discharge reactions also depend on temperature, additives to the active mass, electrolyte formulation, and grid alloy composition. As the surface of the electrodes is covered by $PbSO_4$ (the product of the self-discharge reactions), the state of charge of the electrodes begins to affect the rate of the self-discharge process.

Experiments have shown that the evolution of hydrogen on the negative plate of a 100-Ah stationary battery corresponds to about 2 mA of electric current; that is, the battery will lose about 2% mA of its capacity for 1 month.

1.4.2 Dependence of Lead-Acid Cell Voltage on Temperature and H_2SO_4 Concentration

In a lead-acid battery, charge separation that gives rise to a voltage difference is accomplished by chemical reactions at the electrodes. A lead-acid battery can be considered to be a kind of *charge pump* that acts to move a positive charge from a point of low potential through its interior to a point of high potential. The charge separation that gives rise to a voltage difference is affected by the concentration of the H_2SO_4 electrolyte and the temperature.

With the specific gravity of H_2SO_4 ranging from 1.2 to 1.28, a single lead-acid battery cell voltage at open circuit increases linearly as the acid concentration is augmented. SLI and EV batteries in a charged state have a H_2SO_4 specific gravity of 1.28, and an open-circuit voltage of 2.12 V.

When the H_2SO_4 concentration changes, the pH is altered and the potential of the Pb/PbO_2/$PbSO_4$ electrode is affected much more notably than that of the Pb/$PbSO_4$; that is, the positive part of the battery cell is much more sensitive to H_2SO_4 concentration variations than is the negative one.

The second parameter that affects the battery cell voltage is temperature. Thermodynamically, this relationship is determined by the Gibbs-Helmholtz equation:

$$\Delta E_e = \frac{4.183\Delta H}{nF} + \left(\frac{d\Delta E}{dt}\right)_P \tag{1.14}$$

where ΔH is the change in enthalpy of the reaction at constant temperature and pressure and it is determined by thermodynamic calculations.

Harned and Hamer have determined experimentally the temperature dependence of the cell voltage within the temperature range of 0°C to 60°C. They have presented their results as an empirical equation:

$$\Delta E_e = E_e^o + at + bt^2 \tag{1.15}$$

where t is the temperature, E_e^{υ} is the emf of the cell at 0°C, and a and b are empirical coefficients.

1.4.3 Voltage of Lead-Acid Cell

The voltage of a lead-acid battery cell during charge must exceed the open-circuit voltage. During discharge, the case is reversed. The extent of these deviations with respect to the open circuit voltage is determined by

- Current density
- Degree to which the cell had been charged
- Temperature
- Presence of impurities and additives in the active mass
- Age of the cell

When electric current is flowing through the cell, the closed-circuit voltage depends on both the direction and magnitude of the current and the temperature.

During battery discharge, the voltage of each single cell normally drops from 2.12 V at open circuit to 1.97 V on load. After passing through a shallow minimum, the voltage increases again and reaches 2.00 V. This value is maintained for a given period of time and then decreases slowly. After reaching 1.7 V, rapid decay is observed. This sharp decline in voltage is known as the "knee of the curve." Figure 1.9 shows a typical lead-acid battery voltage during discharge, which contains several characteristic points.

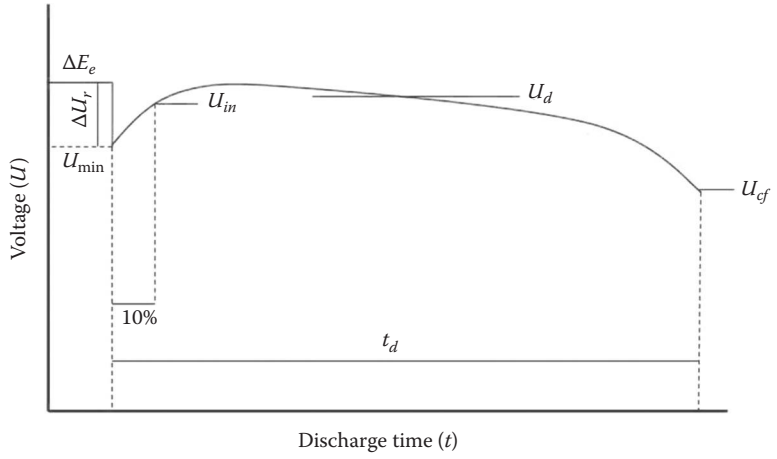

FIGURE 1.9 Lead-acid battery discharge voltage curve.

When electric current flows through the cell, the closed-circuit voltage depends on both the direction and magnitude of the current and the temperature. The discharge voltage of the cell U_d is

$$U_d = \Delta E_e - r_d I_d$$

The charge voltage is

$$U_{ch} = \Delta E_e + r_{ch} I_{ch}$$

where r_d and r_{ch} are the total internal resistances during discharge and charge, respectively, and I_d and I_{ch} are the corresponding currents.

With a new battery, the voltage normally drops from 2.12 V at open circuit to 1.97 V on load per cell. After passing through a shallow minimum, the voltage increases again and reaches 2.00 V. This value is maintained for a given period of time and then decreases slowly. After reaching 1.7 V, a rapid decay is observed.

The voltage/time curve contains several characteristic points (see Figure 1.9):

- *Initial voltage (U_{in})*: To avoid the effect of the initial voltage minimum, the value of the voltage when 10% of the cell capacity has been discharged is accepted as the initial voltage.
- *Cut-off voltage (U_{cf})*: This is usually determined by standards or a quality specification given by the manufacturer and it has a value of 1.70 or 1.75 V at a 5-h discharge rate. Under these conditions, the voltage drops by approximately 0.3 V from the initial voltage during discharge. The cut-off voltage depends on the discharge rate and the temperature.
- *Mean working voltage ($\overline{V}$)*: This is the mean arithmetic value of N voltages U_d measured through equal time intervals:

$$\overline{U_d} = \frac{1}{N} \sum_1^N U_N$$

  This value is used for calculating the energy and power characteristics of the battery.
- *Period of discharge (t_d)*: This is the time from switching on the current until the cut-off voltage is reached. This period is used when evaluating the capacity of the battery.
- *Initial voltage drop (U_r)*: This is determined by the internal resistance of the cell. As mentioned earlier, the battery is considered to be discharged when its voltage reaches 1.70 V. The specific gravity of the electrolyte has a value of ~1.14. If the current is switched off, the voltage increases, tending to reach 2.00 V. The open-circuit voltage of a cell with an electrolyte specific gravity of 1.14 is 2.00 V.

Figure 1.10 shows a set of discharge voltage curves for a 12-V SLI battery for different discharge currents at 25°C [2].

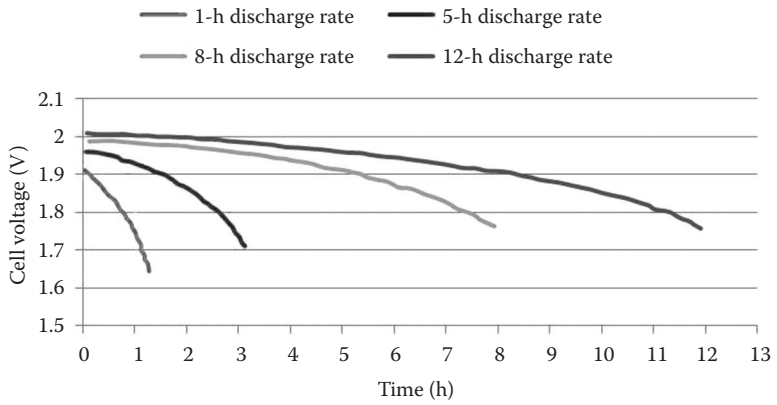

FIGURE 1.10 Discharge voltage curves for a 12-V SLI battery for different discharge currents at 25°C. (*Lead-Acid Battery, Electrochemical Technologies for Energy Storage and Conversion*, Chapter 4. 2012. Copyright Wiley-VCH Verlag GmbH & Co. KGaA. Reproduced with permission.)

When the period of discharge is 1 to 2 h, the cut-off voltage is taken to be 1.75 V per cell. For short discharges, some standards have accepted $U_f = 1.33$ V, whereas others use 1.00 V. During charge, the following reactions take place in the cell:

Reactions:

$$\oplus \quad PbSO_4 + 2H_2O \rightarrow H_2SO_4 + PbO_2 + 2H^+ + 2e^-$$

$$2H_2O \rightarrow O_2 + 2H^+ + 2e^-$$

$$\ominus \quad PbSO_4 + 2H^+ + 2e^- \rightarrow Pb + H_2SO_4$$

$$2H^+ + 2e^- \rightarrow 2H_2$$

Charge acceptance:

$$ChA = \frac{I - I_g}{I} \cdot 100$$

where I is the total current and I_g is the current for water decomposition.

The charge acceptance is connected with the transformation of $PbSO_4$ to Pb and PbO_2 active materials and the decomposition of H_2O.

During charge, the reactions proceed concurrently on the plates. The efficiency of battery charging is related to the suppression of the H_2 and O_2 evolution rates, and enhancement of the rates of Pb and PbO_2 formation. A "charge acceptance" parameter has been introduced to estimate the efficiency of charging. It

represents that part of the current flowing through the cell that is utilized for charging:

$$ChA = \frac{I - I_g}{I} \cdot 100$$

where I is the total current flowing through the cell during which different reactions dominate. The charge can be categorized into three stages as follows:

1. *Efficient charge stage*: The dominant reactions are the transformation of $PbSO_4$ into Pb and PbO_2. The charge acceptance is 100%. During this period, the state of charge reaches 70% to 80%. This stage is over when the cell voltage during charging with current 0.1 A/Ah reaches 2.35 V and gas evolution starts.
2. *Mixed stage*: During this interval, water decomposition proceeds simultaneously with the charging reactions. The charge acceptance is gradually and continuously reduced, and the battery is completely charged at the end of the stage. Cell voltage is increased from 2.35 to ~2.50 V.
3. *Gas evolution stage*: The cells are completely charged. During this stage, water decomposition and self-discharge processes take place in the battery.

These three stages can be clearly identified by galvanostatically charging a battery that has been subjected to three different depths of discharge: 50%, 75%, and 100%, as shown in Figure 1.11.

On charging with a current of 0.1 A/Ah, the gas evolution voltage is 2.35 to 2.40 V at 75% state of charge. This characteristic point marks the end of the efficient charge stage, and it can be checked by a voltage monitoring relay circuit. The duration of the

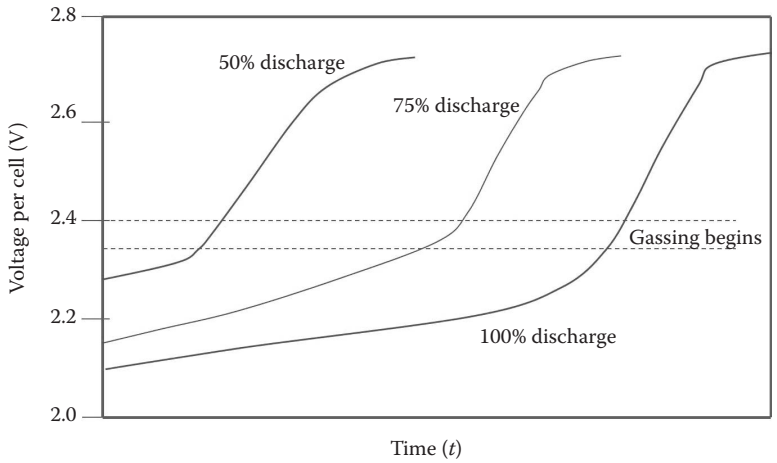

FIGURE 1.11 Charging of batteries undergoes three different depths of discharge: 50%, 75%, and 100% DOD.

mixed stage at a given current density is determined experimentally until the battery is completely charged. In this case, a time relay can be used to automatically restrict the charge duration. After the efficient stage is over, the voltage relay circuit actuates the time relay, which in turn switches off the charger after the predetermined period is over. Thus, the battery can be charged regardless of the previous operating conditions.

A coefficient voltage efficiency (U_E) was introduced to characterize the charge/discharge voltage ratio:

$$U_E = \frac{\overline{U_d}}{\overline{U_{ch}}}$$

This coefficient depends on the value of the current density. The mean voltage during a 5-h discharge period is equal to 1.95 V, and during charge, to 2.35 V, thus $U_E = 0.83$.

1.4.4 Capacity of Lead-Acid Cell

The capacity (C_d) of a cell is the second electrical characteristic. It is determined by the quantity of electricity that can be delivered during discharge at constant current until the final discharge voltage is reached:

$$C_d = I_d \cdot t_d$$

The relationship between capacity and current or discharge time is shown in Figure 1.12.

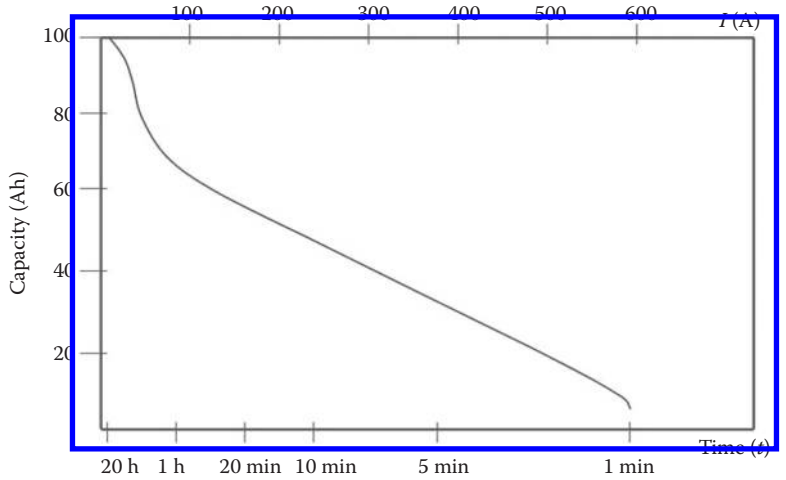

FIGURE 1.12 Capacity versus discharge time or current.

The amount of electricity, capacity, is a function of the discharge current and discharge duration until the cut-off voltage is reached:

$$C_d = I_d \cdot t_d$$

The time required to reach the final discharge is marked on the abscissa in Figure 1.12 and is known as the rate of discharge. To compare batteries within domestic regions and also internationally, standards such as rated capacity and working capacity were applied. Rated capacity is defined by the discharge of each 2-V single battery cell until its $U_{cf} = 1.75$ V at 20°C after 20 or 5 h. Working capacity is defined as 80% of the rated capacity. It is common practice not to discharge a battery beyond 80% of its rated capacity, regardless of the discharge current voltage.

- *Standard C_r-rated capacity*: [$U_f = 1.75$ V; $t^o = 20$°C; $t_d = 20$ or 5 h]
- *Working capacity*: 0.8 C_r % (Peukert equation, 1898)

Many empirical expressions have been proposed in the literature for the capacity/current dependence, but only that formulated by Peukert in 1898 has found wide acceptance:

$$C_d = \frac{K}{I^{n-1}}$$

where n and k are constants and $n = 1.3$. This equation is not valid for low discharge current.

Two characteristics were introduced to determine the electricity passed during the charge and discharge processes:

1. *Coulombic or AhE efficiency*: This is the ratio between the quantity of electricity passed during discharge (C_d) and charge (Q_{ch}):

$$AhE = \frac{C_d}{Q_{ch}}$$

   Since part of the electricity is consumed for the decomposition of water, *AhE* has a value of about 90%.
2. *Charge/discharge coefficient*: This is given by the expression

$$Q_{ch}/C_d$$

   This coefficient is very convenient for expressing the degree of overcharge. Thus, a value of 1.05 means 5% ever charge. In practice, the charge/discharge coefficient is ≈1.05 to 1.15.

1.4.5 Temperature Influence on Capacity of Lead-Acid Cell

Lead-acid battery capacity depends very strongly on temperature. The battery capacity decreases approximately 0.5% to 1% per degree Celsius (typically 0.6% per degree Celsius). The temperature dependence of the capacity is affected by battery design, plate distance, specific surface of the plates, etc.

To refer to capacity C measured at a temperature of 20°C (C_a), the following formula is used:

$$C_a = \frac{C}{1+\delta(t-20)} \quad \delta = 0.006$$

The capacity/temperature dependence $C = f(t)$ is presented in Figure 1.13.

1.4.6 Energy and Power of a Lead-Acid Battery Cell

The amount of energy transferred to a battery during charge (E_{ch}) or delivered by a battery during discharge (E_d) under constant-current condition is given by the following expressions:

$$E_{ch} = U_{ch} I_{ch} t_{ch}$$

$$E_d = U_d I_d t_d$$

where U_{ch} and U_d are the mean voltages.

When the discharge current increases, the energy delivered by the battery decreases. Therefore, for traction applications, or when the battery is used to supply

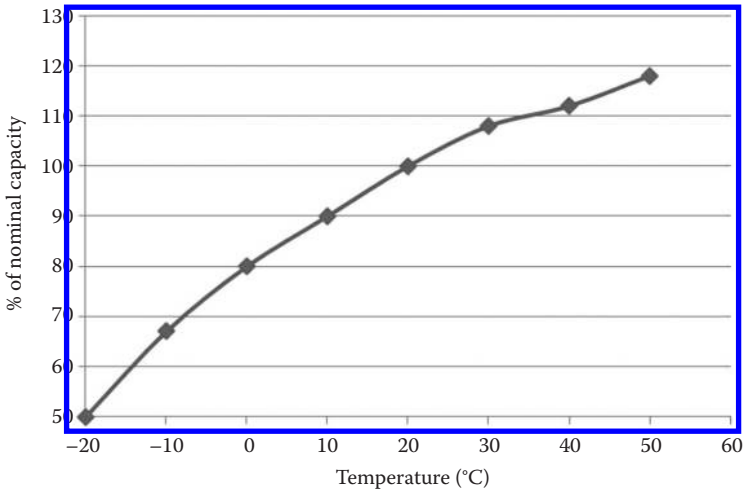

FIGURE 1.13 Capacity (10-h discharge rate) versus temperature.

energy, the discharge has to be carried out with a moderate current at an ~3- to ~10-h discharge rate.

The ratio between the energy utilized during discharge (E_d) and the energy consumed during charge (E_{ch}) is known as the energy coefficient (WhE):

$$WhE = (E_d/E_{ch}) \cdot 100$$

The value of WhE can be obtained as a product of the voltage and the amp-hour efficiencies. Thus, if $AhE = 90$ and $U_E = 0.83$, then $WhE = 75\%$. The faster the charge or discharge rate, the lower the energy efficiency.

The power of a battery is the energy delivered per unit time. The power per unit weight or volume is known as the specific power of the battery. The theoretical power is determined by

$$M = U_d I_d = I_d^2 R + I_d^2 r$$

where the first term is the power delivered by the battery in the external circuit. The second term is lost in the cell. It is dissipated in the battery and leads to heating.

The useful power is equal to

$$I_d^2 R = U_d I_d - I_d^2 r$$

The maximum power of the battery is reached when the resistance of the external circuit is equal to the internal resistance of the battery. Figure 1.14 presents the power versus current dependence for a 100-Ah, 12-V SLI battery.

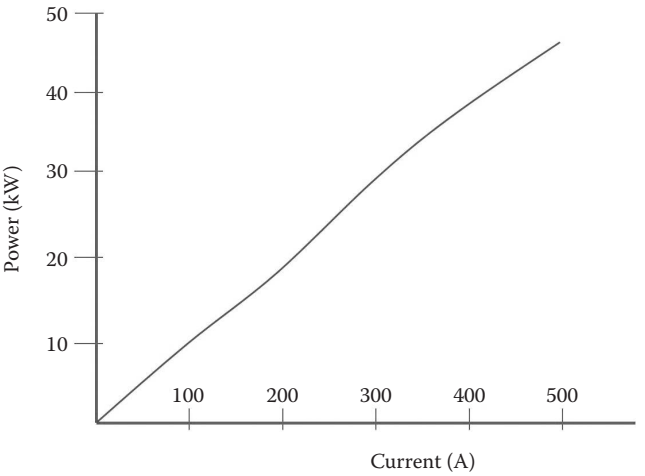

FIGURE 1.14 Power versus current dependence for a 100-Ah, 12-V SLI battery.

When the current increases, the power also augments. Therefore, to deliver high power, batteries have to be discharged at high currents. This is the case with SLI batteries. During discharge, the current is equal to 3 to 5 times the rated capacity.

1.4.7 Electrochemical Reactions of Water Decomposition in a Lead-Acid Battery Cell

Figure 1.15 presents a scheme of the equilibrium potentials of a $PbSO_4$/Pb and PbO_2/$PbSO_4$ electrode system as well as the reactions of H_2 and O_2 evolution [3]. The hatched zones represent the potential regions where the respective electrodes change with changes in H_2SO_4 concentration. The dashed curves give the Tafel dependencies for H_2 and O_2 evolution. The equilibrium potential of O_2 evolution is 1.23 V. When electric current flows through the electrode, however, evolution of O_2 starts at 1.8 V. This potential difference indicates a high overvoltage of O_2 evolution. The case is similar also with H_2 evolution. The high overvoltage of H_2 and O_2 make possible the existence of the lead-acid battery.

When the cell is charged galvanostatically, the potentials of the two electrodes increase. When the electrode potentials reach the potentials of H_2 and O_2 evolution, gassing starts. During overcharge, the basic electrochemical reaction that occurs is that of water decomposition and evolution of H_2 and O_2. When 1 Ah of electricity passes through the electrode, 0.3661 g of H_2O is decomposed to 0.0367 g of H_2 and 0.2985 g of O_2.

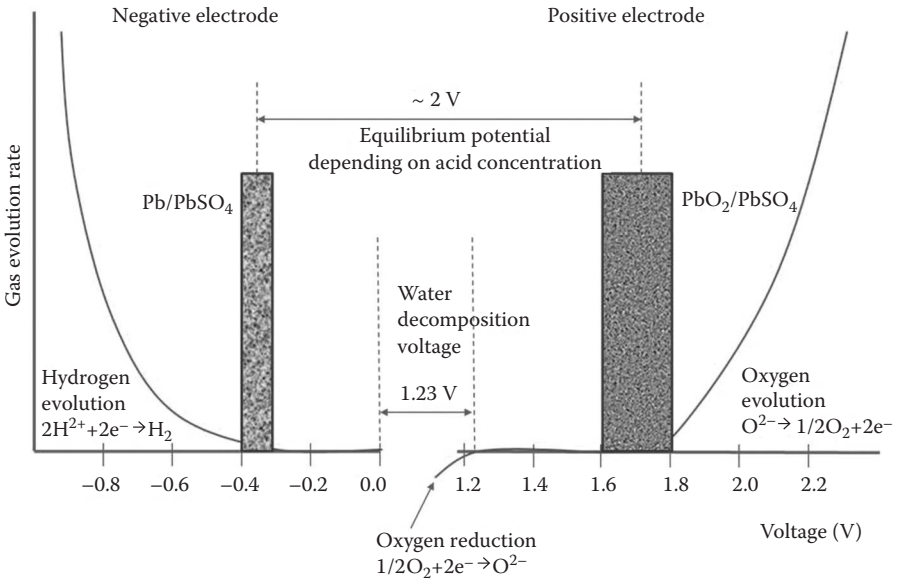

FIGURE 1.15 Electrochemical reactions proceeding in lead-acid cells. (From Pavlov, Lecture Course on VRLA, Beijing, China, 2000.)

The difference between the potential of the electrode when electric current flows through it and its equilibrium potential is called *overvoltage* and is given by the Tafel equation:

$$\eta = E_i - E_e$$
$$\eta_{H_2} = a + b\log i$$
$$\eta_{O_2} = a + b\log i$$

where $a = f_{(\text{nature of the metal})}$ and $b = f_{(\text{mechanism of the processes})}$.

The constant a is determined by the electrode material on which H_2 and O_2 are evolved, and the constant b depends on the mechanism of the processes that occur.

Water decomposition may be reduced during battery operation by three different means, as illustrated in Figure 1.16.

1. First, by increasing the overvoltage of H_2 and O_2 evolution by choosing an antimony-free grid alloy.
2. Second, through recombination of the released O_2 and H_2 to water again. This is accomplished by the use of a catalyst, platinum or tungsten carbide (WC). This process requires equivalent amounts of H_2 and O_2 to be evolved. This reaction is highly exothermic and great amounts of heat are released, which requires special precaution measures to restrict the rate of the process. To avoid these hazards, the reactions of O_2 reduction and H_2 oxidation are separated in space; that is, they proceed at the two electrodes, which are partially immersed in the electrolyte. In this case, the requirement for equivalent amounts of the two gases is no longer valid, because each of the

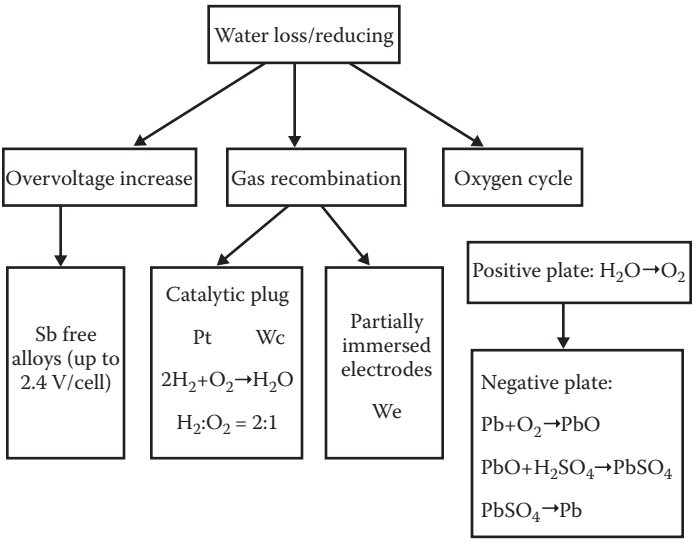

FIGURE 1.16 Possible methods to reduce water loss in a lead-acid battery.

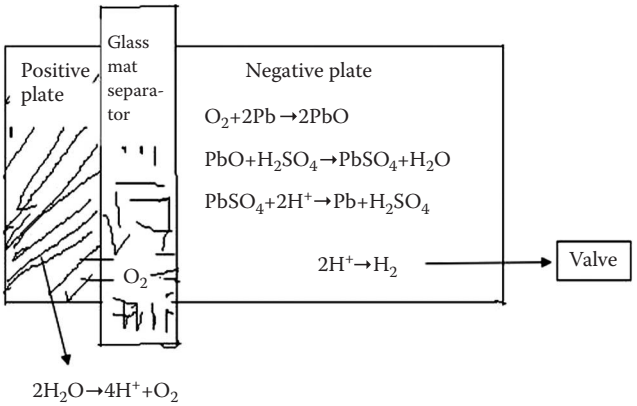

FIGURE 1.17 Oxygen cycle.

gases reacts independently on a separate electrode. For a long time platinum was used as a catalyst for the reaction, but we have recently proposed that WC be used instead.

3. Third, through a closed oxygen cycle, as shown in Figure 1.17. Lead-acid batteries are designed in such a way that their positive plates are charged first and oxygen evolution starts. The generated oxygen diffuses toward the negative plates and oxidizes lead to $PbSO_4$. The chemical reaction of lead oxidation precludes charging of the negative plate, and hence no hydrogen is evolved in the cell, and the oxygen released from the positive plate is fully consumed by the negative one. The whole amount of oxygen must react, provided it is not allowed to enter the space above the active block. This is achieved by the use of gelled electrolytes in which cracks are created that serve as channels for the movement of oxygen, or by the introduction of special glass mat separators. The closed oxygen cycle is considered the ideal case because no hydrogen is evolved on the negative plate. In practice, however, the electrochemical reaction of charging of the plate is always accompanied, though at a lower rate, by a parallel electrochemical reaction of hydrogen evolution.

1.5 BASIC COMPONENTS

The major components in a lead-acid battery include a positive grid, negative grid, positive active material, negative active material, electrolyte, top lead, separator, and plastic container. The weight distributions of common SLI batteries and traction batteries are shown in Figure 1.18.

The weight contribution of the different battery components can be calculated from the following reaction:

$$Pb + PbO_2 + 2H_2SO_4 \rightleftarrows 2PbSO_4 + 2H_2O$$

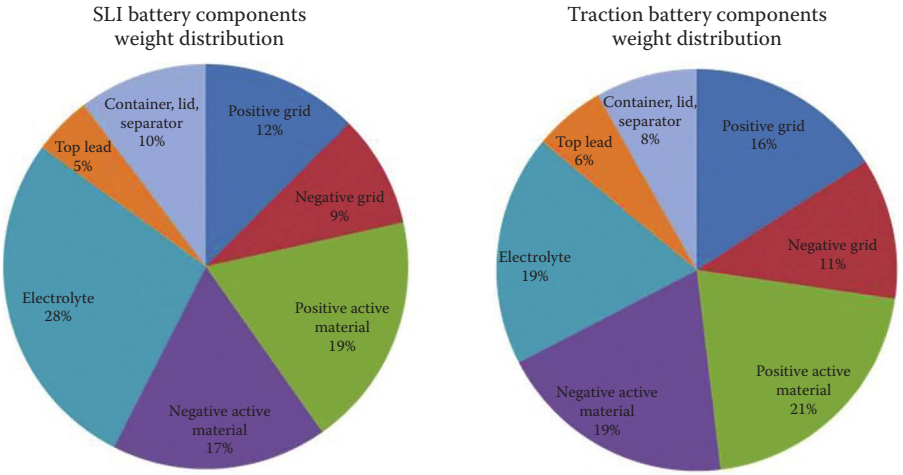

FIGURE 1.18 Weight component of SLI and traction lead-acid batteries.

The maximum amount of electricity that can be stored per unit weight can be calculated from the molar weights of the reactants:

$$2\ F = 53.61\ Ah$$

The weight contributions of the separate battery components are presented in Table 1.4.

The maximum energy that can be delivered by the reaction is equal to $E = QU = 53.61 \times 1.95 = 104.5$ Wh. The specific energy per 1 kg of materials will be 104.5/0.6426 = 162.6 Wh/kg. The denominator is obtained from the sum of the weights of Pb, PbO_2, and H_2SO_4 that take in the reaction.

Figure 1.19 represents the theoretical maximum amount of energy that a lead-acid cell can deliver. For 1 kWh to be delivered by a theoretical lead-acid battery cell, 6.15 kg of active materials are needed for the reaction. To transform this theoretical cell into a practical power source, however, a number of technical components are necessary such as grids, separators, battery container, valve, H_2SO_4 diluted with water in excess amount, etc.

TABLE 1.4
Weight Contributions of the Separate Battery Components

Substance	Molar Weight (g)	Maximum (g/Ah)	Capacity (Ah/kg)
Pb	207.2	3.865	258.7
PbO_2	239.2	4.462	224.1
$PbSO_4$	303.3	5.657	176.8
H_2SO_4	98.08	3.659	273.2
H_2O	18.02	0.6722	1487

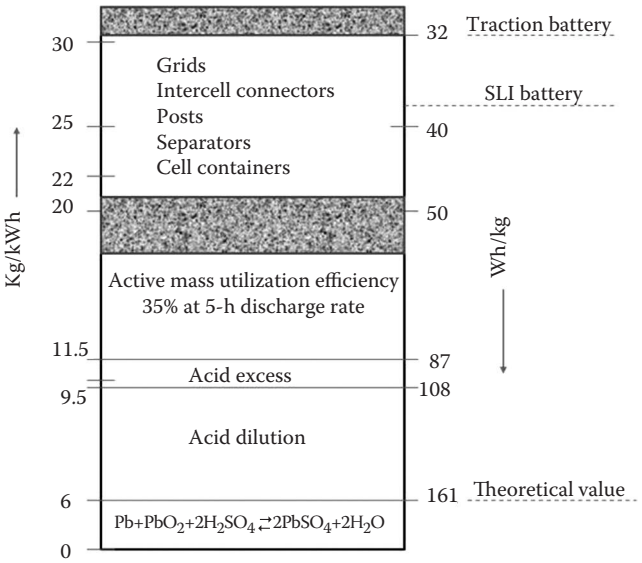

FIGURE 1.19 Theoretical maximum energy of lead-acid battery. (From Pavlov, Lecture Course on VRLA, Beijing, China, 2000.)

In practice, only part of the active materials participates in the reaction. Figure 1.19 also shows the contribution of the different components to making a Pb/PbO_2 cell technically realizable and properly operating.

The reactions in the lead-acid cell proceed on two electrodes detached by a separator and immersed in solution with specific gravity 1.28. The whole system is placed in a container closed by a cover that is fitted with an outlet valve. This construction weighs about 30 kg and yields 1 kWh of energy.

Table 1.5 lists the energy values and the utilization of the active materials for the three major types of batteries.

The high parameter values for SLI batteries are due to the specific battery design and the battery only undergoing shallow discharge on starting of the engine. It serves

TABLE 1.5
Energy Values and Utilization of the Active Materials

	Energy		Active Mass Utilization (Ah/kg)	
Type of Battery	**Wh/kg**	**Wh/L**	**PbO_2**	**Pb**
SLI (20-h rate)	30–40	75–100	110–130	130–160
VRLA (60 Ah)	21–31	45–85	66–90	80–140
Traction cell (5-h rate)	25–32	60–100	60–90	80–100
SLA	20–28	35–60	60–100	80–100

mainly as a source of power. Besides, most of the time the battery is in a safe condition of overcharge or 0°C.

Traction batteries operate under deep charge/discharge conditions and hence the utilization of the active materials should be decreased to ensure sufficiently long battery life. To withstand the strong corrosion attacks, the positive grids of conventional stationary batteries are oversized, which reduces their specific energy. A considerable excess of H_2SO_4 electrolyte is used to reduce voltage decline on discharge. In addition, watering of the battery is seldom needed.

Valve-regulated lead-acid (VRLA) batteries can be small in size, which results in a high ratio between the inactive and active materials used. Consequently, the specific energy is low; when immobilized electrolytes are used, the utilization of the active materials is decreased. In this case, however, the lower H_2SO_4 reservoir, and partially the upper one, too, are removed, resulting in a higher volume specific energy.

1.5.1 Battery Grid (Current Collector)

The function of a battery grid is to act as a current collector, which is used to hold the active material and conduct electricity between the active material and the cell terminals.

Battery grids are often made of a lead alloy because pure lead is too soft. Currently, the trend for the lead alloy used for battery grid production is a quaternary alloy, which contains lead, calcium, tin, and aluminum. Calcium is added to the lead in the range of 0.03 to 0.20 wt% (depending on the battery manufacturers) to harden the lead. The current trend is to lower the calcium level to 0.03% to 0.05% for better corrosion resistance. Tin, in the range of 0.25 to 2 wt%, has been used in the lead-calcium alloy to enhance the alloy's mechanical and corrosion-resistant properties. However, due to the cost of tin, battery manufacturers tend to keep the tin content to a minimum. Aluminum is used to stabilize the drossing loss of calcium while molten. Some battery manufacturers have substituted strontium for calcium. Another metal that is being investigated is barium, but research has shown that its use might be detrimental to performance.

On the other hand, the most common metal used to harden lead is antimony. The amount of antimony has varied between 5 and 12 wt% depending on the battery applications and the cost of antimony. The modern grid manufacturing trend is to lower the antimony content or to be antimony free to allow the battery to be maintenance free. Antimony in the grids dissolves during battery operation and migrates to the negative plates, where it redeposits and promotes water splitting to hydrogen and oxygen; this results in the battery having a high antimony content grid that requires water to be added regularly. As the antimony content goes below 4%, the addition of small amounts of other elements such as cadmium, sulfur, copper, arsenic, selenium, tellurium, and various combinations thereof is necessary to prevent grid fabrication defects and grid brittleness. These added metal elements act as grain refiners to decrease the lead grain size.

In some regions, a widely used lead alloy is lead antimony cadmium. Antimony and cadmium will react to form an intermetallic compound SbCd. During charge, the positive grid undergoes corrosion and produces antimony in the corrosion layer.

The antimony and cadmium give excellent conductivity through the corrosion layer. Although a small amount of cadmium and antimony is leached from the grid corrosion and deposits on the negative grid, research has indicated that the cadmium is plated over the antimony and raises the potential of the negative plate, which diminishes the water loss.

1.5.2 Active Material

1.5.2.1 Determination of the Amount of Active Material in a Lead-Acid Battery Cell

The amounts of active materials (Pb, PbO_2, H_2SO_4) are determined based on Faraday's law. These values are theoretical. In practice, in batteries the coefficient of active mass utilization, r, is used:

$$r = \frac{W_r}{W} = \frac{C_r}{C_{theor}}$$

where W_r is the weight of the active mass that has reacted during discharge, yielding the C_r capacity of the cell, and W is the total active mass weight that would give the theoretical capacity C_{theor} according to Faraday's law. The value of r is determined by the technological level of the battery manufacturer, on their design, and on the conditions of battery operation.

Another two analogous characteristics are also used: the electricity that can be delivered by 1 kg of active material (expressed in Ah/kg) and the amount of active material (in g) that should react during discharge to Q_w to deliver 1 Ah of electricity (W_e).

For the negative plate, according to Faraday's law, when 1 Ah of electricity passes through the cell, theoretically 3.866 g of Pb would react at the negative plate. The theoretical capacity of the negative active mass is equal to

$$C_{theor} = W/3.866 \text{ Ah}$$

where W is measured. The relationship between Q_w and r can be given by the following expression:

$$Q_w = \frac{C_r}{W_r} \cdot r \quad \text{(Ah/kg)}$$

The relationship between Q_w and r is graphically presented in Figure 1.20. This curve allows easy transformation of one coefficient into the other.

For the positive plate, when 1 Ah of electricity passes through the cell, theoretically 4.464 g of PbO_2 would react at the positive plate. The theoretical capacity of the positive active mass (PAM) can be calculated by the following expression:

$$C_{theor} = W/4.463 \text{ (Ah)}$$

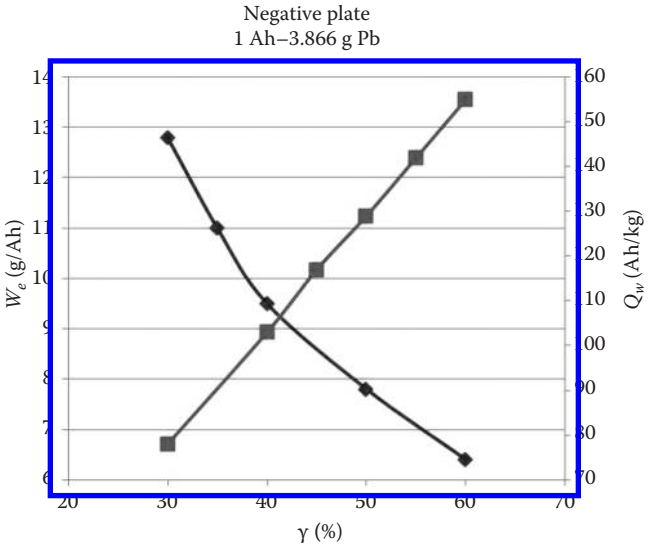

FIGURE 1.20 The relationship between r, Q_w, and W_e for negative plates.

Figure 1.21 represents graphically the relationship between r, Q_w, and W_e for positive plates. The active mass utilization coefficients depend on the technology of plate preparation and on cell and grid design. Through the technology of plate manufacture, appropriate structures of the active mass and the corrosion layer can be obtained that exert a strong influence on the performance of the plates. Thus, the

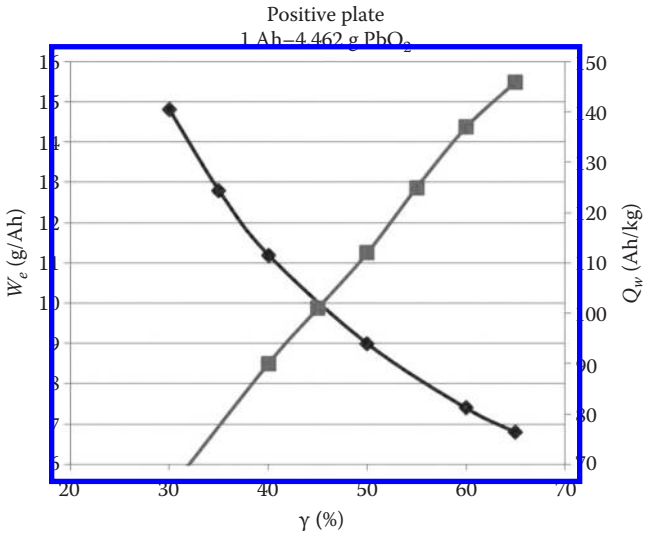

FIGURE 1.21 The relationship between r, Q_w, and W_e for positive plates.

coefficient of active mass utilization may serve as an indicator for the technical level of a given battery manufacturer.

1.5.2.2 Positive Active Material (Cathode Paste)

The positive active material contains lead oxide and other additives such as red lead (Pb_3O_4), which is more conductive than lead oxide. Red lead is produced by further roasting lead oxide in an airflow chamber until the desired oxidation stage is achieved. Generally, red lead will reduce the free lead contained and increase the particle size.

Table 1.6 shows a conventional positive active material recipe.

As mentioned, red lead (Pb_3O_4) is more conductive than lead oxide (PbO), which facilitates the electrochemical formation of lead dioxide (PbO_2).

1.5.2.3 Negative Active Material (Anode Paste)

Table 1.7 shows a conventional negative active material recipe. Additives such as lignosulfonates, $BaSO_4$, and active carbon are added to the negative paste. It has been established that although $BaSO_4$ is isomorphic with $PbSO_4$, it has no effect on the phase composition of the paste. A lignosulfonate is an organic expander that suppresses fully the formation of $4PbO.PbSO_4$ (4BS) and orthorhombic-PbO phases. Formation of 4BS is suppressed due to the suppressed formation of

TABLE 1.6
Positive Active Material Recipe

Material	Unit	Amount
PbO	kg	25
H_2SO_4	L	1.6
Water	L	4.41
Pb_3O_4	kg	1.25
Graphite powder	kg	0.075
Paste density	g/cm^3	3.7

TABLE 1.7
Negative Active Material Recipe

Material	Unit	Amount
PbO	kg	25
H_2SO_4	L	1.5
Water	L	3.65
Barium sulfate ($BaSO_4$)	kg	0.2
Carbon black	kg	0.075
Sodium lignosulfonate	kg	0.04
Humic acid	kg	0.15
Paste density	g/cm^3	4

orthorhombic-PbO, which is a component of the 4BS phase. A family of eight lignosulfonates produced by Borregaard Ligno-Tech (Norway) has been investigated. The beneficial effect of the expander has been found to correlate positively with low average molecular weight of the lignins and of their derivates, high COOH content, low OCH_3 group and organic S content, optimum ArOH content, and high lignin purity. Expanders with a different chemical composition should be selected for different battery type applications. It has also been established that phenol groups of the expander structure react with Sb, Sn, and Ca ions to form organometallic compounds, which influence battery performance.

The function of the barium sulfate is to act as a nucleating agent for lead sulfate produced when the plate is discharged. The lead sulfate discharge product deposits on the barium sulfate particles, ensuring homogeneous distribution throughout the active material and preventing coating of the lead particles. The term *barium sulfate* represents both blanc fixe and barite forms of this compound and mixtures thereof in particle sizes from 0.5 to 5 μm. It is desirable for the barium sulfate crystals to have a very small particle size, of the order of 1 μm or less, so that a very large number of small seed crystals are implanted in the negative active material. This ensures that the lead sulfate crystals, which are growing on the barium sulfate nuclei, are small and of a uniform size so that they are easily converted to lead active material when the plate is charged.

Active carbon such as carbon black increases the electrical conductivity of the active material in the discharged state, which improves its charge acceptance. The carbon is usually in the form of carbon black and/or activated carbon. The amount of carbon in the negative active material of conventional expander formulations is only a small fraction of a percent.

The function of the lignosulfonate is more complex. It is chemically adsorbed on the lead active material, resulting in a significant increase in its surface area. Without lignosulfonate, the surface area is of the order of approximately 0.2 m^2/g while, with 0.50% of lignosulfonate, this is increased to approximately 2 m^2/g. This high surface area increases the efficiency of the electrochemical process, which improves the performance of the negative plate. The lignosulfonate also stabilizes the physical structure of the negative active material, which retards degradation during operation of the battery. This property increases the life of the battery in service. The organic material can be any lignosulfonate compound or other suitable organic material that can be adsorbed on the surface of the negative active material and thereby affect its surface area and electrochemical behavior.

1.5.3 Electrolyte

The electrolyte of a lead-acid battery is sulfuric acid, H_2SO_4. The theoretical amount of H_2SO_4 that would yield 1 Ah of electricity is 3.666 g. To calculate the real volume of electrolyte to be used, the following parameters should also be taken into account:

- Amp-hour capacity of the cell
- Efficient range of H_2SO_4 concentration changes during charge and discharge, etc.

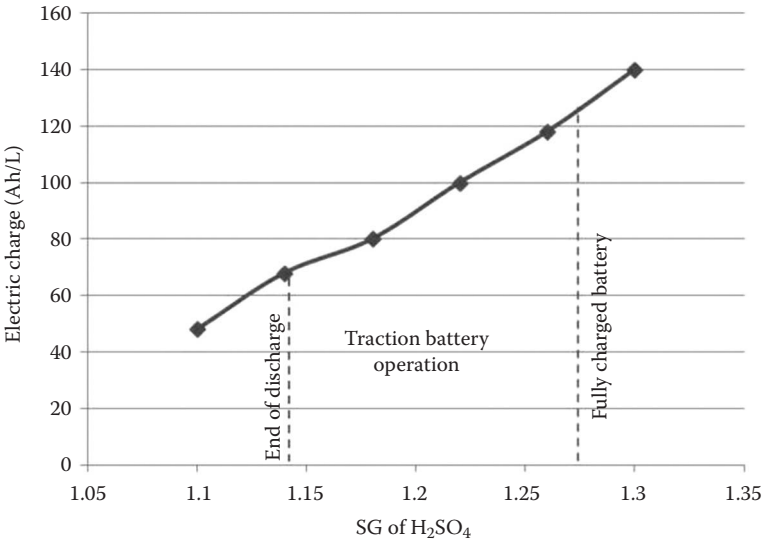

FIGURE 1.22 Relationship between capacity and specific gravity.

The relationship between the specific volume capacity (Ah/L) and the specific gravity of H_2SO_4 is presented in Figure 1.22. Based on Figure 1.22, the capacity (in amp-hours) obtained as a result of the reaction of 1 liter of H_2SO_4 solution with a given density can be determined.

For discharge starter batteries with a 20-h discharge rate, if properly sized, the H_2SO_4 concentration will decrease from 1.28 specific gravity to 1.06 specific gravity. In this case, 1 L of H_2SO_4 electrolyte with specific gravity 1.28 would deliver 106 Ah of electricity after 20 h of discharge (end of discharge H_2SO_4 concentration 1.06 specific gravity). On this basis, the required volume of electrolyte with specific gravity 1.28 can be calculated for the respective Ah capacity of the battery.

The properties of sulfuric acid with different specific gravity are shown in Tables 1.8, 1.9, and 1.10.

1.5.4 Separator

Separators are used to electrically insulate between positive and negative plates to prevent a short circuit. Separators are porous to allow acid transport into or out of the plates. The common separators are microporous polyethylene (PE) or absorptive glass mat (AGM). AGM is a nonwoven fabric made with glass microfiber. It is used widely for VRLAs because it is highly porous (90% to 95%) and can absorb more acid and has small pore size to maintain electrolyte levels in battery. Table 1.11 shows the properties of battery separator materials.

SLI batteries often use microporous PE in either leaf or envelope form, which surrounds either the positive or negative plate, or both. The average pore diameters are in the 5- to 30-μm range. Industrial batteries such as those used for deep-cycle

TABLE 1.8
Properties of Sulfuric Acid

Specific Gravity			H_2SO_4				
at 15°C	at 25°C	Temperature Coefficient α	wt%	vol%	mol/L	Freezing Point (°C)	Electrochemical Equivalent per Liter (Ah)
1.000	1.000	–	0	0	0	0	0
1.050	1.049	33	7.3	4.2	0.82	–3.3	22
1.100	1.097	48	14.3	8.5	1.65	–7.7	44
1.150	1.146	60	20.9	13.0	2.51	–15	67
1.200	1.196	68	27.2	17.7	3.39	–27	90
1.250	1.245	72	33.2	22.6	4.31	–52	115
1.300	1.295	75	39.1	27.6	5.26	–70	141
1.350	1.345	77	44.7	32.8	6.23	–49	167
1.400	1.395	79	50.0	38.0	7.21	–36	
1.450	1.445	82	55.0	43.3	8.20	–29	
1.500	1.495	85	59.7	48.7	9.20	–29	

TABLE 1.9
Sulfuric Acid Properties in Various Types of Lead-Acid Batteries

	Specific Gravity	
Type of Battery	Moderate Environment	Tropical Environment
SLI	1.260–1.290	1.210–1.230
Heavy duty	1.260–1.290	1.210–1.240
Golf cart	1.260–1.290	1.240–1.260
Electric vehicle	1.275–1.325	1.240–1.275
Traction	1.275–1.325	1.240–1.275
SLA	1.210–1.225	1.200–1.220
Railroad	1.250	1.250
Aircraft	1.260–1.285	1.260–1.285

TABLE 1.10
State of Charge versus Specific Gravity of Sulfuric Acid

	Specific Gravity			
State of Charge	A	B	C	D
100%	1.330	1.280	1.265	1.225
75%	1.300	1.250	1.225	1.185
50%	1.270	1.220	1.190	1.150
25%	1.240	1.190	1.155	1.115
Discharged	1.210	1.160	1.120	1.000

TABLE 1.11
Properties of Various Types of Battery Separators

Type	Rubber	Cellulose	PVC	PE	Glass Fiber	Microglass
Year available	1930	1945	1950	1970	1980	1985
Backweb mils	20+	17–30	12–20	7–30	22–26	10–150
Porosity (%)	55–65	60–70	>40	55–65	80–90	>90
Maximum pore size (μm)	>5	35	25	<1	45	15–30
Average pore size (μm)	3	25	15	<0.1	80	10–15
Electrical resistance in H_2SO_4 (mΩ-in.^{2})	30–50	25–30	15–30	8–40	10	<5
Purity	Good	Fair	Good	Good	Good	Excellent
Corrosion resistance	Good	Fair	Excellent	Excellent	Excellent	Excellent
Flexibility	Brittle	Brittle	Brittle	Excellent	Good	Fair

applications often use AGM separators. Heavy-duty batteries usually have microporous rubber or PE separators that have fine pores and a long life. Glass fiber scrim can be found as an additive to some separator material to improve the acid retention.

1.6 FABRICATION

Fabrication of lead-acid batteries includes the production of lead oxide, production of positive and negative current collectors, mixing and pasting of positive and negative active material onto current collectors, positive and negative electrode curing, battery assembly, electrolyte addition, sealing, and battery formation. Figure 1.23 shows a flowchart of the fabrication process [4].

1.6.1 Lead Oxide Production

Lead oxide is the main component of the active material for both the positive and negative electrodes. Lead oxide is made by oxidizing lead by using either the Barton pot process or the Ball mill process.

1.6.2 Paste Production

Both the positive and negative pastes are prepared as a doughlike material by following these steps and using a mechanical mixer:

1. Add lead oxide to the mixer.
2. Add the required additives.
3. Add water.
4. Add sulfuric acid.

Conventional mechanical mixers are batch type. The paste viscosity will rise at the beginning of paste mixing, but will then gradually decrease. Mixing of paste

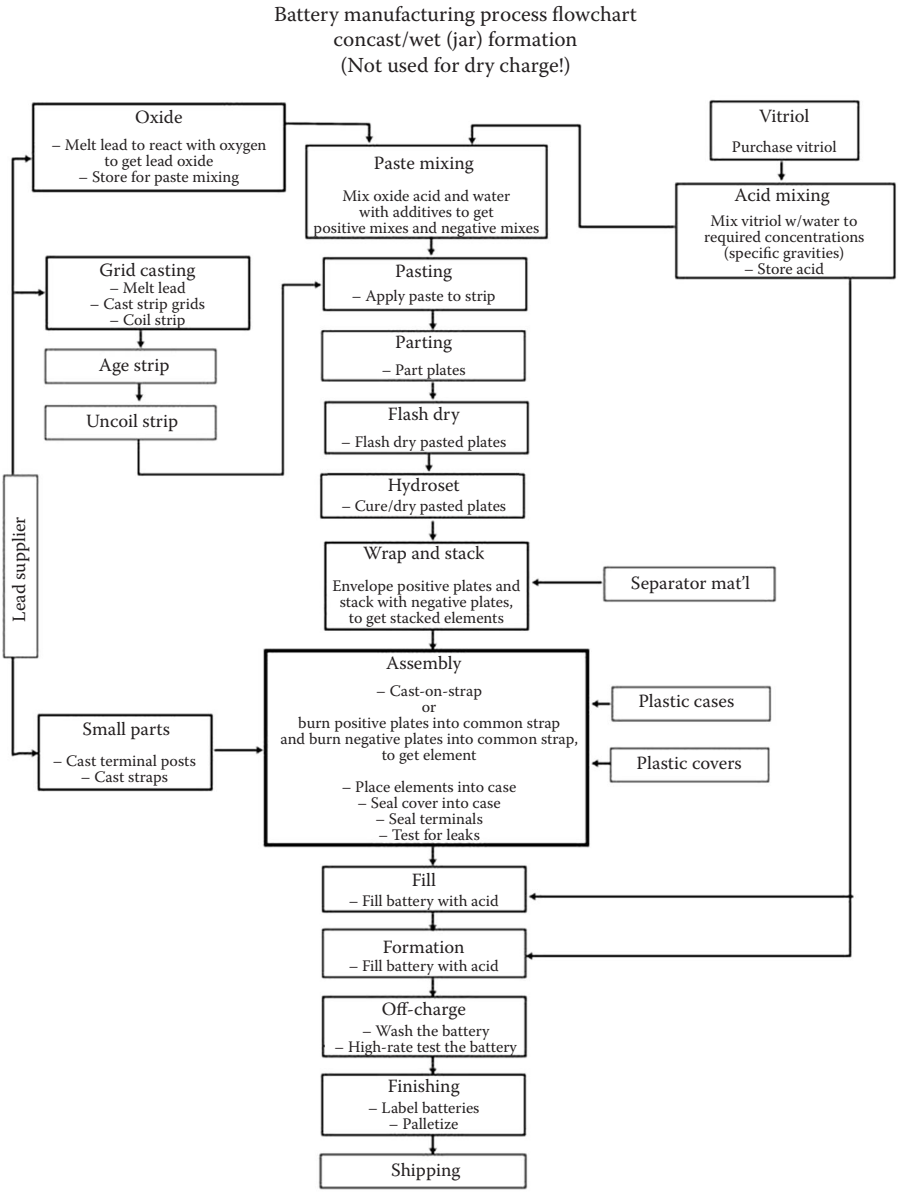

FIGURE 1.23 Battery assembly process. (From http://www.docstoc.com.)

will release heat generated by the reaction of sulfuric acid and lead oxide. The temperature of the paste needs to be controlled and is often controlled by either cooling the mixer or evaporating an extra volume of water in the paste mixture. The ratio of lead oxide, water, and sulfuric acid varies depending on the battery's application. For example, plates for SLI applications generally have a low PbO:H_2SO_4 ratio,

whereas plates for deep-cycle applications have a high $PbO:H_2SO_4$ ratio. In addition, the amount of sulfuric acid affects the plate density: The more acid used, the lower the plate density. Paste density is measured by using a cup with a hemispherical cavity and by the measurement of paste consistency (viscosity) with a penetrometer.

Teck Inc. has developed a continuous paste mixer to produce lead-acid battery paste over a broad output and chemistry range.

1.6.3 Pasting

In the pasting process, the paste is integrated with the grid to produce a battery plate. This process is carried out through extrusion, in which the paste is pressed by a scraper or by machine into the grid interstices. Two types of pasting machines are used by manufacturers: a fixed-orifice paster or a belt paster. An orifice paster pushes paste into both sides of the plate simultaneously, whereas a belt paster presses paste into the open side of a grid that is being conveyed past a paste hopper on a porous belt.

1.6.4 Flash Drying

After pasting, the plates are racked or stacked for curing. Stacked plates contain enough moisture to stick together, thus the plates usually are passing through a high-temperature drier or oven to dry the plate surface prior to stacking, in what is called the *flash-drying process*.

1.6.5 Curing

The curing process is designed to make the paste bond with the current collector and also make the paste into a cohesive, porous material. Generally, the higher the temperature employed during curing, the better the adhesive bond produced. Curing is an important and time-consuming aspect of the manufacture of lead-acid batteries because the wet active paste material precursor was cured and converted to a dry porous mass [5].

The conditions for the curing process vary pending on the paste formulation and the battery applications. The curing process is often carried out using curing ovens with controlled temperature and humidity to ensure sufficient moisture and heat are available to oxidize free lead in the paste. The curing oven temperature ranges from 65°C to 90°C and the curing oven humidity is maintained above 95%. Curing the paste at a higher temperature for extended hours will produce a high percentage of tetrabasic lead sulfate and result in a plate with a lower energy density. At the end of curing, the free lead content of the paste should be lower than 2%. Table 1.12 shows a typical curing profile.

A conventional curing process for SLI plates is the *hydroset process*, which is conducted at low temperature and low humidity for 24 to 72 h. The curing temperature ranges from 25°C to 40°C, and the humidity ranges from 8% to 20% of water. The plates are usually covered by canvas, plastic, or paper to retain their moisture. The hydroset process is usually carried out in an enclosed room where the

TABLE 1.12
Curing Process

No.	Item	Description
1	Loading cycle	Ramp up to 54°C and 95% relative humidity (RH) and hold until all plates are loaded.
2	Curing cycle	Ramp up to 80°C and 95% RH and hold for 72 h.
3	Drying cycle	Ramp up to 90°C and 75% RH and hold for 24 h.

temperature and humidity can be controlled. During the hydroset curing process, the plates undergo an exothermic reaction and reach a peak temperature as the plates cure and temperature and humidity decrease.

Paste that has been insufficiently cured is easily broken. The uncured paste is pale in color and soft. If the plate has been insufficiently cured, it can be rewetted and reheated to force the paste to cure. Another way is to dip the partially cured paste into dilute sulfuric acid, which is called "pickling." The pickling curing process is also used for curing of powder-filled tubular positive plates.

Once the plates have been cured, they have a long shelf life.

1.6.6 Formation

Once the plates have been cured, they need to be electrically formed or charged before they become functional positive and negative electrodes. During formation, the positive paste is converted to brownish black lead dioxide; the negative paste is converted to a soft gray lead. The cured plates can be formed before (tank formation) or after assembly (case formation) into the battery case.

In tank formation the cured plates are formed as doubles, with two to five plates stacked together in a slotted plastic formation tank and facing the counter-electrode in adjacent slots that are spaced 1 in. or less away. In addition, all positive plates are placed on the same side and all negative plates are placed on the other side. All plates with the same polarity are connected to a low-voltage, constant-current power supply. The formation tank is filled with electrolyte with electric current passed until the plates are formed.

Case formation is conducted after the batteries have been assembled and filled with electrolyte. These two formation methods are designed to convert lead monoxide paste to lead dioxide on the positive plates and lead monoxide to lead on the negative plates.

1.6.7 Assembly

Normally, a 2-V cell contains about 3 to 30 plates with separators in between. Plates and separators are stacked by a stacking machine or manually. The stacked plates are then staged on roller conveyors or carts to the interplate welding operations, where the positive plates and negative plates are welded into individual groups. There are

two general methods of welding: The first is done with the lugs of the plates facing upward, and the other is done by immersing the lugs of the plates into a pool of molten lead alloy. The first method is the traditional method for assembling lead-acid batteries, also called *comb mold welding*. The second welding process, in which the plates are welded with the plate lugs facing downward, is called the *cast-on strap* (*COS*) process.

Visual examination is important as the first quality check for the weld. A good weld is required between each plate lug and the strap so that it will have minimum voltage drop during high-rate discharge performance. Electrical testing for short circuits is the second quality check before further assembly.

Once the welding process is done, the groups are dropped into a battery case to carry out the rest of the assembly process. For example, a 12-V lead-acid battery consists of six cells. These cells are connected through either loop over the partition or through the partition wall. The loop-over-partition type requires long intercell connections to be used, where the cell-to-cell connections travel over the intercell partition wall and set in a slot. When connecting the cells through the partition wall, the tabs on the ends of the casted straps are positioned over holes that have been prepunched into the intercell partitions of the battery case and welded together manually using a torch or automatically by a resistance welding machine. This second method also squeezes the tabs and the intercell partition to provide a leak-proof seal.

1.6.8 Case to Cover Seal

Enclosed cells are necessary and important to minimize safety hazards such as internal short circuits from electrolyte mist. The four different types of processes used to seal the case to the cover are as follows:

1. *Heat (fusion) seal*: A heat seal is done by preheating both the case and the cover on a platen, then forcing the two together mechanically or by ultrasonic welding of the case and cover. Once the battery case and cover have been heat sealed, it is almost impossible to repair. If the battery is found damaged, the cover and the case are discarded and replaced in the hopes that the grouped plates can be salvaged.
2. *Epoxy cement seal*: An epoxy cement seal is done by placing epoxy cement into a groove in the cover. The battery is inserted and positioned so that the case and intercell partition lips fit into the epoxy-filled groove. To activate the epoxy cement, the batteries are often passed through a continuous oven.
3. *Tar (asphalt) seal*: Traditionally, lead-acid batteries are sealed using tar. Molten tar is dispensed from a heated kettle to fill a groove between the case and the cover. The tar must be hot enough to flow easily, but cool and viscous enough to solidify. A tar seal allows for easy repair of the battery.
4. *Epoxy glue seal*: An epoxy glue seal employs either solvent cement or a thermal seal. These types of seals are often used for stationary batteries and traction cells so that coolant can be circulated through the terminals.

1.7 TYPES OF LEAD-ACID BATTERIES

The major types of lead-acid batteries are SLI batteries, deep-cycle batteries, stationary batteries, and VRLA batteries.

1.7.1 SLI Battery

Starting, lighting, and ignition (SLI) batteries are widely used in the automotive industry to start an internal combustion engine. SLI batteries endure a work cycle of discharging briefly at a high current to start the engine, then, once the engine is running, a generator recharges the battery and then maintains it on float at a full charge or slight overcharge status. The parasitic electrical load of lights, motors, and electronics causes a gradual discharge of the battery during engine idle. This type of working cycle means that SLI batteries require a high power density and good cycle life while maintaining a low cost.

High power density requires the plates and separators to be thin and very porous with a low paste density. On the other hand, the high cycle life requires premium separators, a high paste density with a paste consisting of α-PbO_2 or another bonding agent, and a high antimony (5% to 7%) containing grid. To maximize the desired type of performance, optimizations and trade-offs between power density, energy density, cycle life, float service life, and cost are required.

The cranking ability of the SLI battery is directly proportional to the geometric area of the plate surface and the total surface area of the positive plates facing the total surface area of the negative plates. To maximize the cranking ability, SLI batteries usually employ an "outside negative" design, in which each 2-V cell consists of $n + 1$ negative plates interspersed with $2n$ separators and n positive plates. Typically, the cranking ability is 0.155 to 0.186 CCAs per square centimeter of positive plate surface at –17.8°C (0°F). The cranking ability is often limited by the positive plate at a higher temperature range (>18°C) and the negative plate at a lower temperature range (<5°C). The high cranking capacity of an SLI battery can be obtained by minimizing electrical resistance with a different grid pattern design, by employing thin plates to allow more surface area for the positive and negative plate facing each other, or by using a higher acid concentration than motive power batteries or stationary batteries. Modern SLI batteries are maintenance free, meaning they do not require the addition of water during their lifetime. An important feature of the maintenance-free battery is the use of low-antimony lead grids or no antimony at all. The use of the low-antimony or nonantimony lead grids reduces the overcharge current significantly, reducing the water loss during overcharge.

As shown earlier in Figure 1.10, an SLI lead-acid battery can be discharged at any rate of current without causing damage to the battery as long as the discharge does not go beyond the point where the battery approaches exhaustion or where the voltage falls below a useful value. At a high discharge rate, the capacity is minimized because the electrolyte in the pore structure of the plates becomes depleted and the electrolyte cannot diffuse rapidly enough, which results in the local electrolyte having a lower electrical conductivity and higher internal resistance. The high internal resistance results in a cell voltage that cannot be maintained. Intermittent discharge,

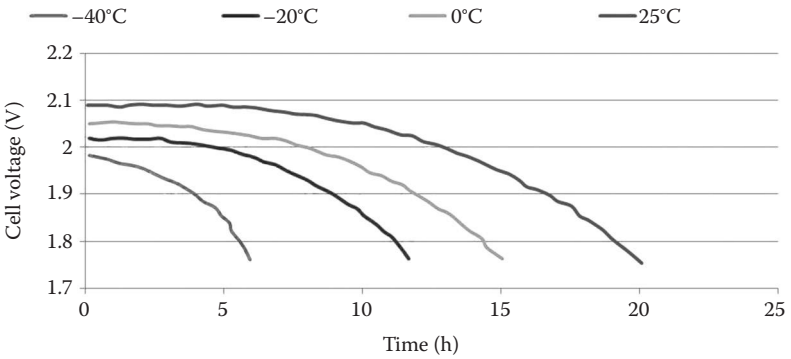

FIGURE 1.24 Temperature effect on capacity of an SLI battery. (Jung, J. *Lead-Acid Battery, Electrochemical Technologies for Energy Storage and Conversion*, Chapter 4. 2012. Copyright Wiley-VCH Verlag GmbH & Co. KGaA. Reproduced with permission.)

which allows time for the local electrolyte to be replenished or recirculated, will improve the performance at a high discharge rate. At a low discharge rate, higher or nominal capacity can be obtained.

The performance of a lead-acid battery is also affected by temperature. Figure 1.24 shows the effect of temperature on discharge capacity. As shown in the figure, the capacity of a 20-h discharge rate battery is greatly affected by lowering the temperature; at –20°C, SLI batteries can deliver less than 60% of the battery capacity at 25°C.

SLI batteries deliver a high current for engine cranking, which requires the batteries to have low resistance and also affects battery design. As stated before, the plate surface area has a relationship with the CCA, which can be related to the electrochemical double layer of the battery active material. The capacitive reactance component of battery impedance can be determined by the voltage difference at two levels of discharge current. The resistance of a lead-acid battery increases nearly linearly during discharge as the specific gravity of the electrolyte decreases. The resistance difference between a charged battery and a discharged battery is about 40%. Temperature also affects the battery resistance where the battery resistance increases approximately 50% between 30°C and –15°C.

Figure 1.25 shows the self-discharge of three lead-acid batteries, each of which employs a different lead grid alloy. Batteries with lead antimony alloy plates can minimize the self-discharge. For example, batteries using lead calcium (nonantimony) negative and lead antimony positive plates have less self-discharge than batteries using a lead antimony lead alloy for both positive and negative plates.

A cranking amps (CA) test, CCA test, and reserve capacity (RC) test are the most common tests done on SLI batteries:

- CA is a rating used to describe the discharge load in amperes. The test is conducted with a new, fully charged battery at 0°C or 32°F to determine if the battery can continuously deliver for 30 seconds, while maintaining a terminal voltage equal or greater than 1.2 V per cell. It is sometimes referred to as *marine cranking amps.*

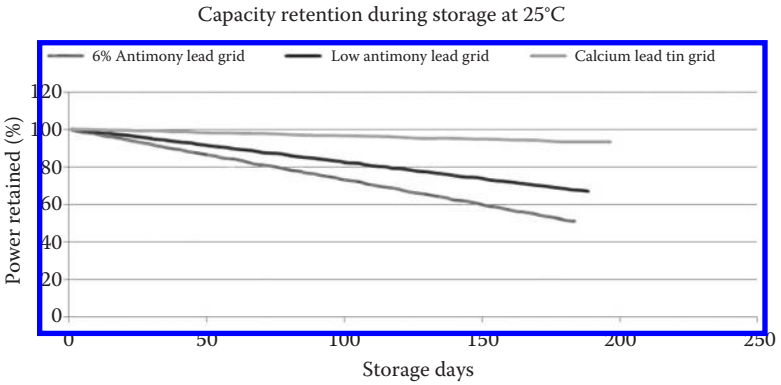

FIGURE 1.25 Impact of current collector material on battery self-discharge. (Jung, J. *Lead-Acid Battery, Electrochemical Technologies for Energy Storage and Conversion*, Chapter 4. 2012. Copyright Wiley-VCH Verlag GmbH & Co. KGaA. Reproduced with permission.)

- CCA is a rating used in the battery industry to define a battery's ability to start an engine in cold temperatures. The rating is the number of amps a new, fully charged battery can deliver at −17.8°C (0°F) for 30 sec, while maintaining a voltage of at least 7.2 V, for a 12–V battery. The higher the CCA rating, the greater the starting power of the battery.
- RC is a battery industry rating that defines a battery's ability to power a vehicle with an inoperative alternator or fan belt. The rating is the number of minutes a battery at 80°F can be discharged at 25 A and maintain a voltage of 10.5 V, for a 12-V battery. The higher the reserve rating, the longer the vehicle can operate should its alternator or fan belt fail.

SLI batteries are not suitable for deep discharge functions like a deep-cycle battery is and vice versa. An SLI battery will not last in deep cycle because the thin sponge-like plates would quickly dissolve with repeated deep cycling. Combination starter/deep-cycle batteries are available for trucks, buses, and public safety and military vehicles, but these units are big and heavy. Table 1.13 compares the typical life of starter and deep-cycle batteries when deep cycled [6].

TABLE 1.13
Cycle Performance of SLI and Deep-Cycle Batteries

Depth of Discharge	Starter Battery	Deep-Cycle Battery
100%	12–15 cycles	150–200 cycles
50%	100–120 cycles	400–500 cycles
30%	130–150 cycles	1000+ cycles

Source: Available at http://www.batteryuniversity.com.

1.7.2 Deep-Cycle and Traction Batteries

Deep-cycle batteries require good cycle life, high energy density, and low cost. The cycle life of a deep-cycle battery is usually longer than that of an SLI battery. The longer cycle life is achieved in the following manner:

1. Use thick plates with high paste density.
2. Cure the plates with a high-temperature and high-humidity profile.
3. Employ a low-specific-gravity electrolyte for formation.

Deep-cycle batteries are usually designed to be capacity limited by the amount of electrolyte instead of the active material in the plates in order to protect the plates and maximize the cycle life. Both positive and negative grids will degrade during cycling, but at the end of battery life, the battery capacity is generally limited by the positive plate. The end of deep-cycle battery life is when the battery can no longer produce 60% to 80% of the rated discharge capacity. The end of deep-cycle battery life is usually caused by disintegration of the positive active material, PbO_2, and corrosion of the positive grids.

Deep-cycle and traction battery cells consist of n positive plates and $n + 1$ negative plates. These batteries are often built to high voltage by assembling multiple individual cells. The advantage of this construction is the possibility of being able to replace one or a few cells when overall battery performance is degraded by a catastrophic failure of those cells. One indication of the suitability of the traction battery for such an application is the change in the specific gravity of the electrolyte during use.

Small traction batteries, such as those used for EVs, are sized to be between full-sized traction batteries and SLI batteries. Small traction batteries employ traction design concepts, which utilize a high paste density and careful control of plate curing and formation to maximize the positive utilization. Small traction batteries can also employ SLI design concepts, which include thin cast radial grids, minimum separator resistance, and a through-the-partition intercell connection. One of the criterions for EVs is high energy density, which results in a longer driving range; in this respect, SLI battery design has prevailed over traction battery design. In cycling batteries, electrolyte homogeneity occurs by convective flow, where the electrolyte has been found to become stratified during high discharge rate applications, such as propulsion in EV applications.

The relationship of discharge current to amp-hour capacity, up to various end voltages, is shown in Figure 1.26. These data are presented on the basis of the positive plate since the cell design and performance data of traction batteries are generally based on the number and size of positive plates that are in the cell. As is typical with most batteries, the capacity decreases with increasing discharge load and increasing end voltage. The effect of temperature on the discharge performance of traction-type batteries is illustrated in Figure 1.27.

The cycle life characteristics of traction batteries are presented in Figure 1.28. This figure shows the relationship of cycle life to DOD at the 6-h discharge rate, cycle life being defined as the number of cycles at 80% of rated capacity. It is quite

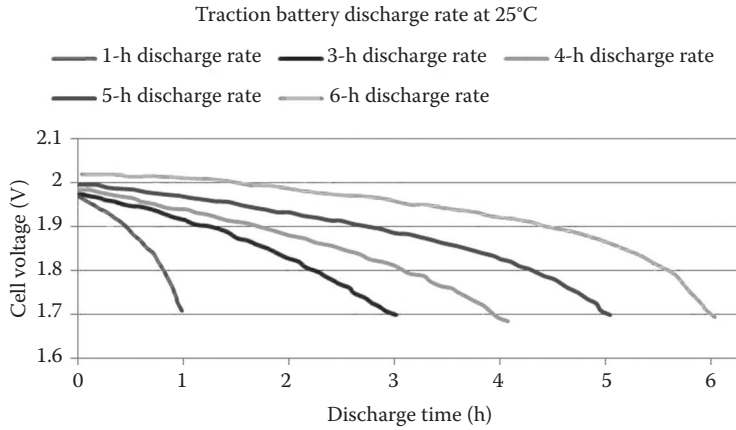

FIGURE 1.26 Capacity of traction battery at various discharge rates. (Jung, J. *Lead-Acid Battery, Electrochemical Technologies for Energy Storage and Conversion*, Chapter 4. 2012. Copyright Wiley-VCH Verlag GmbH & Co. KGaA. Reproduced with permission.)

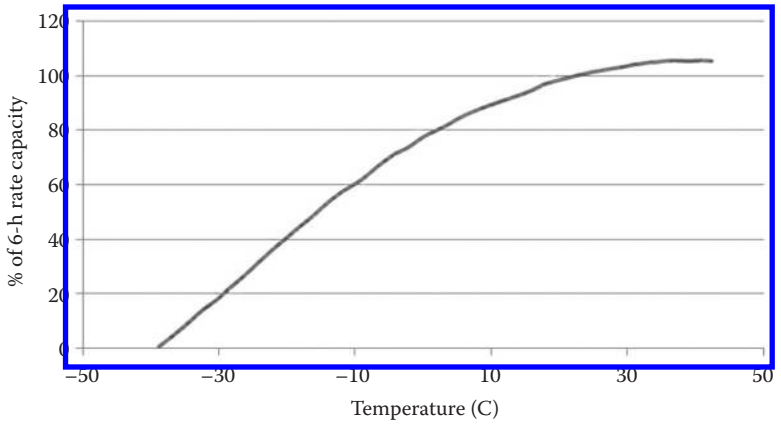

FIGURE 1.27 Temperature impact on traction battery capacity. (Jung, J. *Lead-Acid Battery, Electrochemical Technologies for Energy Storage and Conversion*, Chapter 4. 2012. Copyright Wiley-VCH Verlag GmbH & Co. KGaA. Reproduced with permission.)

evident that the deeper the cells are discharged, the shorter their useful life, and that 80% DOD should not be exceeded if full cycle life expectancy is to be attained. The nominal cycle life of a traction battery is 1500 cycles, which is approximately 6 years.

Traction or motive power batteries are made in many different sizes, limited only by the battery compartment size and the required electrical service. The basic rating unit is the positive-plate capacity, given in amp-hours at the 5- or 6-h rate. The 2-V cell in the traction batteries is grouped with 2 to 16 positive plates, or 5 to 33 positive and negative plates. Traction batteries are often assembled to have battery voltage in

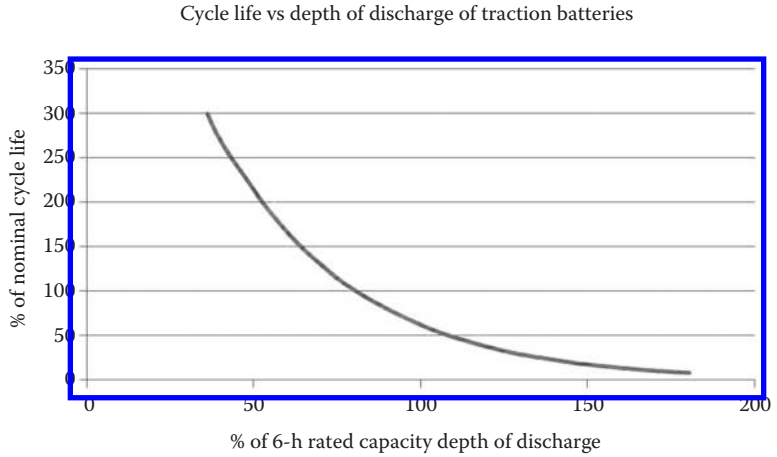

FIGURE 1.28 Impact of DOD on cycle life of traction battery. (Jung, J. *Lead-Acid Battery, Electrochemical Technologies for Energy Storage and Conversion*, Chapter 4. 2012. Copyright Wiley-VCH Verlag GmbH & Co. KGaA. Reproduced with permission.)

6-V increments (i.e., 6, 12, 18, 24, up to 96 V). The popular traction battery sizes are the six-cell, 11-plates-per-cell, 75-Ah positive-plate (375-Ah cell), and the six-cell, 13-plates-per-cell, 85-Ah positive-plate (510-Ah cell) batteries.

1.7.3 Stationary Battery

Stationary or SLA batteries are designed to have a long service life. They are usually under constant float charge. Stationary batteries are constructed with n positive plates and $n + 1$ negative plates (outside-negative design). The extra negative is to provide proper support of the positives, which tend to grow or expand during their life. Some manufacturers make the two outermost negative plates thinner than the inside negative plates due to the outermost surfaces not being easily recharged. Unlike SLI and traction batteries, stationary batteries do not focus on high energy and power densities, and they often have excess electrolyte (highly flooded) to minimize maintenance and the watering interval. Stationary batteries are designed to endure while floated and moderately overcharged. The overcharge operation of stationary batteries requires a large electrolyte volume and the use of nonantimony lead grids to minimize gas generation.

Typical discharge curves for the flat-pasted-type stationary cell at various discharge rates at 25°C are shown in Figure 1.29. Generally, the discharge rate for a stationary battery is identified as the hourly rate (the current in amperes that the battery will deliver or the rate hours) rather than the C rate used for other types of batteries.

Battery life is also related to temperature (Arrhenius-type behavior). The optimal temperature for the use of stationary batteries ranges from 20°C to 30°C, although temperatures from –40°C to 50°C can be tolerated. At higher temperatures, the rated capacity is more available but promotes self-discharge and reduces battery cycle life.

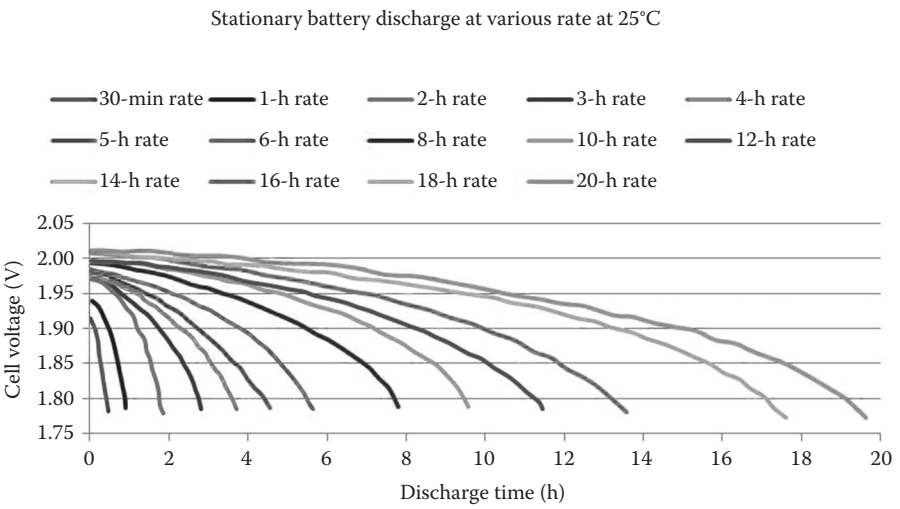

FIGURE 1.29 Capacity of stationary battery at various discharge rates. (Jung, J. *Lead-Acid Battery, Electrochemical Technologies for Energy Storage and Conversion*, Chapter 4. 2012. Copyright Wiley-VCH Verlag GmbH & Co. KGaA. Reproduced with permission.)

Generally, stationary batteries equipped with flat, lead antimony alloy plates can provide 5 to 18 years of battery life. Stationary batteries equipped with flat, lead calcium alloy plates can provide 15 to 25 years of battery life. Tubular stationary batteries can provide 20 to 25 years of battery life, and the Planté batteries have a 25-year battery life.

1.7.4 VRLA Battery

The valve regulated lead-acid (VRLA) battery is also often colloquially called a *sealed lead-acid battery*. The term *valve regulated* does not wholly describe the technology; these are really "recombinant" batteries, which means that the oxygen that evolves at the positive plates will largely recombine with the hydrogen ready to evolve on the negative plates, creating water. The water, rather than being released from the cell, is cycled electrochemically to take up the excess overcharge current beyond that used for conversion of active material. Thus, VRLA batteries can be overcharged sufficiently to convert virtually all of the active material without loss of water.

VRLA batteries have a safety pressure relief valve. The pressure relief valve maintains an internal pressure and this condition aids recombination by retaining the gases long enough within the cell for diffusion to take place. The oxygen generated on the positive plate will react with lead at the negative plate in the presence of H_2SO_4 as quickly as it can diffuse to the lead surface, which reacts with hydrogen and generates water. The valve is a safety feature in case the rate of hydrogen evolution becomes dangerously high. If the valve is activated, the excess amount of hydrogen is released to the atmosphere through the vent or through the plastic container.

Sealable valves are normally closed to prevent the entrance of oxygen from air. The valve allows excess generated hydrogen to be vented under a set pressure. Venting pressures range from a high of 25 to 40 psi for a metal-sheathed, spirally wound cell to 1 to 2 psi for a prismatic battery.

In a VRLA battery, the cell is filled with only enough electrolyte to coat the surfaces, thus creating the starved-electrolyte condition. The electrolyte is absorbed either in the separator material or immobilized in a gel. This condition allows for the homogeneous gas transfer between the plates that is necessary to promote the recombination reactions. The capacity of a VRLA battery is limited by the positive plate or the amount of positive active material. The starved electrolyte and the excess of negative active material facilitate the recombination of oxygen produced during overcharge or float charge with the negative active material.

The electrolyte can be immobilized by using an absorbent glass mat (AGM) separator or a gel electrolyte. AGM is fabricated from microglass fibers. The AGM acts as the separator between the positive and negative electrodes and also the electrolyte reservoir. A VRLA battery that employs AGM is called an AGM battery. AGM batteries were developed by Concorde Aircraft Battery in the late 1980s in San Bernardino, California. AGM battery technology was pioneered to provide a warm weather, vibration-resistant, and chemical alternative to the expensive Ni-Cad batteries in both naval helicopters and fighter aircraft. As production was mechanized, Optima Battery patented a spiral-wound method for producing an AGM battery. Due to the spiral-wound cell configuration, they are also sometimes referred to as *spiral-wound batteries*.

AGM batteries are just like flooded lead-acid batteries, except the electrolyte is being held in the glass mats, as opposed to freely flooding the plates. Very thin glass fibers are woven into a mat to increase surface area enough to hold sufficient electrolyte on the cells for their lifetime. The fibers that comprise the fine glass mat do not absorb nor being affected by the acidic electrolyte in which they reside. These mats are compressed 2% to 5% after being soaked in acids, prior to manufacture completion and sealing. The AGM battery can accumulate more acid than is available and never spill a drop.

All AGM batteries boast some significant performance enhancements over traditional flooded lead-acid cells.

Gelled electrolyte is fabricated by adding fumed silica. The silica compound hardens the electrolyte into a gel. Batteries that use a gelled electrolyte are called *gel batteries* or *gel cells*. During formation charge, some water will be lost and the gel will be dried. As the gel dries, cracks and fissures develop between the positive and negative electrodes, which are acting as the path for the oxygen recombination reaction. Silica reacts with sulfuric acid and the gelation is a chemical as well as physical reaction. Unlike a flooded wet-cell lead-acid battery, gel batteries do not need to be kept upright. Gel batteries reduce the electrolyte evaporation and spillage (and subsequent corrosion issues) common to wet-cell batteries, and they also boast greater resistance to extreme temperatures, shock, and vibration. Chemically, they are the same as wet (nonsealed) batteries except that the antimony in the lead plates is replaced by calcium [7].

The use of VRLA designs is becoming more popular and account for more than 75% of telecommunication and UPS applications. The development of advanced charging

techniques has also increased the use of VRLA batteries in cycling applications such as forklift services. New market opportunities in portable electronics, power tools, and HEVs have stimulated the development of new designs for lead-acid batteries.

On the other hand, VRLA batteries do not have the ability to handle certain types of abuse as well as conventional flooded batteries. The electrolyte, which provides the major internal heat sink in cells, is much more limited in VRLA cells. As a result, VRLA designs are more prone to thermal runaway under abusive conditions. This is particularly true when VRLA batteries are subjected to operations at elevated temperatures.

1.8 CHARGING

Lead-acid batteries are charged using dc electric power to re-form the active material on the battery electrode back from the discharged state to the charged state. During charge, the lead sulfate on the positive electrode is converted to lead dioxide (PbO_2) and the lead sulfate on the negative electrode is converted to sponge lead (Pb). During charging the electrolyte will change from low concentrated sulfuric acid with a specific gravity of 1.21 to higher concentrated sulfuric acid with a specific gravity of 1.30. Charging is temperature sensitive and affected by different charging methods as the sulfate ions change from solid form to liquid form during charging. During charging and discharging, the conversion of the sulfate ions' state between liquid and solid can result in an active material with a different morphology, which causes a redistribution of the active material. The redistribution will cause the active material containing a crystal structure with defects and becoming less chemically and electrochemically active. This is so-called "physical degradation." Physical degradation can be minimized by proper charging.

A lead-acid battery can generally be charged at various charge rates that do not promote excessive gassing, overcharging, or temperature rise. Charging should be controlled such that very little gas is evolved on charge, which minimizes the requirement for watering (i.e., less maintenance is required).

Lead-acid batteries can take a very high charging current during the early stage of the charging process. The voltage will rise as the battery is charged. As shown in Figure 1.22, when a battery is fully discharged, it can take a high charging current with the charging voltage remaining low. When the battery becomes charged, the voltage rises if the charging current remains high. The high voltage will promote gas generation and shedding of paste, which results in the battery having a shorter cycle life and capacity loss. It is important to limit the charge current when the battery becomes charged, as defined in the following relationship:

$$I = Ae^{-t}$$

where I represents the charging current, A is the number of ampere-hours previously discharged from the battery, and t is the time. Figure 1.30 shows the ampere-hour relationship.

The maximum charging voltage is relevant to the current collector and grid material. Research has shown that when using an antimony lead alloy as grid material,

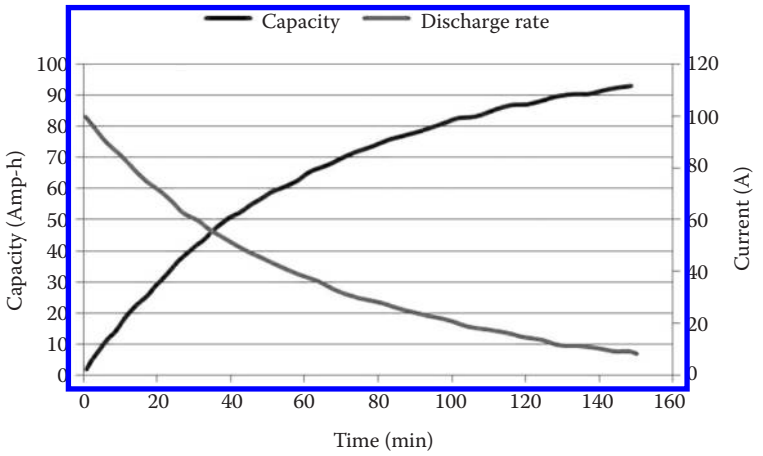

FIGURE 1.30 Ampere-hour relationship of lead-acid battery.

the maximum voltage is in the range of 14.1 to 14.6 V for a nominal 12-V lead-acid battery. When using a lead calcium alloy grid or other nonantimony grid material, the maximum voltage is in the range of 14.5 to 15.0 V.

The available charging methods are as follows:

1. *Constant-current charge (one current charge rate)*: Constant-current charge is used for battery formation and small lead-acid batteries. A constant-current charge is often used in laboratories because of the convenience of calculating ampere-hour input and because of using inexpensive equipment. Constant-current charging at half the 20-h rate can be used in the field to decrease the sulfation in batteries that have been overdischarged or undercharged, which means the batteries that have heavy sulfation can be restored with a long, slow recharge (e.g., 3 to 4 days at 2 to 3 A for 55 Ah, 12-V SLI batteries). However, a low constant-current charge for a normal battery may diminish battery life. A constant-current charge with one current charge rate is not widely used because of the need for current adjustment unless the charging current is kept at a low level through the whole charging process. The disadvantage is that it will prolong the charging time.
2. *Constant-voltage charge*: A constant-voltage (potential) charge is adopted in normal industrial applications to recharge lead-acid batteries. It is often used for on-the-road vehicles and utility, telephone, and UPS applications where the charging circuit is fixed to the battery. As shown in Figure 1.31, under a constant-voltage charge, the maximum allowed current is applied until a predetermined voltage is reached. Once the voltage reaches the set level, the current will start to decrease in order to keep the voltage constant until the battery reaches a 100% state of charge. During the time interval between the batteries being held at constant voltage and getting to the 100% state of charge, the battery is on charge with a low charge current, which can minimize overcharging and the accompanying grid corrosion,

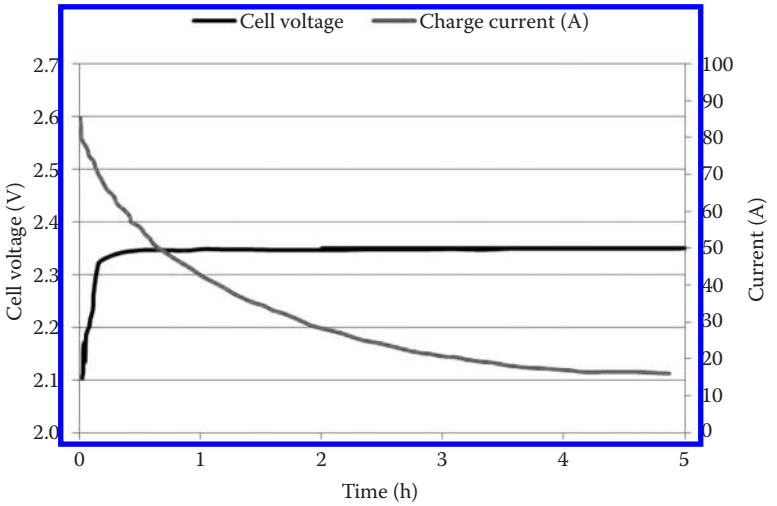

FIGURE 1.31 Constant-voltage charge.

water loss by electrolysis of the electrolyte, and maintenance to replenish the water.

3. *Constant-current charge followed by constant-voltage charge*: A constant-current charge followed by a constant-voltage charge is used for deep-cycle batteries, which are typically discharged at the 6-h rate to reach a depth of 80% before recharge. The recharge is normally completed in an 8-h period. The charger is set for the constant potential of 2.39 V per cell (the gassing voltage), and the starting current is limited to 16 to 20 A per 100 Ah of the rated 6-h ampere-hour capacity. The initial current is maintained constant until the average cell voltage in the battery reaches 2.39 V per cell. The current decreases at constant voltage to the finishing rate of 4.5 to 5 A per 100 Ah, which is maintained to the end of the charge. The total charge time is controlled by a timer. The battery during the total charge time receives a charge capacity of a predetermined percentage of the ampere-hour output of the previous discharge, normally 110% to 120%, or a 10% to 20% overcharge.
4. *Taper charging*: Taper charging is a modified constant-voltage charge. Taper charging uses less sophisticated controls to reduce equipment costs. However, the taper charging method degrades the battery life due to the charge voltage exceeding 2.39 V per cell at 25°C prior to the charge capacity reaching 100% of the prior discharge ampere-hours. As the charge voltage exceeds 2.39 V per cell, the battery will experience gassing and a temperature rise. The gassing voltage decreases with increasing temperature. Table 1.14 shows the voltage correction factors at various temperatures.

   Furthermore, the end of a taper charge is controlled by a fixed voltage instead of a fixed current. A new lead-acid battery has a high counter emf, which will result in a low final charge rate and cause the battery to be

TABLE 1.14
Voltage Correction Factors at Various Temperatures

Electrolyte Temperature (°C)	Cell Gassing Voltage (V)	Correction Factor (V)
50	2.300	–0.090
40	2.330	–0.060
30	2.365	–0.025
25	2.390	0
20	2.415	+0.025
10	2.470	+0.080
0	2.540	+0.150
–10	2.650	+0.260
–20	2.970	+0.508

insufficiently charged. When charging an aged lead-acid battery, the battery has a low counter emf, which will result in a higher finishing rate such that the battery will receive an excessive charge [8].

5. *Pulse charging*: Pulse charging is used for traction applications. During charge, the charger is periodically isolated from the battery and the open-circuit voltage of the battery is automatically measured. If the open-circuit voltage is above a present value, depending on the battery temperature, the charger will stop charging the battery. When the open-circuit voltage decays below that limit, the charge will deliver a dc pulse for a fixed time period. When the battery state of charge is very low, the charging current is connected almost 100% of the time because the open-circuit voltage is below the present level or rapidly decays to it. The duration of the open circuit and the charge pulses are selected so that when the battery is fully charged, the time for the open-circuit voltage to decay is exactly the same as the pulse duration. When the charger senses this situation, the charger is switched to the finish rate current and short charging pulses are given to maintain the battery at full charge.

   If the application has high-voltage batteries such as forklift batteries, keeping each individual 2-V cell in a balanced condition is difficult, especially when the batteries endure long standby periods. An equalizing charge can be applied to bring all the battery cells into the same state of charge. The equalizing charge is designed to completely discharge the battery cells and recharge them periodically. In an equalization charge, the normal recharge is extended for 3 to 6 h at the finishing rate of 5 A per 100 Ah for 5-h rated capacity. This allows the battery voltage to rise uncontrolled. The equalization charge should be carried out until cell voltages and specific gravities rise to a constant, adequate value. It is important to check and maintain the electrolyte levels in the cells because some cells might be gassing more than others during charging.
6. *Trickle charging*: A trickle charge is a continuous constant-current charge at a low rate (*C*/100) that is used to maintain a battery in a fully charged

condition, recharging it for losses due to self-discharge and to restore the energy discharged during intermittent use of the battery.

7. *Float charging*: Float charging is a low-rate, constant-voltage charge that is also used to maintain the battery in a fully charged condition. The method is used mainly for stationary batteries. One example of a float charge is to charge at 2.17 to 2.25 V per cell when charging a nonantimony grid battery with 1.21 specific gravity electrolyte [8].
8. *Rapid charging*: Rapid charging is desirable in many applications to charge the battery within an hour. It is important to maintain the charge current and battery temperature so that the morphology of the electrode will remain. A battery temperature that is too high will promote grid corrosion, conversion of active material to nonconducting oxides, high solubility of active materials, decomposition of active material, gassing, and overcharging.

Rapid charging can combine with pulse discharge to prevent an excessive rise in battery temperature during charging. For example, during rapid charging, a brief discharge pulse of a fraction of a second is built in to the rapid charging protocol.

In general, the charging method should prevent each individual 2-V cell voltage from exceeding the gassing voltage of 2.39 V. When 100% of the previous discharged capacity is reached under this voltage control, the charge rate should decay to the charge finishing rate. The charge finish rate should be at a constant current no higher than this rate, normally 5 A per 100 Ah of rated capacity (or a 20-h rate).

1.9 BATTERY MAINTENANCE AND FAILURE MODES

1.9.1 Maintenance

Proper maintenance of a lead-acid battery can extend its cycle life. The five principles of maintaining lead-acid batteries are as follows:

1. *Charge the battery with a proper charger that meets the charging requirement.* Charging the battery with an inadequate charger is one of the main causes of battery failure. A proper charger will allow the battery to draw only the amount of current that it can accept efficiently, and this current will reduce as the battery approaches a full charge. The specific gravity of the electrolyte should be checked periodically for those batteries that have a removable vent and adjusted to the proper value.
2. *Do not overdischarge the battery.* Overdischarging the battery below its nominal capacity will reduce the electrolyte concentration, which has a deleterious effect on the pore structure of the battery. Battery cycle life has a direct relationship to the DOD, as shown in Figure 1.32 [9].
3. *Do not overheat the battery.* High temperatures (>55°C) will promote battery grid corrosion, solubility of metal components, self-discharge, and loss of battery capacity. High operating temperatures during battery cycles will result in the battery requiring higher charge input than room temperature

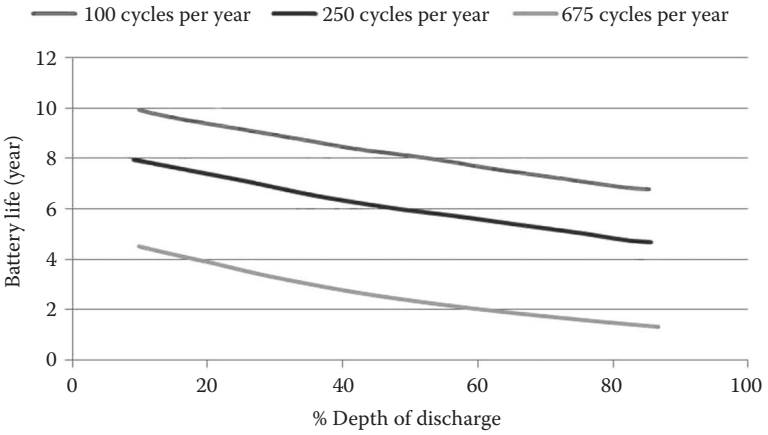

FIGURE 1.32 Effect of DOD on battery life. (From Linden, D., and Reddy, T. B. (Eds.), *Handbook of Batteries*, 3rd ed., McGraw-Hill, New York, 2002.)

(25°C) to restore its discharge capacity and self-discharge losses. The extra charge input is consumed by the electrolysis of water because of the reduction in gassing voltage at higher temperatures. When charging the battery at 35°C, the battery will require a 10% overcharge to restore the battery capacity compared to charging the battery at 25°C. When charging the battery at 60°C to 70°C, it will require a 40% overcharge to restore the battery capacity. For floating charging, an 11-day float at 75°C is equivalent in life to 365 days at 25°C.

Batteries for high-temperature applications can start with a lower initial specific gravity electrolyte to allow extra water to be placed into the battery. Research has shown that adding more expander into the negative paste will also improve the battery performance at high temperature.

4. *Do not overcharge the battery and maintain the electrolyte level in each individual 2-V cell.* The electrolyte level will decrease in each individual 2-V cell as a result of normal operation due to water being evaporated or electrolysis into hydrogen and oxygen. Evaporation is considered a small part of water loss, except in hot and dry climates. Electrolysis is considered the main factor of water consumption. During overcharge, the water is consumed by electrolysis at a rate of 0.336 mL/Ah overcharge. A 10% overcharge can consume 0.3% of the water content each cycle.

   Electrolyte inside the battery cells has two functions, which is to conduct electricity and heat. If the electrolyte is below the plate level, the area that is not covered by the electrolyte is not electrochemically active. The inactive area causes a concentration of heat in other parts of the cell and promotes grid corrosion. Periodically adding water to maintain the electrolyte level can provide an indication of charging efficiency. If the water consumption

is high, which indicates a poor charging efficiency, adjustment of the charging protocol is required.

Water should be replenished after recharge and to reach the high acid level line. The replenish water should be either distilled water, deionized water, or demineralized water. Gassing during charge will stir the water into the acid uniformly; thus, mixing is not required unless in freezing weather because the water might freeze before gassing occurs.

5. *Keep the battery clean*. Keeping the battery clean will minimize the corrosion of the cell post and connectors. Batteries commonly pick up dry dirt and need to be cleaned periodically. If an electrolyte spill occurs, the electrolyte can be neutralized by an alkaline solution such as baking soda with hot water in 1 kg of baking soda to 4 kg (4 L) of water.

1.9.2 Safety

Lead-acid battery safety is governed by the use of proper precautions such as wearing face shields and rubber gloves when handling. When in contact with lead-acid batteries, the following precautions are important:

- Wear safety gear to avoid chemical burns from sulfuric acid.
- Flush immediately with plenty of water if eyes, skin, or clothing come in contact with sulfuric acid.
- Obtain medical attention if necessary.

Generally, lead-acid battery safety concerns include the following:

1. *Short circuit and electrolyte spill*: Operator error that causes a short circuit is a main safety concern in the field. It is important to keep the top of the battery clean to prevent ground short circuits. Operators should be instructed not to place metallic objects or any electrical conductor on the battery. In addition, all tools used in servicing batteries should be insulated. When lifting batteries, use insulated tools to avoid the risk of causing a short circuit between cell terminals and lifting tools.

   Furthermore, when working with lead-acid batteries that have vent caps, it is important to keep the vent caps tight and level to eliminate acid spills. When an electrolyte (acid) spill occurs, an alkaline solution with 1 kg baking soda to 4 kg (4 L) of water can be used to neutralize the acid. The neutralized area should be rinsed with clear water.
2. *Potential explosions from the hydrogen and oxygen generated during overcharge*: One of the common problems that cause batteries to explode is charging the batteries with an unmatched charger, which often causes overcharging, which can lead to an explosion. In spite of the fact that charge currents might be low, when lead-acid batteries are overcharged, the water in the electrolyte is electrolyzed to generate hydrogen and oxygen. The generated hydrogen gas can accumulate, ignite, and cause an

explosion. One ampere-hour of overcharge can generate 0.42 L of hydrogen and 0.21 L of oxygen at room temperature and pressure. The generated gases are explosive when the content of hydrogen in the air exceeds 4 vol%.

In telecommunication applications, where a large number of lead-acid batteries are assembled in a confined room, exhaust fans should be installed to provide good air ventilation and prevent hydrogen buildup. Hydrogen detectors with a detection limit set at 20% of the lower explosive limit should be installed. Because sparks can ignite hydrogen, electrical sources of arcs, sparks, or flame arrestors should be mounted in explosion-proof metal boxes to eliminate static.

3. *The generation of toxic gases such as arsine and stibine*: Antimony and arsenic are used in making the grid to harden it and to reduce the rate of grid corrosion during cycling. The batteries containing small quantities of antimony and arsenic will form arsine (AsH_3) and stibine (SbH_3) when hydrogen comes in contact with arsenic or antimony alloy material. The arsine and stibine are colorless and odorless gases and are extremely dangerous. Exposure to arsine and stibine will cause severe illness and death. In 1975, the U.S. Department of Labor's Occupational Safety and Health Administration regulated the concentration limits for AsH_3 and SbH_3 to 0.05 and 0.10 ppm, respectively, emitted in any 8-h period.

1.9.3 Failure Modes

The failure modes of lead-acid batteries depend on the battery applications and battery construction and design. Lead-acid batteries usually fail from positive plate degradation, which is caused by grid corrosion or paste shedding. Table 1.15 shows the common failure modes.

Positive grid corrosion can be caused by the grid alloy, grid casting conditions, and active material composition. Shedding of positive active material can be caused by battery construction, active material structure, battery cycles, DOD, and charge

TABLE 1.15
Common Failure Modes

Battery Application	Battery Life	Failure Mode
SLI	Several years	Grid corrosion
Maintenance-free SLI	Several years	Water loss, grid corrosion, positive material shedding
Golf cart	350–600 cycles	Positive material shedding, grid corrosion, sulfation
SLA	6–25 years	Grid corrosion
Traction	Minimum 1500 cycles	Positive material shedding, grid corrosion

method. Sulfation can be caused by the temperature, charge method, and lack of maintenance.

1.10 ADVANCED BATTERY TECHNOLOGY

1.10.1 Negative Current Collector Improvement

1.10.1.1 Ultrabattery

Furukawa Battery in Japan and CSIRO in Australia have codeveloped a hybrid lead-acid battery that they have called the Ultrabattery. In this hybrid, the battery and supercapacitor are integrated at the electrode plate level. Figure 1.33 shows the structure of the Ultrabattery.

The Ultrabattery comprises a lead-acid battery and asymmetrical capacitor combined in a single cell. The lead-acid battery has a positive electrode of lead dioxide and a negative electrode of spongy lead. The asymmetrical capacitor, for its part, has the same positive electrode as the battery, lead dioxide, and a negative electrode of porous carbon. Because both have a positive electrode of lead dioxide, the lead negative electrode and the capacitor negative electrode can be connected in parallel and housed in the same cell with the positive electrode. The resulting battery has the capacitor electrode bearing a portion of the load of the lead storage electrode [10].

The capacitor electrodes are made of porous carbon, which would generate hydrogen gas during charge. Hydrogen inhibitors (additives) are important in the Ultrabattery chemistry to suppress the evolution of hydrogen gas during charging to a level similar to that of the lead electrode.

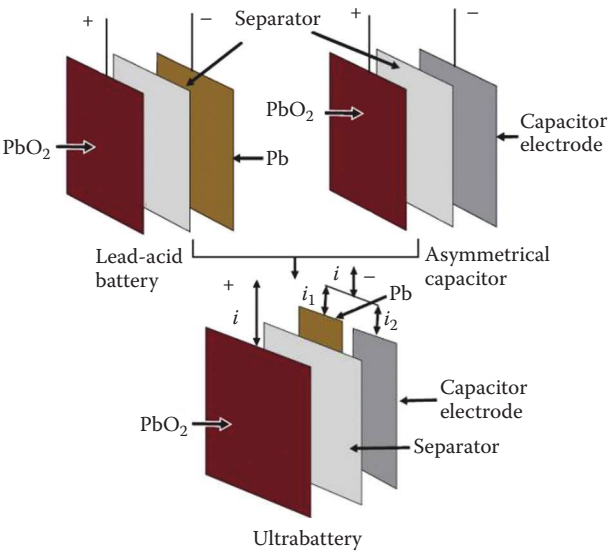

FIGURE 1.33 Structure of the Ultrabattery.

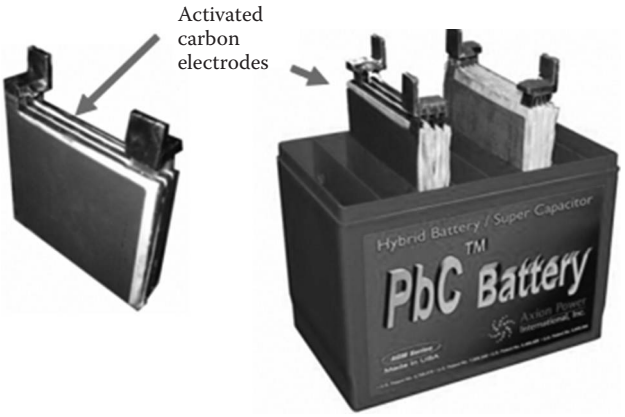

FIGURE 1.34 PbC battery.

1.10.1.2 PbC Capacitor Battery

Axion Power International Inc. has developed a PbC capacitor battery, as shown in Figure 1.34. The full technical description of Axion's proprietary *PbC*® technology is a "multi-celled asymmetrically supercapacitive lead-acid-carbon hybrid battery." Like a lead-acid battery, the PbC battery consists of a series of cells. Within the individual cells, however, the construction is more complex. Whereas the negative electrodes in lead-acid batteries are simple sponge lead plates, the negative electrodes in a PbC battery are five-layer assemblies that consist of a carbon electrode, a corrosion barrier, a current collector, a second corrosion barrier, and a second carbon electrode. These electrode assemblies are then sandwiched together with conventional separators and positive electrodes to make the PbC battery, which is filled with an acid electrolyte, sealed and connected in series to the other cells [11].

Axion has revealed test data showing that *PbC*® batteries have withstood 1600 cycles before failure. The test protocol calls for a complete charge–discharge cycle every 7 h to a 90% DOD. In comparison, most lead-acid batteries designed for deep-discharge applications can only survive 300 to 500 cycles under these operating conditions.

Axion has stated that the PbC battery has several key performance advantages over conventional lead-acid batteries:

- Significantly faster recharge rates
- Significantly longer cycle lives in deep-discharge applications
- Minimal required maintenance

1.10.1.3 Firefly Oasis Battery

In 2009, Firefly Energy Inc. revealed its Oasis battery, which was developed by Kurt Kelly. This battery is equipped with conventional lead grids as the positive current collector and carbon-graphite foams as the negative current collector. Firefly has named the carbon-graphite technology as 3D technology. Because of the replacement of

FIGURE 1.35 Firefly carbon-graphite foam negative current collector.

conventional lead grids with a carbon-graphite foam grid, the battery would provide much-improved negative active material utilization, an enhanced fast recharge capability, and greater high-rate discharge cycle life and low-temperature performance [12].

The negative carbon-foam plate has a structure in which each plate contains hundreds or thousands of spherical microcells. The microcells provide a high surface area, which increases the interface area between the active chemistry and current collectors. Each microcell has its full complement of negative sponge lead paste and sulfuric acid electrolyte. Liquid diffusion distances in the microcell are reduced from the traditional levels of millimeters over linear paths to the level of micrometers. The diffusion path lengths in the 3D space within the discrete microcells collectively comprise a totally new type of structure. Such a structure results in much higher power and energy delivery and rapid recharge capabilities when compared to conventional lead-acid batteries. As such, Firefly stated that the Oasis battery has driven up both gravimetric and volumetric energy and power values [13–15].

Figure 1.35 shows Firefly's carbon-graphite foam negative current collector.

1.10.2 Current Collector Improvement

The relationship between battery specific energy in watt-hours/kilogram (Wh/kg) and number of battery discharge–charge cycles for both flooded and valve-regulated type lead-acid batteries is that the higher the battery specific energy the lower the number of discharge–charge cycles and, hence, the battery cycle life. Typically, a flooded battery with a specific energy of 40 Wh/kg can be used for about 500 discharge–charge cycles, whereas a battery producing only 30 Wh/kg can be employed for about 850 cycles. Thus, there is clearly a need to improve both the specific energy and cycle life of lead-acid batteries in order to make them more suitable for electric traction applications.

It is well known that the low utilization efficiency of the active mass, especially on the positive electrode, in conjunction with the heavy weight of the lead current collectors, limits the actual specific energy of the lead-acid battery. The structure of the current collector plays an important role in determining the utilization efficiency of the positive active mass (PAM). During discharge, on the positive electrode, the structure of the current collector must allow for significant volume increase (e.g., molar ratio of $PbSO_4$ to PbO_2 is 1.88) while maintaining electrical contact with the active material and ensuring ionic transport to the electroactive sites. $PbSO_4$ has a significantly larger volume (about 37% more) than the charged active material. The expansion from the volume change stresses the electrode structures and induces

mechanical forces that deform the grid. The resulting expansion and deformation of the plates also causes active material to separate from the current collectors.

1.10.2.1 Lead Alloy–Coated Reticulated Carbon Current Collectors

In 2001, Elod Gyenge and Joey Jung developed a high surface area current collector for both positive and negative electrodes. The current collectors were fabricated via deposited lead-tin alloy on reticulated carbon plate. Figure 1.36 shows a comparison between the conventional grid and the lead-tin alloy–coated current collector.

The reticulated carbon-based current collector structure is porous and has a high specific surface area (e.g., >500 m^2/m^3) and high void fraction (i.e., between 70% and 98%). A number of materials could also serve as the above-mentioned substrate, such as reticulated aluminum and reticulated copper. The deposited lead-alloy layer has a thickness ranging from 100 to 300 μm. The thickness of the lead-tin coating depends on the intended application and battery cycle life. The lead-tin–coated RVC is used as the positive and/or negative current collector in lead-acid batteries.

Figure 1.37 shows the nominal capacities (Peukert diagram) at discharge rates between 0.5 and 15 h for the positive-limited reticulated battery. At a discharge

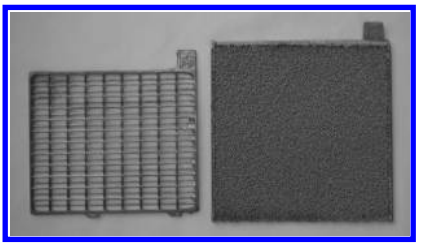

FIGURE 1.36 Comparison of conventional lead grid with lead alloy–coated RVC current collector.

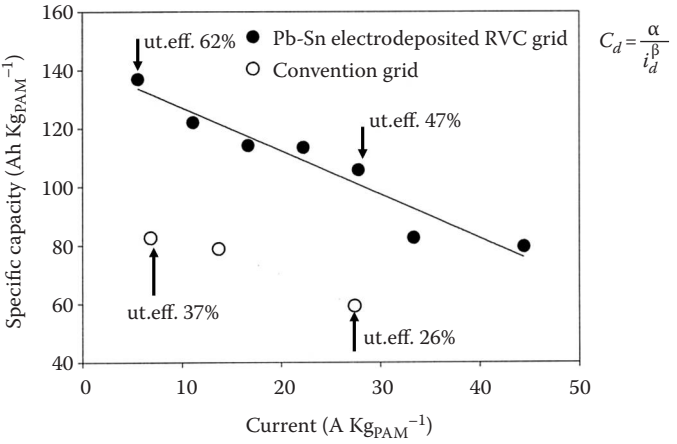

FIGURE 1.37 Peukert diagram. ut.eff., Utility efficiency.

current of 27 A/kg PAM, corresponding to a discharge rate of 3 h, the PAM utilization efficiency on the electrodeposited reticulated collector was 47% (specific capacity 107 Ah/kg PAM) compared to 26% on the conventional lead grid. Discharging the reticulated battery at 15 h rate (6.5 A/kg PAM) yielded a PAM utilization of 62% corresponding to a capacity of 135 Ah/kg PAM, where the conventional lead grid yields a 37% PAM utilization [16–19].

1.10.2.2 Lead Alloy–Coated Polymer Current Collectors

In 2009, Joey Jung developed a high surface area current collector for both positive and negative electrodes with a multiconductive substrate. The current collectors were fabricated via deposited lead alloy on reticulated, multiconductive substrates. The substrate material can be carbon foam or polymer. Figure 1.38 shows a comparison of the multiconductive polymer-based current collector and the conventional grid.

The multiconductive current collector consisted of two regions, a frame region and a body region. The frame may also include one or more strips that run through the plate. The frame region is stronger and more rigid than the body region. The frame region has a high specific surface area relative to the body, where the electrical current distribution properties will be enhanced and at the same time the frame will be denser and stiffer than the body to provide structural support for the current collector. This allows one to dispense with traditional lead frames. The multiconductive current collector can be manufactured to various thicknesses ranging from 0.8 to 10 mm. Table 1.16 shows comparison data for 100-Ah, 12-V batteries discharged at

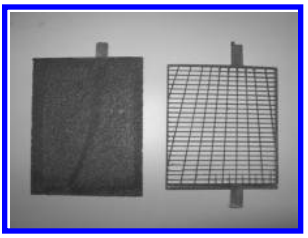

FIGURE 1.38 Comparison of multiconductive polymer-based current collector and conventional grid.

TABLE 1.16
Comparison Data for Various 100-Ah Batteries

100-Ah Battery Characteristics	Multiconductive	Carbon Foam Based	Conventional Grid
Total current collector weight (g)	5562	8037	8994
Total number of current collectors	90	54	90
Total paste weight (g)	10,267	17,112	17,112
Total battery weight (g)	24,278	27,943	38,400
PAM utilization efficiency (%)	63	55	25
Lead use reduction (%)	36.78	27.23	0
Energy density (Wh/kg)	50	43	31
Power density (W/kg)	344	215	259

a 10–h discharge rate (*C*/10). The battery energy density and power density from the multiconductive current collector are increased by 16% and 60%, respectively, over those from the carbon foam counterpart, and by 61% and 33%, respectively, over those from the conventional current collector [20,22].

1.10.3 Battery Construction

1.10.3.1 Horizon Battery

Unlike conventional lead-acid batteries, which orient battery electrodes vertically, a Horizon battery orients the battery electrodes horizontally to provide equal, controlled pressure over the whole electrode area, as its configuration shows in Figure 1.39. The current collectors in the Horizon battery have a high-tensile-strength fiberglass substrate. Lead or lead alloy was extruded onto the fiberglass substrate and the lead-coated fiberglass was woven to have a grid structure using conventional wire weaving equipment.

The Horizon battery stacks the plates to share the same electrolyte environment. It also employs a biplate design in the construction of lead-acid batteries to eliminate the need to group the electrodes and connect the 2-V cells. Figure 1.39 also shows the biplate design, which contains two sections. The upper section is pasted with positive active material to act as the positive electrode, and the lower section is pasted with

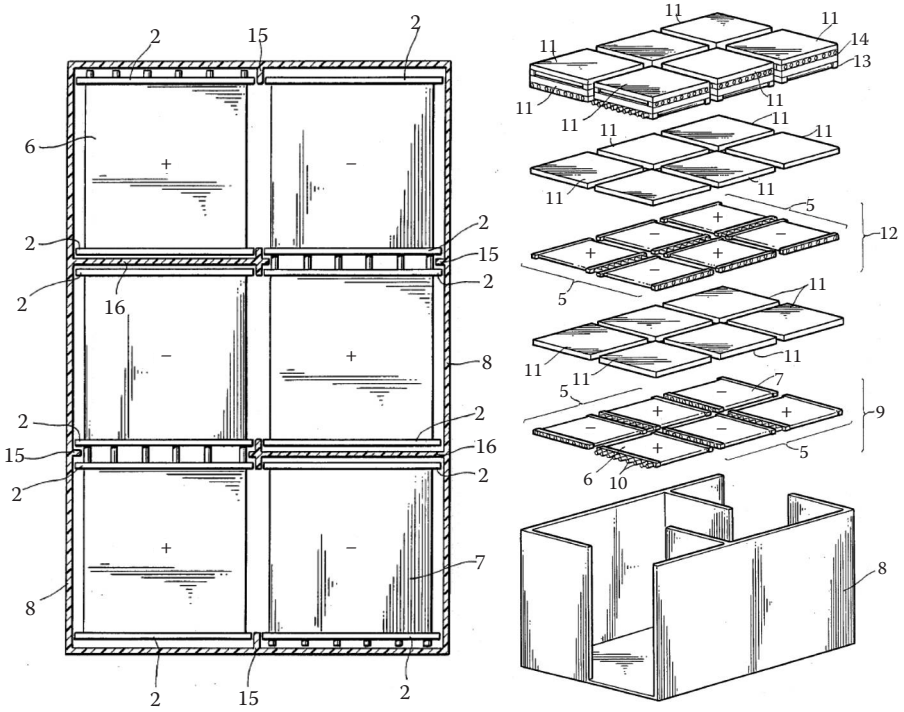

FIGURE 1.39 Horizon battery design.

negative active material to act as the negative electrode. Due to the unique orientation, the Horizon battery does not need further grouping of the electrodes nor does each 2-V cell need to be connected to make a 12-V battery [23–26].

1.10.3.2 Bipolar Battery

A bipolar lead-acid battery eliminates grouping of positive and negative plates and the connections between cells. Bipolar battery construction shortens the current path between the positive and negative terminals of the battery, which reduces the battery's internal resistance to current flow and improves power delivery. The bipolar battery configuration is particularly suitable for high-voltage batteries because bipolar construction requires less space compared to conventional lead-acid batteries.

The bipolar design creates a uniform current distribution and load potential over the entire surface of the electrodes, which provides more efficient utilization of paste materials. A bipolar battery is assembled by stacking bipolar electrodes together. The bipolar electrode is constructed by pasting positive active material onto one side of the conductive, nonporous substrate. The negative active material is pasted onto the other side of the same substrate. Figure 1.40 compares the concepts of the monopolar (conventional lead-acid battery construction) and bipolar battery designs. The bipolar concept shown in Figure 1.40 shortens the long, complex path of current flow that is used in the monopolar design.

In 2009, Atraverda achieved a bipolar element, Ebonex®, that meets the bipolar design requirements by combining Ebonex powder with thermoset resins and lead alloy foil. Ebonex powder is a titanium suboxide material that has an electrical conductivity comparable to that of carbon and a high oxidation resistance. The Ebonex is a bipole element that serves as both the support structure and divider for the positive and negative electrode paste material.

Each Ebonex, when assembled with electrode paste material, forms a 2-V cell. This bipolar design has a dramatic reduction in the number of components and amount of raw material used in the battery, and hence reduces the weight and size of

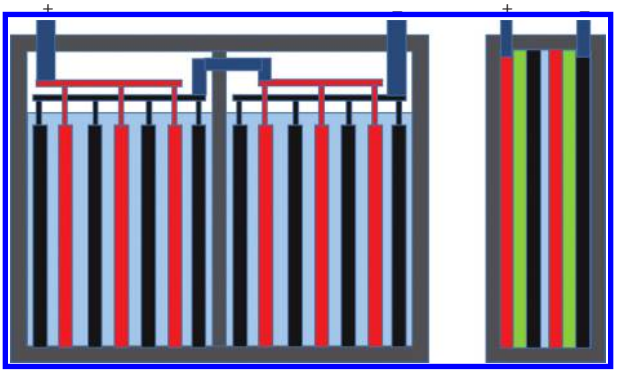

FIGURE 1.40 Comparison of (a) monopolar and (b) bipolar 4V battery designs.

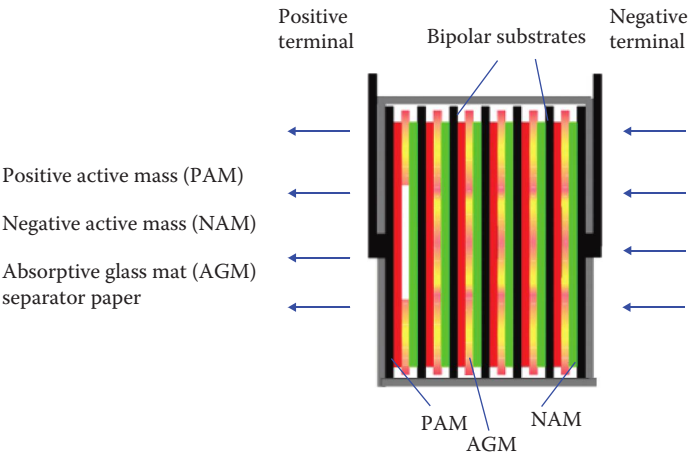

FIGURE 1.41 Schematic representation of a bipolar 12-V battery with six cells.

the battery compared to a conventional a lead-acid battery. Figure 1.41 is a schematic representation of a bipolar 12-V battery made up of six cells [27].

1.10.4 Electrolyte Improvement

1.10.4.1 Gel Silicon Electrolyte

Gel silicon electrolyte was introduced in battery design to eliminate spilling and the need for constant maintenance. A gel battery (also known as a *gel cell*) is a VRLA battery with a gelled electrolyte; the sulfuric acid is mixed with silica fume or silica additives, which makes the resulting mass gel-like, stiff, and immobile. Unlike a flooded wet-cell lead-acid battery, these batteries do not need to be kept upright. Gel batteries reduce the electrolyte evaporation and the spillage (and subsequent corrosion issues) common to the wet-cell battery, and they boast greater resistance to extreme temperatures, shock, and vibration. Chemically they are the same as wet (nonsealed) batteries except that the antimony in the lead plates is replaced by calcium.

The recharge voltage on this type of cell is lower than that of other types of lead-acid battery. This is probably the most sensitive cell in terms of adverse reactions to overvoltage charging. Gel batteries are best used in *very* deep-cycle applications and may last a bit longer in hot weather applications. If the incorrect battery charger is used on a gel cell battery, poor performance and premature failure are certain.

The sealed gel technology was developed a number of years ago by the Sonnenschein Company in West Germany. Simply stated, a gel cell is a lead-acid battery that uses a thick chemotropic gelled electrolyte that is the consistency of candle wax once it "sets up" and is pressurized and sealed using special valves. It uses a recombination technique to replace the oxygen and hydrogen normally lost in a wet-cell battery, and it is maintenance free and nonspillable [7,28].

As noted earlier, a gel cell is a "recombinant" battery. This means that the oxygen that is normally produced on the positive plates in all batteries recombines with the hydrogen given off by the negative plates. The combination of hydrogen and oxygen produces water, which replaces the moisture lost in "wet-cell" batteries. Therefore, the battery is maintenance free, because it never needs water to be added.

The oxygen is trapped in the cell by special pressurized sealing vents. It travels to the negative plates through tiny fissures or cracks in the gelled electrolyte. The sealing vent is critical to the performance of the gel cell. The cell must maintain a pressure of approximately 1.5 lb/in.^{2}, otherwise the recombination of the gases will not take place and the cell will not perform. Likewise, the valve must safely release excess pressure that may be produced during charging. Otherwise, the cell could be irreparably damaged. It is important to note that a gel cell must never be opened once it leaves the factory. If opened, the cell loses its pressure and the outside air will "poison" the plates and cause an imbalance that destroys the recombinant chemistry.

1.10.4.2 Liquid Low Sodium Silicate Electrolyte

An electrolyte with a low sodium silicate concentration was developed to overcome the disadvantages of conventional lead-acid batteries and gel lead-acid batteries. A conventional lead-acid battery uses a sulfuric acid electrolyte, which is a health hazard and pollutes the environment. A gel lead-acid battery has disadvantages of difficulty in filling the gel electrolyte, crack and hardness of the electrolyte, low fluidity, and high internal resistance.

The low concentration sodium-containing silicate electrolyte is prepared by a magnetization method using these steps [21]:

1. Add deionized water to a silica gel containing 40 to 60 wt% SiO_2.
2. Use a Baumé densimeter to measure the concentration, and add deionized water until the concentration is 0.65 to 0.85 Bé.
3. Add inorganic acid to the mixture until the pH value is between 1 and 4. The inorganic acid can be hydrochloric acid (HCl), oxalic acid, or sulfuric acid.
4. Put the solution into a magnetic field of 1000 to 6000 G for 5 to 10 min of magnetization.
5. Stir the magnetized solution at 700 to 1400 rpm for 5 to 10 min until the viscosity of the solution is decreased to 0.02 P.

Battery manufacturers that have adopted the low sodium silicate electrolyte into their lead-acid battery production process have stated the following advantages over conventional and gel-type lead-acid batteries:

- The composition of the electrolyte is changed from sulfuric acid.
- The magnetization treatment results in the electrolyte having low viscosity and good fluidity, which resolve the difficulty of electrolyte filling.
- The internal resistance of the batteries using the electrolyte containing a low concentration of sodium silicate is very low, which contributes to a longer cycle life.

- The batteries can be operated over a wide temperature range from –50°C to +60°C.
- No acidic smog is released during the battery manufacturing process.
- The batteries have negligible self-discharge. The storage period is increased from the normal 8 months to 18 months.

1.11 SUMMARY

Lead-acid batteries were the first rechargeable battery used commercially. Conventional lead-acid batteries have a significant history in providing energy storage for a variety of end-use applications, both mobile and stationary. Despite its advanced age, the lead chemistry continues to be in wide use today, and there are good reasons for its popularity: Lead-acid technology is dependable and inexpensive on a cost-per-watt base. Few other batteries are able to deliver bulk power as cheaply as lead-acid ones, and this makes the battery cost effective for automobiles, golf carts, forklifts, marine applications, and UPSs.

On the other hand, a lead-acid battery is heavy and less durable than nickel- and lithium-based systems when deep cycled. Depending on the depth of discharge, lead-acid batteries for deep-cycle applications provide 200 to 300 discharge–charge cycles. The primary reasons for their relatively short cycle life are grid corrosion on the positive electrode, depletion of the active material, and expansion of the positive plates. These changes are most prevalent at elevated operating temperatures and high-current discharges.

Most types of lead-acid batteries are not suitable for fast charging. Normally, a full charge takes 14 to 16 hours, and lead-acid batteries must always be stored at a full state of charge. A low charge causes sulfation, which contributes to the degradation of battery performance. Lead-acid batteries work well at cold temperatures and are superior to lithium-ion ones when operating in subzero conditions. Table 1.17 lists the advantages and limitations of common lead-acid batteries in use today.

TABLE 1.17
Advantages and Limitations of Lead-Acid Batteries

Advantages	Inexpensive and simple to manufacture; low cost per watt-hour
	Low self-discharge; lowest among rechargeable batteries
	High specific power; capable of high discharge currents
	Good low- and high-temperature performance
Limitations	Low specific energy; poor weight-to-energy ratio
	Slow charge; fully saturated charge takes 14 to 16 hours
	Must be stored in charged condition to prevent sulfation
	Limited cycle life; repeated deep cycling reduces battery life
	Flooded version requires watering
	Transportation restrictions on the flooded type
	Not environmentally friendly

Source: http://www.batteryuniversity.com.

With the recent demand for more dynamic energy storage services, which necessitate better technical performance characteristics (energy density, power density, charge acceptance) and lower life cycle costs (improved battery cycle life), conventional lead-acid batteries cannot provide the level of performance demanded by these emerging applications and complementary technologies. This increased demand on battery performance and the adoption of renewable energy generation and advanced vehicle technologies, such as hybrid and micro-hybrid vehicles, are driving innovation in the lead-acid battery industry. New technologies like those described in Section 1.10 are being tested and finding success in these applications. It is believed that lead-acid batteries will continue to play an important role in the rechargeable battery market for the next decade.

REFERENCES

1. East Penn Manufacturing Co.
2. Jung, J., "Chapter 4," in *Lead-Acid Battery, Electrochemical Technologies for Energy Storage and Conversion*, Wiley-VCH, New York, 2012.
3. Pavlov, *Lecture Course on VRLA*, Beijing, China, 2000.
4. Available at http://www.docstoc.com.
5. Mayer, G., "Paste curing additive," U.S. Patent Application, US 2006/0093912 A1, 2006.
6. Available at http://www.batteryuniversity.com.
7. Varma, P., "Lead-Acid Battery with Gel Electrolyte," U.S. Patent 4,317,872, 1982.
8. Mayer, G., "Effect of Charging on Life of Float Operated Lead-Acid Battery," International Stationary Battery Conference, 2000.
9. Linden, D., and Reddy, T. B. (Eds.), *Handbook of Batteries*, 3rd ed., McGraw-Hill, New York, 2002.
10. Nakanno, K., Takeshima, S., and Furukawa, J., "Technological Trends in Lead-Acid Batteries for Automotive Applications," *Furukawa Review*, Vol. 32, pp. 49–55, 2007.
11. Available at http://www.axionpower.com.
12. Kurt Kelly, 2002. Available at http://www.fireflyenergy.com/images/stories/pdfs/white%20paper%204.25.08.pdf.
13. Jang, Y., Dudney, N., Tiegs, T., and Klett, J., "Evaluation of the Electrochemical Stability of Graphite Foams as Current Collectors for Lead-Acid Batteries," *Journal of Power Sources*, Vol. 161, pp. 1392–1399, 2006.
14. Kelly, K., and Votoupal, J., "Battery Including Carbon Foam Current Collectors," U.S. Patent 6,979,513 B2, 2005.
15. Available at http://www.fireflyenergy.com.
16. Gyenge, E., Jung, J., and Mahato, B., "Electroplated Reticulated Vitreous Carbon Current Collectors for Lead-Acid Batteries: Opportunities and Challenges," *Journal of Power Sources*, Vol. 113, pp. 388–395, 2003.
17. Gyenge, E., Jung, J., and Snaper, A., "Current Collector Structure and Methods to Improve the Performance of a Lead-Acid Battery," U.S. Patent 7,060,391, 2006.
18. Czerwinski, A., and Zelazowska, M., "Electrochemical Behavior of Lead Oxide Deposited on Reticulated Vitreous Carbon (RVC)," *Journal of Power Sources*, Vol. 64, pp. 29–34, 1997.
19. Das, K., and Mondal, A., "Studies on a Lead-Acid Cell with Electrodeposited Lead and Lead Dioxide Electrodes on Carbon," *Journal of Power Sources*, Vol. 89, pp. 112–116, 2000.

20. Jung, J., "Multiply Conductive Matrix for Battery Current Collectors," PCI Patent Application, PCT/CA2010/000006, 2010.
21. Feng, Y., Han, Y., and Feng, Y., "Liquid Low-Sodium Silicate Electolyte Used for a Storage Battery and Manufactured by Magnetization Process, and the Usage Thereof," U.S. Patent Application, US 2008/0044726 A1, 2008.
22. Available at http://www.evtpower.com.
23. Caven, W., "Horizon Sealed Lead-Acid Battery in Electric Vehicle Application," in *11th Annual Battery Conf. on Applications and Advances*, IEEE, Long Beach, CA, January 9–12, 1996, pp. 159–162.
24. Blanyer, R., "Method and Apparatus for Coating a Core Material with Metal," U.S. Patent 4,658,623, 1985.
25. Blanyer, R., "Battery Grid Structure Made of Composite Wire," U.S. Patent 4,865,933, 1989.
26. Morris, C., "Lead-Acid Rechargeable Storage Battery," U.S. Patent 4,964,878, 1990.
27. Available at http://www.atraverda.co.uk.
28. Chreitzberg, A., and Chiaccho, F., "Method of Making a Sealed Lead-Acid Battery with a Gel Electrolyte and Sealed Lead-Acid Storage Battery Made According to This Method," U.S. Patent 4,687,718, 1987.

2 Negative Electrodes of Lead-Acid Batteries

Vladimir Neburchilov and Jiujun Zhang

CONTENTS

2.1 INTRODUCTION

The negative electrode is one of the key components in a lead-acid battery. The electrochemical two-electron transfer reactions at the negative electrode are the lead oxidation from Pb to $PbSO_4$ when charging the battery, and the lead sulfate reduction from $PbSO_4$ to Pb when discharging the battery, respectively. The performance of a lead-acid battery, in terms of energy efficiency, energy/power densities, and cycle life, is highly dependent on the electrode material composition/morphology,

electrode design/structure, electrolyte composition electrode, and fabrication procedures. The composition, structure, morphology, and design of negative active material (NAM) can significantly affect battery performance. To facilitate battery reactions and to achieve high performance, several technical requirements for negative electrodes as described in the later sections of this chapter have to be met. In this chapter, the composition, morphology, structure, design, and fabrication processes for NAM are described to give the reader an overall picture of a lead-acid battery negative electrode. In addition, technological challenges and possible research directions aimed at further improving the performance of lead-acid batteries are discussed in this chapter.

2.2 ELECTROCHEMICAL PROCESSES OCCURRING AT THE NEGATIVE ELECTRODE OF A LEAD-ACID BATTERY

The main electrochemical reactions occurring at the negative electrode are the conversion between Pb and $PbSO_4$ [1–4]:

$$\begin{gathered} Pb + H_2SO_4 \leftrightarrow PbSO_4 + 2H^+ + 2e^- \\ \left(E^{O}_{Pb/PbSO_4} = -0.355\,V \text{ versus SHE at Nernst conditions}\right) \end{gathered} \tag{2.1}$$

where SHE refers to the standard hydrogen electrode. The forward reaction direction in Reaction 2.1 is the discharge process, and the backward reaction is the charge process. In addition to Reaction 2.1, however, two additional reactions may occur at the negative electrode: One is hydrogen evolution, and the other is oxygen recombination [5]. The H_2 evolution reaction is undesirable, but the O_2 recombination reaction may be useful. The side reaction of H_2 evolution can cause negative effects such as jeopardizing human, system, and facility safety; causing a fire or explosion; causing battery corrosion or self-discharge. To mitigate these negative effects, some measures have been developed, including installing a proper ventilation system, having dedicated flooded battery rooms/separation, minimizing static/electrical discharges, ensuring safe distances are maintained, and using external H_2–O_2 recombinant catalysts to make water.

2.2.1 Hydrogen Evolution at the Negative Electrode

Regarding H_2 evolution at the negative electrode in lead-acid batteries, the reaction can be expressed as follows:

$$H_2SO_4 + Pb \rightarrow PbSO_4 + H_2 \uparrow \text{ (Self-discharge)} \tag{2.2}$$

$$\begin{gathered} H^+ + 2e^- \rightarrow H_2 \uparrow \left(E^{O}_{H^+/H_2} = -0.000\,V \text{ versus SHE at Nernst conditions}\right) \\ \text{(Battery overcharge)} \end{gathered} \tag{2.3}$$

As indicated by Reaction I, the negative electrode potential is about –0.3 V versus SHE in H_2SO_4 aqueous solution, whereas the H_2 evolution reaction is about 0.0 V versus SHE, as indicated by Reaction 2.2. Even when the battery is at the open circuit voltage, the Pb still has a strong thermodynamic tendency to react, causing self-discharge. In the case of battery charging, particularly overcharging, the electrode potential will be more negative than –0.3 V versus SHE. Although Pb has less tendency to be oxidized, H^+ will have an even stronger tendency to be reduced to H_2 according to Reaction 2.3 if the water is oxidized to O_2 at the positive electrode. In such a case, the overall side reaction within the battery is the water decomposition: $2H_2O \rightarrow 2H_2 \uparrow + O_2 \uparrow$. Note that the rate of hydrogen evolution is strongly dependent on the temperature, electrode/electrolyte composition, and battery operating conditions.

2.2.2 Oxygen Recombination at the Negative Electrode

For a flooded lead-acid battery, as shown in Figure 2.1, when it is charged or overcharged, the electrochemical reaction of H_2O oxidation can produce gaseous oxygen [6]:

$$2H_2O \rightarrow 4H^+ + 4e^- + O_2 \uparrow \left(E^{O}_{H_2O/O_2} = 1.23\,\text{V versus SHE at Nernst conditions}\right) \quad (2.4)$$

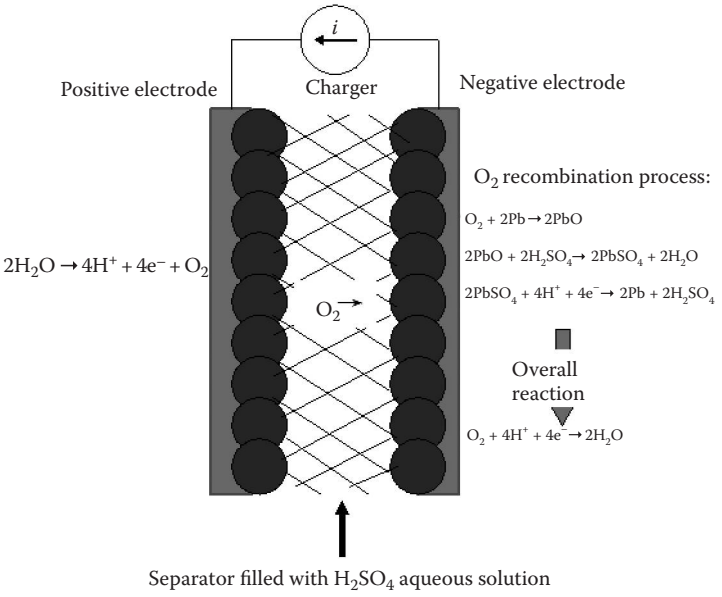

FIGURE 2.1 Scheme showing O_2 recombination on the negative electrode of a lead-acid battery. (From R. Nelson, *J. Minerals Metals Mater. Soc.*, 53(1), 28–33, 2001.)

During the overcharge, oxygen at the positive electrode will partially dissolve into the electrolyte, then transport to negative electrode within the battery, where it will react with Pb through the following mechanism [7]:

$$O_2 + 2Pb \rightarrow 2PbO \tag{2.5}$$

$$2PbO + 2H_2SO_4 \rightarrow 2PbSO_4 + 2H_2O \tag{2.6}$$

$$2PbSO_4 + 4H^+ + 4e^- \rightarrow 2Pb + 2H_2SO_4 \tag{2.7}$$

The oxygen recombination reaction can be obtained by summing Reactions 2.5 through 2.7:

$$O_2 + 4H^+ + 4e^- \rightarrow 2H_2O \tag{2.8}$$

Reaction 2.8 is the opposite of the positive-plate overcharge reaction (Reaction 2.4), indicating that there appears to be no net change in the chemistry of the cell. The water produced by this oxygen recombination process may help the water management in the battery. The oxygen recombination reaction is limited by the diffusion rate of oxygen to the negative electrode. To facilitate the diffusion of O_2, adsorptive glass mat (AGM) or cracks in gelled electrolyte are used as the separator in valve-regulated lead-acid batteries (VRLAs).

It is worth mentioning that the entire reaction process just described, which includes oxygen evolution, transport, and recombination, is called a *closed oxygen cycle* (COC). If the rate of oxygen evolution exceeds a certain limit of oxygen recombination during battery overcharge, extra O_2 will be produced, building up pressure in the cell. In this case, the closed venting valve of the battery will open and release some gas. Another way to remove the O_2 and H_2 produced is to install a catalytic plug in the battery to catalyze their reaction and produce water.

2.3 NEGATIVE ACTIVE MATERIALS AND THEIR PROPERTIES

2.3.1 Composition of Negative Active Materials

The negative electrode is composed of a metal Pb layer coated on the lead or lead-alloy grid. This Pb layer is the active mass and it contains two kinds of Pb crystal structures: (1) the primary skeleton structure formed by interconnected lead crystals and (2) a structure that is composed of small lead crystals deposited on the first, primary skeleton, as shown in Figure 2.2. The primary skeleton is formed by the partial reduction of PbO and $PbSO_4$ to Pb in the pores of cured plates filled by an electrolyte solution during the first stage of formation (charge). The secondary structure of separate lead crystals is formed during the second stage of formation, when $PbSO_4$ is reduced to Pb in H_2SO_4 electrolyte [1]. The secondary structure of lead crystals is involved in the discharge–charge processes, while the primary structure is part of the current collector. To increase the amount of the secondary structure, an expander can be added to the negative electrode material to promote the formation of the secondary structure of Pb crystals with favored particle size and morphology. These

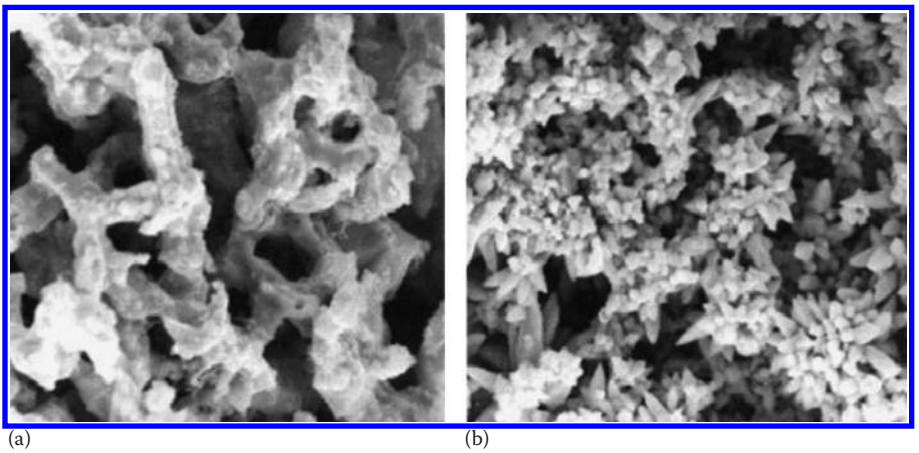

FIGURE 2.2 Negative electrode structure: (a) skeleton of interconnected lead crystals and (b) secondary structure of separate lead crystals deposited on the lead skeleton surface. (From D. Pavlov, and V. Iliev, *J. Power Sources*, 7, 153, 1981.)

expanders can also improve the skeleton structure of the active mess, protecting it from sinking and resulting in enhancement of the battery cycle life [2].

During oxidative polarization of the lead anode in H_2SO_4 electrolyte, two products can be observed, a majority of $PbSO_4$ and a minority of PbO, analyzed by x-ray spectroscopy [3,8–10]. Observations of $PbSO_4$ crystals indicate they have pores that are permeable for water and protons but not for SO_4^{2-} ions. PbO is formed through the reaction between Pb^{2+} ions formed on the interface of $Pb/PbSO_4$ and water, forming $Pb(OH)_2$, which is dehydrated to form tet-PbO. In general, the typical negative electrode material has a specific surface area of 0.6 to 1 m^2/g.

In brief, the NAM consists of the skeleton (primary structure) formed by interconnected lead crystals and a secondary structure of separate lead crystals deposited on this skeleton (see Figure 2.2). The skeleton forms at the partial reduction of PbO and $PbSO_4$ to Pb in pores of cured plates filled with a neutral solution during the first stage of formation (charge). The secondary structure of separate lead crystals forms during the second stage of formation when $PbSO_4$ is reduced to Pb in H_2SO_4.

2.3.2 Conductivity of Negative Active Materials

The addition of carbon in NAM can increase the electronic conductivity of the electrode layer, which improves the battery recharge. In spite of the fact that the conductivity of carbon is less than that of lead, carbon can form some conducting pathways between lead sulfate crystals in a partial state of charge (PSOC). Carbon in the mixture with insulator PbO in an electrode paste can significantly increase its electronic conductivity. The carbon decreases the conductivity of NAM at a concentration of 1.5 wt% dosing level (Figure 2.3) [11]. The higher conductivity of carbon acetylene black-containing mixtures can be understood by noting that the carbon particles are very small and can easily fit between the sulfate grains and that the number of particles

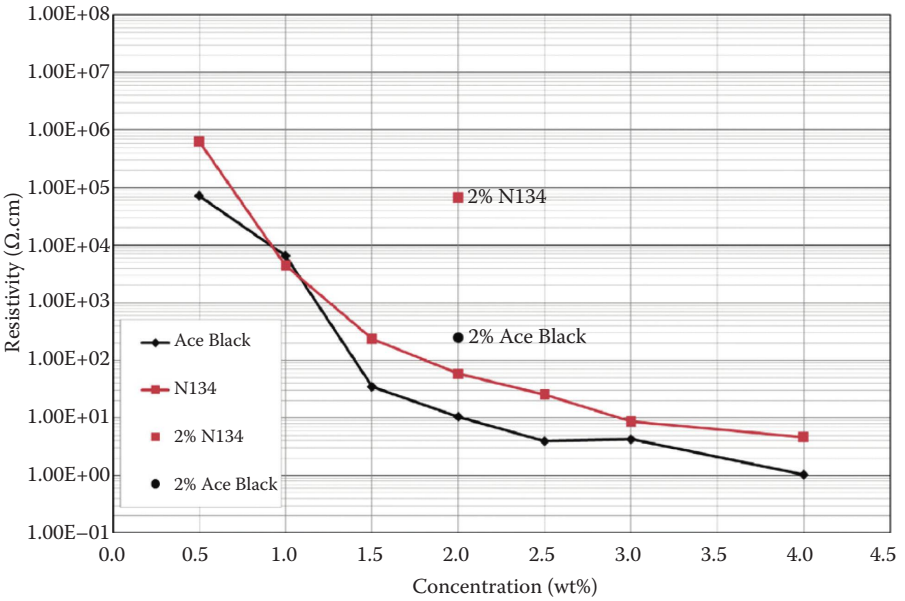

FIGURE 2.3 Resistivity of carbon blacks (carbon black N134 and acetylene carbon black) in lead sulfate and at 2% dry loading in dry, unformed active material. (From D. P. Boden et al., *J. Power Sources*, 195(14), 4470–4493, 2010.)

per gram is very large. Because the conductive behavior of carbon is attributable to the degree of sp^2:sp^3 hybridization, it follows that the more amorphous carbons are generally poorer conductors, but particle density and size also play an important role.

2.4 NEGATIVE ELECTRODE MATERIALS, THEIR FUNCTIONS, AND CURING/FORMATION

The most popular design for negative electrodes is called the Faure design, in which a layer of active mass is coated on the Pb-alloy grid. Normally, the starting materials for the negative electrode active mass are PbO, H_2SO_4, barium sulfate, carbon black, sodium lignosulfonate, humic acid, and water [10]. The design ratio between these components depends on the type of lead-acid battery; for example, a low ratio of PbO:H_2SO_4 is used for starting, lighting, and ignition (SLI) batteries, and a high ratio of PbO:H_2SO_4 for deep-cycle batteries. $BaSO_4$, lignosulfonate, and carbon (expanders) are used to prevent the passivation of the lead surface, which is caused by the deposition of $PbSO_4$ film. Furthermore, these additives can increase the utilization of lead up to 20% to 50% at its oxidation.

As observed, lignosulfonate (0.5 wt%) can adsorb on lead particles, preventing the continuous growth of $PbSO_4$, increasing the surface area of the lead material, and suppressing the formation of orthorhombic PbO phase [12]. The adsorption of an expander can affect the anodic oxidation of Pb, cathodic reduction of lead sulfate, morphology of lead sulfate, and both porosity and surface area of NAM. An

expander also limits the crystal growth of the porous lead active material and, thereby, enhances the specific surface area of NAM. When carbon black or active carbon is used as the expander, the specific surface area, conductivity, and porosity of NAM can be increased, leading to an enhancement in battery performance. $BaSO_4$ is a nucleating agent (particle size of 0.5 to 5 μm), which can promote the deposition of porous $PbSO_4$ crystals, leading to a smooth formation of Pb particles during battery charging. The homogeneous distribution of small $BaSO_4$ particles can help minimize the size of growing $PbSO_4$ crystals during battery discharge and also maximize their conversion to lead during charge. In contrast to lignosulfonates, $BaSO_4$ does not change the overpotential of the negative electrodes [13], and barium sulfate and lead sulfate interactions with lignosulfonates are very similar [14]. Table 2.1 summarizes all possible materials and their functions in the negative electrode of lead-acid batteries [10,15–17].

During fabrication of the negative electrode, the negative paste (or cream) containing the starting materials listed in Table 2.1 is coated onto the negative grid (also called Pb-alloy current collectors) by extrusion, followed by pressing with a scrapper and flush drying. The adhesion of the paste with the current collector is achieved by a curing process at a controlled temperature and humidity. At the curing stage, paste can react with the grid Pb-alloy surface to reach a strong adhesion. In the curing process (95% humidity), if the temperature is controlled at $T > 70°C$, the paste can form a tetrabasic lead sulfate $4PbO \cdot PbSO_4$ (4BS) dominated crystal structure, which is promoted by adding Pb_3O_4; if the temperature is controlled at $T < 70°C$, a tribasic lead sulfate $3PbO \cdot PbSO_4 \cdot H_2O$ (3BC) dominated crystal structure can be formed [10,18–25]. Normally, 3BC has shorter crystals (3 μm) than 4BC ($\gg$3 μm), which

TABLE 2.1
Composition of the Paste and Its Component Functions for NAM of Lead-Acid Batteries

Starting Materials for Negative Electrode	Content (wt%)	Functions
PbO	83.5 [10]	Active material
H_2SO_4	2.7 [10]	Solvent
Barium sulfate	0.7 [10] (0.2–1.0% [15])	Nucleating agent for lead sulfates
Sodium lignosulfonate	0.13 [10] (0.2–0.4% [15])	Suppresses the formation of $4PbO \cdot PbSO_4$ and PbO phase, increases surface area, and stabilizes the paste structure (4BS/3BS)
Carbon (carbon black, activated carbon)	0.25 [10] (0.15–0.3 [15])	Increases conductivity, specific surface area, and charge acceptance
Humic acid	0.5 [10]	
Water	12.2 [10]	

Source: R.S. Shi, L. Zhang, X. Sun, H. Liu, J. Zhang, *Electrochemical Technology for Energy Storage and Conversion*, Vol. 1. 2009. Copyright Wiley-VCH Verlag GmbH & Co. KGaA. Weinheim, Germany. Reproduced with permission; R. Flores, and L. M. Blanco, *J. Power Sources*, 78, 30–34, 1999; M. Fernández et al., *J. Power Sources*, 195, 4458–4469, 2010; P. T. Moseley, *J. Power Sources*, 191, 134–138, 2009.

can form a more uniform porous coating. After curing, all Pb(II)-related materials are electrochemically reduced to metal Pb with a porous matrix structure (formation stage). The discharge capacity of a lead-acid battery is strongly dependent on the porosity and surface area of this Pb coating.

In SLI lead-acid batteries for automobile applications, 3BC in negative plate is the preferable material for the anode coating, whereas the 4BS compound is preferred in deep-cycle lead-acid batteries. After curing of negative plates, they are all converted to a lead electrode.

2.5 NEGATIVE ELECTRODE DESIGN AND FABRICATION

In general, lead-acid batteries have three types of negative electrode designs: Planté, Faure (pasted), and tubular [4]. The Planté electrode is made by cycling lead with a high specific surface area in acid to form a thick PbO layer. This kind of design is mainly used in industrial applications that do not require high energy density. The Faure negative electrode is made by the deposition of lead paste on perforated lead alloy grids. (Pb-Ca alloys are preferable due to their minimized gassing and corrosion.) The lead paste consists of lead oxide, sulfuric acid, water, carbon, and expanders (C, $BaSO_4$, or lignosulfonate). The first step is to attach the paste onto the Pb-alloy grid, the second step is to cure this paste plate at a controlled temperature and humidity, and the final step is to electrochemically reduce this cured plate in acidic solution to form a Pb metal active mass layer (this process is called *formation*). The tubular electrode design includes a vertical fiber tube coated by PbO_2 (positive electrode) with a parallel, inserted negative tubular electrode on which a metal Pb layer is coated. The modern process for negative electrode fabrication consists of the following several steps [10] (Figure 2.4 [26]):

1. *Paste preparation process.* In this step, PbO, H_2SO_4, water, and expanders (carbon particles, $BaSO_4$, or lignosulfonate) are mechanically mixed together to form a wet paste. A pony, muller, or vertical muller mixer is used for the mixing process. The viscosity of the paste thus formed typically decreases with mixing time at a controlled temperature. The ratio of PbO:H_2SO_4 in paste can vary depending on the type of lead-acid battery. For example, the ratio of PbO:H_2SO_4 in negative paste for an SLI lead-acid battery is normally lower than that of a deep cycle one.
2. *Paste deposition process.* In this step, an extrusion process is used for the paste deposition onto Pb-alloy grid, followed by a pressing step using a scraper or machine (fixed-orifice paster or belt paster). The amount of paste is normally regulated by the spacing of a hopper above the grid. The grid is automatically placed on the transfer belt. The final step in this process is to flush dry the pasted plates in a high-temperature drier, giving the paste a hard surface.
3. *Curing process.* The curing process converts wet active paste into dry porous material and provides interaction between the paste and the grid. In this curing process, the paste reacts with the Pb grid, leading to the formation of dominated tetratribasic lead sulfate $4PbO \cdot PbSO_4$ (4BS) at $T > 70°C$ or dominated tribasic lead sulfate $3PbO \cdot PbSO_4 \cdot H_2O$ (3BS) at $T < 70°C$

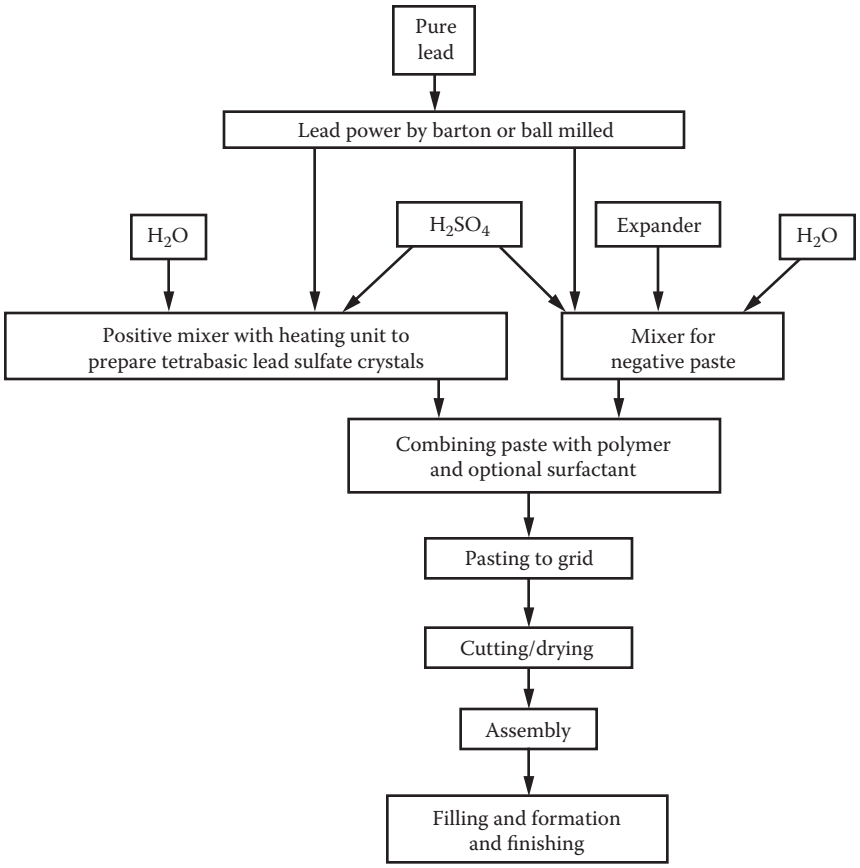

FIGURE 2.4 Fabrication of negative electrode. (From C. Rongrong et al., U.S. Patent 6755874, 2004.)

[27–32]. In general, when the temperature is lower than 70°C, the formed paste contains $3PbO.PbSO_4.H_2O$ (3BS) + tet-PbO + orthorhombic-PbO + Pb at the ratio of H_2SO_4:PbO less than 12%. The paste will contain the maximum content of 3BS at an H_2SO_4:PbO ratio of 10% when the temperature is greater than 70°C [18,20,22]. At such temperatures, the formed active mass contains $4PbOPbSO_4$ (4BS) + tet-PbO + orthorhombic-PbO + Pb at an H_2SO_4:PbO ratio of less than 7%, and the maximum content of 4BS is at the H_2SO_4:PbO ratio of 6.5% [29–31]. 3BS and orthorhombic-PbO are formed first and then 4BS is formed. Expanders can hinder the formation of 4BS and orthorhombic-PbO. The addition of red lead (Pb_3O_4) into the mass can promote the formation of 4BC in a wider range of temperatures and humidity, which has a significant effect on the discharge capacity of the battery due to the change in both porosity and specific surface area of the negative electrode [28]. 3BS crystals typically have sizes of 2 to 4 μm, and 4BS crystals can reach sizes of 20 to 50 μm. The larger 4BS crystal has a

length of 300 μm, width of 60 μm, thickness of 50 μm, and a surface area of 72,000 μm^2. The 3BS-based active anode material precursor is preferable in high-discharge-rate batteries, and 4BS precursors are preferable in deep-cycle and long-life stationary batteries [4].

4. *Formation process.* In this process, the cured active negative pastes on Pb-alloy grids are reduced to Pb in H_2SO_4 aqueous solution to convert the plate into a Pb negative electrode.

2.6 EFFECTS OF EXPENDERS IN NEGATIVE ACTIVE MATERIALS ON THE PERFORMANCE OF NEGATIVE ELECTRODES

The composition and morphology of the negative electrode active mass can determine the performance of a lead-acid battery. One of the main elements of NAM is an expander, which can affect the crystallization of Pb during charge and $PbSO_4$ during discharge, the overvoltage of hydrogen evolution during the charge, the self-discharge, the capacity, the cold cranking ability (CCA), and the cycle life of the battery. Therefore, in NAM, expanders play a significant role in the function of the negative electrode. As shown in Figure 2.5, different expenders in NAM can lead to different performances of the lead-acid battery [20].

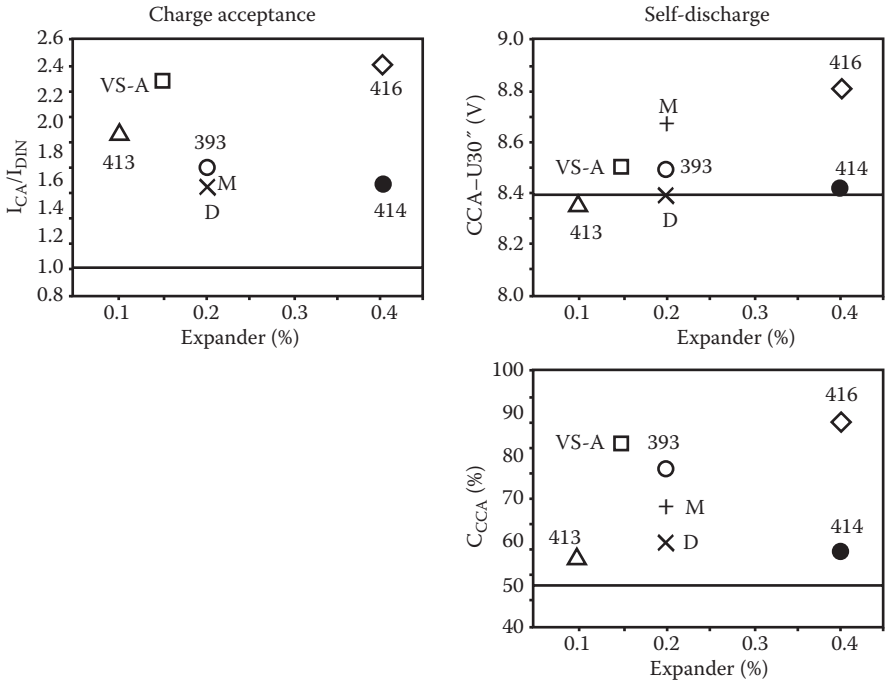

FIGURE 2.5 Effect of expander on lead-acid battery charge acceptance and self-discharge UP-393 (0.2%), UP-417 (0.2%), UP-417 (0.2%), UP-393 (0.2%), UP-417 (0.2%), UP-413 (0.1%), M (0.2%), UP-414 (0.4%). (Maschinenfabrik Gustav EIRICH [Germany].)

Organic expanders are mainly chemically treated lignins or derivatives of the latter with methoxyl, phenolic, carboxyl, and ketonic functional groups [12,19–24, 29–46]. It has been found that the phenol groups have a beneficial effect on the negative plate's characteristics [20,24]. Quinones and their derivatives (benzoquinone, quinhydrone, cyclohexanol, etc.) also have expander properties [47]. For example, Pavlov et al. [20] tested eight lignosulfonates (Borregaard LignoTech) to determine their efficiency as expanders in the negative plates of SLI lead-acid batteries. It was observed that NAM with Lignins UP-393, Vaniperse-A, and UP-414 could demonstrate beneficial performance. It was also discovered that the conversion of the skeleton could lead to the formation of shapeless lead crystals with smaller surface area and large macropores in between, which could give the battery a longer cycle life. Normally, the favorable expander should have an average molecular weight of the lignins and their derivatives, high –COOH content, low $-OPCH_3$ and organic S contents, optimum Ar-OH content, and high lignin purity.

Depending on the type of battery used, the specific expander as well as its content in NAM should be selected. For example, VRLA batteries normally use a higher expander concentration than conventional flooded batteries. Expanders such as Indulin AT and Kraftplex (both lignins) increase the active material utilization when increasing their concentration in the range of 0.25 to 0.75 wt%. The Lignotech D-1380 expander can improve the battery's capacity as its concentration is increased, as shown in Figure 2.6.

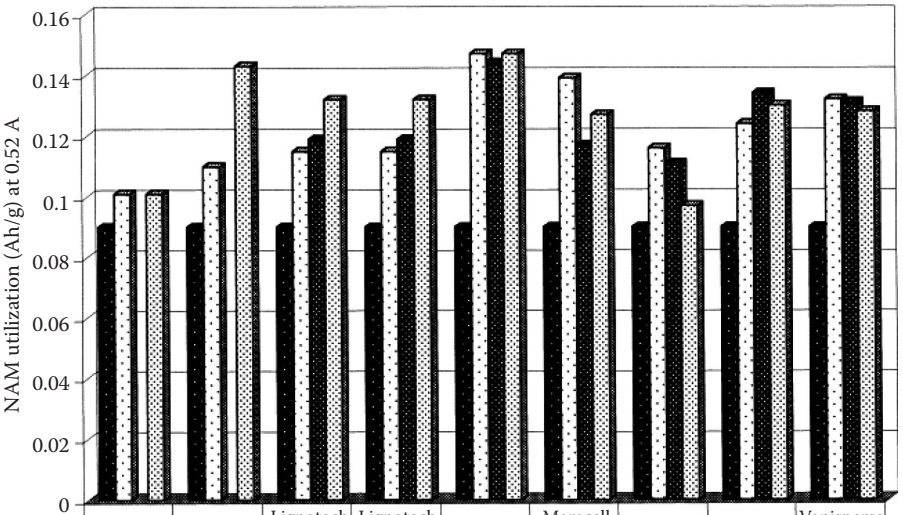

	Indulin AT	Kraftplex	Lignotech D-1271	Lignotech D-1380	Lomar B	Maracell XC-2	BNF	GKD	Vanisperse A
0.00%	0.09	0.09	0.09	0.09	0.09	0.09	0.09	0.09	0.09
0.25%	0.101	0.11	0.115	0.115	0.147	0.139	0.116	0.124	0.132
0.50%			0.119	0.119	0.144	0.117	0.111	0.134	0.131
0.75%	0.101	0.143	0.132	0.132	0.147	0.127	0.097	0.13	0.128

FIGURE 2.6 Utilization of negative active material with different expanders with concentrations of 0.25, 0.50, and 0.75 wt% at 0.52 A. (From K. Nakamura et al., *J. Power Sources*, 59, 153, 1996.)

It was established that both Vanisperse (Vs) and Indulin (In) expanders could provide higher NAM stability at 40°C [23]. However, the recrystallization of $PbSO_4$ in a VRLA battery can lead to an increase in the size of the Pb crystal, resulting in a capacity loss. Pulsing charging and the addition of carbon blacks to NAM can minimize the formation of "hard sulfates." The addition of 2% carbon (carbon black or graphite) could hinder sulfate formation, probably due to the formation of conducting bridges in carbon particles surrounding the sulfate crystals [48]. It has been established that the improvement of the cycle life of a negative electrode in a PSOC can be achieved by the addition of graphite and titanium dioxide. Large pores of this NAM are occupied by graphite, and the lead sulfate growth will be disturbed [49].

2.7 EFFECTS OF BATTERY OPERATING CONDITIONS ON THE PERFORMANCE OF NEGATIVE ELECTRODES

The lead anode layer can have a different composition and morphology depending on the applied potentials, which significantly affect anode performance (Figure 2.7) [49–52]: lead sulfate ($PbSO_4$ [crystal]) when polarization at a potential range of –0.95 to –0.40 V (Hg/Hg_2SO_4) (Figure 2.7a); lead oxide (tet-PbO sublayer under $PbSO_4$) at a range of –0.40 to 0.95 V (Figure 2.7b); and lead dioxide (α-PbO_2 + β-PbO_2) at a range of >0.95 V (Figure 2.7c).

Normally, the $PbSO_4$ film on the anode surface is impermeable for SO_4^{2-} and HSO_4^-, but permeable for protons [53], which determines a different potential across the $PbSO_4$ film during Pb anode oxidation. Using cyclic voltammetry, Visscher [54] detected the formation of α-PbO_2 and β-PbO_2 under the $PbSO_4$ film and their reduction to, respectively, $PbSO_4$ at 1.65 V (RHE) and $nPbO_X \cdot PbSO_4$ at $E > 1.65$ V.

The operating conditions of lead-acid batteries can significantly affect the structure of the negative plate and its performance. The NAM thickness at the charged state is different from that at the discharged state [51]. The thickness of the NAM layer

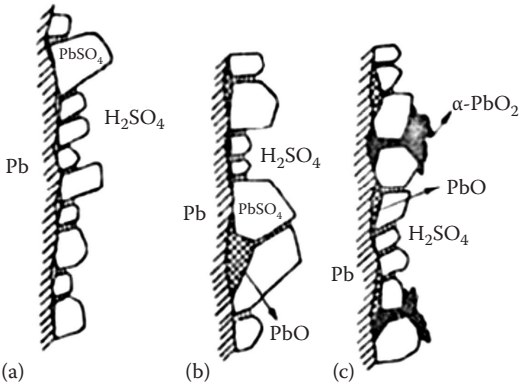

FIGURE 2.7 Anodic layers on Pb anodes in a lead-acid battery at (a) E = –0.95 to –0.40 V (Hg/Hg_2SO_4); (b) E = –0.40 to 0.95 V; and (c) $E > 0.95$ V. (From D. Pavlov, and N. Iordanov, *J. Electrochem. Soc.*, 117, 1103, 1970.)

increases during Pb oxidation to $PbSO_4$ due to the higher mole volume of $PbSO_4$ (48 cm^3 mol^{-1}) than that of Pb (12.3 cm^3 mol^{-1}) [1]. Recrystallization of $PbSO_4$ at the discharge decreases the stress of negative plates. Furthermore, during cycling, the NAM loses its macrohomogeneity due to "breathing" of active mass, allowing the exchange of ionic flows in macropores. A stress concentrated in these macropores could break a skeleton structure, causing an electrochemically inactive zone, leading to decreased electrode capacity. To avoid the Pb skeleton breaking, sodium lignosulfonate (SLS) can be used as the expander, which does not change the skeleton branches of NAM but expands it due to the formation of hydrogen bubbles and pulsation of active mass deep breathing of the negative plate (Figure 2.8c and d). (In contrast to SLS, the SNK expander (0.6%

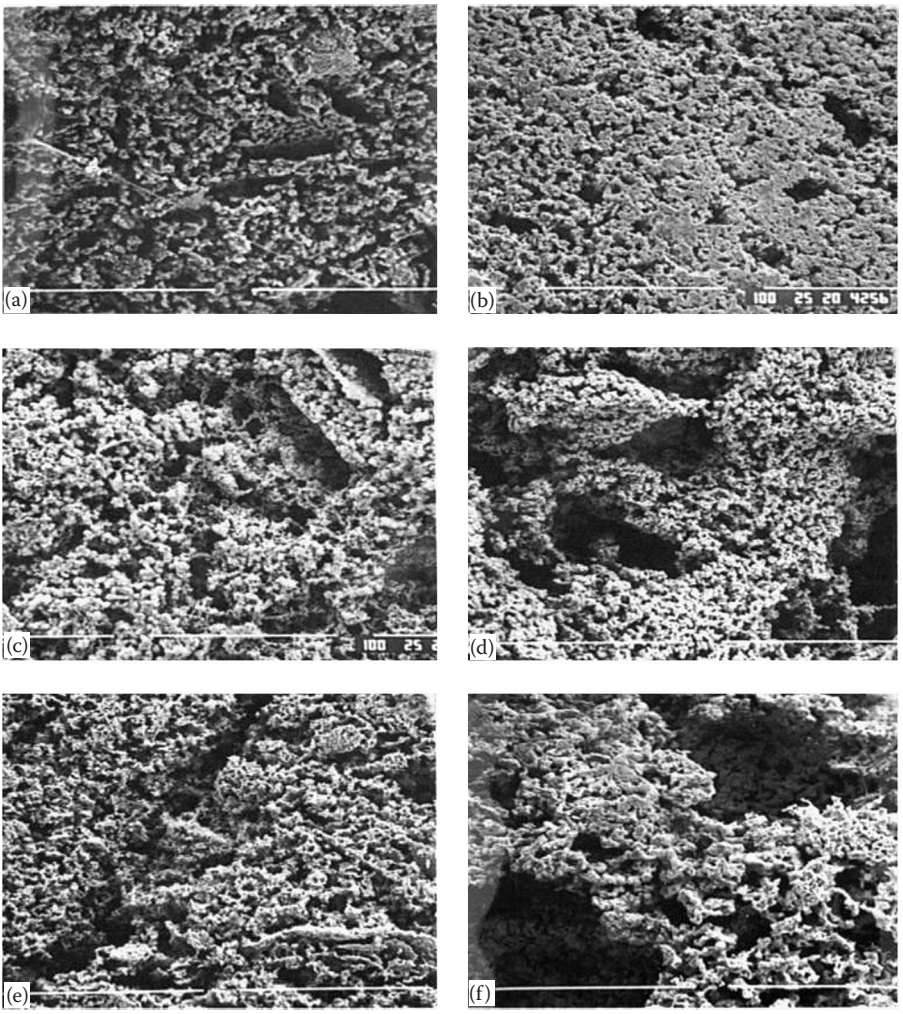

FIGURE 2.8 SEM images of the skeleton of the active mass (a, c, e) at the seventh cycle and (b, d, f) at the 60th cycle of plates (a, b) without an expander, (c, d) with NaLS, and (e, f) with SNK. Scale bar: 100 μm. (From D. Pavlov, and S. Ignatova, *J. Appl. Electrochem.*, 17, 715, 1987.)

Sintan NK) could provide higher stability and the absence of "breathing" of the negative plate after 60 cycles (Figure 2.8e) [55].

2.8 TESTING AND DIAGNOSIS OF NEGATIVE ELECTRODES

2.8.1 Performance Testing of Negative Electrodes

Testing the negative electrode of a lead-acid battery includes the following tests [48]: (1) cycle life test, (2) capacity test, (3) charge rate acceptance test, (4) storage test, (5) overcharge test, and (6) dynamic stress test. Brief descriptions of the testing processes for some of the main tests follow:

1. *Cycle life test* [16,34]. Normally, the battery capacity decreases with cycle number due to sulfation of negative plates. A cycle life is a measure of the charge acceptance of the electrode and recovery of this charge during a cycle. The battery cycle life is the amount of cycles that can occur until capacity drops to 70% of its initial value. The test protocol for high-rate partial-state-of-charge (HRPSOC) operation (HRPSOC cycling test) is as follows [34]: (a) cell assembly; (b) capacity testing at 1C rate (1.74 A); (c) recharging and repeating for 10 cycles; (d) recharging to 100% state of charge (SOC); (e) discharging to 50% SOC at 1C rate (0.87 Ah); (f) cycling at 2C rate (3.48 A), discharging 60 sec, resting 10 sec, charging 60 sec, and resting 10 sec; (g) cycling until end-of-discharge voltage ≤ 1.70 vpc; (h) recharging to 100% SOC; and (i) capacity testing at 1C rate and recharging.
2. *Capacity test*. Lead-acid battery discharges at ambient temperature, for example, at the 1-, 3-, and 5-h rates (1.98, 0.78, and 0.52 A) to a cut-off voltage of 1.70 after 1 h on the open circuit after charging [34].

2.8.2 Performance Diagnosis for Negative Electrodes

Diagnosis of negative electrode performance in a lead-acid battery can be carried out using several methods: (1) step and cyclic voltammetry, (2) potential transient analysis, and (3) electrochemical impedance spectroscopy. These methods are mainly used to diagnose performance to determine material/device design optimization and the performance degradation for developing a mitigation strategy. The brief diagnosis processes for these methods are described next.

2.8.2.1 Cyclic Voltammetry

Cyclic voltammetry (CV) at the potential scan rate of 2 mV/s can be carried out on a negative electrode at $E = -1.2$ to -0.7 V (Hg/Hg_2SO_4) because all reactions at the Pb electrode can be completely developed in this potential range without a side reaction such as hydrogen evolution. The potential cycling can be continued until a stable cyclic voltammogram has been achieved. For example, the charges of negative electrode NAMs without an expender, corresponding to the areas of the anodic peaks on their corresponding cyclic voltammograms, can be used to estimate the charge

change with a cycle number, allowing for determination of the effect of expanders on battery performance [56,57].

2.8.2.2 Chronocoulometry

A chronocoulometric test with a single potential step can be used to evaluate the quantity of charge, allowing a percentage of charge recovery $[(Q_c/Q_d) \times 100]$ to be calculated. After discharge, a potential of –1.350 V is applied for 360 sec. Potentiostatic transients can be used for the analysis of formation and reduction of lead sulphate at the applied potential step in the anodic direction.

2.8.2.3 Electrochemical Impedance Spectroscopy

Electrochemical impedance spectroscopy of a negative electrode can be carried out after preliminary polarization at –1.3 V versus Hg/Hg_2SO_4 at the frequency range of 10^4 to 10^{-2} Hz with an amplitude for the interrupting signal of 5 mV [58,59].

2.9 CYCLE LIFE DEGRADATION MECHANISMS, FAILURE MODES, MITIGATION STRATEGIES, AND TECHNICAL PERSPECTIVES OF NEGATIVE ELECTRODES

In general, similar to other types of batteries, lead-acid battery performance can be degraded with increasing cycling numbers, as shown in Figure 2.9. The main processes leading to the cycle life degradation of a lead-acid battery are as follows: (1) electrode corrosion (grid, plate-lug, strap, and post), (2) positive active mass degradation and loss of adherence to the grid, (3) irreversible formation of lead sulfate in the active mass (crystallization and sulfation), (4) short circuits, and (5) loss of water.

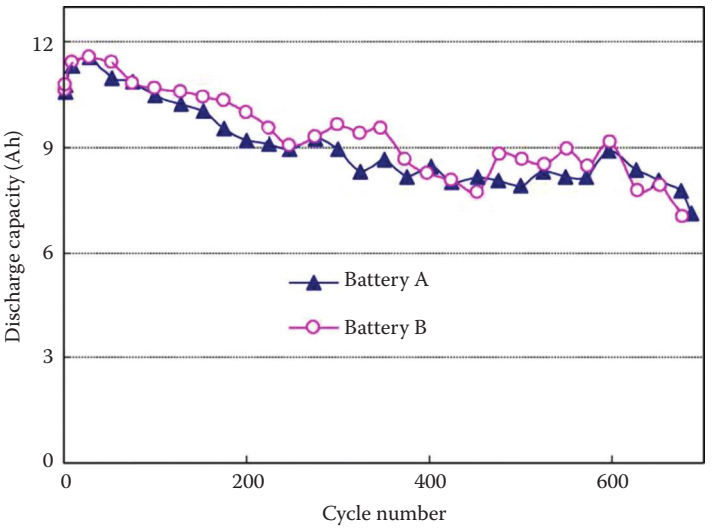

FIGURE 2.9 Evolution of discharge capacity of two VRLA batteries in the cycles at 100% depth of discharge. (From Y. Guo et al., *J. Power Sources*, 191, 127–133, 2009.)

Aging mechanisms of lead-acid batteries are interdependent; for example, corrosion of negative grids can increase the active mass degradation and lead to short circuits. The rate of cycle life degradation is also dependent on the type of lead-acid battery [60]. Normally, the SLI battery suffers from aging due to grid corrosion, but the VRLA battery degrades due to the negative active mass sulfation or water loss. The rate of water loss due to evaporation or hydrogen evolution at the negative electrode (self-discharge) can be increased with increasing temperature. Furthermore, degradation of the negative electrode cycle life also depends on acid concentration. For example, corrosion of grids can be increased with decreasing H_2SO_4 concentration, but the rates of hydrogen evolution (self-discharge) and sulfation on the negative electrode can also be increased with increasing H_2SO_4 concentration.

Regarding the degradation mechanisms of negative electrodes, three major processes should be emphasized: (1) sulfation, (2) agglomeration of finely divided lead, and (3) passivation of the negative grid surface [61,62].

1. *Sulfation*. Sulfation is the process of recrystallization of $PbSO_4$ [61,62]. In battery operation, it is desirable for the lead sulfate to form small crystals that readily redissolve during the charging process, allowing the active materials to revert to their original form. The lead sulfate crystals can grow larger, however, making it difficult to convert back to the active material. The growth of the nonconductive lead sulfate on the negative electrode during discharge can lead to the formation of the passive $PbSO_4$ film, resulting in the loss of battery capacity over time. In the operation of lead-acid batteries, if the battery operating conditions enable it to easily recharge to $PbSO_4$, the process is called "soft sulfation"; if the recharge is difficult, the process is called "hard sulfation." The solutions that are commonly used to overcome sulfation problems are (a) to use charging pulses to minimize "hard sulfation" [63] and (b) to add carbon to the negative paste [64].
2. *Agglomeration of finely divided lead*. Agglomeration of lead particles in the negative electrode is caused by metal fusion [62]. Normally, metals are known to undergo contact fusion at a temperature below their melting point. Even if an expander is added into the negative active mass, the fusion of charged lead with grid Pb can also occur if the expander's content is not optimized. Therefore, a sufficient and optimized expander can be added to the active mass to prevent the lead from fusing.
3. *Passivation of the negative grid surface*. The major cause of passivation of the negative grid is the formation of a PbO or $PbSO_4$ film at the interface between the grid (current collector), surface, and lead active mass as a result of a reaction between the Pb grid and acid. PbO or $PbSO_4$ film can increase electrode resistance and then decrease its capacity. Although charging the battery can cause this passivation film to reduce to Pb, complete reduction may not be achieved every time. To reduce the issue of passivation, the Pb-Ca-alloy has been used as the grid material, a process that has shown some improvement and is normally better than pure Pb or a Pb-Sb alloy. One prospective approach to minimizing the negative grid passivation is to use carbon-graphite foam to replace the Pb-alloy as the negative grid.

The results thus achieved have shown significantly increased material utilization (from 20% to 50% to 70% to 90%), improved recharge capability, prolonged high-rate-discharge cycle life, and enhanced performance at low temperatures [65]. The other prospective development for a durable negative grid is to use a lead-tin-alloy–coated reticulated carbon plate. The results thus achieved have shown high conductivity and specific surface area >500 m^2/g [66].

The development of advanced lead-acid batteries such as lead-carbon batteries (PbC® from Axion Power International Co.) [67] and hybrid batteries (LAB+ asymmetric supercapacitor; UltraBattery® from East Penn Manufacturing) [68] may lead to new perspectives for the improvement of the design of negative electrodes. These cost-effective batteries with advanced electrode designs can be used for "stop–start" and "micro–mild" hybrid technologies that can compete with the plug-in and all-electrical vehicles using expensive Li-ion and NiMH batteries. The addition of carbon (flake, synthetic graphite, graphitized carbon, carbon black, and activated carbon) into the NAM of lead-acid batteries subjected to a PSOC can significantly increase their cycle life (over 6000 capacity turnovers) [17] and the utilization of the active material as well. Axion's multicelled asymmetrically supercapacitive lead-acid carbon hybrid battery [67] could provide high performance. It employs an advanced negative electrode consisting of a five-layer coating with a carbon electrode, a corrosion barrier, a current collector, a second corrosion barrier, and a second carbon electrode.

2.10 SUMMARY

This chapter reviewed all aspects of the negative electrodes for lead-acid batteries in terms of their design, fabrication, and performance degradation/mitigation. The electrochemical reactions occurring on the negative electrodes, including the conversion between Pb and $PbSO_4$, hydrogen evolution (self-discharge), and the oxygen recombination mechanism, were presented. The materials used for both negative grids and active mass layers were described in terms of their morphologies, structures, compositions, and functions.

It is worth emphasizing that the development of advanced negative electrode active materials with optimal composition (using optimal organic expanders, such as Sintan NK instead of traditional SLS), porosity, stability, and perspective grid materials (such as a sponge Pb-Ca-alloy, Pb-Sn–coated carbon, carbon-graphite foam) may allow for a significant increase in the utilization of electrode materials and minimization of the recrystallization of lead sulfate and self-discharge on negative electrodes. These, in turn, will lead to high energy efficiency and prolonged battery cycle life.

REFERENCES

1. D. Pavlov, and V. Iliev, *J. Power Sources*, 7 (1981), 153.
2. V. Iliev, and D. Pavlov, *J. Appl. Electrochem.*, 15 (1985), 39.
3. D. Pavlov, *Lead-Acid Batteries: Science and Technology*, Elsevier, Oxford, UK, (2011).

4. K. R. Bullock, "Lead-Acid Batteries," *J. Power Sources*, 51 (1994), 1–17.
5. C. O'Donnell, and M. Schiemann, "Hydrogen Gas Management for Flooded Lead-Acid Batteries." Available at http://www.battcon.com/PapersFinal2008/ODonnellPaper2008PROOF_6.pdf.
6. R. Nelson, *J. Minerals Metals Mater. Soc.*, 53(1) (2001), 28–33.
7. J. P. Pompon, and J. Bouet, Paper 17.4 in *INTELEC '89 Conf. Proc.*, IEEE, Piscataway, NJ (1989).
8. H. Bode, *Lead-Acid Batteries*, Wiley-VCH Co. (1977).
9. P. T. Moseley, J. Garche, C. D. Parker, and D. A. J. Rand, *Valve-Regulated Lead-Acid Batteries*, Elsevier, Oxford, UK (2004).
10. R. S. Liu et al. (Eds.), *Electrochemical Technology for Energy Storage and Conversion*, Vol. 1. Wiley-VCH Co. (2009).
11. D. P. Boden, D. V. Loosemore, M. A. Spence, and T. D. Wojcinski, *J. Power Sources*, 195(14) (2010), 4470–4493.
12. E. J. Ritchie, *J. Electrochem. Soc.*, 59 (1996), 53.
13. K. R. Bullock, *J. Power Sources*, 195 (2010), 4513–4519.
14. Y.-B. O. Myrvold, *J. Power Sources*, 117 (2003), 187.
15. R. Flores, and L. M. Blanco, *J. Power Sources*, 78 (1999), 30–34.
16. M. Fernández, J. Valenciano, F. Trinidad, and N. Munoz, *J. Power Sources*, 195 (2010), 4458–4469.
17. P. T. Moseley, *J. Power Sources*, 191 (2009), 134–138.
18. D. Pavlov, S. Gancheva, and P. Andreev, *J. Power Sources*, 46 (1993), 349–359.
19. S. Gancheva, and D. Pavlov, *Proc. Int. Conf. LABAT'93*, Varna, Bulgaria (June 7–11, 1993), 156.
20. D. Pavlov, B. O. Myrvold, T. Rogachev, and M. Matrakova, *J. Power Sources*, 85 (2000), 79.
21. B. O. Myrvold, and D. Pavlov, *J. Power Sources*, 85 (2000), 92.
22. T. J. McNally, M. E. Sanford, B. O. Myrvold, D. Pavlov, T. Rogachev, G. Rapazov, and M. Matrakova, U.S. Patent 6346347B1 (2002).
23. G. Papazov, D. Pavlov, and B. Monahov, *J. Power Sources*, 113 (2003), 335.
24. M. Matrakova, T. Rogachev, D. Pavlovand, and B. O. Myrvold, *J. Power Sources*, 113 (2003), 345.
25. G. Petkova, P. Nikolov, and D. Pavlov. *J. Power Sources*, 158 (2006), 841.
26. C. Rongrong, S. Harrison, and K. Wellington, U.S. Patent 6755874 (2004).
27. V. Iliev, and D. Pavlov, *Appl. Electrochem.*, 9 (1979), 555.
28. D. Pavlov, and N. Kapkov, *J. Electrochem. Soc.*, 137 (1990), 16.
29. D. Pavlov, and N. Kapkov, *J. Power Sources*, 31 (1990), 189.
30. D. Pavlov, S. Ruevski, P. Eirich, and A. C. Burschka, *The Battery Man*, 40 (1998), 16–36.
31. D. Pavlov, and S. Ruevski, *J. Power Sources*, 95 (2001), 191.
32. E. Lamaire-Potteau, X. Vallve, D. Pavlov, G. Papazov, N. V. der Borg, and J. F. Sarrau, *J. Power Sources*, 162 (2006), 884.
33. F. S. B. Martinez, D. Marin, P. Spinelli, and F. Trinidad, *J. Power Sources*, 15 (2001), 174–179.
34. D. P. Boden, J. Arias, and F. A. Fleming, *J. Power Sources*, 95(1–2) (2001), 277–292.
35. V. Iliev, and D. Pavlov, *J. Appl. Electrochem.*, 15 (1985), 39.
36. A. C. Zachlin, *J. Electrochem. Soc.*, 98 (1951), 321.
37. E. Willinganz, *Trans. Electrochem. Soc.*, 92 (1947), 148.
38. E. G. Yampol'skaya, and B. N. Kabanov., *Sov. J. Appl. Chem.*, 48 (1973), 465.
39. E. G. Yampol'skaya, M. I. Ershova, V. V. Surikov, I. I. Astahov, and B. M. Kabanov, *Elektrokhimiya*, 8 (1972), 1209.

40. E. G. Yampol'skaya, M. I. Ershova, V. V. Surikov, I. I. Astahov, and B. M. Kabanov, *Elektrokhimiya*, 2 (1966), 1327.
41. B. K. Mahato, *J. Electrochem. Soc.*, 127 (1980), 1679.
42. E. J. Ritchie, *J. Electrochem. Soc.*, 100 (1953), 53.
43. M. P. J. Brenan, and N. A. Hampson, *J. Electroanal. Chem.*, 48 (1973), 465.
44. M. P. J. Brenan, and N. A. Hampson, *J. Electroanal. Chem.*, 52 (1974), 1.
45. T. F. Sharpe, *Electrochim. Acta*, 1 (1969), 635.
46. G. I. Aidman, *J. Power Sources*, 59 (1996), 25.
47. D. Pavlov, S. Gancheva, and P. Andreev, *J. Power Sources*, 46 (1993), 349.
48. K. Nakamura, M. Shiomi, K. Takahashi, and M. Tsubota, *J. Power Sources*, 59 (1996), 153.
49. M. Calabek, K. Micka, P. Krivak, and P. Baca, *J. Power Sources*, 158 (2006), 864–867.
50. D. Pavlov, *Berichte der Bunsen-geselschaft*, 71 (1967), 398.
51. D. Pavlov, C. N. Poulieff, E. Klaja, and N. Iordanov, *J. Electrochem. Soc.*, 116 (1969), 316.
52. D. Pavlov, and N. Iordanov, *J. Electrochem. Soc.*, 117 (1970), 1103.
53. P. Ruetschi, *J. Electrochem. Soc.*, 120 (1973), 679.
54. W. Visscher, *J. Power Sources*, 1 (1976/77), 257–266.
55. D. Pavlov, and S. Ignatova, *J. Appl. Electrochem.*, 17 (1987), 715.
56. R. Flores, and L. M. Blanco, *J. Power Sources*, 78 (1999), 30–34.
57. M. Saakes, P. J. van Duin, A. C. P. Ligtvoet, and D. Schmal, *J. Power Sources*, 32 (1991), 25.
58. C. Francia, M. Maya, P. Spineli, F. Saez, B. Martinez, and D. Marin, *J. Power Sources*, 85 (2000), 102–109.
59. M. Saakes, and P. A. van Duin, *41st Meeting ISE*, Czechoslovakia (1990).
60. P. Ruetschi, *J. Power Sources*, 127(1) (2004), 33–44.
61. A. Henry, A. Catherino, F. Fred, F. Feres, and F. Trinidad, *J. Power Sources*, 129 (2004), 113–120.
62. Y. Guo, S. Tang, G. Meng, and S. Yang, *J. Power Sources*, 191 (2009), 127–133.
63. M. Calabek, K. Micka, P. Krivak, and P. Baca, *J. Power Sources*, 158 (2006), 864–867.
64. K. Nakamura, M. Shiomi, K. Takahashi, and M. Tsubota, *J. Power Sources*, 59 (1996), 153.
65. Firefly Energy. Available at http://www.fireflyenergy.com/images/stories/pdfs/white%20paper204.25.08.pdf (retrieved December 23, 2013).
66. E. Guenge, J. Jung, and B. Mahato, *J. Power Sources*, 113 (2003), 388–396.
67. Axion Power International. Available at http://www.axionpower.com/PbC_battery (retrieved December 23, 2013).
68. East Penn Manufacturing. Available at http://www.dekabatteries.com (retrieved December 23, 2013).

3 Positive Electrodes of Lead-Acid Batteries

Zhongqi Li

CONTENTS

3.1 BACKGROUND OF THE POSITIVE ELECTRODE

The positive electrode is one of the key and necessary components in a lead-acid battery. The electrochemical reactions (charge and discharge) at the positive electrode are the conversion between PbO_2 and $PbSO_4$ by a two-electron transfer process. To facilitate this conversion and achieve high performance, certain technical requirements have to be met, as described in the later sections of this chapter. In general, battery performance in terms of both energy efficiency and cycle life is strongly dependent on the material composition/morphology, electrode design/structure, and manufacturing procedure. In this chapter, the composition/morphology of Pb/PbO_2-based materials, their corresponding electrode design/structure, and the fabrication

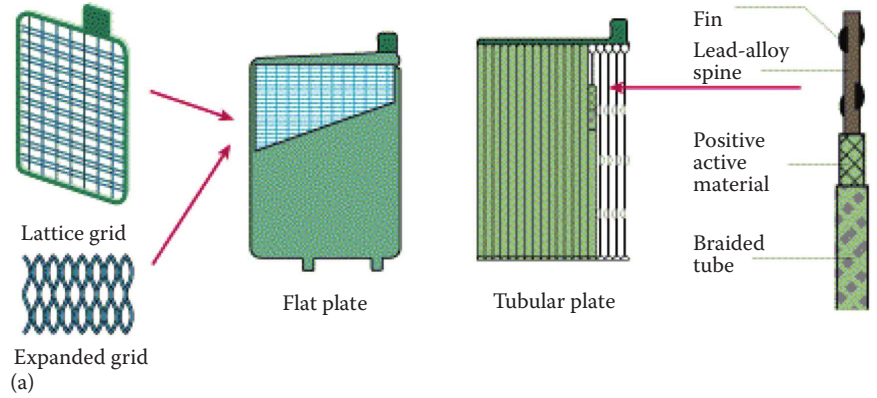

FIGURE 3.1 Lead-acid battery electrode structures: (a) flat and tubular plates; (b) pasted flat electrode, in which the two grids on the left are made of carbon and lead, respectively. After the grid is pasted and cured, the electrode is formed as shown at right. ([a] From http://www.checkthatcar.com/carfaq2.asp. [b] From A. Kirchev et al., *J. Power Sources*, 196(20), 8773–8788, 2011.)

process are described to give the reader an overall picture of the positive electrode in a lead-acid battery.

As shown in Figure 3.1, the structure of the positive electrode of a lead-acid battery can be either a flat or tubular design depending on the application [1,2]. In general, the flat plate design is the more popular one. The plate electrode normally consists of a lead skeleton (net or other forms) called a *grid* and a dry paste that tightly coats the entire surface of the grid.

As mentioned, when fabricating positive electrodes, the first step is to make the grid, which is then pasted by the precursor paste, which contains Pb, PbO, $PbSO_4$, H_2SO_4, and H_2O. After this pasted plate has dried, it is cured by putting it in a chamber containing air and humidity at a controlled temperature. After curing, a formation step electrochemically oxidizes the cured paste (PbO and $PbSO_4$) to PbO_2. Normally, during curing of the precursor paste, the paste forms a microporous skeleton structure, which is tightly bound to the plate grids. However, several technological parameters can affect the paste's structure: (1) acid density, (2) phase composition of the paste, (3) current density, (4) paste density, and (5) temperature. Note that the formation processes for the positive plate can lead to changes in chemical composition of the paste as well as changes in potential on polarization and open circuit voltage.

Curing and formation processes are discussed in more detail in a later section.

3.2 GRID OF THE POSITIVE ELECTRODE

As discussed above, the grid is a necessary component of the positive electrode; it serves as both mechanical support for the positive paste and current collector [3,4]. It is generally recognized that this grid plays a vital role in the performance of lead-acid batteries. To make a high-performing battery with high energy density, good efficiency, and a long cycle life, one of the major approaches battery manufacturers use is to maximize the working area of the active material. This can be achieved if thin plates are produced, allowing assembly of a maximum number of plates in a smaller space in the battery container. However, the manufacture of thin plates requires the use of a thin grid. To achieve a thin grid, the physicochemical properties of the metals used for grid production are crucially important because the grid is both the "backbone" and the "blood circulatory" system of the plate, which, as mentioned, provides mechanical support for the active material and, at the same time, is the main route for current flow. This complex function of the grid means that the design and materials used for grid production must meet several specific characteristics.

3.2.1 Grid Design, Structure, and Fabrication

Various grid designs are used, depending on the specific application for which the grid will be used [3]. The commonly used grids in commercial lead-acid batteries are conventional plate, tubular, expended metal, and fiber types. Regardless of the type of grid, however, it has two necessary and essential portions. One is the framed metal mesh or net, and the other is the electric connect or probe on the frame. The mesh serves as the current collector, which conduct the electric current (charges) to and from every point in the plate and collects it in the grid lug. To obtain a uniform current distribution across the plate overall, the design can be carried out using modeling and calculation.

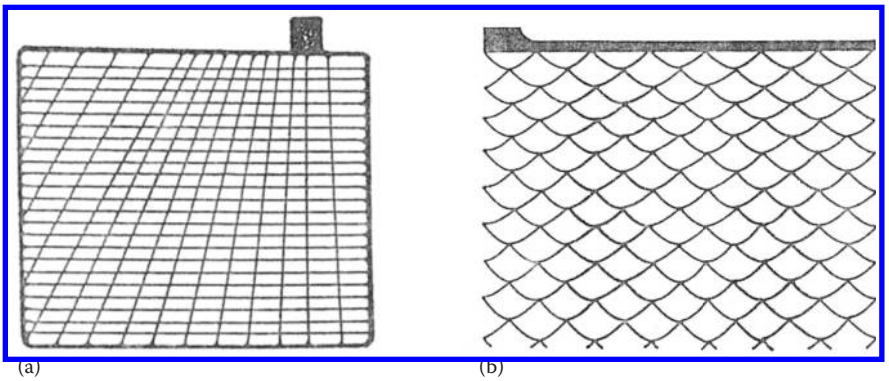

FIGURE 3.2 (a) Classical cast grid for starting, lighting, and ignition (SLI) batteries; (b) expanded grid for SLI batteries. (From G. Pavlov, *Lecture Course on VRLA*, Beijing and Zhangjiajie, China, 2000.)

Figure 3.2a and b show typical grid designs for a classical cast and an expanded one, respectively, for commercially available lead-acid batteries [3]. It can be seen that if the grid is coated with active mass paste such as PbO_2, the volume of PbO_2 will be confined to between the grid bars, thus each grid bar can collect or conduct the electric current from a certain volume of the active mass during the battery charge–discharge process. The Pb or Pb-alloy grid bars have high electric conductivity (10^6 to 10^7 S/m), but the PbO_2, a degenerated semiconductor, has a lower conductivity of 10^3 to 10^4 S/m, which is approximately three orders of magnitude lower than that of Pb. Despite that, the active mass volumes between the grid bars have to be used as the current pathway before the current can reach the metal bars. Therefore, both optimizing the grid design to minimize the electric resistance of the active mass volumes and improving the conductivity of the active mass seem very important in achieving high performance from the positive electrode. It should also be emphasized that tightening the contact between the active mass and the grid, maximizing the utilization of the active mass, and reducing the plate corrosion rate—as well as finding a compromise among these three factors—are also necessary tasks of grid design.

Note that the contact between the active mass PbO_2 and the grid rib surface Pb plays an important role in the power performance of the battery. For example, the total surface of a grid with a rectangular geometry is about 0.005 m^2. If it is coated by 100 g of wetted active mass (PbO_2), the area of the electrochemical reactions during battery operation is about 500 m^2, which is 1 million times larger than the surface area of the grid (current collector). The current generated on such a 500-m^2 surface has to be concentrated to pass through the current collector with an area as small as 0.005 m^2. If the contact between the grid and the active mass paste is not good enough, interface resistance will increase, leading to low battery power output. Therefore, special attention should be given to this issue when designing the grid.

In general, the grid geometry has a strong effect on both the active mass utilization and the plate corrosion rate. For example, the utilization of active mass is found

to increase from 25% to 92% as the distance between the grid bars decreases from 6 mm to 0.1 to 0.2 mm [3,4]. The corrosion rate of the positive grid, a critical factor for the lifetime of the battery, can be enhanced by decreasing the rib cross section. Therefore, grid design efforts also need to include finding a compromise between the active mass utilization and the corrosion rate. Furthermore, in grid design, the grid material's properties have to be considered, including the type of materials such as Pb and Pb alloys, physical properties, chemical/electrochemical corrosion stability, and mechanical strength.

Regarding grid fabrication, four techniques are being used in lead-acid battery production at the current state of technology: (1) gravity casting, (2) continuous casting, (3) the expanded metal sheet method, and (4) the punched sheet method. Of these four techniques, gravity casting is still the most common technique for fabricating grids for lead-acid batteries. For high-quantity, quality production of automobile lead-acid batteries, expanded grids and continuous cast grids are normally used.

3.2.2 Grid Design Parameters

In designing positive plates, a coefficient α, which is the ratio between the inactive lead grid weight (W_{grid}) and the weight of the paste active mass (PAM) PbO_2 (W_{PAM}) is used [3–5]:

$$\alpha = \frac{W_{grid}}{W_{PAM}} \tag{3.1}$$

For automobile lead-acid batteries, this coefficient usually has a value between 0.35 and 0.60. This parameter is normally used for efficiency evaluations.

The second coefficient used for grid/positive plate design, γ, is the ratio between the weight of the PAM PbO_2 (W_{PAM}) and the grid surface area (S_{grid}):

$$\gamma = \frac{W_{PAM}}{S_{grid}} \tag{3.2}$$

It can be seen that γ measures the current load of the grid/PAM interface, which is widely used in plate design practice. Normally, to achieve high battery power, the γ coefficient should be smaller than 1.0 g/cm^2.

In general, the value of the γ coefficient and its uniform distribution over the surface of the grid have great effect on the power performance of a battery. Different grid designs have different γ values, leading to different battery power performances.

The general grid design principles can be summarized as follows:

1. *Optimize the* α *value.* As shown by Equation 3.1, a lower α value results in a higher PAM quantity plate capacity, and also a higher γ coefficient, resulting in lower battery power and lower PAM utilization. Therefore, the value of α should be optimized.
2. *Optimize the* γ *value.* Normally, a higher γ value could give a lower battery power output and lower PAM utilization. So a lower γ value would give a

higher power output and better PAM utilization, but would also lead to faster grid corrosion and thus a shorter cycle life. Therefore, γ should be optimized.

3. *Consider corrosion resistance.* When selecting the appropriate grid design, the corrosion resistance of the grid alloy should be taken into account.

3.2.3 Lead Alloys for Grid Materials

3.2.3.1 Lead-Antimony Alloys

In the literature, numerous lead alloys containing almost all other elements of the periodic table have been tested in an effort to meet the miscellaneous requirements of the lead-acid battery industry [3]. Among those alloys explored, the most widely used ones are antimony-containing lead alloys.

The antimony content has a strong effect on castability. For example, if the content is lower than 8%, there is no significant change in the castability, and the casting process can be controlled by regulating the melt and mold temperature. An alloy with an Sb content below 5% exhibits a tendency to form hot cracks, making the grids more brittle. Normally, solidification results in a coarse grain structure containing cracks along the grain boundaries, leading to poor grid quality. This may be one of the reasons why low-antimony Pb-Sb alloys are not widely used in the lead-acid battery industry.

To avoid the cracking of low-antimony-content Pb-Sb alloys, a fine grain structure should be developed for the casting. In the lead-acid battery industry, attempts to use low-Sb alloys as the grid materials have experienced some technological failures because of grid cracking and accelerated intercrystalline corrosion. Therefore, the use of low-antimony-content Pb-Sb alloys as the grid materials was abandoned by the industry. To overcome the cracking issue, the introduction of nucleants to the alloy melt during casting was explored, and the results showed complete elimination of the grid cracking. These additives can crystallize in the melt at a temperature above that of lead dendrite formation. Thus even though the nucleation of solid-solution lead crystals can occur at a faster rate, these additives can suppress their growth rate, leading to a fine-grained structure for the alloy, preventing dendrite formation and hence cracking. The most suitable nucleants for low-antimony alloys are selenium, sulfur, and copper. Selenium and sulfur can form Pb-Se and Pb-S phases, which then act as nuclei. In general, the effect of Se in reducing grain size is much stronger than that of S. This can be attributed to the higher solubility of Se in the Pb-Sb alloy when compared to that of S. The addition of copper can increase the solubility of S in the melt, improving the nucleation effect. For this reason S is normally used in combination with copper. In addition, Cu can also be used in combination with As, forming Cu_3As and resulting in a nuclei formation effect. Regarding the concentrations of Cu and S, the contents generally used are between 0.05% and 0.06% and 0.006% to 0.007%, respectively. In practice, a wide variety of low-Sb alloys with nucleants are used. The contents of nucleants are as follows: 1.5% to 2.5% Sb, 0.1% to 0.2% As, 0.1% to 0.2% Sn, 0.02% to 0.03% Se, 2% Sb, 0.15% As, 0.2% Sn, 0.05% to 0.06% Cu, and 0.005% to 0.007% S.

In general, the use of Pb-Sb alloys has some drawbacks such as enhancing water decomposition and lowering the tolerance to cold flow (positive plates "grow" during service life, and slow hardening). To overcome these drawbacks, the additives explored in the literature are normally arsenic, tin, and silver [2]. Regarding arsenic

addition, if the amount added is more than 0.2%, the size of the α-Pb dendrites will be decreased, leading to exceptionally fast hardening of Pb-Sb-As alloys. At such concentrations above 0.1%, arsenic could reduce the rate of chemical oxidation of the melt, and effectively inhibit the intercrystalline corrosion. Furthermore, an addition of 0.1% to 0.2% As to Pb-Sb alloys could also reduce the flowability of the alloy during casting. This effect is enhanced when the antimony content in the alloy is decreased.

Regarding the addition of tin to the alloy, the oxidation of immobilized Pb-Sb melts could be reduced due to the formation of a protective SnO_2 film on the melt surface, resulting in fewer metal losses caused by slag formation. It has been observed that during the casting of alloys, the major part of the tin that accumulates in the slag is in the form of SnO_2, and only a small portion remains in the grid metal. The formation of SnO_2 film could increase the surface tension and thus improve the flowability of the melt. Such high-flowability melts can fill the grid molds at low temperature, leading to a high casting rate. Furthermore, both the mechanical properties and corrosion resistance of the alloys can be affected only when the Sn concentration is higher than 0.4%. These effects of Sn can be observed both in Pb-Sb-Sn and Pb-Sb-As-Sn alloys. In general, the amount of Sn added to the latter alloys is in the concentration range between 0.1% and 0.5% and is dependent on economic and technological considerations.

3.2.3.2 Lead-Calcium Alloys

Normally, adding a small amount of Ca and Sn such as 0.1% Ca–0.5% Sn into Pb could give adequate mechanical properties for lead-acid battery electrodes [2]. The maximum solubility of calcium in lead is about 0.1% at the peritectic temperature 328°C and 0.01% at room temperature. Normally, the content of Ca in the alloy should be controlled at below 0.07% for positive grids. Experiments showed that a 0.07% Ca content was the optimum Ca concentration [3]. It has also been demonstrated that maintaining a constant Ca content in the melt is very important in reducing the impact of Ca oxidation. In practice, if 0.01% to 0.03% Al is added to the melt, the content of Ca could be preserved unchanged. Even the addition of 0.006% of Al seems sufficient to protect Ca from oxidation. The addition of Al to Pb-Ca alloys results in a constant level of Ca being maintained at 0.07%. The addition of Al can affect the structure of the alloy and facilitate the processing of Pb-Ca alloys with lower Sn content. This is very important for batteries subjected to deep discharges. The addition of Sn to the Pb-Ca alloys has shown some beneficial effect. Battery operation has demonstrated that Sn is an appropriate additive for improving the mechanical characteristics of Pb-Ca alloys.

3.3 TYPES OF POSITIVE ELECTRODES

The four main types of positive electrodes in lead-acid batteries are as follows:

1. *Pasted type*. This type is made by pasting the cream in the positive plate, drying, and then formatting.
2. *Tubular type*. This type is made by putting the fiber pipe knitted on the positive plate, and then adding the active materials in the pipe. This method can protect the positive active materials from shedding.

3. *Formation type.* This type is made using pure lead. The active materials come from the lead itself.
4. *Half formation type.* This type is between the pasted type and formation type, in which the positive plate is a grid with small squares made by pure lead. Pure lead grid will act as a role of formation type plate when the active material is shedding.

3.4 POSITIVE ELECTRODE PASTES

3.4.1 Compositions of the Positive Pastes and Their Effect on Performance

The positive paste is prepared at controlled temperatures by mixing the H_2SO_4 aqueous solution and the oxidized lead powder (LO) [6,7]. The prepared mixture is a nonequilibrium composite consisting of crystalline basic lead sulfates and oxides, and amorphous sulfate-containing components. The composition is strongly dependent on the H_2SO_4:LO ratio, temperature, additives, and length of mixing time. Several important crystalline compositions in the paste should be mentioned here: $PbO \cdot PbSO_4$ (1BS, where "1" means 1 PbO molecule and "BS" means 1 basic lead sulfate molecule), $3PbO \cdot PbSO_4 \cdot H_2O$ (3BS, where "3" means 3 PbO molecules and "BS" means 1 basic lead sulfate molecule), and $4PbO \cdot PbSO_4$ (4BS, where "4" means 4PbO molecules and "BS" means 1 basic lead sulfate molecule). In general, pastes containing different types and contents of these crystal components give different performances. It has been recognized that the phase composition of pastes plays an important role in the performance of the positive battery plates. Therefore, the life span and the capacity of the battery are strongly dependent on the process of paste preparation.

For example, pastes prepared at temperatures lower than 60°C, with up to 10% H_2SO_4 content, contain mainly 3BS crystals, and those with 8% to 12% H_2SO_4 also contain 1BS. Those prepared at temperatures higher than 70°C with 4% to 6% H_2SO_4 are composed mainly of 4BS. The paste prepared using 8% H_2SO_4 at such temperatures contains 3BS, 4BS, and 1B, whereas that with 12% H_2SO_4 contains 3BS and 1BS. The active mass obtained from pastes containing no H_2SO_4 has a very low capacity irrespective of temperature. The active mass obtained from pastes containing 3BS and 1BS (12% H_2SO_4) have a very high initial capacity, but a rather short cycle life. The active masses obtained from 4BS pastes can give the longest cycle life although their initial capacity is lower than the rated value. Although the pastes containing 3BS crystals have an initial capacity equal to or close to the rated one, their life span is normally shorter than that of plates prepared with 4BS pastes. Note that the sizes of the 3BS crystals are normally in the range between 1 and 3 μm, whereas those of the 4BS crystals are about 40 μm, suggesting that crystal size has a strong effect on the performance of the positive paste. Normally, positive plates made with 4BS pastes are favored because they can exhibit high stability of the active mass structure, thus ensuring long cycle life of the plates during battery operation. Note that because 4BS crystals are large in size, their oxidation to PbO_2 at formation is slower, resulting in a low initial capacity.

3.4.2 Preparation of the Positive Pastes

In practice, semisuspension technology is normally employed for preparation of 4BS pastes using an Eirich Evactherm® paste mixer. During the process, at a temperature higher than 90°C, 4BS crystals with dimensions between 20 and 30 μm are formed first from a semisuspension. Then the excess water is removed from the semisuspension under vacuum until the desired paste density is obtained. During this vacuum treatment, small 4BS and PbO crystals are formed with decreasing temperature. These 4BS and PbO crystals can be converted into PbO_2 particles in which the large 4BS crystals can build up the PbO_2 skeleton of positive active mass, and the small crystals can form the energetic PbO_2 structure, which participates in the charge–discharge processes of battery cycling.

As discussed earlier, although the positive plates fabricated with 4BS pastes can exhibit a long cycle life during battery operation, the large size of the 4BS crystals can cause a low initial capacity. To improve that, a technology to prepare 4BS pastes in the presence of Pb_3O_4 has been developed [8–10]. In this technology, three types of pastes can be prepared depending on the method of Pb_3O_4 introduction: (1) A mixture of 4BS and Pb_3O_4 is used as initial material for paste preparation, (2) 4BS is obtained in the presence of Pb_3O_4, and (3) Pb_3O_4 is pre-decomposed with H_2SO_4 to $PbO_2 + PbSO_4$ and then used for paste preparation. It has been demonstrated that the initial capacity could be above 100% versus the rated capacity. In addition, the battery life was also considerably longer than that of batteries produced with the classical pastes generally used in the batteries [8–10].

3.4.3 Structure of the Positive Pastes after Formation

After plate formation, the structure of the PAM can be studied using the scanning electron micrograph (SEM) technique. Normally, PbO_2 particles in the paste have three forms: spherical, egg shaped, and crystal needle-like particles. Figure 3.3 shows the schemes for positive paste structures.

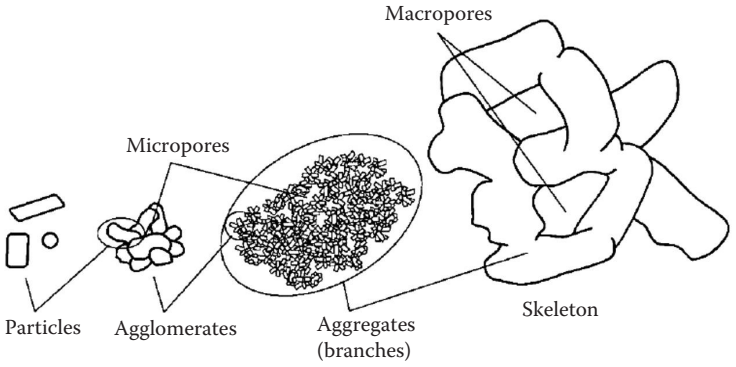

FIGURE 3.3 Structure of the lead dioxide active mass. (From D. Pavlov, and E. Bashtavelova, *J. Electrochem. Soc.*, 131, 1468, 1984; D. Pavlov, and E. Bashtavelova, *J. Electrochem. Soc.*, 133, 241, 1986; D. Pavlov et al., "Structure of the Lead-Acid Battery Active Masses," in *Proc. Int. Symp. Advances in Lead-Acid Batteries*, Vol. 84-14, p. 16, Electrochemical Society, Pennington, NJ, 1984.)

Actually, the paste layer is a microporous matrix structure. From Figure 3.3, we can see that the smallest building element of the PAM structure is the PbO_2 particle, which can interconnect with agglomerates. Many agglomerate branches pack together to form the microporous skeleton. The latter contains micropores between the particles. A huge number of agglomerates interconnect with an aggregate (branch). The aggregates (branches) interconnect to form a skeleton. When this PAM comes into contact with the aqueous electrolyte, a dehydration process happens by means of the following reaction to convert the particle's crystal zone into a hydrated zone [11–13]:

$$2(\alpha\text{-}PbO_2)\ (\text{or } 2(\beta\text{-}PbO_2)) + 2H_2O \leftrightarrow PbO(OH)_2 + H_2PbO_3 \tag{3.3}$$

Reaction 3.3 is an equilibrium between lead hydroxide and lead dioxide in the presence of water. Then this water can transform the PbO_2 particle into an open system. This open PbO_2 particle allows for the transfer of ions between the solution outside the particles and the hydrated zones of the particle. Actually, the hydrated zones occupy about 30% of the PAM. Besides the equilibrium between the hydrated and crystal zones, hydrated zones are also in equilibrium with ions in the solution. In this way, the hydrated linear polymer chains containing Pb, O, and OH can be formed, which plays a critical role in both electron and proton conductions. Both high electron and proton conductivities of these polymer-like chains are necessary conditions for the reaction of discharge of PbO_2 to proceed.

In general, the hydration (or gel) crystal structure can influence plate capacity. If the PAM is built only from PbO_2 crystals, its electron conductivity is high, but its proton conductivity will be low, leading to low capacity. By contrast, if the PAM is composed only of gel, it will exhibit a high proton conductivity, but a low electron conductivity, also leading to low capacity. If the PAM is a gel/crystal mixed system, both its electron and proton conductivities will be high, resulting in high plate capacity.

In summary, the agglomerates within the PAM matrix can form a structure with both gel and crystal zones when they contact with aqueous electrolyte. The gel zone is composed of Pb-O-OH polymer chains, which can serve as the paths for proton transfer, and the crystal zone can serve as the electron transfer paths. In this way, the PAM can have both high electron and proton conductions for the charge and discharge processes.

3.5 CURING OF PASTED POSITIVE PLATES

As discussed earlier, during the process of paste preparation, particles (crystals) of 3BS or 4BS are formed in the paste layer. However, the particles of the paste are spread over the grid and are tightly bound neither to each other nor to the grid. These particles are surrounded by liquid films and hydrated shells, exhibiting a separated microstructure. The curing procedure will make these particles interconnected to form a continuous, strong skeleton that is tightly bound to the grid.

During the curing process, two major processes take place in the paste:

1. *The PbO_2 skeleton is built up.* During this is process, the small crystals in the paste dissolve and the big ones grow in size. At the same time, the 3BS or 4BS crystals are interconnected into a strong skeleton with the evaporation

of water contained in the thin liquid films between the particles. Note that if this skeleton is built from 3BS crystals, its branches (dendrites) are normally thin because its crystal size is small. If the skeleton is built from 4BS crystals, some thick branches (dendrites) can be formed with stronger mechanical strength but having small surface area.

2. *The grid lead and the free lead in the paste are oxidized.* The lead in the grid alloy is oxidized, forming a corrosion layer on the grid rib surface, which is tightly bound to the paste skeleton. The free lead in the paste is also oxidized.

3.5.1 Oxidations of Paste Free Lead and Grid Lead Alloy

The paste free lead is normally first oxidized by O_2, then the oxidation of the grid lead alloy follows. These two processes should be the same except they proceed at different rates because alloy additives affect the rate of grid corrosion. For these two oxidation reactions, moisture water serves as the catalyst, and the heat produced can help with water removal from the paste.

3.5.2 Corrosion Process on the Grid Surface during Curing

The curing process is normally conducted at high temperature and humidity for a period of 24 h, during which the corrosion layer occurs between the grid surface and its contacted PAM interface, as shown in Figure 3.4 [14]. The corrosion process can be expressed as Reaction 3.4:

$$Pb + 1/2O_2 \rightarrow PbO \tag{3.4}$$

where O_2 is from the humidified air. This formed corrosion layer can provide a strong connection between the PAM and the grid. However, the curing conditions have a strong effect on the tightness and contact.

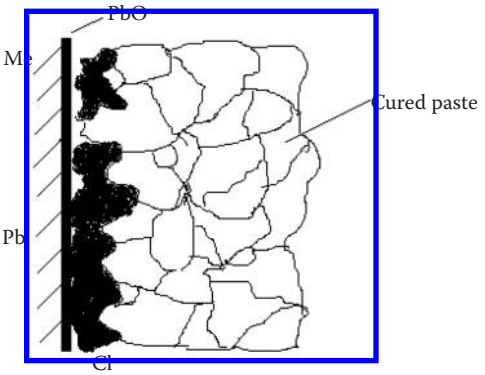

FIGURE 3.4 Scheme of the grid/PAM interface where a corrosion layer is formed during the curing process. (From M. Dimitrov, and D. Pavlov, *J. Power Sources*, 93, 234, 2001.)

If the curing is carried out at high temperatures, a much thicker corrosion layer can be formed, which could provide a good contact between the grid and the PAM. Therefore, high temperature has a beneficial effect on plate curing. Regarding the effect of humidity on the curing process, an optimized humidity content is needed.

3.5.3 Generation of 3BS and 4BS Skeletons in the Cured Paste and Their Pore Volume Distribution

Two types of skeletons in the paste can be formed during the plate curing process; one is the 3BS crystal-based skeleton, and the other is the 4BS crystal-based one. The 3BS skeleton can be formed when paste preparation is performed at temperatures between 30°C and 60°C and the plate curing is conducted within the same temperature range. The 4BS skeleton can be formed when the paste is prepared at a temperature range between 70°C and 95°C. Regarding the pore volume distribution, pastes containing 4BS have larger average pore radii than those with 3BS, because 4BS crystals are much bigger than 3BS ones.

3.5.4 Processes during Drying of the Paste

Basically two processes are used in the drying of the cured plate that determine the adhesive and cohesive strengths during curing: (1) During the first stage of drying, the capillary water can be evaporated from the paste and then from the thin liquid layers between the particles, leading to a porous mass; and (2) during the second stage of drying, the wedge water can be evaporated from the paste, resulting in "welding" of the particles and agglomerates (i.e., the skeleton of the porous mass becomes harder and stronger).

3.6 FORMATION OF THE CURED POSITIVE PLATES

The final step of positive plate fabrication is the formation process. This process converts all of the positive paste into β-PbO_2 active mass. Normally, the formation of positive plates can be divided into two stages [15]:

1. *First stage*: The cured paste containing PbO and basic lead sulfates is partially oxidized to α-PbO_2 with a small amount of β-PbO_2, and the remaining part reacts with H_2SO_4 to form $PbSO_4$ (~30%).
2. *Second stage*: After about a 6-h formation process, all $PbSO_4$ has been oxidized to β-PbO_2.

Figure 3.9 shows a scheme for the stoichiometric reactions during the first stage. In Figure 3.9, the overall formula $\frac{m}{m+1}\mathrm{PbO}\,\frac{1}{m+1}\mathrm{PbSO_4}$ is valid for the PbO and basic lead sulfates, where the coefficient m represents their individual compositions. It can be seen that when $m = \infty$, the respective values for the stoichiometric coefficient of PbO and $PbSO_4$ in the overall formula are 1 and 0, respectively; that is, only PbO is present in the paste; if $m = 3$, the paste contains $\frac{3}{4}\mathrm{PbO}\,\frac{1}{4}\mathrm{PbSO_4}\,(\rightarrow 3\mathrm{PbO}\cdot\mathrm{PbSO_4})$,

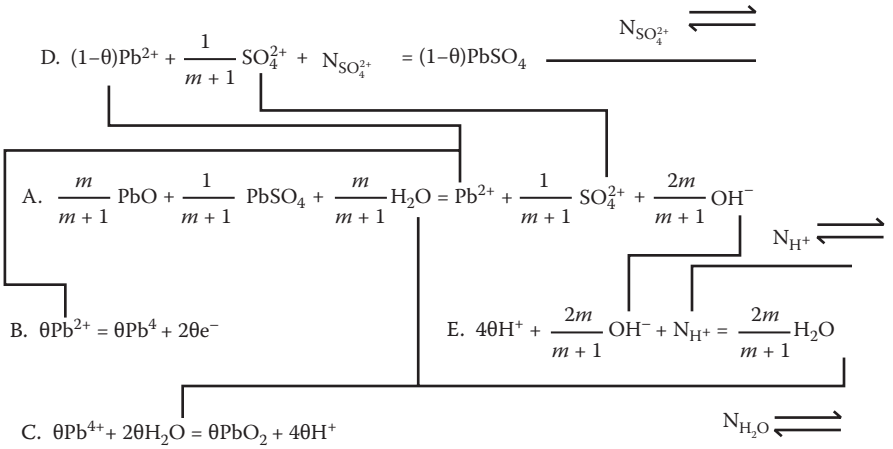

FIGURE 3.5 Electrochemical and chemical reactions proceeding during the first stage of formation of the cured positive paste. (From M. Dimitrov, and D. Pavlov, *J. Power Sources*, 93, 234, 2001.)

which is 3BS; if $m = 4$, the paste contains $\frac{4}{5}PbO\frac{1}{5}PbSO_4 (\rightarrow 4PbO \cdot PbSO_4)$, which is 4BS; if $m = 1$, the phase will contain $\frac{1}{2}PbO\frac{1}{2}PbSO_4 (\rightarrow PbO \cdot PbSO_4)$, which is 1BS; and if $m = 0$, $PbSO_4$ is the only material. Furthermore, θ in Figure 3.9 represents the amount of Pb^{2+} ions that participate in the electrochemical Reaction B, leading to the formation of PbO_2 according to Reaction C. Note that $(1 - \theta)$ is the remainder of the Pb^{2+} ions reacting to form $PbSO_4$ (Reaction D).

A reaction scheme for the second stage of positive electrode paste formation during which $PbSO_4$ is oxidized to PbO_2 is shown in Figure 3.10. It can be seen that the oxidation of $PbSO_4$ proceeds entirely in a strong acidic medium and thus β-PbO_2 is formed.

The reaction schemes shown in both Figures 3.5 and 3.6 indicate that the overall rate of the formation process not only depends on the rates of the involved elementary chemical and electrochemical reaction rates, but also on the rate of the diffusion ion flows and on the electron conductivity of the solid phases. All of these rates determine the direction in which the electrochemical processes will advance along the plate cross section.

In practice, to enhance the formation of positive plates, some conductive agents are needed as additives to the positive pastes. These additives can increase the conductivity of the cured paste and also benefit the uniform current distribution throughout the entire PbO_2 layer. Note that these additive compounds should be chemically stable in strong H_2SO_4 solution. The additive materials are normally (1) carbon, (2) conductive polymers (polyaniline, polypyrrole; polyparaphenylene and polyacetylene in the form of powers or fibers), (3) doped SnO_2, and (4) lead or red lead.

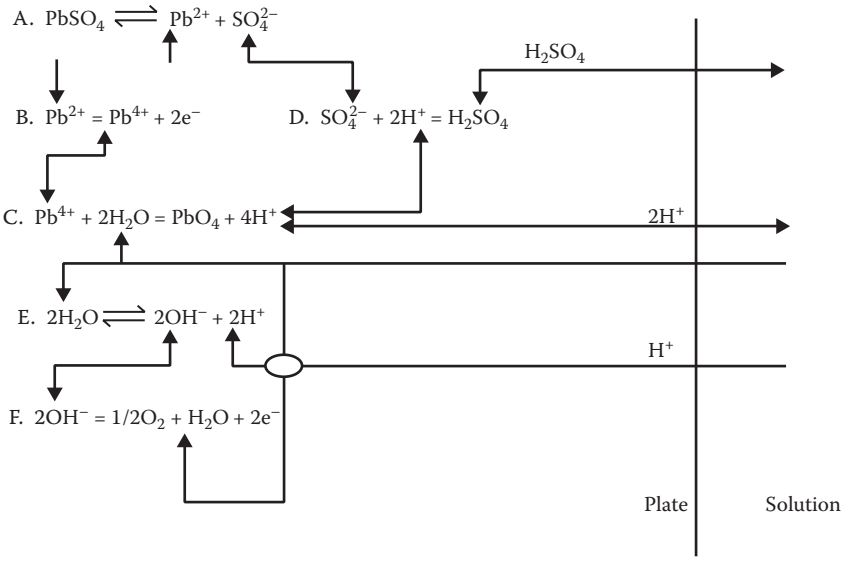

FIGURE 3.6 Electrochemical and chemical reactions proceeding during the second stage of the formation of positive paste. (From M. Dimitrov, and D. Pavlov, *J. Power Sources*, 93, 234, 2001.)

3.7 POSITIVE ACTIVE MATERIALS AND THEIR REACTION MECHANISMS

3.7.1 Mechanism of Charge–Discharge in Positive Electrodes

3.7.1.1 Liquid and Solid Phase Reaction Mechanisms

Currently, two mechanisms are used for positive electrode reactions: a liquid phase mechanism and a solid phase mechanism.

A liquid phase mechanism is one in which the reaction has an intermediate step, a redox reaction through lead ion in sulfuric acid. The process is shown in Figure 3.7.

Figure 3.7 shows that the Pb^{4+} of the lead dioxide crystal can accept an electron from the external circuit and be reduced to Pb^{2+} during discharge. Then it will react with the solution HSO_4^- ion to form $PbSO_4$ on the electrode. At the same time, O^{2-} will react with H^+ in the solution to form water. More and more $PbSO_4$ is produced on the electrode as the discharge process proceeds. Generally, $PbSO_4$ will not cover PbO_2, but sometimes this situation can happen, resulting in decreased performance of the positive electrode. This situation is called *cathodic passivation*.

The situation is opposite to discharge when a positive electrode is charged. The Pb^{2+} will be oxidized to Pb^{4+} by accepting electrons from the external circuit. Simultaneously, H^+ is left in the solution from the water molecule. The O^{2-} and Pb^{4+} will react in the PbO_2 lattice. So $PbSO_4$ will dissolve gradually with the assumption of Pb^{2+}. Regarding the state of Pb^{4+}, there are many hypotheses, including $PbO(OH)^+$, $Pb(OH)_2$ $(SO_4)_2$, and so on. In addition, the solution-diffusion and crystallization

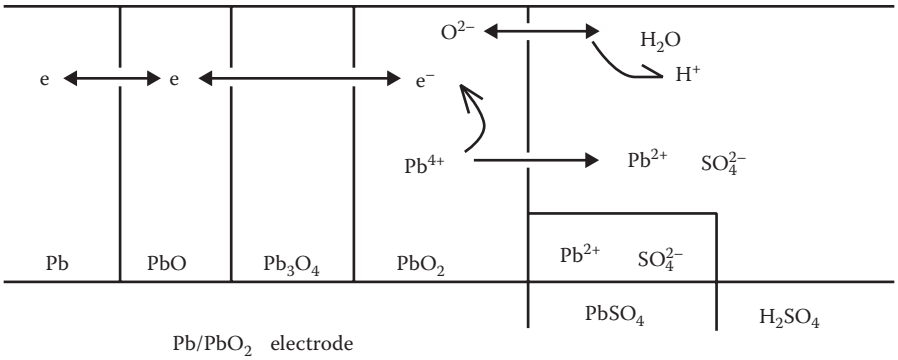

FIGURE 3.7 Reaction scheme for $PbO/PbSO_4$. (From G. Pavlov, *Lecture Course on VRLA*, Beijing and Zhangjiajie, China, 2000.)

process of $PbSO_4$ is very important in the redox reaction according to the liquid phase mechanism.

The solid phase reaction mechanism is the lead dioxide reduction, which forms a series of intermediate oxide materials without ion coming from the solution. As a result, the degree of oxide will be decreased gradually during discharge.

The reaction mechanisms during the charge and discharge processes can be expressed as follows:

$$Pb \underset{\text{deposit}}{\overset{\text{dissolve}}{\rightleftharpoons}} Pb^{2+} + 2e^- \tag{3.5}$$

$$H_2O \underset{\text{deposit}}{\overset{\text{dissolve}}{\rightleftharpoons}} O^{2-} + 2H^+ + 2e^- \tag{3.6}$$

The total reaction is

$$2H_2O + Pb^{2+} \underset{\text{discharge}}{\overset{\text{charge}}{\rightleftharpoons}} PbO_2 + 4H^+ + 2e^- \tag{3.7}$$

If there is H_2SO_4, the reaction is

$$PbO_2 + 3H^+ + HSO_4^- + 2e^- \underset{\text{charge}}{\overset{\text{discharge}}{\rightleftharpoons}} PbSO_4 + 2H_2O \tag{3.8}$$

3.7.1.2 Nonstoichiometric Lead Dioxides

It is generally believed that lead dioxide has semiconductor properties. Actually, the atomic ratio between lead and oxygen is not 1:2 like that in the PbO_2 formula. In this case, a formula of PbO_n can be used to indicate this molecule is not stoichiometric; instead, it is "nonstoichiometric." Furthermore, there are amorphous PbO_n variants except α-PbO_2 and β-PbO_2. Differential thermal analysis (DTA), x-ray, and nuclear

magnetic resonance (NMR) measurements showed that the protons exist inside the newly formed lead dioxide in the form of either H_2O or OH^- to give the lead oxides such as α-PbO_2(OH), α-PbO_2(OH) · H_2O, β-PbO_2(OH), and amorphous PbO_2(OH) [4].

Actually, in either of these three types of lead dioxide materials, active and inactive portions exist. For example, there is an inactive lead dioxide portion in the electrode after the formation process. Even an active portion could also become inactive with increasing charge–discharge cycles, which is one of the most important reasons for capacity loss and battery failure.

3.7.1.3 Side Reaction in the Oxidation of Lead Sulfate

A side reaction of oxygen evolution at the positive electrode occurs before lead sulfate can be completely oxidized. This can reduce the charge efficiency of a lead-acid battery. In this case, 100% of the charge current cannot be used for charging. In general, this side reaction reduces the charging efficiency to 70% to 80%.

The side reaction of oxygen evolution can be expressed as

$$2H_2O + 4e^- = O_2 + 4H^+ \tag{3.9}$$

The rate determining step in Reaction 3.9 can be expressed as

$$H_2O \rightarrow H_2O_{adsorption} + H^+ + e^- \tag{3.10}$$

As observed, the overpotentials of oxygen evolution at α-PbO_2 and β-PbO_2 electrode particles are different [4]. For β-PbO_2, the overpotential is a little bit higher because the oxygen proportion is high.

3.7.1.4 Self-Discharge of Lead Dioxide Electrode

Self-discharging at the positive electrode can be driven by the electrode potential difference. For example, the equilibrium potential of an $PbO_2/PbSO_4$ electrode is 0.6 V more positive than that of an oxygen H_2O/O_2 electrode. This potential difference can make the following reaction happen, consuming PbO_2:

$$PbO_2 + H_2SO_4 \rightarrow PbSO_4 + \frac{1}{2}O_2 + H_2O \tag{3.11}$$

At the negative electrode of a lead-acid electrode, the electrode potential of Pb/$PbSO_4$ is 0.35 V more negative than that of the H_2/H^+ couple, which can drive the self-discharge reaction to produce H_2, then consuming Pb:

$$Pb + H_2SO_4 \rightarrow PbSO_4 + H_2 \tag{3.12}$$

Therefore, both Reactions 3.11 and 3.12 could happen simultaneously, consuming both Pb and PbO_2 and causing the battery to self-discharge. However, even though both of these reactions are thermodynamically possible, they must necessarily happen at high reaction rates, which are mainly controlled by the reaction overpotentials.

In practice, although the overpotentials for both of these reactions are high, the self-discharge rates could be kept at insignificant levels. As observed in practical lead-acid batteries, the currents of the self-discharge reactions are very low due to the high overpotentials of the H_2 and O_2 evolution reactions.

Actually, the rates of self-discharge reactions depend on temperature, additives to the active mass, electrolyte formulation, and grid alloy composition. If the surface of the electrodes is covered by $PbSO_4$ (the product of the self-discharge reactions), the state of charge of the electrodes will also affect the rates of the self-discharge processes. As a result of these self-discharge processes, the open circuit voltage of the lead-acid cell is practically equal to the difference between the rest potentials of the two electrodes. However, due to the insignificant self-discharge currents, the difference between the thermodynamic equilibrium potentials of $PbSO_4$/Pb and PbO_2/$PbSO_4$ electrodes and the rest potentials is very small, so that the cell voltage of a lead-acid battery is normally equal to its theoretical equilibrium cell voltage.

3.7.2 Crystal Variants of Lead Dioxide

3.7.2.1 Crystal Structures of Lead Dioxides and Their Related Performance

As discussed earlier, lead dioxide positive electrode materials are polycrystalline compounds with four variants: α-PbO_2, β-PbO_2, amorphous PbO_2, and unstable false tetragonal. They can be formed in different circumstances and their physical and chemical properties are also different. For example, as measured by x-ray diffraction (XRD), in a positive electrode containing 90% lead dioxide, after the formation process, 23% β-PbO_2, 43% α-PbO_2, and 34% amorphous PbO_2 are found [4].

Regarding the geometric structure of the lead dioxide, the crystalline grain of α-PbO_2 is thicker (about 1 μm) and its face is smoothly rounded. The crystalline grain of β-PbO_2 is tiny and acicular or dendritic. An example of the crystal structure of lead dioxide is shown in Figure 3.8.

Regarding the electronic resistivity, lead dioxides are normally the *n*-semiconductors with a positive temperature coefficient of about 10^{-3}/K, as shown in Figure 3.9.

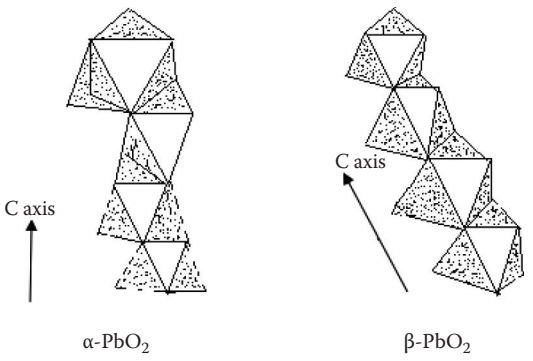

FIGURE 3.8 Accumulated parameters of α-PbO_2 and β-PbO_2. (From R. Nelson, *Lecture Course on VRLA*, Beijing, China, 2003.)

It can be seen that the resistivity and carrier densities of different crystal structures are different.

Regarding the electrode potentials of α-PbO_2/$PbSO_4$-H_2SO_4 and β-PbO_2/$PbSO_4$-H_2SO_4, their relationships with electrolyte pH are also different. Normally in the low pH range, β-PbO_2/$PbSO_4$-H_2SO_4 has a higher potential than does α-PbO_2/$PbSO_4$-H_2SO_4 [4].

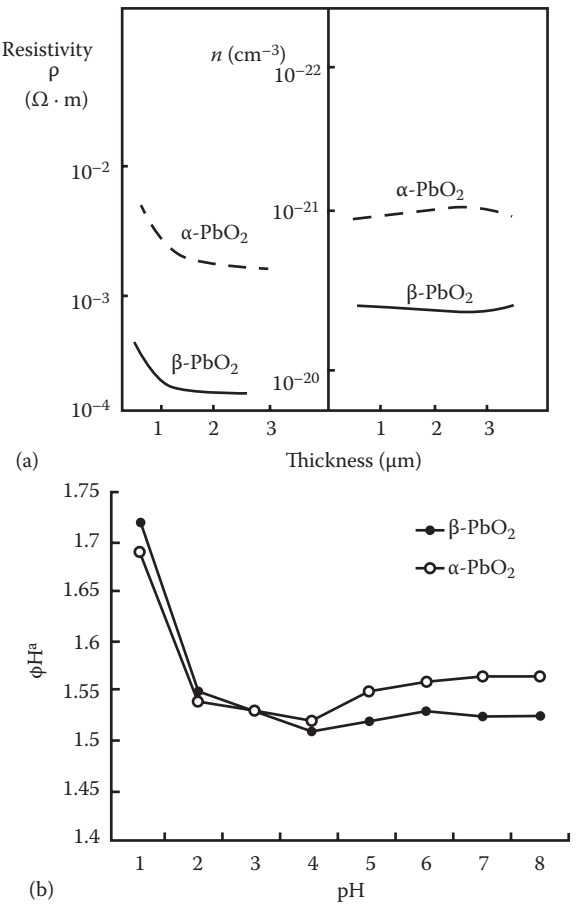

FIGURE 3.9 (a) Relation between resistance and thickness and (b) relation between electrode potential and pH. (From R. Nelson, *Lecture Course on VRLA*, Beijing, China, 2003.)

3.7.2.2 Requirements for Lead Dioxide Variant Formation and Transformation

In electrolysis production of lead dioxides for lead-acid battery positive electrodes, α-PbO_2 can be prepared in an alkaline and neutral solution. For example, in an electrolyte containing 2 mol/dm^3 NaOH with saturated Pb^{2+} salt, using 0.8 to 1.6 mA/cm^2 current densities could give α-PbO_2 [4]. However, α-PbO_2 could also be produced in an acid solution if the electrolysis current density and concentration of the lead ion can be carefully controlled [4]. Normally, β-PbO_2 is prepared in an acid solution. For example, electrolyzing with 5 to 10 mA/cm^2 current density in a mixed solution of 0.7 mol/dm^3 $Pb(NO_3)_2$ and 2 mol/dm^3 HNO_3 could produce β-PbO_2 [4]. Therefore, in producing lead dioxides for the positive electrode of a lead-acid battery, the pH of the electrolyte solution has a strong effect on the types of variants.

Under certain conditions, such as gridding and pressing at a controlled temperature range, β-PbO_2 can be transformed into α-PbO_2. In addition, a high pH, low current density, and higher lead ion are the necessary conditions for the formation of α-PbO_2. Furthermore, the pH change can also change the ratio of the internal active material α-PbO_2 and external material β-PbO_2.

In fabricating a lead-acid battery positive electrode, using more sulfuric acid in the positive paste can improve the battery capacity. This is because more sulfuric acid can increase the quantity of lead sulfate in the positive paste, leading to more production of β-PbO_2 due to the oxidation of lead sulfate in the formation process. The additional benefit is that the plate porosity can be increased with increasing lead sulfate in the paste. The increased lead sulfate can go into the internal active materials, improving the use ratio of lead dioxide.

The density of the positive paste cream can also affect the formed ratio of α-PbO_2 and β-PbO_2. A dense paste favors the formation of α-PbO_2 in the internal plate. When the temperature rises, the density of the paste will be decreased, and the spread of lead sulfate will be accelerated, resulting in more formation of β-PbO_2.

3.7.2.3 Lead Dioxide Variant and Its Discharge Performance

Differences in the electrochemical activity of lead dioxides can be characterized by their discharge performances. Normally, β-PbO_2 has a 1.5 to 3 times higher capacity than does α-PbO_2, as shown in Figure 3.10.

The reasons why the discharge capacity of β-PbO_2 is higher than that of α-PbO_2 can be explained as follows: (1) The β-PbO_2 crystal particle is about half of the α-PbO_2 crystal particle; thus, β-PbO_2 has a bigger surface area than α-PbO_2, as shown in Table 3.1; and (2) the lattice parameters of α-PbO_2 are similar to lead sulfate, so it can act as crystal seeds of lead sulfate during discharge, producing new lead sulfate, which then covers the surface of α-PbO_2, making the spread of acid sulfate difficult, such that the electrochemical reaction of active materials only happens on the surface. However, this situation does not happen in β-PbO_2 because

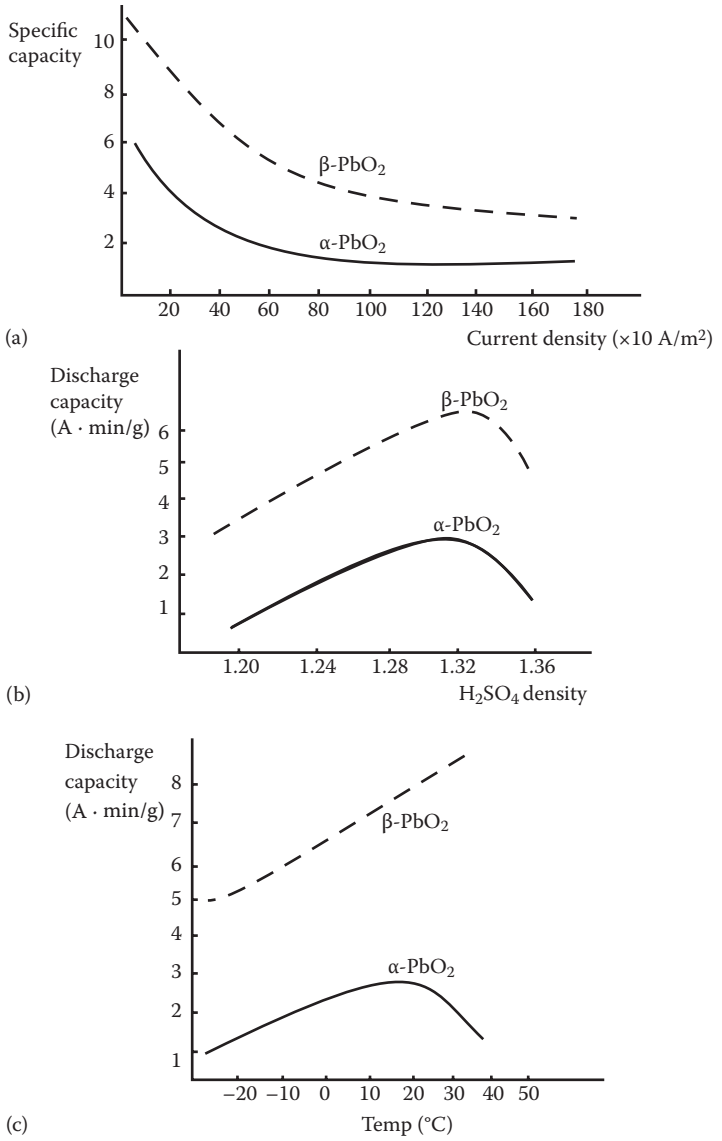

FIGURE 3.10 Specific discharge capacities of α-PbO_2 and β-PbO_2 as functions of (a) discharge current density, (b) acid sulfate concentration, and (c) temperature. (From R. Nelson, *Lecture Course on VRLA*, Beijing, China, 2003.)

its lattice parameters are significantly different from those of lead sulfate. The newly generated lead sulfate will only grow on the old lead sulfate, creating more pores that are in favor of penetrating the acid sulfate, resulting in a higher capacity. Therefore, a higher ratio of β-PbO_2:α-PbO_2 is normally desired for the positive electrode material.

TABLE 3.1
Virtual Surface Areas of α-PbO_2 and β-PbO_2

	Surface Area in BET Method		
Crystal Form	**1**	**2**	**Average Area**
α-PbO_2	0.50	0.47	0.48 ± 0.05
β-PbO_2	9.51	9.56	9.53 ± 0.15

Source: R. Nelson, *Lecture Course on VRLA*, Beijing, China, 2003.

3.8 DETERIORATION OF THE PERFORMANCE OF LEAD DIOXIDE ACTIVE MASS

Deterioration of lead dioxide is one of the most important causes of damage in a lead-acid battery. As generally observed, new lead dioxide has both high mechanical strength and activity, but it deteriorates with an increasing number of discharge–charge cycles, resulting in reduced battery capacity. The causes of lead dioxide deterioration can be summarized as follows:

1. *Change of active mass's polymorphs.* Normally, α-PbO_2 transforms into β-PbO_2 at the beginning of a cycle, so the capacity will be increased by increasing the quantity of β-PbO_2. However, β-PbO_2 can be taken off easily due to the poor bonding force between β-PbO_2 particles, leading to decreased capacity after lots of cycles have occurred.
2. *Reduced bonding force between particles.* In general, there are good bonding forces between lead dioxide particles or between particles and plates when the electrode is newly prepared. However, with increasing charge–discharge cycling, volume contraction and expansion will happen in both the grid and lead dioxide; thus, the bonding force will become poor and the resistance will increase, as shown in Figure 3.11a, and the porosity will become smaller, as shown in Figure 3.11b, resulting in a reduced capacity and oxygen evolution effect. Oxygen evolution in the positive electrode can compact active materials and reduce the bonding force between the active materials and the grid, as shown in Figure 3.11c resulting in low capacity.
3. *Recrystallization of lead dioxide during the cycles.* In one charge–discharge cycle, lead sulfate is dissolved and lead dioxide is recrystallized in the old lead dioxide, but rearranged and destroyed in the original uniform distribution. With increasing numbers of cycles, it becomes more and more difficult for acid sulfate to penetrate into the internal plate, the internal active materials cannot be used anymore, and the surface active materials can also be softened and festered, resulting in reduced capacity.
4. *Effect of charge/discharge conditions and impurities.* In general, charge–discharge current densities can affect the structure of the lead dioxide layer, leading to a different cycle life. At low charge current densities, the dense

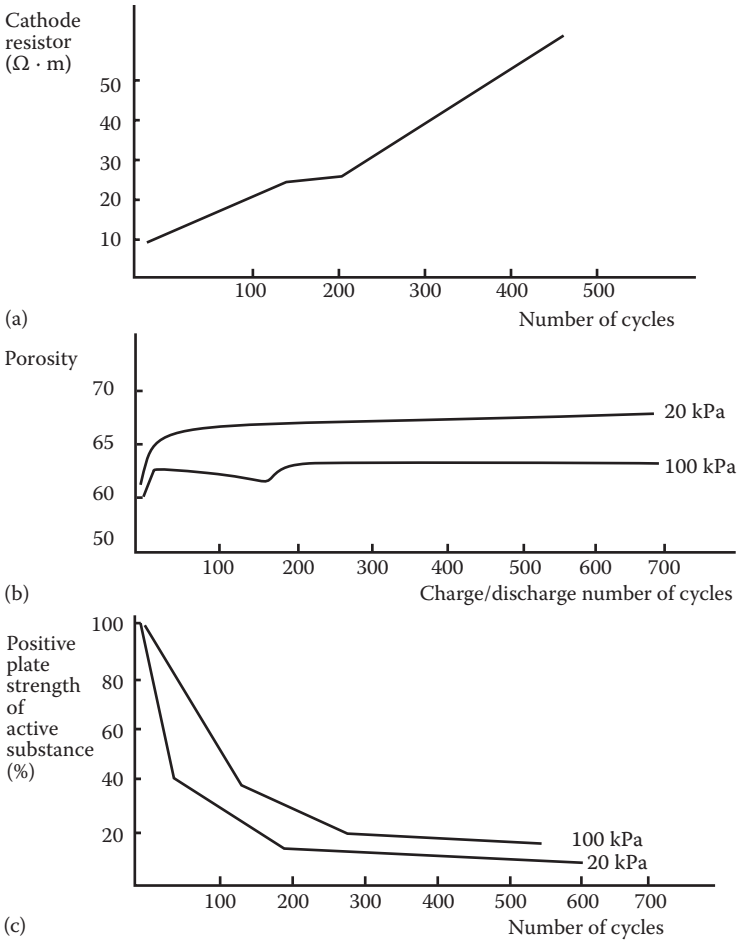

FIGURE 3.11 Changes of (a) resistance, (b) porosity, and (c) bonding force of positive lead dioxide materials with increasing charge/discharge cycling. (From R. Nelson, *Lecture Course on VRLA*, Beijing, China, 2003.)

lead dioxide layer can be obtained; at high current densities, the resulting lead dioxide layer is a softened lead dioxide layer, which is easier to take off. A small discharge current density can result in coarse and porous lead sulfate, which could be converted to dense lead dioxide during charge. Therefore, the particle size and porosity of lead sulfate is strongly dependent on the discharge conditions. Temperature, current density, solution concentration, and depth of discharge all can affect the lead sulfate crystal structure, leading to a different cycle life. Normally, a low electrolyte concentration and low current density are both benefits to the formation of porous lead sulfate during discharge. In addition, the impurity inside the positive active material could have a negative effect on battery cycle life.

For example, if the positive electrode is contaminated by negative electrode expanders such as $BaSO_4$ or $SrSO_4$, the positive active material could be easily taken off.

3.9 IMPROVEMENT OF POSITIVE ELECTRODE PERFORMANCE

To improve the positive electrode performance of lead-acid batteries, some approaches for optimizing the composition of active material seem to be feasible. For example, integrating additives into the positive active material has been carried out and proved to be effective.

3.9.1 Addition of Phosphoric Acid/Phosphate to the Electrolyte Solution

Phosphoric acid or phosphate can improve the performance of lead-acid batteries through shedding of positive active materials, resulting in a prolonged cycle life. It can also decrease the self-discharging of batteries, especially those using a Pb-Ca metal grid. XRD measurements show that phosphoric acid or phosphate in electrolyte solution can generate an intermediate such as $Pb_3(PO_4)_2$ during the oxidation process, thus preventing the electrode from corrosion if the grid used is made of Pb or Pb-Sb [5]. The role of $Pb_3(PO_4)_2$ is to improve the bonding force between α-PbO_2 and β-PbO_2. It can also change the kinetics between lead dioxide and lead sulfate. In electrochemical measurements, the linear potential sweep indicated that the reduction peak of lead dioxide to lead sulfate was lower in the presence of phosphoric acid than in the absence of phosphoric acid [5]. In practice, the quantity of phosphoric acid/phosphate inside the electrolyte should be controlled at a level lower than 1% in order to enhance both the capacity and lifetime [5].

Actually, different quantities of phosphoric acid in the electrolyte solution can have different affecting mechanisms. Even if the concentrations of phosphoric acid are the same, their effects on α-PbO_2 and β-PbO_2 are different.

3.9.2 Addition of Antimony to the Positive Material

In general, adding antimony to the lead dioxide can result in some perfective structures, leading to increased conductivity and reactivity, which in turn result in enhanced electrode performance. It has been reported that when 0.05% to 1.0% of Sb_2O_3 was added to the positive electrode when a Pb-Sb grid was used, the bonding force between the grid and the positive material was enhanced [5].

Note that the added antimony could move to a negative electrode, leading to both higher hydrogen evolution and water loss rates, which should be avoided.

3.9.3 Usage of Adhesives

Adding Teflon emulsion, conductive polymers, carbon fiber, and rutile structured oxidate to PAM as adhesives can promote the transformation of α-PbO_2 into β-PbO_2, enhancing electrode performance.

3.10 SUMMARY

The positive electrode is a necessary and key component in a lead-acid battery. It determines the battery's performance in terms of energy density and efficiency, power density, and cycle life. This chapter provided detailed descriptions of electrode design, materials and structures, fabrication, electrode process mechanisms, performance degradation, and degradation mitigation strategies.

The positive electrode normally contains a grid (Pb), which serves as both the mechanical support for the active mass paste and the current collector, and a layer of active mass (PbO_2). The designs and materials used for the grid were described in detail. In particular, various Pb alloys used for grid construction were discussed in terms of their compositions, functions, and their beneficial effect on electrode performance. Regarding the active mass pastes, the paste composition, curing, and formation processes, as well as associated physical/chemical processes, were described and discussed. Furthermore, fabrication procedures for positive electrodes were briefly introduced. We hope readers have found this chapter useful in their study and experimental approaches.

REFERENCES

1. Available at http://www.checkthatcar.com/carfaq2.asp.
2. A. Kirchev, N. Kircheva, and M. Perrin, "Carbon Honeycomb Grids for Advanced Lead-Acid Batteries. Part I: Proof of Concept," *J. Power Sources*, 196(20) (2011), 8773–8788.
3. G. Pavlov, *Lecture Course on VRLA*, Beijing and Zhangjiajie, China, 2000.
4. R. Nelson, *Lecture Course on VRLA*, Beijing, China, 2003.
5. Z. Li, *Lecture Course on VRLA*, China, 2003.
6. D. Pavlov et al., *J. Electrochem. Soc.*, 137 (1990), 16, 21.
7. D. Pavlov et al., *J. Appl. Electrochem.*, 6 (1976), 339.
8. D. Pavlov et al., *J. Electrochem. Soc.*, 131 (1984), 1468.
9. D. Pavlov et al., *J. Electrochem. Soc.*, 13 (1986), 241.
10. D. Pavlov et al., *J. Power Sources*, 30 (1990), 77.
11. D. Pavlov, and E. Bashtavelova, "A Model of the Structure of the Positive Lead-Acid Battery Active Mass," *J. Electrochem. Soc.*, 131 (1984), 1468.
12. D. Pavlov, and E. Bashtavelova, "Structural Properties of the PbO_2 Active Mass Determining Its Capacity and the 'Breathing' of the Positive Plate during Cycling," *J. Electrochem. Soc.*, 133 (1986), 241.
13. D. Pavlov, E. Bashtavelova, and V. Iliev, "Structure of the Lead-Acid Battery Active Masses," in *Proc. Int. Symp. Advances in Lead-Acid Batteries*, Vol. 84-14, p. 16, Electrochemical Society, Pennington, NJ, 1984.
14. M. Dimitrov, and D. Pavlov, *J. Power Sources*, 93 (2001), 234.
15. D. Pavlov, G. Papazov, and V. Iliev, *J. Electrochem.*, 119 (1972), 8.

4 Lead-Acid Batteries
Fundamentals, Technologies, and Applications

J. Kevin Whear

CONTENTS

4.1 INTRODUCTION

The ability to store energy in a galvanic cell is generally understood by those trained in basic chemistry. However, what is not known or understood is the role or even the existence of a separator in such cells. The role of the separator was quickly defined as the galvanic cell moved from the laboratory into commercial applications more than a century ago. The battery separator allows the cells to be designed in such a way as to minimize space between the corresponding electrodes while preventing electronic shorts. To prevent shorting, the separators must act as an insulator when electronic currents are concerned. At the same time, the separator must allow for ionic flow between the electrodes so that the electrochemical reactions can proceed. To achieve both functions, separators are constructed from nonconducting materials that are made in a porous manner that does allow ionic conductance.

4.2 MATERIALS AND PROPERTIES

Besides being nonconductive and able to be rendered porous, materials used to manufacturer lead-acid battery separators must also be wettable and stable in strong sulfuric acid. A short review of the history of separators will highlight the differing materials of construction. One of the first commercial separators produced was made from wood shingles where the lignin was purposely leached out, resulting in a porous structure. Most notably, shingles produced by Port Orford Cedars were durable and resistant to attack by strong oxidizers and they were primarily used from the early 1900s to the 1950s. As the available stock of trees dwindled, alternative solutions were sought, primarily in the area of synthetic materials [1]. The new materials used to construct separators included polyvinyl chloride (PVC), rubber, and resin-impregnated cellulose. These materials replaced the Port Orford Cedar shingles and, from the 1950s onward, they were the separator materials of choice [2]. In the 1970s, a wave of new materials was used to manufacture separators, and these new materials ultimately replaced the aforementioned ones.

In the 1970s, W. R. Grace introduced the polyethylene (PE) separator to the battery market. This separator is constructed out of ultra-high-molecular-weight polyethylene (UHMWPE), precipitated silica, and mineral oil [3]. The UHMWPE is a unique material in that the estimated molecular weight is between 1.0 and 9.0 million, depending on the particular grade. This is important to note because this molecular weight is at least one, if not two, orders of magnitude higher than other similar types of polyethylene. This extremely high molecular weight yields unique properties that are ideally suited for separators because of their high mechanical

strength, stability in acid, and resistance to oxidation. Since its introduction in the 1970s, the PE separator has, for the most part, replaced the earlier-mentioned materials to become the material of choice in flooded lead-acid batteries.

In this same time period, another technology breakthrough in lead-acid batteries occurred in which the separator was instrumental. Gates Energy Products developed the valve-regulated lead-acid (VRLA) battery and the key aspect of this technology is that the electrolyte is completely immobilized by an absorptive glass mat (AGM) separator [4]. Another method used to immobilize the acid is to create a thixotropic gel using fumed silica, as was invented by Jache at Sonnenshein [5]. These gel electrolyte or "Dryfit" batteries utilized a separator that was introduced by W. R. Grace, also in the 1970s, called Darak. Darak is a composite material made by cross linking a phenolic impregnated nonwoven polyester. Darak has been widely adopted in this application because it exhibits a high porosity and is stable against phosphoric acid, which is often added to gel batteries.

By way of a quick survey, the materials of choice in separators today include the PE separator, AGM, Darak, rubber, cellulosic, and PVC. From the 1980s until today, the aforementioned materials of choice for separators have been regularly improved to meet the application requirements. The general trend has been to optimize these materials with regard to assembly or use in an application or to take steps to remove costs by eliminating unnecessary design features. Table 4.1 shows the various market segments where such materials are used as separators.

The various separator materials have been utilized in different end market segments, in large part due to the difference in key properties, which are explained next.

4.2.1 Porosity, Pore Size, and Pore Shape

As mentioned earlier, the separator has the dual function of preventing electronic conductance between opposing electrodes while allowing ion flux. To meet these needs

TABLE 4.1
Separator Types and Applications

Separator Type	Automotive	Flooded Backup Power	Sealed Backup Power	Fork Truck	Golf Car and Renewable Energy	Dry Charge
Polyethylene	+++	++		+++	++	++
Darak		++	+			
Extruded PVC		++	+	+		
Absorptive glass mat	++		+++			
Rubber		++			++	
Cellulosic	+	+				++

Note: +++ = dominant; ++ = frequently used; + = sometimes used.

simultaneously, separators are made of nonconducting materials that are porous. The porous nature of the separator is quantified by measuring porosity, which is simply the ratio of void volume to the apparent geometric volume. To state it another way, a separator with 60% porosity has that same void volume, and the remaining portion, in this case 40%, consists of solid material.

Maximizing porosity is usually desirable because this increases the available acid between the electrodes and improves the rate of ionic transfer. However, porosity only tells part of the story with regard to the intended purpose of preventing electronic shorting because the pore size also plays an important role. In lead-acid batteries, the positive active material is prone to shedding, especially with frequent deep discharges. The lead particle of the positive active material is typically a few microns in diameter. To prevent dendritic formation of any shed particles, the pores of the separator should be smaller than the individual lead particle. In earlier years, the pore size of separators was classified as macro in that they were larger than 1 μm in diameter and many of the separators had typical pore diameters in excess of 30 μm (Figure 4.1). For the most part, separators with large pore sizes have been displaced by separator types with pore sizes classified as submicron, or less than 1 μm in diameter (Figures 4.2 through 4.4). The typical pore sizes are 0.1 μm, or 100 nm.

When characterizing pore size, a few points should be mentioned. First off, some separator materials of construction have an asymmetrical pore structure. For instance, fiber materials such as an AGM separator may have very different pore structures when measured in the various planes of orientation. For prevention of shorts, the pores should be characterized in the plane of the separator that is parallel to the surface of the electrodes. One method that is used for pore characterization is based on the first bubble method, where the void space of the separator is filled with a given liquid and then gas pressure is applied on the surface until a breakthrough occurs. Based on the pressure required and the intrusion liquid, the pore size can be quantified.

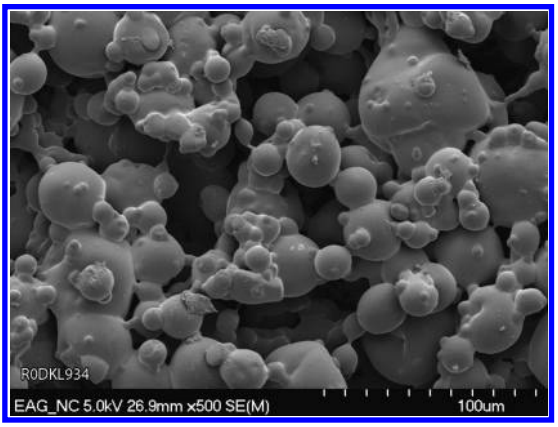

FIGURE 4.1 Sintered PVC separator.

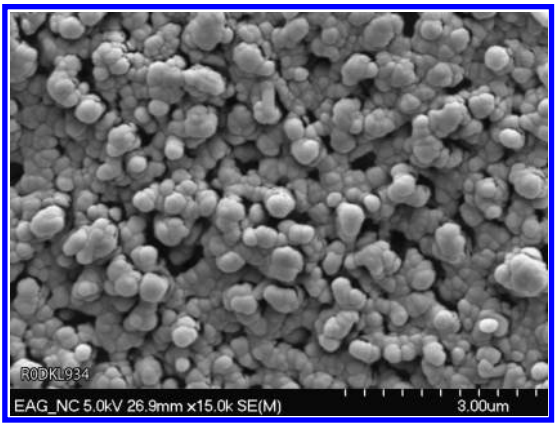

FIGURE 4.2 Phenol-formaldehyde resin resorcinol separator.

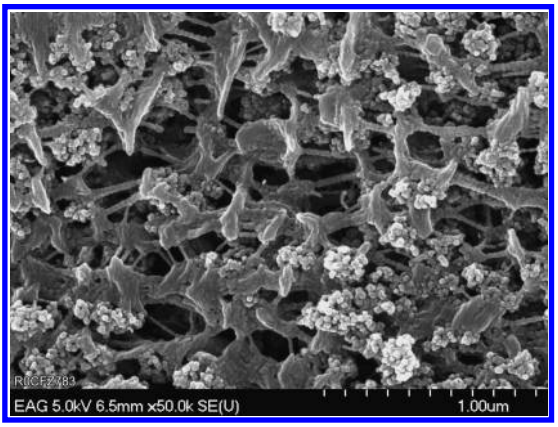

FIGURE 4.3 Microporous polyethylene separator.

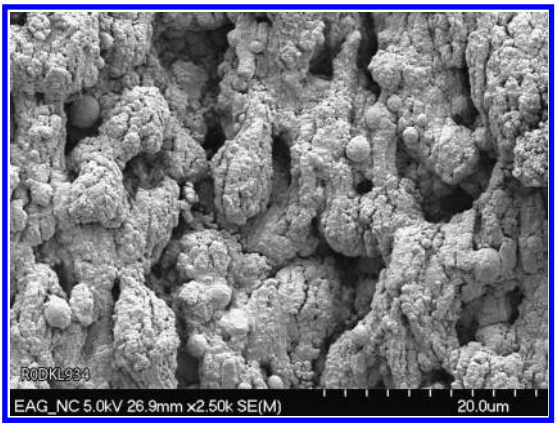

FIGURE 4.4 Rubber separator.

In addition to pore diameter, pores are also characterized by their shape. Conceptually, we can think of pores as channels or tunnels that fully traverse through the separator material. These channels, however, do not normally form a uniform or straight path. To describe this attribute, we often speak of the tortuosity of the pore structure, which can be described as

$$T = L/d \tag{4.1}$$

In Equation 4.1, the tortuosity factor (T) is given for different separator types, and d is the thickness of the substrate in the direction that is perpendicular to the electrode surface [6]. The path length of the pore (L) can only be equal to or larger than the value of d. The larger the tortuosity factor, the more deviations in the path length of the pore as compared to the distance of the substrate thickness.

4.2.2 Ionic Resistance

The battery separator, by definition, consists of a porous nonconductive material that allows ionic current to pass through it. The ionic resistance or the electrical resistance of the separator is defined as the total resistance of the separator filled with electrolyte minus the resistance of a layer of electrolyte of equal thickness:

$$R(\text{separator}) = R(\text{electrolyte + separator}) - R(\text{electrolyte}) \tag{4.2}$$

For our situation, we will define resistance, R, with the following equation:

$$R = 1/\alpha \cdot L/q_{open} \tag{4.3}$$

where $1/\alpha$ is the specific electrolyte conductivity, which is a temperature-dependent material constant. The variable L is the length of the ion path, and q is the area of the ion flow. To determine the length of the ion path, L and the tortuosity factor of the separator must be taken into account, as shown earlier in Equation 4.1.

In Equation 4.1, tortuosity factor T is a given for different separator types, and d is the thickness of the substrate or membrane. The remaining variable to solve in Equation 4.3 is q. For this we must take into account the porosity (P) of the separator as defined in Equation 4.4:

$$P = \frac{\text{void separator volume}}{\text{geometric separator volume}} = (q_{open} \cdot L)/(d \cdot q) \tag{4.4}$$

Equation 4.4 can be transformed, solving for the void separator area, q_{open}:

$$q_{open} = q \cdot P/T \tag{4.5}$$

Making the appropriate substitutions back into Equation 4.3, we can now solve for the resistance of the separator.

$$\begin{aligned} R(\text{separator}) &= (1/\alpha \cdot L/q_{open}) - (1/\alpha \cdot d/q) \\ &= 1/\alpha(d \cdot T \cdot T/(q \cdot P) - d/q) \\ &= 1/\alpha \cdot d/((T^2/P) - 1) \\ &= R(\text{electrolyte}) \cdot [(T^2/P) - 1] \end{aligned} \tag{4.6}$$

The separator resistance is firstly dependent on the tortuosity T, which is inherently defined by the structure of the separator and modified. However, the porosity of lead-acid separators can vary from 35% to 95%, which will yield a wide range of electrical resistance variation, as seen in Figure 4.5.

From Equation 4.6, we can also see that the separator resistance is proportional to the thickness d and has a dependency on temperature and concentration of the electrolyte, which will impact the conductivity. The specific conductivity of sulfuric acid in typical batteries with a density of 1.28 g/cm^{-3} at 25°C is 1.26 Ω cm.

The separator resistance for a typical polyethylene separator used in a starter battery with $d = 0.20$ mm, $P = 0.6$, and $T = 1.3$ over an area of 1 cm^2 calculates to

$$R(\text{sep}) = 1.26\ \Omega\ \text{cm}\ (0.020\ \text{cm}/1\ \text{cm}^2) \cdot [(1.3^2/0.6) - 1] = 0.046\ \Omega$$

The resistance of a separator is stated in reference to the related area. Therefore, the above case would be stated as 46 mΩ cm^2. Thus far, our consideration for electrical resistance has taken into account the porosity and the tortuosity of the separator and this has yielded a value that can be validated by independent measurement either between electrodes or with specific laboratory equipment such as the Palico electrical resistance tester [7].

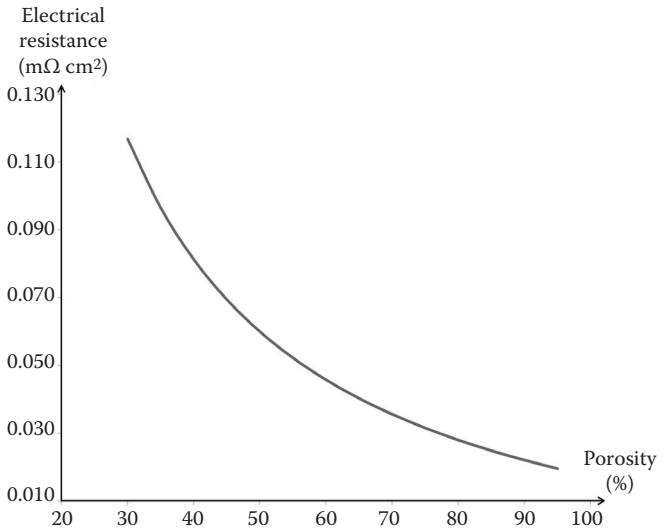

FIGURE 4.5 Electrical resistance as a function of separator porosity.

The measured or calculated electrical resistance of the separator does not account for all of the energy losses that might be related to the separator, especially in a flooded battery. For instance, starting, lighting, and ignition (SLI) batteries are often characterized by measuring cold cranking amps (CCA). In this standard test, batteries are routinely characterized with regard to the amount of power they can deliver in the very short time of less than 30 sec. In preparation for the CCA test, batteries are overcharged to ensure they are fully charged. While being overcharged the batteries will go into gassing mode, due to the hydrolysis of water and oxygen, and hydrogen gas will be formed respectively at the positive and negative plates. Ultimately, these gases will evolve out of the electrolyte, but for a time these gases will collect on the surfaces immersed in the electrolyte.

In preparation for the CCA test, the battery is taken off charge and placed in a freezer at –19°C for 24 h to ensure uniformity of the core temperature. After this period, a fair amount of gas can be liberated from the battery. The gases that are attached to surfaces along the ionic flow path, such as plate and separator surfaces, are of concern. Because gas bubbles are infinitely resistant to ionic flow, the surface area occupied by the gas will essentially be blinded and cause an increase in overall battery resistance. To account for the influence of entrapped gas, it is therefore appropriate to think of the functional resistance instead of measured or calculated electrical resistance [8]:

$$ERf = ERm * (1 - GA)^{-1} \tag{4.7}$$

In Equation 4.7, the functional electrical resistance (ERf) is calculated from the measured electrical resistance (ERm) divided by the fraction of remaining area open for ionic flow. The area open for ionic flow is calculated by subtracting the fraction of area occupied by gas (GA) from the whole.

4.2.3 Electrochemical Compatibility

The primary purpose of a lead-acid battery is to store and discharge energy; therefore, we must avoid any action that would diminish this primary function. As stated earlier, the primary role of the separator is to allow ionic flow while preventing electronic conductance. As we consider the different materials of construction of the battery, including the separator, we must also consider some important aspects regarding electrochemical compatibility.

Some time ago, scientists at the Bell Laboratories developed the electrochemical compatibility test [9]. This test essentially utilizes cyclic voltammetry equipment that screens materials to determine the influence on pure lead electrodes over the whole range of charging and discharging voltages.

The test method essentially soaks prospective materials in hot sulfuric acid for a reasonable length of time, allowing for the leaching of any soluble compounds. The acid leachate is placed in the cyclic voltammetry equipment and charge and discharge curves are produced and then compared against curves generated with the acid, which serves as the control. Experienced electrochemists will look for shifts in various peaks indicating the presence of materials that could disrupt the energy storage capability of the cell.

When such shifts are found in the charging and discharging curves, they can often be correlated back to different trace elements. Certain trace elements can function as a shuttle mechanism for ion transfer and actually increase the rate of self-discharge. Other elements can cause a shift in the electrode potential and initiate the hydrolysis of water and should be avoided [10,11]. Through experience, the battery industry has developed different standards for trace elements to be present in the battery. Obviously, the concentration of any detrimental elements will need to be considered in all materials in the battery, including the separator [12].

4.2.4 Acidic and Oxidation Stability

The environment of the lead-acid battery is challenging simply due to the presence of strong sulfuric acid, a typical weight of 30%, and the production of nascent oxygen at the positive electrode during overcharge. Thus, the materials of construction for the separator must be selected in such a manner as to last the intended serviceable life of the battery. To evaluate the acidic and oxidation stability of the separator, many tests have been developed over the years.

Early on, separators were evaluated by the amount of weight loss realized in hot sulfuric acid for a given time. Other more aggressive tests were developed in which oxidizing species were added to the hot sulfuric acid such as dichromate or hydrogen peroxide [13]. In these tests, the perception was that the lower the weight loss, the higher the oxidation or acid resistance—and this was true to a degree. As separators became more complex with time, certain components were added to improve pore wetting or to reduce the amount of antimony poisoning. By design, many of these additives are soluble in acid and this point needs to be considered when considering the output of the acid weight loss test. While the components of the separator dictate the pore structure and provide protection against shorting, they should be stable in the environment.

The goal of such tests is to make sure that the separator is still able to perform one key function, which is to prevent electronic conductance. If the separator is sufficiently oxidized, the barrier for electronic shorting is gone. Therefore, over time, different tests have been developed to better simulate or estimate the degree of oxidation stability. One such test is the Perox 80 test. In this test, a mechanical property of the separator is measured by puncture resistance, elongation, or tensile strength to break. Then the separator is subjected to a solution of sulfuric acid and hydrogen peroxide, which is held at 80°C. The separators are removed at different time intervals and the residual mechanical properties are measured, and from this data, the rate of decay curves can be developed. This test is useful when comparing a type of separator to itself where various changes to the formula or process have been made.

The overcharge test comes even closer to simulating the actual use of the material. In this test, separators are put into batteries or cells and the cells are overcharged to make sure the oxidizing species are present and controlled at an elevated test to accelerate the rates of reaction. Like the Perox 80 test, separators are removed from the cells at different time intervals so the mechanical properties can be evaluated and the rate of decay curves can be developed and compared. Another similar test is the Japanese Industrial Standards (JIS) corrosion test, in which a test separator is placed between two large lead blocks in an acidic solution [14]. A constant voltage is

applied to these opposing lead blocks to create gassing and thus oxidize the species. The lead blocks also serve the purpose of creating a pressure on the separator that causes mechanical stress to the material. With the combination of oxidation attack and mechanical stresses, the separator will ultimately rupture, and the float current will spike with the fixed voltage; this will indicate the presence of the electronic short.

4.2.5 Puncture Resistance

Because the separator is in immediate contact with the electrodes, there is a real possibility for the material to rupture, especially during high-speed assembly. For instance, with automotive batteries, the electrodes are typically enveloped with the separator. Because the electrodes are thin and rectangular, the corners will act as stress concentrators, especially in reference to the separator. If a separator in one cell is ruptured during the assembly process, the functionality of the particular cell and the entire battery is now jeopardized. A ruptured separator is likely to be associated with electronic conductance.

To prevent shorting from a ruptured separator, a standardized test method has been developed to measure the puncture resistance of the separator. The need to increase the puncture resistance of the separator was highlighted during the 1990s with the introduction of expanded metals grids because these types of grids increased the potential for a ruptured separator [15]. For separators utilized in flooded automotive-type batteries, many advances were made to improve the puncture resistance of the separator material. First, there is a positive relationship between puncture resistance and substrate or back-web thickness, so one solution would be to simply increase thickness. As shown in Figure 4.6, increasing the back-web thickness by 10% resulted in a similar improvement in puncture resistance, but unfortunately this also increased the separator cost, electrical resistance, and acid displacement; thus other solutions were sought.

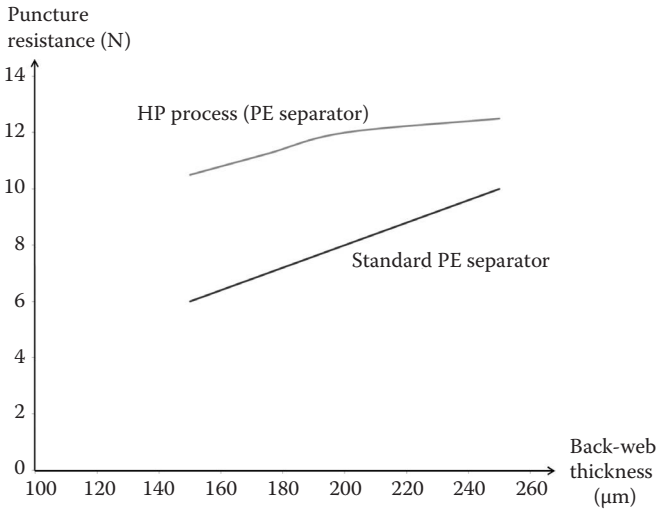

FIGURE 4.6 Puncture resistance as a function of back-web thickness.

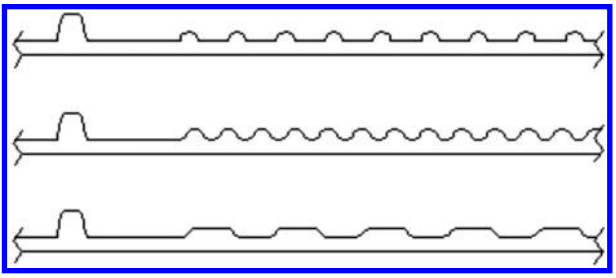

FIGURE 4.7 Sealing rib designs for preventing ruptured separators.

A breakthrough came with the introduction of the high puncture (HP) process, which involved a different method for handling and forming the UHMWPE chains. This breakthrough decoupled the essentially linear relationship between back-web thickness and puncture resistance and improved puncture resistance by more than 50%. This allowed battery manufacturers to utilize the expanded metal grid manufacturing process while maintaining reasonable yields associated with ruptured separators.

Besides increasing the absolute puncture resistance of the separator, work was also done to modify the area where the rupture was mostly likely to occur. Because the corner of the plate is more likely to have a sharp corner or protruding wire, this is where a rupture is likely to occur. To that end, many designs were made to prevent or direct contact by deflecting the grid wire or sharp edge from having intimate contact with the separator back-web or substrate, as illustrated in Figure 4.7 [16–19].

Thus far, the focus has been on improving the puncture resistance of separators used in flooded lead-acid batteries primarily for automotive applications. A need was also identified for VRLA batteries utilizing an AGM separator. Because the AGM separator is comprised of glass microfibers, with no binders, the mechanical properties are primarily defined by the entanglement of the fibers. Mechanical properties, including puncture resistance, could be modified by blending a certain percentage of larger and smaller fibers into the recipe. A large step came when synthetic fibers were included in the recipe. One embodiment was to utilize a bicomponent fiber with a lower melting point polymer, such as PE, as the outer sheath [20]. Once in the matrix, the separator was subjected to temperatures where the outer sheath polymer was softened and this allowed points of connectivity to the glass fibers and acted as reinforcement to strengthen the mechanical properties such as puncture resistance.

4.2.6 Surface Area

The physical attribute of internal surface area is important when we consider the AGM separator. Besides preventing electronic conductance and allowing ionic conductance, the AGM separator also immobilizes the electrolyte in a VRLA-designed battery. Therefore, it is understood that the greater the internal surface area, the greater the immobilizing forces and the ability to prevent acid stratification, which becomes more of a concern with the height of monoblock batteries in a standard

configuration. Changes to the internal surface area are achieved by changing the proportion of fine fibers with a diameter <0.5 μm and large fibers having a diameter >1.0 μm. Separators with 100% fine fibers may have an internal surface exceeding 2.0 $m^2 g^{-1}$; blending in larger fibers can lower the value below 0.7 $m^2 g^{-1}$ [21].

The surface area is an indication of concentration of the fine fibers in a given separator, and it plays a role in defining the pore size and resiliency forces. Because fine fibers are more costly to produce, work has been done to impart surface area via other means. One method was to include colloidal silica in the AGM structure. Colloidal silica is essentially made out of silicon dioxide, like the glass fibers, but made with a more developed structure such that the internal surface area is two orders of magnitude greater (e.g., 300 $m^2 g^{-1}$). Thus, adding small amounts of this silica can be very effective in changing the internal surface of the composite.

4.3 SEPARATOR SYNTHESIS

4.3.1 Polyethylene Separator

The process for manufacturing PE separators was first developed in the 1960s by W. R. Grace and it entails five primary steps: (1) mixing, (2) extrusion, (3) calendering, (4) extraction, and (5) finishing. In the mixing step, 55 wt% mineral oil is combined with 32% precipitated silica and 12% UHMWPE [3]. The remaining 1% of the components is what is referred to as minor ingredients such as colorant, extrusion aids, and antioxidants. Because oil is the primary component in the mix, one might expect the mixture to have the constituency of slurry. This is not the case, however, because the precipitated silica has a high surface area and the bulk of the oil is absorbed. The resultant mix is a tacky, but transferred powder that is fed into the throat of a twin screw extruder, as seen in Figure 4.8. With the aforementioned tacky powder, more oil is added to the extruder such that the total concentration is between 60 and 70 wt%.

The twin screw extruder performs the function of first devolatizing the mix mostly of air and moisture. The extruder is designed to mechanically work the mixture, which generates heat and allows the UHMWPE to solvate into the mineral oil. The mixed powder/liquid mixture is transformed into a melt extrudate that then exits the die via a slot or sheet die. This extrudate film is received by a pair of calendar

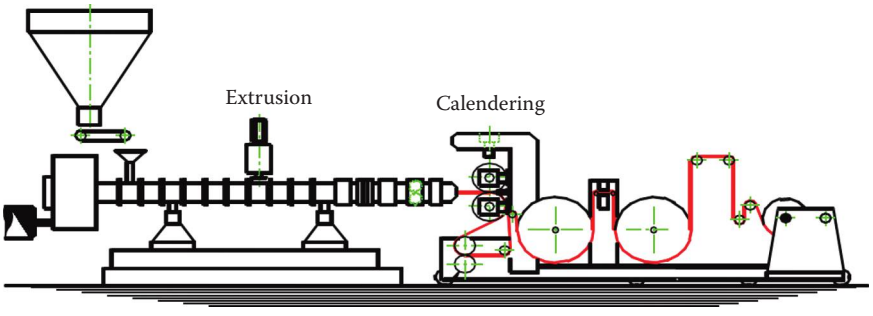

FIGURE 4.8 Polyethylene extrusion process.

rolls, which normally have a reverse image of the profile or rib pattern. Because the extrudate is hot and molten, the material is thermally formed into a three dimensional (3D) structure and cooled below the softening point of the polymer to fix the shape and allow for ease of transportation. To meet the various market needs, numerous calendar roll combinations are needed.

This oily 3D web is now transferred to the next step of extraction. Here the web is pulled through where the solvent is directionally flowing countercurrent to the web. Because the affinity of the solvent, typically hexane or trichloroethylene, is high regarding the oil, the oil will leach out of the separator into the solvent. Thus, the extraction process will reduce the oil content in the separator material from 65 to approximately 15 wt% and the porosity is created from the resultant voids. Depending on the thickness of the oily separator material, it will stay in the solvent baths for 45 sec to 4 min to reach the desired residual oil level. For economic reasons, the path length in the solvent bath can be quite extensive, upwards of 50 to 120 m.

With regard to the extraction process, a few other practical matters must be considered. Once the separator material comes to the end of the leach baths, it is removed but it is still laden with solvent. The solvent is selected in such a manner that it can be easily volatized with heat without approaching the softening point of the polymer, because this could cause deformation. Thus, the solvent-laden sheet is processed through a solvent drying oven and the solvent is condensed and recovered. A by-product of the extraction process is a solvent and oil mixture. This dirty solvent stream is further processed in a distillation process in which the oil and solvent are separated and recycled back to the extrusion and the extraction processes, respectively.

The last step in the PE process is referred to as the finishing step. The width of the material in the extrusion and extraction process is normally 4 to 8 times wider than the customer can use. Semifinished or bull rolls coming off the extraction process are slit to the finished customer width and may be cut to a final length assuming they are sold in a leaf format. The finishing step may also include laminating a glass or synthetic mat to the PE separator. Because the PE separator can be welded to itself using sonic waves, heat, or mechanical forces, three-sided envelopes and two-sided sleeves can also be produced in the finishing step.

4.3.2 Absorptive Glass Mat Separator

The AGM separator is classified as a nonwoven, wet-laid material and as such it is produced on equipment associated with paper manufacturing. Before speaking of mat formation, it is worth mentioning a note or two concerning the fiber-making process. Glass marbles, which are primarily silicon dioxide (SiO_2), are fed into a furnace operated at temperatures in excess of 1500°C and melted. Next, the molten glass is fed through a bank of bushings, or orifices with micron openings, and the initial filament structure is formed. When the initial coarse glass filaments have been formed, there are two options regarding subsequent processing or attenuation: *flame blowing* or *rotary fiberization*. The intent of both processes is to further reduce the fiber diameter and then cut the fibers so they can be densified and baled [22].

Because the fiber manufacturing process is quite specialized and capital intensive, many AGM separator manufacturers purchase their fibers from suppliers. To

convert the primary feedstock of microglass fibers into an AGM separator, the paper making process is utilized, which consists of four main steps. The fibers are normally received in a bulk form and then placed into the first step, called *pulping* or *hydropulping*, which provides mechanical agitation to the bulk fibers while in the presence of water to create a suspension. It is interesting to note that the fibers are typically 0.5 wt% in the slightly acidic aqueous solution [23].

This aqueous suspension of fibers is formed into a mat in the next step, called *formation*. Here the slurry is fed to a head box that evenly disperses a layer on a porous belt where the fibers are collected. At the same time the water is allowed to drain off or is drained via vacuum assist. The speed of the belt, in comparison to the feed rate of the liquid from the head box, will determine the basis weight of the material. The various types of equipment used include fourdriniers, rotoformers, and inclined wires. As the mat leaves the formation step, the web is still 60 to 80 wt% water and has limited strength [24].

The third major step in the process is *drying*. This step renders a mat with less than 1 wt% water. Because the heat of vaporization is quite high for water, the most efficient means to remove water are used including conduction, convection, and radiation heating in the drying chamber.

The final step involves *converting*. This is where the dried mat is wound onto cores as large as 6 m wide. Unlike other wet-laid material, the AGM separator typically does not contain chemical binders and the mechanical properties are derived from fiber entanglement. Therefore, winding these rolls must be completed carefully to control the forces placed on the material. These master or bull rolls will then be slit down or cut on auxiliary equipment to the final dimensions that meet customer requirements.

4.3.3 Darak® Separator

In the 1960s, W. R. Grace invented the phenolic resin separator, also called Darak [25]. The basis of the process is a curing reaction using an aqueous solution of a modified phenolic resin that is polymerized by means of heat to form a microporous structure, with water ultimately serving as the pore-forming agent. In practical terms, the aqueous phenol-formaldehyde solution is impregnated into a thin fleece material, which ultimately serves as the skeletal structure of the separator. This impregnated mat is fed into two moving belts, which are engraved with a reverse image of the final rib configuration. The excess phenolic resin fills the cavities of these belts to ultimately form the rib patterns. Next, the engraved belts with the impregnated fleece are subjected to an elevated temperature, which initiates the polymerization of phenol and formaldehyde. During the step growth, or polymerization, a phase separation occurs because the resin cross links to a solid 3D microporous structure and the water is retained within the pores. The spaces occupied by water will dictate the pore volume, which is typically 70%.

Once the structure has been sufficiently polymerized, it is removed from the space between the rotating belts and has sufficient strength to be handled through the next step of the process. The next step involves washing and removing the unreacted components and then drying and finishing the curing of the resin to get it to its final state. This process makes possible the unique ability to change the pore volume and the pore size.

4.3.4 Rubber Separators

The process used to make rubber separators involves mixing precipitated silica, water, and natural rubber to create a thin film. The natural rubber is received in smoked sheets or slabs, and it is normally worked in various pieces of equipment so that the silica, laden with water, can be incorporated. This rubber, silica, and water mixture is then fed to an extruder to create a thin, uniform layer that is sufficiently malleable to be fed into a calendar stack, which has grooved voids in the roll that will create the rib structure.

Once the calendaring step is complete, the 3D structure that was created is ready to be cured. The older method used for curing involved winding material onto spools and then batch vulcanizing or sulfur curing the material to cross link the rubber. A newer method is to cross link the rubber by passing the formed sheet through an electron beam chamber, which can be done as an inline process [26]. After the curing is complete, whether by sulfur cure or electron beam, the water is then removed from the sheet to create the porosity and then the material is ready for the final step, which is finishing. This last step of the process is where the glass mat is attached to the material, which is then slit and cut to the desired width and height.

4.4 SEPARATOR STRUCTURE DESIGN AND FABRICATION

4.4.1 Positive Ribs

In a flooded lead-acid battery, the sulfuric acid serves as both the electrolyte for conductance of the ions and it also promotes the electrochemical reaction. To achieve optimum performance from a battery, the amount of sulfuric acid should be stoichiometrically balanced around the other reactants, namely, the positive and negative active material. The amount of electrolyte between electrodes is fixed by the 3D structure of the flooded lead-acid separator. Normally facing the positive electrode, there are ribs protruding off the planar surface of the substrate that serve to fix the distance between the electrodes and thus the volume available for the electrolyte [27]. Figures 4.9 and 4.10 illustrate some typical profiles.

With the positive ribs facing the positive electrode, added oxidation protection is provided to the separator substrate or back-web thickness. In a typical automotive

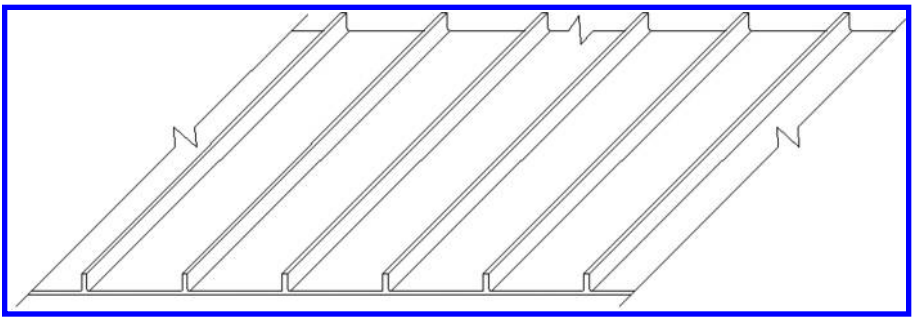

FIGURE 4.9 Universal profile.

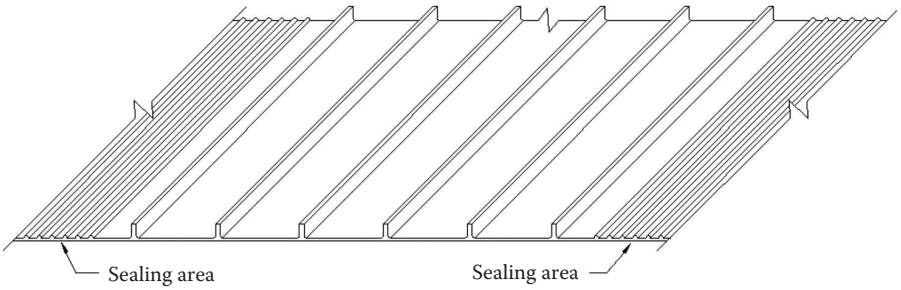

FIGURE 4.10 Panel profile.

battery, the separator back-web thickness can be 150 to 250 μm, while the positive rib height can be 0.45 to 1.50 mm. At the surface of the positive electrode in an overcharge condition, nascent oxygen is being produced, which will degrade the polymer. To protect the separator back-web from intimate contact with the oxidizing species, the major ribs normally face the positive electrode. In battery designs with very close plate spacing, smaller ribs have been placed between larger ribs to prevent the intimate contact while minimizing the size of the rib mass.

In deeply discharged lead-acid batteries, the positive rib design is important for extending the functional life of the battery. As the battery is discharged, the active material is converted to lead sulfate, which is more voluminous than either lead or lead oxide. As such, the active material will expand. During recharge, the lead sulfate needs to be in intimate contact with the lead or lead oxide to be efficiently converted and the design of the ribs can be useful here. In deep-cycle batteries, the number and orientation of the ribs are modified to optimize performance; various options are seen in Figure 4.11. Sinusoidal, diagonal, or tightly spaced rib patterns are often selected to provide maximum compression to prevent slipping into the low spot of the tube (Figure 4.12).

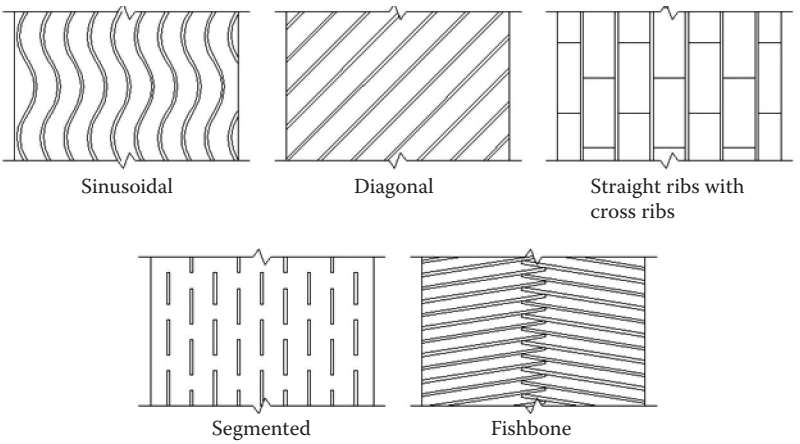

FIGURE 4.11 Various positive rib profiles.

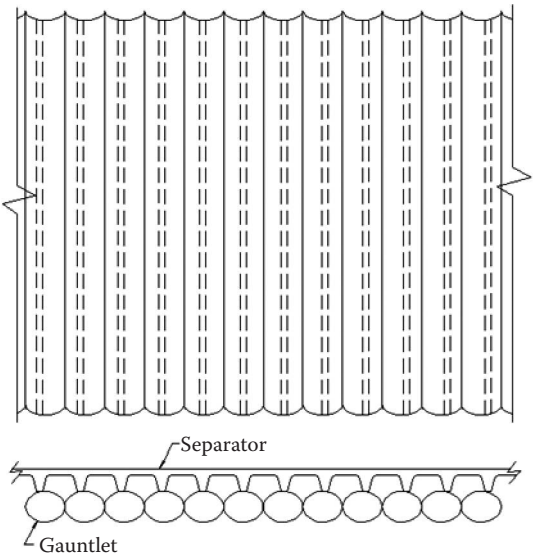

FIGURE 4.12 Tubular plate and straight rib separator.

4.4.2 Negative Ribs

While intimate contact with the positive electrode is likely to oxidize the separator at the negative electrode, hydrogen ions that serve as a reducing species are produced during overcharge. This situation poses no real threat to the separator and the back-web is often in direct contact in most flooded designs. In deep-discharge batteries, where the plate spacing or overall thickness is relatively high, it has proved beneficial to utilize the use of a negative rib to span the total thickness. In applications prone to high vibration, such as with diesel engines or rough road conditions, negative ribs have been employed to reduce shorts associated with vibration, as seen in Figure 4.13. In this way, ribs are in intimate contact with both the positive and negative electrodes and the back-web or substrate will avoid direct friction with other surfaces.

Negative ribs have been utilized recently to resolve another issue. In normal applications, the separators have not been the typical failure mode of the battery. As such, there has been an effort to reduce the mass of the separator. This is achieved by reducing the back-web thickness. Over the years the typical back-web has migrated from 300 μm to as low as 150 μm. Even at 150 μm for the back-web thickness, the

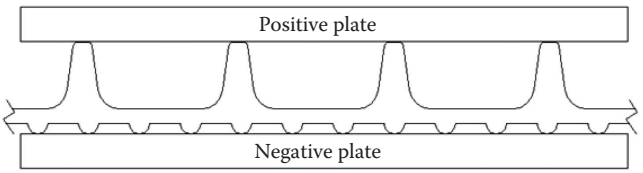

FIGURE 4.13 Positive/negative rib profile.

separator may not be the failure mode in the battery. However, getting this thin backweb material into a battery can be more challenging because the material is flimsy as measured by cross machine bending resistance. To improve the cross machine bending resistance, negative cross ribs have been employed [28,29].

4.4.3 Embossed/Corrugated

As mentioned earlier, the separator in a flooded lead-acid battery serves to fix the electrode spacing with a 3D shape. With the development of advanced synthetic materials such as the PE and PVC separator, it became possible to achieve the 3D shape by embossing [30–32]. Embossing is normally achieved by feeding a flat substrate into a pair of mated rolls with the desired 3D shapes. This technology is regularly utilized in various nonwoven applications. Similar to embossing is the concept of corrugating a substrate, which is simply a matter of bending or folding the material into a desired shape. Once corrugated, the substrate must be modified in some manner for the shape to be fixed with further cross linking of molecules or a postchemical treatment.

4.4.4 Compression/Resiliency

With regard to flooded lead-acid battery separators, the normal materials of construction are relatively noncompressible and they fix the electrode distance, providing a degree of compression on the electrodes, at least where the ribs contact the plate surface. In flooded designs, separators with a laminate layer are regularly utilized to provide more support of the active material that is likely to shed during deep discharge. Because the laminate thickness is normally a small portion, say, 10% to 20%, of the total structure thickness, the amount of compression or resiliency is minimized.

In VRLA battery designs utilizing an AGM separator, the degree of compression or resiliency becomes a more important issue. A critical aspect of the VRLA design is that during any overcharge, the oxygen generated at the positive electrode is transferred to the surface of the negative electrode and is immediately reduced to water, thus eliminating gas evolution and water loss. For this recombination cycle to function, the AGM separator must be in intimate contact with both electrode surfaces, and to this end compression is required.

If the VRLA battery is cycled to any depth of discharge, the electrodes will grow when in the sulfated state and when recharged the electrode thickness will likely shrink. During this expansion or contraction, it is important for the separator material to have sufficient resiliency to maintain intimate contact with the electrode surfaces so that the battery can continue to function. To that end, much work has been done to develop compression and resiliency curves for various AGM materials both in a dry and wet state [33].

4.4.5 Fabrication

Initially, all batteries were assembled by hand and this included putting together the cell elements with alternating negative and positive plates with separators in

between. Today, some batteries are still assembled by hand in regions of the world where the labor rates are low or where speciality battery production makes it challenging to automate. Because the first separators were sold as cut pieces, the first step in automation was to utilize pick-and-place equipment for coordinating the separator between the positive and negative plates. Different forms of this equipment are still being utilized for the manufacture of industrial-type batteries.

For high-volume automotive-type batteries, the fabrication process was substantially modified with the introduction of the PE separator and its two unique properties: flexibility and weldability. Unlike previous separators, the PE separator could be wound onto a roll and could be completely wrapped around the plate without breaking and cracking. Additionally, the PE separator was weldable unto itself either by sonic, mechanical, or heat welding. These two properties opened up the opportunity for further assembly optimization of which the equipment suppliers soon advanced the technology to meet the need [34]. The assembly equipment automatically wraps a separator around the bottom of the PE separator and then mechanically seals the sides to create a three-sided pocket around the plate. This pocket minimizes the potential for bottom and side shorts.

The same envelopers were adapted for fabricating batteries using AGM separators. Like the PE separator, the AGM separators were wrapped around the plate, but not sealed on the sides. Thus, the AGM separator provides some protection against bottom shorts. As one can imagine, the technology surrounding these envelopers has improved with time. When first introduced, enveloping 50 plates a minute was impressive, especially when compared to what could be done via hand assembly. Today, these modified envelopers can process as many as 200 to 300 plates a minute. The enveloping technology is essentially used for all automotive batteries today, at least those made for direct sales to automobile manufacturers.

For automotive batteries, where the plate height was 160 mm and less, envelopers were quickly adapted. For other deep-cycling batteries, the plate height could be 200 mm and higher and envelopers were not utilized in assembly; instead, automation came in the form of sleeves. One embodiment of a sleever is to position a plate between two layers of separators and then weld the separators onto each other, thus creating a sleeve with sealed sides to prevent shorts. In this construction the bottom is open and this is preferred by battery manufacturers to encourage acid circulation. Protection against bottom shorts is not a concern in these batteries because they still employ a mud room, where shed active material has a place to collect without leading to shorts.

4.5 EFFECTS OF MATERIAL COMPOSITION, MORPHOLOGY, AND SYNTHESIS CONDITIONS ON BATTERY PERFORMANCE

4.5.1 Antimony Poisoning and Water Loss

Alloying the plate grids or current collectors with antimony was helpful because it improved the process of casting the grids, increased the resistance against the positive grid, and mechanically strengthened the plates to resist the forces associated with expansion and contraction of active material during deep cycling. For all

of its benefits, however, antimony did have a noticeable side effect in that it would ultimately collect on the surface of the active material and depolarize the negative electrode. As the battery is charged with constant voltage, the positive electrode entered an overpotential situation and this initiated the hydrolysis of water. To remediate this situation, flooded batteries are designed so that they can be regularly watered.

For automotive batteries, the manufacturing processes have changed to the point that antimony has been replaced by other alloys such as calcium, which has drastically decreased, but not eliminated, the loss of water in a battery. Interestingly enough, many early batteries were constructed with hard rubber cases and, as mentioned earlier, the separator used were made from Port Orford Cedar shingles. As they were replaced with synthetic solutions, it was often noticed that issues with antimony poisoning were more detrimental. Over the years, it was found that the rubber and the residual lignin found in the separator played a beneficial role in mitigating the poisoning of the negative electrode [35].

Separators made from rubber have found a useful niche to mitigate the effect of antimony poisoning, which allows the battery to perform longer in a serviceable life. However, rubber separators are available only in leaf form and can suffer breaks and cracks from handling issues. Therefore, separator manufacturers have sought to combine the superior mechanical properties of the PE separator with the electrochemical benefits of the rubber separator into one material. Many additives have been proposed for the PE separator matrix to mitigate the antimony poisoning including lignin, grass lignin, uncross-linked rubbers, cross-linked rubbers, and synthetic compounds. These types of products have steadily displaced the rubber separator in many applications [36–39].

Over the years battery manufacturers have reduced or eliminated the use of antimony especially in automotive-type batteries. For these same automotive-type batteries, the need to reduce water loss continues to be an issue of importance. The bulk of the automotive batteries is located in the engine compartment, which has become smaller and more aerodynamic, causing the operating temperatures to increase. Even though antimony has been eliminated from the grids, it is still often used in the strap to connect the various plates. In addition, other trace elements are also present in the lead or the acid that can encourage water loss. In an effort to improve the charge acceptance of lead-acid batteries, one prescription is to add special carbons to the negative active paste, which also results in water loss.

Therefore, the desire to lower water loss in automotive batteries has found renewed interest. In the market there are specially formulated PE separators that can lower water loss from 20% to 40% compared to the typical PE separator and these are referred to as Daramic HP-V® and DuraLife® [40]. Research and testing has shown us that as the water loss of a maintenance-free battery is lowered, the life of the battery can also be extended. As the water loss associated with hydrolysis of water is lowered, the overall current that is passed through the positive grid is also reduced. Lowering the overall current lowers the rate of positive grid corrosion. Because positive grid corrosion is the primary failure mode, lowering the water loss can extend the battery life in both lab testing and the field.

4.5.2 Low Electrical Resistance

The primary purpose of an automotive battery is to simply start a car engine with a high burst of power. Therefore, SLI batteries are usually rated for their CCAs and the general trend has been toward maximizing the CCAs in a given box or container size or power density per volume. The separator has played an important role in this trend. First, to increase the CCAs, battery manufacturers increased the electrode area, often resulting in reduced thickness of the electrode and separator. Second, to maintain the correct acid ratio to active material, the back-web thickness has decreased from a nominal thickness of 250 μm to as low as 150 μm. Decreasing the back-web thickness has served to lower the separator resistance, which is a part of the overall electrical resistance of the battery.

Further improvements in lowering separator electrical resistance have come with the use of wetting agents to ensure complete wetting of the pores, and modifications to the silica concentration or silica type in the separator [41]. Besides lowering the measured separator resistance, a proposal has been made to also lower the functional electrical resistance. The functional resistance of the separator is the measured resistance compensated for area occupied by gas bubbles. Therefore, any work to lower the entrapped gas of the separator will also serve to improve the measured power output of a battery [8].

With microhybrid or mild hybrid automotive applications, there is renewed interest to further maximize power and thus minimize the electrical resistance of the battery. In these hybrid applications, the battery is likely to be operated at a partial state of charge, which means lower electrolyte gravity, partial sulfating of the active material, and less than maximum stored energy. All of these factors are working to lower the available power potential of the battery. Therefore, any strategy to further lower resistance and that of the separator is welcomed.

4.6 EFFECT OF BATTERY OPERATING CONDITIONS ON SEPARATOR PERFORMANCE

4.6.1 Basic Condition/Extreme Shrinkage

The bulk of lead-acid battery separators are comprised of silicon dioxide either in the form of glass fiber or precipitated silica. In acidic pH, the glass fibers and precipitated silica are very stable, but a slightly basic solution will initiate dissolution. One function of the silica is to support the porous structure so if any portion is dissolved, extreme shrinkage (in the range of 20%) can be observed. With such extreme shrinkage, the separator will no longer cover the opposing faces of the electrode and the risk of shorting will increase substantially.

Fortunately, this occurrence is relatively rare but can be challenging to resolve. First off, it is not normally expected that a lead-acid battery will experience a basic condition during operation; however, the analytical techniques confirm the loss of silica in the separator. It has been observed that during the initial soaking period, the sulfuric acid will react with the lead and lead oxide and may render the pH

slightly alkaline. This situation is more likely to occur when the active material to acid ratio is out of balance and the battery is allowed to soak for an extended period of time before being placed on charge [42].

4.6.2 Hydration Shorts

Because the sulfuric acid serves the purpose of electrolyte and reactant, it is important to maintain the proper balance with the other reactants, namely, the positive and negative active materials. Batteries can be designed in such a manner that there is insufficient sulfuric acid, so that when filling before formation or when the battery is deeply discharged, it is completely spent. With very low gravity acid or high pH, the lead can be soluble, especially with elevated temperatures [43]. As the lead becomes soluble, it will be in ion form and given enough time it will diffuse throughout the aqueous solution. All battery separators are designed to allow the free flow of ions with their nanometer particle size, which are magnitudes smaller than the typical pore size of a microporous separator.

Assuming the lead becomes soluble upon recharge, the electrolyte will become acidic and the ions will immediately precipitate even in the pores of the separator. If sufficient ions are allowed in solution or if this process is repeated numerous times, soft or hydration shorts will form through the separator. These hydration shorts can be very difficult to see with the human eye unless they become large enough that sufficient current is flowing through the established path and they oxidize a hole in the separator. The problem of hydration shorts has largely been overcome with the addition of sodium sulfate, which is the battery electrolyte that takes advantage of the common ion effect and hinders the lead from going into solution [44].

4.6.3 Extreme Oxidation

In a battery there are situations where extreme oxidation of the separator can occur. By design, battery manufacturers add phosphoric acid to the sulfuric acid to improve the cycle-ability and this is often seen in gel batteries [45]. However, the addition of phosphoric acid creates an extreme oxidation of certain separators such that they show signs of deterioration in a fraction of the time in which this is normally expected to occur. This can become the failure mode of the battery. With the addition of the phosphoric acid, normal PE separators will be oxidized very quickly but cross-linked separators such as Darak will not show any signs of oxidation.

While phosphoric acid is added purposely to the battery, there are other elements that may enter the battery inadvertently either with the lead or via the acid. For instance, if acid comes in contact with normal carbon steel via either storage vessels, piping, pumps, or control valves, chromium will leach into the acid. Chromium and manganese can act as strong oxidizing agents, destroying standard PE separators in a matter of months, assuming part per million levels are present in the electrolyte as shown in Figure 4.14. In various parts of the world, dry charge batteries are produced and shipped to local distributors who add acid at the point of purchase and not under the immediate control of the battery producer.

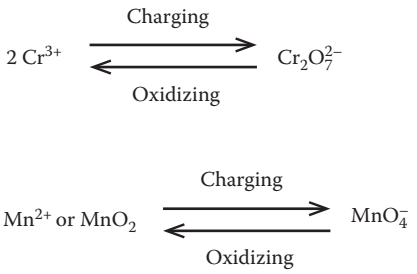

FIGURE 4.14 Oxidizing reactions of impurities.

Battery manufacturers have found that older style cellulosic separators are reasonably resistant to attack by chromium or manganese, but they eliminate the ability to automate the assembly process or pocket the plates to prevent side and bottom shorts. In these cases, battery manufacturers are left with a compromise in battery design. Recent advances have been made in improving the oxidation resistance of the PE separator by a factor of 5 when in the presence of strong oxidizers. This newly formulated PE separator is referred to as Daramic Multi-Sep® [40].

4.7 TECHNICAL CHALLENGES, MITIGATION STRATEGIES, AND PERSPECTIVES

4.7.1 High-Power Starter Batteries

In high-power starter batteries, all field studies suggest that the separator is not a failure mode even as the back-web thicknesses have decreased from 250 to 150 μm on average [46]. In this highly competitive marketplace, one can only imagine that there will be ongoing pressure to reduce the cost of the component while maintaining appropriate functionality. One method for reducing cost is to further reduce the mass of the separator, and this can be done with modified rib designs and thinner back-webs.

When mass is removed, the amount of acid between the plates is increased. This is generally seen as a neutral to positive action. The electrical resistance of the separator will also decrease as the mass is reduced, which can improve performance. However, with less mass, the puncture, oxidation, and bending resistances are all likely to suffer.

Depending on the methods of assembly, a certain minimum level of puncture resistance is required in the separator; otherwise, the electronic shorts are likely to decrease. To improve puncture resistance, the polymer concentration can be increased at the expense of silica. Also, work will continue to optimize the ribbing designs to prevent the potential of plate snagging, especially when performing side alignment of the elements. Increasing the polymer content will also serve to increase the oxidation resistance of the separator.

With existing equipment, it is assumed that a certain amount of bending resistance is required to process material on high-speed envelopers. If the material becomes too flimsy, the envelopes will be distorted and they will not be functional.

Other industries have gone through exercises to minimize the mass while still delivering the intended mechanical properties. Mechanical properties can be improved by alloying the polymer with various additives and here we see a whole new field being explored with nanoparticles. Second, the inherent formation of material at the molecular level can dictate the ultimate yield of the mechanical properties. With regard to polymers, this is often done by understanding and exploiting the crystallinity of the polymer in the formed matrix to achieve optimized properties. Finally, the bending stiffness can be substantially modified through the shape of the final article. To that end, the use of cross ribs on either the negative or positive side of the separator are the first step in that direction [29].

4.7.2 Deep-Cycle Batteries

In deep-cycle batteries, two general trends have been observed. First, AGM batteries have found growth opportunities because they demonstrate low or no water loss, have the ability to prevent acid stratification, positively support the positive active material, and prevent shedding. In these same applications, a high resistance to heat, the ability to prevent soft shorts, and lower costs are normally associated with flooded battery designs and the separators utilized. Obviously, the best designed battery would combine all of the aforementioned attributes and the separator appears to be one of the primary paths to realize these goals. As with all design modifications, desired properties need to be prioritized for each individual application because trade-offs are likely between attribute performances and component costs. At the same time, other avenues will be pursued to modify the lead-acid chemistry or other electrochemical systems.

4.8 SUMMARY

In basic terms, the separator plays a passive role by insulating the opposing electrodes from electronic conductance while allowing ionic flow. However, modifications to the separator have often opened the door for improvements in battery design or performance. The PE separator that makes use of enveloping eliminated the need for mud rooms, which provided better utilization of a given volume and allowed for tighter spacing of electrodes and higher power output while improving manufacturing efficiencies. The advances of the VRLA battery with the recombination cycle were primarily dependent on the AGM separator. Rubber separators or those where rubber is added are critical for the functionality of deep-discharge batteries where substantial amounts of antimony (5% to 7%) are alloyed with the lead in the grid construction. Without such unique properties derived from the separators, batteries would not fully serve the needs of the market as they do today.

Going forward, we can only imagine that separators will also play a role in resolving acid stratification, reducing water loss to extend battery life, and possibly improving charge acceptance. With the benefits of this highly engineered product that we have reviewed, it is even more surprising to consider that the cost of the separator is approximately 3% to 5% of the overall cost of the battery. Obviously, the major costs of the battery are lead and energy.

REFERENCES

1. R. G. Robinson, and R. L. Walker, *Batteries Research and Development in Non-Mechanical Electrical Power Sources*, D. H. Collins, Ed., Pergamon, Oxford, 1963, 15–41.
2. J. Q. Selsor, "Battery Separators," *The Battery Man* (1985).
3. D. Larson, and C. Kehr, U.S. Patent 3,351,495 (1967).
4. D. H. McClelland, and J. L. Dewitt, U.S. Patent 3,257,237 (1975).
5. O. Jache, U.S. Patent 3,172,782 (1965).
6. L. Pisani, "Simple Expression for Tortuosity of Porous Media," *Transp. Med.*, 88 (2011), 193–203.
7. Palico Instrument Laboratory, 6189 Fieldstone Ct. Stacy, MN 55079.
8. J. K. Whear, "Lead Acid Batteries in Heavy Duty Cycling Applications," presented at 14th Asian Battery Conference, Hyderabad, India, 2011.
9. A. D. Butherus, W. S. Lindenberger, and F. J. Vaccaro, *Bell System Tech. J.*, 49, 7 (1970), 1377–1392.
10. J. R. Pierson, C. E. Weinlein, and C. E. Wright, in *Power Sources*, Vol. 5, D. H. Collings, Ed., Academic Press, London, 1975, 97.
11. R. D. Prengaman, *J. Power Sources*, 144 (2005), 426–437.
12. H. K. Kiehne, "Battery Technology Handbook, Akkumulatoren; Elektrolyt und Nachfüllwasser," DIN 43 530 Teil 1 u.2 u.3, Part 2, Elektrolyt für Blei-Akkumulatoren, p. 227.
13. BCI Battery Technical Manual, Section 03B (March 2011).
14. Japanese Industrial Standards (JIS), C 2313, Revision 4 (July 1995).
15. J. K. Whear, "Separator for Processing Expanded Metal Grids," presented at 114th Annual Convention of Battery Council International, Orlando, FL, April 2002.
16. D. Hercamp, and T. Key, U.S. Patent 6,001,503 (1997).
17. C. Boehle, and E. Nann, U.S. Patent 4,788,113 (1986).
18. L. Lemorini, and G. Fossati, EP Patent 0 484 295 (1991).
19. D. Weerts, and G. Dobbie, U.S. Patent Application 09/293,046 (1999).
20. G. C. Zguris, and F. C. Harmon, Jr., WO Patent 1998000875 A1 (1996).
21. K. Ihmels, and W. Boehnstedt, "Valve-Regulated Lead Acid Batteries, Chap. 7," in *Separator Materials for Valve-Regulated Lead-Acid Batteries*, Amsterdam, 2004.
22. G. C. Zguris, *The Battery Man*, 34(9) (1992), 42–48.
23. M. J. Zientek, and R. J. Bender, "Battery Conference on Applications and Advances Characterization of Microglass Laid on Non-wovens Used as Battery Separators," *11th Long Beach Battery Conference*, 1996, 273.
24. I. M. Hutten, *Handbook of Nonwoven Filter Media*, Elsevier, New York, 2007.
25. E. Decker, U.S. Patent 3,475,355A (1965).
26. S. L. Paik, and G. Terzaghi, "Re-Inventing Hard Rubber Separators," Batteries International, England, 1993.
27. J. K. Whear, "Separator Profile Selection for Optimal Battery Performance," *J. Power Sources*, 177 (2008), 226–230.
28. W. Bohnstedt, U.S. Patent 5,776,630 (1994).
29. E. H. Miller, and J. K. Whear, U.S. Patent Application 2012/904371 (2012).
30. J. Young, F. E. Alexander, and D. E. Weerts, U.S. Patent 6,132,899 (1997).
31. V. Toniazzo, *J. Power Sources*, 158(2) (2006), 1124–1132.
32. E. H. Miller, J. K. Chambers, and J. R. Timmons, U.S. Patent Application 2012/066233 (2012).
33. K. McGregor, H. Ozgun, A. J. Urban, and G. C. Zguris, *J. Power Sources*, 111 (2002), 288–203.
34. P. E. Johnson, U.S. Patent 4,407,063 (1981).

35. W. Boehnstedt, C. Radel, and F. Scholten, *J. Power Sources*, 19 (1987), 301.
36. W. Boehnstedt, and C. Radel, European Patent 0 507 0909 (1991).
37. J. Navarrete, J. Chapman, C. Parikh, and R. Toomey, U.S. Patent 6,485,867 (2000).
38. S. L. Paik, R. A. Wimberly, and M. E. Gilchrist, U.S. Patent 6,242,127 (1999).
39. T. J. Clough, U.S. Patent 6,818,355 (2002).
40. J. K. Whear, "The Uniqueness of the Asian Market and the Resultant Novel Separators," presented at 15th Asian Battery Conference, Singapore, 2013.
41. R. W. Pekala, U.S. Patent 7,211,322 (2006).
42. R. Kiessling, "Lead Acid Battery Formation Techniques," Digatron Firing Circuits, 1992.
43. D. N. Craig, and G. W. Vinal, *J. Res. Natl. Bur. Stand.*, 22 (1939), 55–70.
44. G. W. Mao, and A. Sabation, U.S. Patent 3,948,680 (1974).
45. E. Miessner, *J. Power Sources*, 67 (1997), 135–160.
46. Technical Subcommittee, "Failure Modes of Batteries Removed from Service," Battery Council International, Austin, TX, 2010.

5 Electrolytes of Lead-Acid Batteries

Hongyu Chen

CONTENTS

5.1 INTRODUCTION

In most batteries, the electrolyte is an ionic conductive liquid located between the positive and negative electrodes. Its primary function is to provide a path for charge to flow from one electrode to another through ion movement, and thus to maintain charge balance when the oxidation–reduction reactions take place. In a lead-acid battery, the ion such as proton in electrolyte (mainly the H_2SO_4 aqueous solution) also participates in both the discharge and recharge reactions. In other words, the sulfuric

acid electrolyte is also considered an active material. In general, this H_2SO_4 electrolyte solution can have a strong effect on the energy output of lead-acid batteries.

Lead-acid batteries have two kinds of electrolytes. One is the normal aqueous H_2SO_4 solution, and the other is the gel or colloidal solution containing H_2SO_4.

5.1.1 Sulfuric Acid Solution

The sulfuric acid solution used in lead-acid batteries is a kind of conductive electrolyte. This electrolyte not only serves as the ion conductor, but is also widely used in lead-acid battery processes such as mixing the cream (wet paste), leaching the grid, and formatting the grid. The purity, density, and quantity of the sulfuric acid solution can strongly affect the processes of mixing the cream and formation as well as the performance of the battery.

In normal use, concentrated sulfuric acid refers to acids with a concentration higher than 70%. The sulfuric acid used in lead-acid batteries should meet the requirements listed in Table 5.1 [1,2].

When a sulfuric acid does not meet the purity requirements listed in Table 5.1, the impurities could cause high self-discharge, thus affecting the cycle life of the lead-acid battery. Concentrated sulfuric acid has a well-known property of strong oxidability. When it meets some metals, such as iron, copper, zinc, lead, mercury, and molybdenum, it reacts with them, particularly at high temperatures (200°C to 300°C), mainly producing metal ions, sulfate, sulfur dioxide, sulfur, hydrogen sulfide, and water. The strong oxidability of concentrated sulfuric acid comes from the hexavalent sulfur in the H_2SO_4 molecule, which is the highest valence state of sulfur.

The sulfate ion produced by sulfuric acid disassociation $\left(H_2SO_4 \leftrightarrow 2H^+ + SO_4^{2-}\right)$ plays a necessary role in the charge–discharge processes of lead-acid batteries.

TABLE 5.1
Requirements of Sulfuric Acid Used in Lead-Acid Batteries

Index	First Grade	Second Grade
Sulfuric acid content (%)	>92	92
Nonvolatile matter (%)	<0.03	0.05
Mn content (%)	<0.00005	0.0001
Fe content (%)	<0.005	0.012
As content (%)	<0.00005	0.0001
Cl content (%)	<0.0005	0.001
N_2O_3 content (%)	<0.00005	0.0001
$KMnO_4$ reducing substances (mL)	<4.5	<8

Source: H. Bode: *Lead-Acid Batteries*. R. J. Brodd and K. Kordesch, Eds. p. 42. 1997. Copyright Wiley-VCH Verlag GmbH & Co. KGaA. Reproduced with permission; M. Barak, *Electrochemical Power Sources*, Peter Peregrinus, England, 159, 1980.

During charge, the insoluble lead sulfate coated on the negative electrode will be reduced to Pb and soluble SO_4^{2-}, which enters the electrolyte solution, and at the same time, the insoluble lead sulfate coated on the positive electrode will be oxidized to PbO_2 and SO_4^{2-}, which also enters into solution. The opposite processes can happen during the discharge to produce lead sulfate at both the negative and positive electrodes. The charge–discharge reactions can be expressed as

$$Pb + H_2SO_4 \leftrightarrow PbSO_4 + 2e^- + 2H^+ \text{ (negative electrode)} \tag{5.1}$$

$$PbO_2 + 2H^+ + 2e^- + H_2SO_4 \leftrightarrow PbSO_4 + 2H_2O \text{ (positive electrode)} \tag{5.2}$$

In Reactions 5.1 and 5.2, the forward reactions are the discharge process, and the backward ones are the charge process, respectively. The overall lead-acid battery reactions can be written as

$$PbO_2 + Pb + 2H_2SO_4 \leftrightarrow 2PbSO_4 + 2H_2O \tag{5.3}$$

From these reactions, it can be seen that the insolubility property of $PbSO_4$ is very important, because it makes $PbSO_4$ self-sticking on the electrode surface for the battery reactions.

In a sulfuric acid solution, lead sulfate can also be formed by the direct reaction between PbO and H_2SO_4:

$$PbO + H_2SO_4 \leftrightarrow PbSO_4 + H_2O \tag{5.4}$$

This reaction can happen during the electrode curing process.

In a sulfuric acid solution, the reaction between Pb and protons can also occur due to the difference between the thermodynamic electrode potentials of H^+/H_2 and $Pb/PbSO_4$ couples:

$$Pb + H_2SO_4 \leftrightarrow PbSO_4 + H_2 \tag{5.5}$$

Reaction 5.5 is the self-discharge reaction at the negative electrode, causing a loss of capacity in a lead-acid battery. This reaction is normally slow, but it will occur quickly if impurities are present or the battery temperature is high. Another self-discharge reaction also can happen on the positive electrode in a sulfuric acid solution due to the difference between the thermodynamic electrode potentials of $PbO_2/PbSO_4$ and O_2/H_2O couples:

$$PbO_2 + H_2SO_4 \leftrightarrow PbSO_4 + H_2O + \frac{1}{2}O_2 \tag{5.6}$$

This reaction can also cause a capacity loss due to the consumption of active PbO_2. Reaction 5.6 is also slow.

5.1.1.1 Density of Sulfuric Acid

The mass of per unit volume of a substance is called the density of the substance. Its symbol is ρ, and the unit is kg/m^3 or g/cm^3. When talking about density, temperature must be specified because the volume of the substance is changed with changing temperature due to thermal expansion and contraction. For example, the density of sulfuric acid is quite different at different temperatures. The densities of 38% sulfuric acid are 1.293, 1.286, and 1.278 when the temperatures are 10°C, 20°C, and 30°C, respectively. In this sense, when we prepare a sulfuric acid solution with a desired density, temperature should be controlled carefully. With respect to this, Table 5.2 should be very useful.

Actually, the corresponding values for the densities of a sulfuric acid solution at different temperatures can be roughly calculated. In the density range between 1.200 and 1.290 g/cm^3, the density's temperature coefficient is about 0.0007 g/cm^3 T^{-1}, meaning that if the temperature of the sulfuric acid solution is increased or decreased by 1°C, the density will be increased or decreased 0.0007 g/cm^3. This coefficient will be 0.0005 g/cm^3 T^{-1} in the density range of 1.100 to 1.200 g/cm^3, and 0.0003 g/cm^3 T^{-1} in the density range of 1.040 to 1.050 g/cm^3.

5.1.1.2 Resistivity of Sulfuric Acid

The resistivity of the sulfuric acid solution changes with changing density and/or temperature. Generally, the resistivity is the smallest when the density values are in the range of 1.100 to 1.300 g/cm^3, which is the appropriate density range for a lead-acid battery. In practice, a narrow density range of 1.280 to 1.300 g/cm^3 is commonly used, in which the lowest resistivity is at 1.220 g/cm^3 T^{-1}.

Normally, the resistivity can be reduced when increasing solution temperature. The quantitative relationship can be expressed as [3]

$$\rho_t = \rho_o(1 - \beta(t - 18))$$

where ρ_o is the resistivity of sulfuric acid solution at 18°C, β is the temperature coefficient, t is the temperature, and ρ_t is the resistivity of sulfuric acid solution at different temperatures (Table 5.3) [4].

5.1.1.3 Dilution Heat of Sulfuric Acid

In preparing sulfuric acid solution, mixing concentrated sulfuric acid with water can generate considerable heat, and this heat is called *dilution heat*, as listed in Table 5.4 [5]. The overall mixing process during the mixing of concentrated sulfuric acid and water can be expressed as two processes, ionization and hydration:

$$\begin{aligned} &H_2SO_4 \rightarrow H^+ + HSO_4^- \\ &\text{and } HSO_4^- \rightarrow H^+ + SO_4^{2-} \end{aligned} \quad \text{(ionization)} \tag{5.7}$$

$$\begin{aligned} &H^+ + H_2O \rightarrow H_3O^+ \\ &HSO_4^- + nH_2O \rightarrow HSO_4^- \cdot nH_2O \\ &\text{and } SO_4^{2-} + mH_2O \rightarrow SO_4^{2-} \cdot mH_2O \end{aligned} \quad \text{(hydration)} \tag{5.8}$$

TABLE 5.2
Different Densities of Sulfuric Acid with Different Temperatures and Concentrations

	Temperature (°C)										
Concentration (%)	**0**	**10**	**15**	**20**	**25**	**30**	**40**	**50**	**60**	**80**	**100**
1	1.0074	1.0068	1.0060	1.0051	1.0038	1.0022	0.9986	0.9944	0.9898	0.9779	0.9645
2	1.0147	1.0138	1.0129	1.0118	1.0104	1.0087	1.0050	1.0006	0.9956	0.9839	0.9705
3	1.0219	1.0206	1.0197	1.0184	1.0169	1.0152	1.0113	1.0067	1.0017	0.9900	0.9766
4	1.0291	1.0275	1.0264	1.0250	1.0234	1.0216	1.0176	1.0129	1.0078	0.9961	0.9827
5	1.0364	1.0344	1.0332	1.0317	1.0300	1.0281	1.0240	1.0192	1.0140	1.0022	0.9888
6	1.0437	1.0414	1.0400	1.0385	1.0367	1.0347	1.0305	1.0256	1.0203	1.0084	0.9950
7	1.0511	1.0485	1.0469	1.0453	1.0434	1.0414	1.0371	1.0321	1.0266	1.0146	1.0013
8	1.0585	1.0556	1.0539	1.0522	1.0502	1.0481	1.0437	1.0386	1.0330	1.0209	1.0073
9	1.0660	1.0628	1.0610	1.0591	1.0571	1.0549	1.0503	1.0451	1.0395	1.0273	1.0140
10	1.0735	1.0700	1.0681	1.0661	1.0640	1.0617	1.0570	1.0517	1.0460	1.0338	1.0204
11	1.0810	1.0773	1.0753	1.0731	1.0710	1.0686	1.0637	1.0584	1.0526	1.0403	1.0269
12	1.0886	1.0846	1.0825	1.0802	1.0780	1.0756	1.0705	1.0651	1.0593	1.0469	1.0335
13	1.0962	1.0920	1.0898	1.0874	1.0851	1.0826	1.0774	1.0719	1.0661	1.0536	1.0402
14	1.1039	1.0994	1.0971	1.0947	1.0922	1.0897	1.0844	1.0788	1.0729	1.0603	1.0469
15	1.1116	1.1069	1.1045	1.1020	1.0994	1.0968	1.0914	1.0857	1.0798	1.0671	1.0537
16	1.1104	1.1145	1.1120	1.1094	1.1067	1.1040	1.0985	1.0927	1.0868	1.0740	1.0605
17	1.1272	1.1221	1.1195	1.1168	1.1141	1.1113	1.1057	1.0998	1.0938	1.0809	1.0674
18	1.1351	1.1298	1.1271	1.1243	1.1215	1.1187	1.1129	1.1070	1.1009	1.0879	1.0744
19	1.1430	1.1375	1.1347	1.1318	1.1290	1.1261	1.1202	1.1142	1.1081	1.0950	1.0814
20	1.1510	1.1453	1.1424	1.1394	1.1365	1.1335	1.1275	1.1215	1.1153	1.1021	1.0885
21	1.1590	1.1531	1.1501	1.1471	1.1441	1.1410	1.1349	1.1288	1.1226	1.1093	1.0957
22	1.1670	1.1609	1.1579	1.1548	1.1517	1.1486	1.1424	1.1362	1.1299	1.1166	1.1029

(*Continued*)

TABLE 5.2 (CONTINUED)
Different Densities of Sulfuric Acid with Different Temperatures and Concentrations

	Temperature (°C)										
Concentration (%)	**0**	**10**	**15**	**20**	**25**	**30**	**40**	**50**	**60**	**80**	**100**
23	1.1751	1.1688	1.1657	1.1626	1.1594	1.1563	1.1500	1.1437	1.1373	1.1239	1.1102
24	1.1832	1.1768	1.1736	1.1704	1.1672	1.1640	1.1576	1.1512	1.1448	1.1313	1.1176
25	1.1914	1.1848	1.1816	1.1783	1.1750	1.1718	1.1653	1.1588	1.1523	1.1388	1.1250
26	1.1996	1.1929	1.1896	1.1862	1.1829	1.1796	1.1730	1.1665	1.1599	1.1463	1.1325
27	1.2078	1.2010	1.1976	1.1942	1.1909	1.1875	1.1808	1.1742	1.1676	1.1539	1.1400
28	1.2160	1.2091	1.2057	1.2023	1.1989	1.1955	1.1887	1.1820	1.1753	1.1616	1.1476
29	1.2243	1.2173	1.2138	1.2104	1.2069	1.2035	1.1966	1.1898	1.1831	1.1693	1.1553
30	1.2326	1.2255	1.2220	1.2185	1.2150	1.2115	1.2046	1.1977	1.1909	1.1771	1.1630
31	1.2409	1.2338	1.2302	1.2267	1.2232	1.2196	1.2126	1.2057	1.1988	1.1849	1.1708
32	1.2493	1.2421	1.2385	1.2349	1.2314	1.2278	1.2207	1.2137	1.2068	1.1928	1.1787
33	1.2577	1.2504	1.2468	1.2432	1.2396	1.2360	1.2289	1.2218	1.2148	1.2008	1.1866
34	1.2661	1.2588	1.2552	1.2515	1.2479	1.2443	1.2371	1.2300	1.2229	1.2088	1.1946
35	1.2746	1.2672	1.2636	1.2599	1.2563	1.2526	1.2454	1.2383	1.2311	1.2169	1.2027
36	1.2831	1.2757	1.2720	1.2684	1.2647	1.2610	1.2538	1.2466	1.2394	1.2251	1.2109
37	1.2917	1.2843	1.2805	1.2769	1.2732	1.2695	1.2622	1.2550	1.2477	1.2334	1.2192
38	1.3004	1.2929	1.2891	1.2855	1.2818	1.2780	1.2707	1.2635	1.2561	1.2418	1.2276
39	1.3091	1.3016	1.2978	1.2941	1.2904	1.2866	1.2793	1.2720	1.2646	1.2503	1.2361
40	1.3179	1.3103	1.3065	1.3028	1.2991	1.2953	1.2880	1.2806	1.2732	1.2589	1.2446
41	1.3263	1.3191	1.3153	1.3116	1.3079	1.3041	1.2967	1.2893	1.2819	1.2679	1.2532
42	1.3357	1.3280	1.3242	1.3205	1.3167	1.3129	1.3055	1.2981	1.2907	1.2762	1.2619
43	1.3447	1.3370	1.3332	1.3294	1.3256	1.3218	1.3144	1.3070	1.2996	1.2850	1.2707
44	1.3538	1.3401	1.3423	1.3384	1.3346	1.3308	1.3234	1.3160	1.3086	1.2939	1.2796

(*Continued*)

TABLE 5.2 (CONTINUED)
Different Densities of Sulfuric Acid with Different Temperatures and Concentrations

	Temperature (°C)										
Concentration (%)	**0**	**10**	**15**	**20**	**25**	**30**	**40**	**50**	**60**	**80**	**100**
45	1.3630	1.3553	1.3515	1.3476	1.3437	1.3399	1.3325	1.3251	1.3177	1.3029	1.2886
46	1.3724	1.3646	1.3608	1.3569	1.3530	1.3492	1.3417	1.3343	1.3269	1.3120	1.2976
47	1.2819	1.3740	1.3702	1.3663	1.3624	1.3586	1.3510	1.3435	1.3362	1.3212	1.3067
48	1.3915	1.3835	1.3797	1.3758	1.3719	1.3680	1.3604	1.3528	1.3455	1.3305	1.3159
49	1.4012	1.3931	1.3893	1.3854	1.3814	1.3775	1.3699	1.3623	1.3549	1.3399	1.3253
50	1.4110	1.4029	1.3990	1.3951	1.3911	1.3872	1.3795	1.3719	1.3644	1.3494	1.3343
51	1.4209	1.4128	1.4088	1.4049	1.4009	1.3970	1.3893	1.3816	1.3740	1.3590	1.3444
52	1.4310	1.4228	1.4188	1.4148	1.4109	1.4069	1.3991	1.3914	1.3837	1.3687	1.3540
53	1.4412	1.4329	1.4289	1.4248	1.4209	1.4169	1.4091	1.4013	1.3963	1.3785	1.3637
54	1.4515	1.4431	1.4391	1.4350	1.4310	1.4270	1.4191	1.4113	1.4036	1.3884	1.3735
55	1.4619	1.4535	1.4494	1.4453	1.4412	1.4372	1.4293	1.4214	1.4137	1.3984	1.3834
56	1.4724	1.4640	1.4598	1.4557	1.4516	1.4475	1.4396	1.4317	1.4239	1.4085	1.3934
57	1.4830	1.4746	1.4703	1.4662	1.4621	1.4580	1.4500	1.4420	1.4342	1.4187	1.4035
58	1.4937	1.4852	1.4809	1.4768	1.4726	1.4685	1.4604	1.4524	1.4446	1.4290	1.4137
59	1.5045	1.4959	1.4916	1.4875	1.4832	1.4791	1.4709	1.4629	1.4551	1.4393	1.4240
60	1.5154	1.5067	1.0524	1.4983	1.4940	1.4898	1.4816	1.4735	1.4656	1.4497	1.4344
61	1.5264	1.5177	1.5133	1.5091	1.5048	1.5006	1.4923	1.4842	1.4762	1.4602	1.4449
62	1.5487	1.5398	1.5354	1.5310	1.5267	1.5225	1.5140	1.5058	1.4977	1.4815	1.4660
63	1.5487	1.5398	1.5354	1.5310	1.5267	1.5225	1.5140	1.5058	1.4977	1.4815	1.4660
64	1.5600	1.5510	1.5465	1.5421	1.5378	1.5335	1.5250	1.5167	1.5086	1.4923	1.4766
65	1.5714	1.5623	1.5578	1.5533	1.5490	1.5446	1.5361	1.5277	1.5195	1.5031	1.4873
66	1.5828	1.5736	1.5691	1.5646	1.5602	1.5558	1.5472	1.5388	1.5305	1.5140	1.4984

(*Continued*)

TABLE 5.2 (CONTINUED)
Different Densities of Sulfuric Acid with Different Temperatures and Concentrations

	Temperature (°C)										
Concentration (%)	**0**	**10**	**15**	**20**	**25**	**30**	**40**	**50**	**60**	**80**	**100**
67	1.5943	1.5850	1.5805	1.5760	1.5715	1.5671	1.5584	1.5499	1.5416	1.5249	1.5089
68	1.6059	1.5965	1.5920	1.5874	1.5829	1.5785	1.5697	1.5611	1.5528	1.5359	1.5198
69	1.6176	1.6081	1.6035	1.5989	1.5944	1.5899	1.5811	1.5724	1.5640	1.5470	1.5307
70	1.6293	1.3198	1.6151	1.6105	1.6059	1.6014	1.5925	1.5838	1.5753	1.5582	1.5417
71	1.6411	1.6315	1.6268	1.6221	1.6175	1.6130	1.6040	1.5952	1.5867	1.5694	1.5527
72	1.6529	1.6433	1.6385	1.6338	1.6292	1.6246	1.6155	1.6067	1.5981	1.5806	1.5637
73	1.6648	1.6551	1.6503	1.6456	1.6409	1.6363	1.6271	1.6182	1.6095	1.5919	1.5747
74	1.6768	1.6670	1.6620	1.6574	1.6526	1.6480	1.6387	1.6297	1.6209	1.6031	1.5857
75	1.6888	1.6789	1.6740	1.6692	1.6644	1.6597	1.6503	1.6412	1.6322	1.6142	1.5966
76	1.7008	1.6808	1.6858	1.6810	1.6761	1.6713	1.6619	1.6526	1.6435	4.6252	1.6074
77	1.7128	1.7026	1.6976	1.6927	1.6878	1.6829	1.6734	1.6640	1.6547	1.6361	1.6181
78	1.7247	1.7144	1.7093	1.7043	1.6994	1.6944	1.6847	1.6751	1.6657	1.6469	1.6286
79	1.7365	1.7261	1.7209	1.7158	1.7108	1.7058	1.6959	1.6862	1.6766	1.6575	1.6390
80	1.7482	1.7376	1.7323	1.7272	1.7221	1.7170	1.7069	1.6971	1.6873	1.6680	1.6493
81	1.7597	1.7489	1.7435	1.7383	1.7331	1.7279	1.7177	1.7077	1.6978	1.6782	1.6594
82	1.7709	1.7599	1.7544	1.7491	1.7437	1.7385	1.7281	1.7180	1.7080	1.6882	1.6692
83	1.7815	1.7704	1.7649	1.7594	1.7540	1.7487	1.7382	1.7279	1.7179	1.6979	1.6787
84	1.7916	1.7804	1.7748	1.7693	1.7639	1.7585	1.7479	1.7375	1.7274	1.7072	1.6878

(*Continued*)

TABLE 5.2 (CONTINUED)
Different Densities of Sulfuric Acid with Different Temperatures and Concentrations

	Temperature (°C)										
Concentration (%)	**0**	**10**	**15**	**20**	**25**	**30**	**40**	**50**	**60**	**80**	**100**
85	1.8009	1.7897	1.7841	1.7786	1.7732	1.7678	1.7571	1.7466	1.7364	1.7161	1.6966
86	1.8095	1.7983	1.7927	1.7872	1.7818	1.7763	1.7657	1.7552	1.7449	1.7245	1.7050
87	1.8173	1.8061	1.8006	1.7951	1.7897	1.7842	1.7735	1.7632	1.7529	1.7324	1.7129
88	1.8243	1.8132	1.8077	1.8022	1.7968	1.7914	1.7809	1.7705	1.7602	1.7397	1.7202
89	1.8306	1.8195	1.8141	1.8087	1.8033	1.7979	1.7874	1.7770	1.7669	1.7464	1.7269
90	1.8361	1.8252	1.8198	1.8144	1.8091	1.8038	1.7933	1.7829	1.7729	1.7525	1.7331
91	1.8410	1.8302	1.8248	1.8195	1.8142	1.8090	1.7986	1.7883	1.7783	1.7581	1.7388
92	1.8453	1.8346	1.8293	1.8240	1.8188	1.8136	1.8033	1.7932	1.7832	1.7633	1.7439
93	1.8490	1.8384	1.8331	1.8279	1.8227	1.8176	1.8074	1.7974	1.7878	1.7681	1.7485
94	1.8520	1.8415	1.8363	1.8312	1.8260	1.8210	1.8109	1.8011	1.7914		
95	1.8544	1.8439	1.8388	1.8337	1.8286	1.8230	1.8137	1.8040	1.7944		
96	1.8560	1.8457	1.8406	1.8355	1.8305	1.8255	1.8157	1.8060	1.7965		
97	1.8569	1.8466	1.8414	1.8364	1.8314	1.8262	1.8166	1.8071	1.7977		
98	1.8567	1.8463	1.8411	1.8361	1.8310	1.8261	1.8163	1.8068	1.7976		
99	1.8551	1.8445	1.8493	1.8342	1.8292	1.8242	1.8145	1.8050	1.7928		
100	1.8517	1.8409	1.8409	1.8305	1.8255	1.8205	1.8107	1.8013	1.7922		

Source: Z. Li, "Manufacturing Technique of Lead-Acid Batteries," *Handbook of Physical Chemistry.*

TABLE 5.3
Resistivity and Temperature Coefficient of Sulfuric Acid

Density (kg/L)	Resistivity (Ω·m)	Temperature Coefficient
1.050	346	1.24
1.100	190	1.36
1.150	150	1.46
1.200	136	1.58
1.250	138	1.68
1.300	140	1.77
1.350	161	1.86
1.400	185	1.94
1.450	218	2.02
1.500	264	2.10
1.550	330	2.30
1.600	424	2.50
1.650	558	2.70
1.700	764	3.00
1.800	996	3.50

Source: Z. Li, "Manufacturing Technique of Lead-Acid Batteries," *Handbook of Physical Chemistry*, 109.

TABLE 5.4
Heat of Dilution of Sulfuric Acid

Moles of Water Mixed with Sulfuric Acid (n)	Pure Sulfuric Acid Content in 100 Solutions	Density at 15°C (kg/L)	Heat of Dilution (kJ)	Thermal Capacity (J/K)
–	96.0	1.842	–	1.3816
1	84.4	1.779	26.71	1.5910
2	73.0	1.651	39.44	1.8000
3	64.4	1.551	46.64	2.0096
5	52.1	1.421	54.89	2.3864
9	37.7	1.288	62.59	2.9726
19	22.3	1.161	68.08	3.4332
49	10.0	1.069	69.84	3.8100
99	5.2	1.035	70.59	3.9775
199	2.6	1.081	71.43	4.0612
399	1.3	1.009	72.47	4.1450
1599	0.3	–	74.48	–

Source: Z. Li, "Manufacturing Technique of Lead-Acid Batteries," *Handbook of Physical Chemistry*, 111.

The hydration step expressed by Reaction 5.8 can release the most mixing heat in the mixing process.

5.1.1.4 Contraction of Sulfuric Acid Solution

The volume of the prepared sulfuric acid solution will be smaller than the total volume of the raw sulfuric acid and the water. This is a result of the contraction of the sulfuric acid solution. Shrinkage amounts are listed in Table 5.5 [6].

5.1.1.5 Freezing Point of Sulfuric Acid

The freezing points of different density sulfuric acid solutions are different even at the same temperature, as shown in Table 5.6 [7].

In a lead-acid battery, when the charge is completed, the density of sulfuric acid electrolyte solution is between 1.2800 and 1.2900 g/cm^3. However, when the

TABLE 5.5
Shrinkage of Sulfuric Acid Solution

Density of Dilute Sulfuric Acid (kg/L)	Shrinkage of Mixed Liquor in 1 Kilogram (L)	Density of Dilute Sulfuric Acid (kg/L)	Shrinkage of Mixed Liquor in 1 Kilogram (L)
1.000	0	1.500	60×10^{-3}
1.100	25×10^{-3}	1.600	62×10^{-3}
1.200	42×10^{-3}	1.700	60×10^{-3}
1.300	51×10^{-3}	1.800	48×10^{-3}
1.400	57×10^{-3}	–	–

Source: Z. Li, "Manufacturing Technique of Lead-Acid Batteries," *Handbook of Physical Chemistry*, 112.

TABLE 5.6
Freezing Points of Sulfuric Acid Solutions

Density (kg/L) (15°C)	Freezing Point (°C)	Density (kg/L) (15°C)	Freezing Point (°C)
1.000	0	1.450	–29
1.050	–3.3	1.500	–29
1.100	–7.7	1.550	–38
1.150	–15	1.600	–
1.200	–27	1.650	–
1.250	–52	1.700	–14
1.300	–70	1.750	+5
1.350	–49	1.800	+6
1.400	–36	1.835	–34

Source: Z. Li, "Manufacturing Technique of Lead-Acid Batteries," *Handbook of Physical Chemistry*, 113.

discharge is completed, the electrolyte's density will become 1.100 to 1.500 g/cm^3. In general, the sulfuric acid electrolyte is not easy to freeze because of the solution's low freezing point.

5.1.1.6 Viscosity of Sulfuric Acid Electrolyte Solution

Viscosity, with a unit of Pa·s, refers to the resistance or internal friction existing in a solution when the solution flows. The nature of the viscosity is the interaction of the molecules in the solution. Table 5.7 lists the viscosity of sulfuric acid solution as a function of temperature and sulfuric acid concentration [8].

In general, the diffusion rate of sulfuric acid in the solution is greatly influenced by the viscosity of the acid.

5.1.1.7 Vapor Pressure of Sulfuric Acid Solution

Concentrated sulfuric acid is a kind of strong drier and it can easily absorb water from the air. The water vapor pressure of sulfuric acid solution as a function of solution density and temperature is listed in Table 5.8 [9].

When the solution is exposed to air, the relative water vapor pressure values of the sulfuric acid solution and air determine whether the solution will absorb water or evaporate water. When the water vapor pressure of sulfuric acid solution is larger than that in air, the solution will evaporate water in the air, and vice versa.

Generally, the water vapor pressure of the sulfuric acid solution and that in the air are different. An open lead-acid battery will lose a lot of water as a result of evaporation. A sealed lead-acid battery, however, will lose only a small amount of water because the density of the sulfuric acid solution is higher and the battery is sealed.

TABLE 5.7
Viscosity of Sulfuric Acid Electrolyte Solution

	Viscosity (×10^{-3} Pa·s)				
Temperature (°C)	**10%**	**20%**	**30%**	**40%**	**50%**
30	0.976	1.225	1.596	2.160	3.070
25	1.091	1.371	1.784	2.410	3.400
20	1.228	1.545	2.006	2.700	3.790
10	1.595	2.010	2.600	3.480	4.360
0	2.160	2.710	3.520	4.700	6.520
–10		3.820	4.950	6.600	9.150
–20			7.490	9.890	13.600
–30			12.200	16.000	21.700
–40				23.800	
–50				58.500	

Source: Z. Li, "Manufacturing Technique of Lead-Acid Batteries," *Handbook of Physical Chemistry*, 114.

TABLE 5.8
Water Vapor Pressure of Sulfuric Acid Solution as a Function of Solution Density and Temperature

Density (kg/L at 15°C)	H_2SO_4 (Content %)	0°C Vapor Pressure (Pa)	15°C Vapor Pressure (Pa)	25°C Vapor Pressure (Pa)	35°C Vapor Pressure (Pa)
1.000	0.0	613.32	1706.24	3172.54	5625.26
1.100	14.3	559.86	1599.86	1599.65	5198.70
1.200	27.2	479.88	1359.66	2492.71	4505.54
1.300	39.1	346.58	99.75	1839.54	3332.50
1.400	50.0	213.28	599.85	1130.05	2052.82
1.500	59.7	106.64	266.60	546.53	973.09
1.600	68.6	26.66	79.78	173.29	346.58
1.700	77.1		26.66	53.32	106.64

Source: Z. Li, "Manufacturing Technique of Lead-Acid Batteries," *Handbook of Physical Chemistry*, 116.

5.1.2 Colloid Solution

In general, the properties of a colloid solution are different from other dispersion systems because the degree of dispersion of colloid is high, and it is a kind of multiphase system [10]. In lead-acid batteries, a sulfuric acid-based colloid solution is one of the important electrolytes with some unique properties.

5.1.2.1 Preparation of Colloid Solution

Two methods are used to prepare the colloid solution: the dispersion method and the condensation method. In the dispersion method, the dispersoid and dispersant are ground repeatedly by a colloid grinder until they meet the required degree of dispersion. The condensation method includes two options. One is the chemical reaction option through hydrolysis or metathesis, and the other is the change solvent option.

5.1.2.2 Preparation and Properties of Silicone Gel

Silicone gel-based electrolyte is probably the most commonly used electrolyte in lead-acid batteries. Silicone gel is prepared using either a reaction between fumed silica dioxide and a base (sodium hydroxide, potassium hydroxide, etc.) or hydrolysis of silica dioxide.

The gel has a continuous 3D-shaped structure and its formation can be divided into two steps. The first step is a reversible reaction through hydrogen bonding; the second step is an irreversible reaction to generate strong Si–O–Si bonding within the silica dioxide particles.

The reversible reaction in gel formation plays an important role in colloid electrolyte-based lead-acid batteries. Like other chemical reactions, the temperature can have a strong effect on gel formation. The formation rate and stability of the gel are also dependent on pH, type of salts, quantity of silica dioxide, size of particles,

and gel time. The pH can affect the surface charge of SiO_2 and also the cell voltage of the lead-acid battery.

Regarding the effect of solution density and type of salt, a high salt concentration will decrease the cell voltage and weaken the repulsion between the silica dioxide particles, thus enhancing the intensity of the colloid. Ion such as sulfate can promote the formation of colloid as a bridge between the silica dioxide particles. For example, sulfate ion can promote SiO_2 to form a colloid when the pH is not so high in a lead-acid battery. This advantage of a common ion effect can be utilized to increase the sulfate ion concentration. If 1.0% to 1.5% sodium is added to the gel solution, the battery could be covered from the state of discharge because of the common ion effect contributed by sodium, making the solubility of $PbSO_4$ larger.

The quantity and the size of SiO_2 have the most important effect on battery performance when a colloid electrolyte is used. The 3D structure of the electrode active layers will become stronger as the quantity of SiO_2 is increased. The size of colloid particles can affect the volume of the pores and the average pore size of the electrode active masses. Therefore, the volume of the pores and the average pore size will be smaller when the quantity of SiO_2 is increased. The effect of SiO_2 quantity on electrolyte structure is summarized in Table 5.9.

In preparing a gel electrolyte for a lead-acid battery, the gel process with 5 M H_2SO_4 colloid was observed as the particles first got together and then as they became siloxane [10]. The gel normally holds a positive charge in low-pH acid solution and the sulfate ion acts as the bridge for the adjacent SiO_2 particles, thus promoting the process of gelling and the formation of siloxane, as shown in Figure 5.1. After that, silica gel is condensed, which is the dispersion and reunifying process of the internal silica particles.

The colloid structure obtained from silica colloid is different from that obtained from vapor silica dioxide, which is a 3D structure linked by a certain aggregation of SiO_2. The aggregation number of SiO_2 depends on the concentration of SiO_2.

In preparing gel electrolyte for a lead-acid battery, different types of SiO_2 can result in different gel electrolytes. There are three different types of SiO_2: water glass, vapor silica dioxide, and colloidal silica sol. SiO_2 water glass has a high impurity content, limiting its use for battery gel preparation.

Colloid prepared from vapor silica dioxide is widely used in lead-acid batteries. Colloid prepared from vapor silica dioxide has the advantages of strong cohesion, high active surface, and superior electrode performance. However, it is relatively

TABLE 5.9
Effect of Silica Content on Colloidal Structure

Number	SiO_2 Content (vol%)	Colloidal Porosity (%)	Pore Volume ($cm^3 \cdot g^{-1}$)
6	52	48	0.4
3	5	95	8.4
2.3	1.3	987	35
3.3	0.83	99.2	54

Source: D. W. G. Lambert et al., *J. Power Sources*, 107, 173–179, 2002.

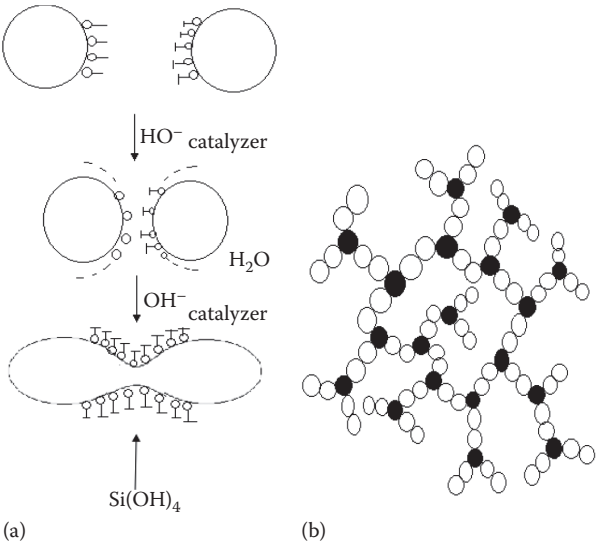

FIGURE 5.1 Scheme of colloid structure: (a) colloid formation process; (b) gel. (From D. W. G. Lambert et al., *J. Power Sources*, 107, 173–179, 2002.)

expensive, its viscosity is high, and its thixotropy is strong so that it is difficult to irrigate it into the battery. Experiment indicates that it is difficult to control its performance and quality without special viscosity regulators (i.e., a stabilizer and catalyst). Furthermore, vapor silica dioxide also has impurities that will affect the lifetime of the battery if this type of colloid is used.

Colloidal silica sol is not commonly used to generate colloid for lead-acid batteries. It does, however, have a lot of advantages when preparing gel electrolytes: simple preparation, storage, and irrigation; absence of the phenomenon of sol; high strength of sol; easily controlled sol times and strength (by adding gels); higher concentration of SiO_2; high purity without environmental impact; easy crafting; and low cost.

5.2 IMPACT OF ELECTROLYTES ON BATTERY PERFORMANCE

The two major types of electrolytes in lead-acid batteries are the running electrolyte, such as a sulfuric acid solution, and the immobile electrolyte, such as a colloidal electrolyte solution. Actually, both of them can participate in the charge and discharge processes through sulfate ions, so they should be treated as a third reacting material in addition to Pb and PbO_2. The electrolyte compositions could be significantly different, depending on the battery's application. In a normal lead-acid battery, the density of the sulfuric acid electrolyte is normally controlled in the range of 1.200 to 1.300 g/cm^3. The electrolyte has two functions in a lead-acid battery. One is to join the electrochemical reactions through the sulfate ion at both the positive and negative electrodes, and the other is to act as the ion conductor between the positive and negative plates. Due to the participation of electrolyte sulfate ion in the electrode reactions, the density of the electrolyte will decrease during discharge because sulfate ions are

deposited onto the electrodes, but the density will be recovered when the process of charge proceeds to release the sulfate ions into the electrolyte from both electrodes.

One important requirement for electrolyte solution is high purity. This is because impurities in the electrolyte can cause undesired side reactions such as hydrogen evolution. Furthermore, the density of the electrolyte solution should be appropriate, because density can have a significant effect on the battery's electrical power, capacity, and cycle life.

5.2.1 Electrolyte Sulfuric Concentration Effect on the Cell Voltage of a Lead-Acid Battery

Equations 5.1, 5.2, and 5.3 express the overall reactions of a lead-acid battery, from which it can be seen that both of the reactions at the positive and negative plates will generate $PbSO_4$ during discharge, leading to potential changes in both the positive and negative plates. Due to the deposition of sulfate ions onto the electrodes, the density of the sulfuric acid solution will be reduced. Based on Equations 5.1, 5.2, and 5.3, the electrolyte sulfuric concentration effect on the Nernst electrode potentials and open circuit cell voltage (or electromotive force) can be expressed as

$$E_{Pb/PbSO_4} = E^{o}_{Pb/PbSO_4} + \frac{RT}{2F}\ln\left(\frac{a_{PbSO_4}a^2_{H^+}}{a_{Pb}a_{H_2SO_4}}\right) \quad \text{(negative electrode)} \tag{5.9}$$

$$E_{PbO_2/PbSO_4} = E^{o}_{PbO_2/PbSO_4} + \frac{RT}{2F}\ln\left(\frac{a_{PbO_2}a^2_{H^+}a_{H_2SO_4}}{a_{PbSO_4}a^2_{H_2O}}\right) \quad \text{(positive electrode)} \tag{5.10}$$

where $E_{Pb/PbSO_4}$ and $E_{PbO_2/PbSO_4}$ are the Nernst electrode potentials for negative and positive electrodes; $E^{o}_{Pb/PbSO_4}$ (= –0.356 V versus the standard hydrogen electrode [SHE]) and $E^{o}_{PbO_2/PbSO_4}$ (= 1.685 V versus SHE) are the Nernst electrode potentials of negative and positive electrodes at standard conditions, respectively; a_{PbSO_4}, a_{H^+}, a_{Pb}, $a_{H_2SO_4}$, a_{PbO_2}, and a_{H_2O} are the activities of $PbSO_4$, H^+, Pb, H_2SO_4, PbO_2, and H_2O, respectively; and R, T, and F are the universal gas constant, temperature, and Faraday's constant, respectively. The theoretical cell voltage (V_{cell}) can be calculated based on Equations 5.9 and 5.10:

$$\begin{aligned} V_{cell} &= E_{PbO_2/PbSO_4} - E_{Pb/PbSO_4} \\ &= E^{o}_{PbO_2/PbSO_4} - E^{o}_{PbO_2/PbSO_4} + \frac{RT}{2F}\ln\left(\frac{a_{Pb}a_{PbO_2}a^2_{H_2SO_4}}{a^2_{PbSO_4}a^2_{H_2O}}\right) \end{aligned} \tag{5.11}$$

Due to a_{PbSO_4}, a_{Pb}, a_{PbO_2}, and a_{H_2O} all being equal to 1, Equation 5.11 can be rewritten as

$$V_{cell} = E^{o}_{PbO_2/PbSO_4} - E^{o}_{PbO_2/PbSO_4} + \frac{RT}{F}\ln\left(a_{H_2SO_4}\right) \tag{5.12}$$

TABLE 5.10
Actual and Calculated Values for a Lead-Acid Battery

Sulfuric Acid Concentration		Electromotive Force	
Molality (mol/kg)	Concentration Percentage (%)	Actual Value (V)	Calculated Value (V)
0.05	0.488	1.762	1.764
0.10	0.970	1.796	1.799
0.20	1.925	1.831	1.831
0.50	4.675	1.881	1.880
1.00	8.933	1.919	1.920
2.00	16.400	1.971	1.974
3.00	22.737	2.014	2.016
4.00	28.179	2.053	2.056
5.00	32.901	2.090	2.091
6.00	37.047	2.124	2.134
7.00	40.707	2.155	2.165

Source: R. C. Weast, *CRC Handbook of Chemistry and Physics*, 58th ed., CRC, Boca Raton, FL, B-254, 1977–1978.

Equation 5.12 indicates that sulfuric acid has a strong effect on the cell voltage of the lead-acid battery. Table 5.10 lists the calculated and measured open cell voltages (or electromotive force) as a function of sulfuric acid concentration [11]. It can be seen that the cell voltage increases with an increasing sulfuric acid concentration, which is exactly the tendency predicted by Equation 5.12.

As predicted by Equations 5.9 and 5.10, when the acid concentration changes, the solution pH is altered. The potential of the positive $PbO_2/PbSO_4$ electrode is affected much more notably than that of the $Pb/PbSO_4$ one; that is, the positive electrode potential is much more sensitive to H_2SO_4 concentration variations than is the negative one.

It is worth pointing out that temperature can also affect the cell voltage of a lead-acid battery. A change in cell voltage with temperature may be obtained by differentiating Equation 5.12, which can be expressed as

$$\frac{\partial V_{\text{cell}}}{\partial T} = \frac{\partial E^{\circ}_{PbO_2/PbSO_4}}{\partial T} - \frac{\partial E^{\circ}_{Pb/PbSO_4}}{\partial T} + \frac{R}{F}\ln\left(a_{H_2SO_4}\right) + \frac{RT}{Fa_{H_2SO_4}}\frac{\partial a_{H_2SO_4}}{\partial T}$$

5.2.2 H_2SO_4 Concentration Effect on Operation of a Lead-Acid Battery

As discussed earlier, sulfuric acid in electrolyte solution is an active material that participates in the cell reaction. Therefore, the sulfuric acid concentration changes during both battery discharge and charge processes. In addition, as predicted by Equation 5.12, the open circuit voltage of a lead-acid cell is a function of electrolyte concentration according to the Nernst equation. Furthermore, the specific resistance of the electrolyte and its freezing point can also depend on the acid concentration.

A detrimental effect of a higher acid concentration on the cycle life of lead-acid batteries has been established. The effects of acid concentration and temperature on the dry-out of VRLA batteries were studied by Bullock et al. [12–14]. Several other studies also tried to explain the deadline in battery cycle life on the basis of linear sweep voltammetry measurements on the planar lead electrode. Currently, lead-acid battery manufacturers still use a high sulfuric acid concentration in batteries for electric vehicle and hybrid electric vehicle applications. Several studies have investigated the kinetics and mechanism of anodic oxidation of Pb to $PbSO_4$ at different electrolyte concentrations, observing that larger lead sulfate crystals were formed at low acid concentrations. A low acid concentration could promote the growth of large $PbSO_4$ crystals that were difficult to be reduced. In addition, linear sweep voltammetry in a wide range of sulfuric acid concentrations proved that the kinetics of lead sulfate reduction were practically independent of acid concentration. A number of studies reported the effects of $PbSO_4$ solubility on cathodic reduction of $PbSO_4$ at different acid concentrations [15,16]. They concluded that the properties of Pb(II) were not responsible for the linear decrease in cycle life at higher acid concentrations. On the contrary, many studies considered the solubility of $PbSO_4$ crystals, which depends on acid concentration, to be the main factor limiting lead sulfate reduction on the negative plate. In addition, electrolyte concentration could also affect the rate of the side reactions, such as hydrogen evolution and self-discharge, that proceed on the lead electrode. All of these findings illustrate the specific and complete effect of H_2SO_4 concentration on negative plate performance.

5.2.3 Relationship between the Quantity of Active Materials and the Capacity of a Lead-Acid Battery

As is well known, a lead-acid battery is a kind of chemical power that can convert chemical energy into electrical energy. Therefore, the specific capacity or energy stored inside the battery is one of the most important performance indicators. In general, the specific capacity is strongly dependent on how much active material is used for the battery. Therefore, the relationship between the quantity of active materials and the electrical capacity should be clear before constructing a lead-acid battery.

In a lead-acid battery, according to Reaction 5.3, the quantity of active materials for PbO_2, Pb, and H_2SO_4 can be calculated to be 4.469, 3.860, and 3.660 g for 1.0-Ah capacity. The total quantity of active materials is 11.98 g/Ah, as seen in Table 5.11. In practice, 1 kg of active materials will give a capacity of 83.472 Ah, which is called theoretical ratio capacity [17].

Actually, not 100% of the active materials can be utilized. To reflect the utilization of the active materials, a parameter η, called the ratio of the theoretical quantity to the actual quantity, is introduced. For example, if the use ratio of positive active material is 55% (η_+), and the use ratio of negative active material is 60% (η_-), the actual quantity of positive active materials is $4.46\ g(PbO_2)/0.55(\eta_+) = 8.1 \times 10^{-3}$ kg/Ah; and the actual quantity of negative active materials is $3.86\ g(Pb)/0.60(\eta_-) = 6.4.1 \times 10^{-3}$ kg/Ah, respectively. If the electrolyte contains 38% sulfuric acid, it can generate a capacity of 116.8 Ah/L, which suggests that 10.68 g of this type of sulfuric acid is needed when the battery generates 1.0 Ah of capacity.

TABLE 5.11
Electrochemical Equivalent of Related Materials in a Lead-Acid Battery

Material	Molar Mass (g/mol)	Gains and Losses of Electrons	Electrochemical Equivalent (g/Ah)	Weight Capacity (Ah/g)
Lead	207.19	4	1.93260	0.51744
		2	3.86520	0.25872
Lead oxide	233.19	2	4.16388	0.24017
Lead dioxide	233.19	4	2.23108	0.44821
		2	4.46216	0.22410
Lead sulfate	303.25	2	5.65723	0.17676
Oxygen atom	15.9993	2	0.29874	3.35038
Hydrogen atom	1.0079	1	0.03760	26.59193
Water	18.0152	2	0.33608	2.97548
		1	0.67216	1.48774
Acid sulfate	98.078	2	1.82964	0.54656
		1	3.65928	0.27328
Oxygen	31.9988	4	0.20907 (dm/Ah)	4.78316 (Ah/dm)
Hydrogen	2.0158	2	0.41813 (dm/Ah)	2.39158 (Ah/dm)

Source: D. Polov, *Lead-Acid Batteries, Technology and Operation*, Hangzhou, China, KLT-13, 2000.

In practice, the quantity of sulfuric acid (d = 1.2900 g/cm^3) should not be lower than 10.2 mL/Ah in a starter battery, which is called the lowest rated ratio quantity of acid. Generally, 11.4 mL/Ah is used in lead-acid batteries and is called the effective quantity of acid. In a fixed battery, the quantities of sulfuric acid (d = 1.210 g/cm^3) in a fixed battery are 26.5 and 32.0 mL/Ah. This is because the utilization is low—just about 39% in a fixed battery.

5.2.4 H-Region and N-Region of Sulfuric Acid Concentration and Their Effects on Performance

Regarding electrolyte in lead-acid batteries, one concept often used in industry is the specific gravity of the battery electrolyte (*sp.gr*). This is the most accurate and direct way to test the state of charge of a battery cell. In general, the higher the *sp.gr* value, the higher the state of charge. During the operation of a lead-acid battery, the best way to monitor the battery's lifetime is to regularly take and record specific gravity readings.

Regarding H_2SO_4 utilization, two *ap.gr* regions can be distinguished as follows:

1. *H_2SO_4 concentration is lower than 1.27 sp.gr.* In the range, the utilization coefficient of H_2SO_4 is higher than both those of negative active material and positive active material; hence, sulfuric acid dictates the limits on battery capacity in this concentration region. This region is normally called the *H-region*.
2. *H_2SO_4 concentration is higher than 1.27 sp.gr.* The utilization coefficient of the negative active material is higher; hence, the negative plate will limit the capacity. This region is called the *N-region*.

The influences of H_2SO_4 concentration on battery capacity in these two concentration regions (H-region and N-region) are different. In the H-region where the sulfuric acid concentrations are lower than 1.270 *sp.gr*, the utilization of negative active mass varies between 40% and 63%, and that of H_2SO_4 is between 68% and 80%. During battery operation, the discharging current is fairly low, and the H_2SO_4 will have sufficient time to diffuse from the bulk electrolyte to the inner parts of the plates, leading to high H_2SO_4 utilization. In the N-region where H_2SO_4 concentrations are higher than 1.27 *sp.gr*, the utilization of H_2SO_4 is from 57% to 68%, and the utilization of the negative active mass is between 63% and 70%. These utilization values are somewhat higher and the negative plates will determine the capacity of the batteries.

The sulfuric acid concentration also has an effect on the cold cranking amps (CCA) of a lead-acid battery. CCA is defined as the number of amperes a lead-acid battery at 0°F (–17.8°C) can deliver for 30 sec and maintain at least 1.2 V per cell (7.2 V for a 12-V battery). In other words, CCA determines how much power you have to start your car on cold winter mornings. Figure 5.2 shows the acid concentration effect on the CCA of a lead-acid battery, in which $V_{30'}$ is the battery cell voltage after 30 sec of discharge at 0°F. Figure 5.2 shows that $V_{30'}$ increases with increasing acid concentration up to 1.240 *sp.gr*. If the electrolyte concentration is higher than 1.240, $V_{30'}$ does not change anymore with further increasing acid concentration. Figure 5.3 indicates that the CCA capacity increases almost linearly with increasing acid concentration with a slope of 0.48 Ah per 0.01 *sp.gr* of H_2SO_4. Normally, batteries with acid concentrations above 1.240 *sp.gr* are required to meet the DIN standard, namely, cell voltage 9.0 V after 30 sec of discharge and cold cranking capacity of 0.2 C_{20}. Under the CCA discharge conditions, the utilizations of all active

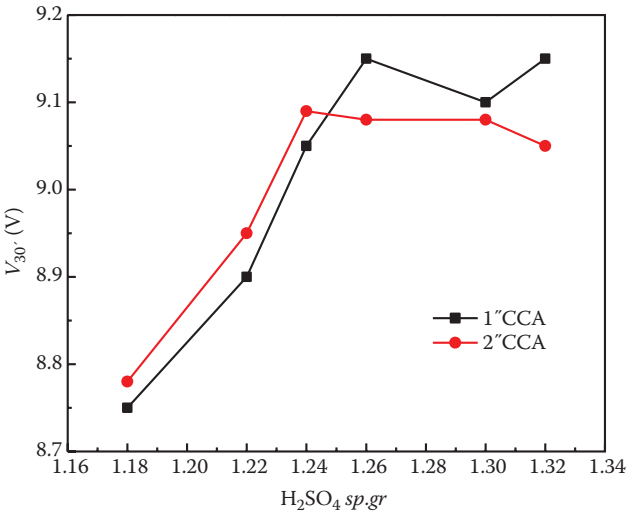

FIGURE 5.2 Relationship between $V_{30'}$ and the concentration of H_2SO_4. (From Z. Li, *Lecture Course on VRLA*, China, 2003.)

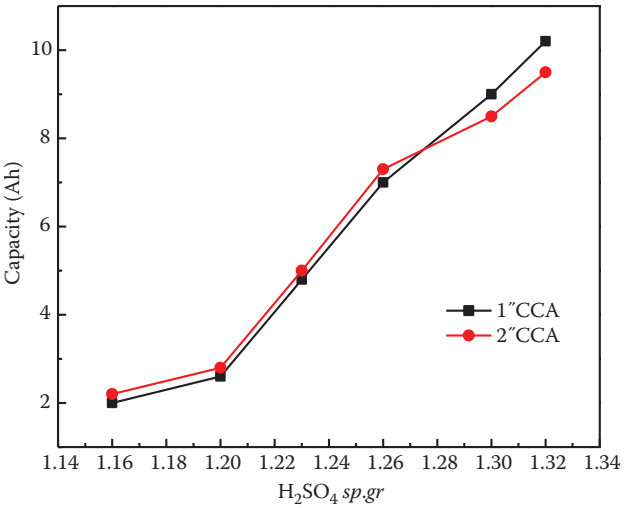

FIGURE 5.3 Relationship between the CCA capacity and the concentration of H_2SO_4. (From Z. Li, *Lecture Course on VRLA*, China, 2003.)

materials (positive active material, negative active material, and H_2SO_4) are less than 10.5% in the entire range of H_2SO_4 concentrations.

Sulfuric acid concentration in electrolyte can also affect the charge acceptance [18]. The charge acceptance of a lead-acid battery at different states of charge (SOC) is normally determined from the current after 10 sec of charge (I10S) for two voltage limits, 14.4 and 15.2 V, respectively. This I10S has different values at the H-region and N-region of sulfuric acid concentration. Within the investigated concentration range, the values of I10S at 15.2 V are considerably higher than those obtained at 14.4 V. This may be related to gassing reactions that proceed readily at higher voltages.

The measurement results indicate that a high charge acceptance can be achieved at a lower state of charge for both charge voltages in the entire H_2SO_4 concentration range. For example, at SOC = 40%, the highest charge acceptance was obtained within the N-region; at SOC = 80% and 90%, the charge acceptance in the H-region was higher than that in the N-region of acid concentrations [18]. Therefore, batteries operating at a higher state of charge should be filled with electrolyte with concentration lower than 1.27 *sp.gr.*

The two different sulfuric acid concentration regions can have different battery cycle lives. For example, batteries with different sulfuric acid concentrations were tested for cycle life at C/10 and C/3 discharge rates, and capacity versus cycle number data were obtained at both the H- and N-concentration regions, as shown in Figure 5.4 [18]. Figure 5.4 indicates that the battery cycle life performance is strongly dependent on the H_2SO_4 concentration.

From the curve of capacity versus cycle number (see Figure 5.4), two periods can be distinguished. One is the initial period (E1), and the other is the second period (E2). In the initial period, the battery capacity declines quickly to a certain value. Both the negative mass material (NAM) and positive mass material (PAM)

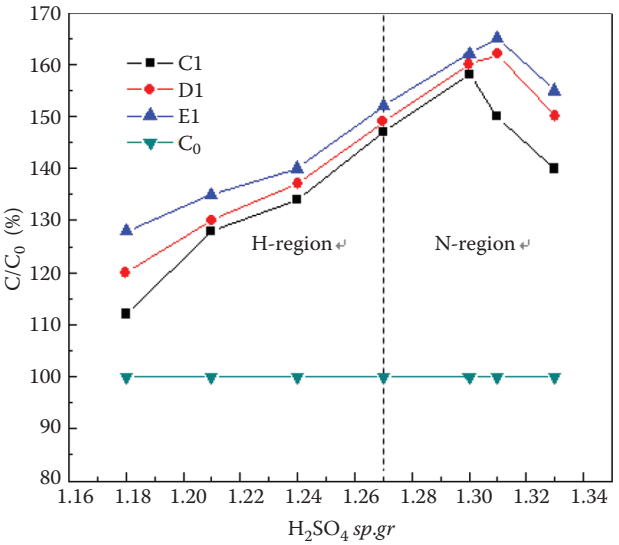

FIGURE 5.4 Lead-acid battery capacity as a function of cycle number in two different sulfuric acid concentration regions, the H-region and N-region. (From Z. Li, *Lecture Course on VRLA*, China, 2003.)

structures obtained during the formation process can be transformed into operative structures. It is expected that the spongy lead structure of NAM can be produced by electrochemical reduction of PbO and 3BS ($3PbO{\cdot}PbSO_4{\cdot}H_2O$) in diluted H_2SO_4. The thin spongy lead structure of NAM can provide high initial capacity, as shown in Figure 5.4. During battery operation, lead sulfate is formed on discharge and is then reduced back to lead on charge; thus, the initially formed NAM structure can be partially destroyed, resulting in a decline in capacity.

In the second period, the capacity of the batteries decreases with increasing cycle number. The reversibility of the process occurring in the operating NAM structure determines the capacity decrease on cycling and thus the cycle life of the lead-acid battery. The results shown in Figure 5.4 indicate that the electrolyte H_2SO_4 concentration has a strong influence on these electrode processes during cycling. The cycling behavior of the battery differs significantly in the two H_2SO_4 concentration regions. It can be seen that in the N-region of concentrations, where NAM limits battery capacity, the cycle life is shorter than that in the H-region. For example, batteries with an H_2SO_4 concentration of 1.330 *sp.gr* have a cycle life of 50 cycles for both discharge currents. The cycle life of a battery with an H_2SO_4 concentration of 1.270 *sp.gr* can be increased to 180 cycles for a C/10 discharge rate. These results also show that the battery with this latter concentration can endure 110 cycles at the C/3 discharge rate. In the H-region of acid concentrations, the amount of H_2SO_4 limits battery capacity. The cycle life of the batteries is longer than 200 cycles for both discharge current densities. At H_2SO_4 concentrations equal to 1.180 *sp.gr*, the cycle life can reach up to 400 cycles at I = C/3(A). This may indicate the high degree of reversibility of the reaction at NAM, which leads to a completed recovery of the

NAM structure, thus ensuring longer battery cycle life. We should point out that the cycle life of a battery with electrolyte concentrations in the H-regions can be also limited by side effects and probably corrosion of the positive grid.

The experimental data also indicated that the discharge current can strongly influence battery capacity on cycling [18]. For example, at I = C/10(A) the capacity was decreased slowly from 120% to 90%, followed by a rapid capacity decline [18]. While at I = C/3(A), the capacity was arrested between 95% and 85%, and thus the battery was operated at a lower discharge capacity.

Figure 5.5 shows the cycle life of a lead-acid battery under rest as a function of H_2SO_4 concentration for both discharge currents. It can be seen that the cycle life decreases with increasing H_2SO_4 concentration in the entire concentration range.

Sulfuric acid concentration can also affect the charge efficiency of lead-acid batteries. The effect of acid concentration on battery charge behavior during cycling has been studied extensively [18]. The results showed that the charge process was dependent on H_2SO_4 concentration and also on discharge current. In these studies, an open cell voltage of 13.62 V for a 6-cell battery (2.27 V/cell^{-1}) was accepted as the upper voltage limit for effective charge, above which water decomposition might start. The time to achieve this voltage limit ($t_{\text{eff.ch}}$) and the corresponding charge capacity were used as the measure of charge efficiency. Charge efficiency (Ch_{eff}) can be determined by

$$Ch_{\text{eff}} = \frac{I_{\text{ch}} t_{\text{eff.ch}}}{C_{n-1}} \tag{5.13}$$

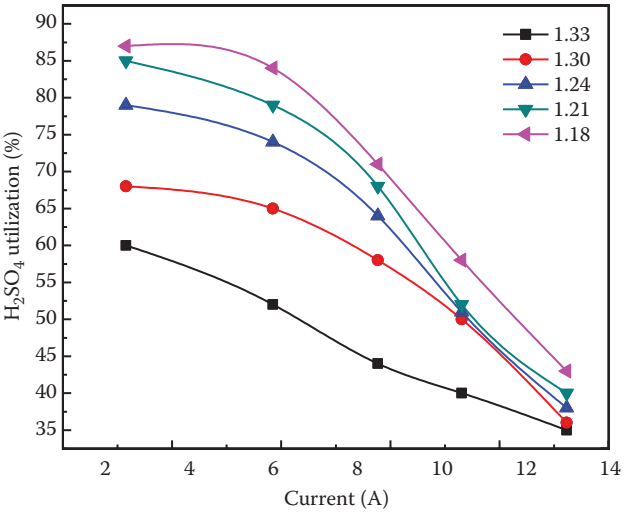

FIGURE 5.5 Lead-acid battery cycle life as a function of H_2SO_4 concentration, recorded at discharge currents of I = C/10(A) and I = C/20(A), respectively. (From Z. Li, *Lecture Course on VRLA*, China, 2003.)

where I_{ch} is the charge current in the period of $t_{eff.ch}$, and C_{n-1} is the capacity during the preceding discharge cycle. Note that this parameter differs from the charge acceptance discussed in the previous section. Charge acceptance normally determines the power of the battery, while charge efficiency is a ratio between the quantity of charge return in the battery before the beginning of water decomposition and the battery capacity during the preceding discharge. It was observed that high charge efficiencies on H_2SO_4 concentration within the H-region could be obtained, which was decreased slightly with an increase in the H_2SO_4 concentration [18]. In the N-region of acid concentrations, the charge efficiency was decreased substantially with increasing acid concentration for both discharge rates. An increase in acid concentration above 1.270 *sp.gr* could impede battery charge.

5.2.5 Dependence of $PbSO_4$ Solubility on Sulfuric Acid Concentration

As generally observed, irreversible formation of lead sulfate is one of the main reasons for capacity decay of lead negative plates. It is known that the solubility of $PbSO_4$ can affect the electroreduction of lead sulfate, and thus the charge process of the negative plate can become ineffective. In general, the solubility of sulfate lead is dependent on H_2SO_4 concentration, therefore, the relationship between $PbSO_4$ solubility and H_2SO_4 concentration should be understood. With regard to this, Danel and Plichon [15] presented the dependence of lead sulfate solubility on acid concentration, as shown in Figure 5.6 and Table 5.13. It can be seen that both of them gave similar data. From other literature [16], it can be concluded that $PbSO_4$ solubility is the high impacting factor on battery cycle life. Both the charge efficiency and $PbSO_4$ solubility decrease with increasing H_2SO_4 concentration; and the increased charge efficiency was due to the increased solubility of $PbSO_4$ at low H_2SO_4 concentration.

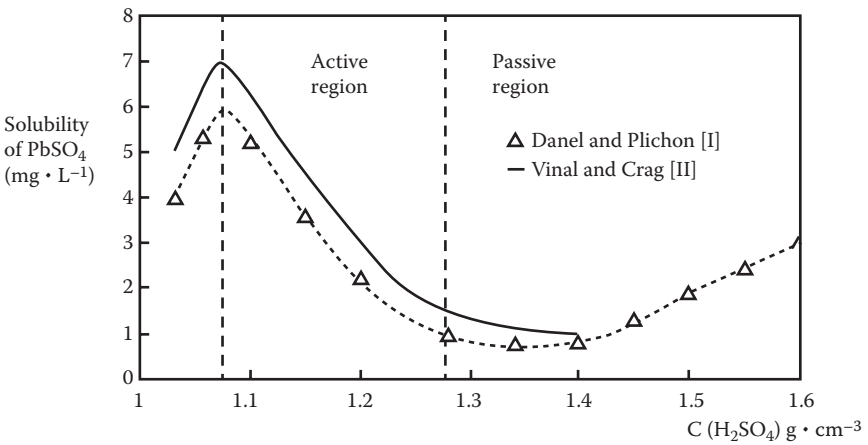

FIGURE 5.6 Correlation between solubility $PbSO_4$ of crystals and H_2SO_4 concentration. (From V. Danel and V. Plichon, *Electrochim. Acta*, 27, 771, 1982; G. W. Vinal and D. N. Crag, *J. Res. Nat. Bureau Standards*, 22, 55, 1939.)

TABLE 5.12
Electrochemical Equivalent of H_2SO_4 Solution

Concentration Percentage (%)	Density (kg/L)	Molality (mol/kg)	Electrochemical Equivalent (Ah/L)
10	1.064	1.133	28.1
12	1.089	1.390	35.4
14	1.092	1.660	41.9
16	1.107	1.942	48.4
18	1.122	2.238	55.1
20	1.137	2.549	62.0
22	1.152	2.875	69.3
24	1.167	3.220	76.5
26	1.133	3.582	34.0
28	1.199	3.965	91.5
30	1.215	4.370	99.5
32	1.231	4.798	107.2
34	1.248	5.252	110.8
36	1.264	5.735	124.0
38	1.281	6.249	133.0

Source: R. C. Weast, *CRC Handbook of Chemistry and Physics*, 58th ed., CRC, Boca Raton, FL, B-254, 1977–1978.

TABLE 5.13
Lead Sulfate Solubility as a Function of Sulfuric Acid Concentration

H_2SO_4 Solution of Relative Density	Solubility of $PbSO_4$ (mg/L)
1.280	1.5
1.100	5.5
1.300	1.0
0.5 M	6.0–6.5

Source: V. Danel and V. Plichon, *Electrochim. Acta*, 27, 771, 1982; G. W. Vinal and D. N. Crag, *J. Res. Nat. Bureau Standards*, 22, 55, 1939.

5.2.6 Additives to Improve the Performance of Electrolytes

To improve the performance of lead-acid batteries, some soluble sulfate such as $SnSO_4$, Na_2SO_4, and Li_2SO_4 can be added to the electrolyte to help the battery recover from deep discharge according to the common ion effect. As a general rule, the total quantity of the additive should not be more than 15 g/L. This kind of additive mainly improves sulfation and recrystallization. Furthermore, such additives

can help transform crude lead sulfate crystals into fine lead sulfate crystals. This type of additive has been practically developed and used in electrolytes with a proper quantity of 1 to 7 g/L.

5.3 SUMMARY

An electrolyte solution containing sulfuric acid is a necessary and key component of a lead-acid battery. It determines the battery's performance in terms of energy density and efficiency, power density, and cycle life. In lead-acid batteries, two kinds of electrolyte solutions are used: a liquid sulfuric acid solution and a gel containing sulfuric acid. This chapter gave a detailed description of electrolyte properties, composition, preparation, structure, related electrode process mechanisms, and fabrication. In particular, the H_2SO_4 concentration effects on lead-acid battery performance, including cell voltage, charge–discharge processes, energy capacity, cold-start property, and cycle life, were discussed in detail. In addition, many important tables containing useful data and electrolyte-related information were provided in the chapter. We hope readers have found this chapter useful in their study and experimental approaches.

REFERENCES

1. H. Bode, in *Lead-Acid Batteries*, R. J. Brodd and K. Kordesch, Eds., John Wiley, New York, 1997, 42.
2. M. Barak, *Electrochemical Power Sources*, Peter Peregrinus, England, 1980, 159.
3. Z. Li, "Manufacturing Technique of Lead-Acid Batteries," *Handbook of Physical Chemistry*, 2003.
4. Z. Li, "Manufacturing Technique of Lead-Acid Batteries," *Handbook of Physical Chemistry*, 109 (2003).
5. Z. Li, "Manufacturing Technique of Lead-Acid Batteries," *Handbook of Physical Chemistry*, 111 (2003).
6. Z. Li, "Manufacturing Technique of Lead-Acid Batteries," *Handbook of Physical Chemistry*, 112 (2003).
7. Z. Li, "Manufacturing Technique of Lead-Acid Batteries," *Handbook of Physical Chemistry*, 113 (2003).
8. Z. Li, "Manufacturing Technique of Lead-Acid Batteries," *Handbook of Physical Chemistry*, 114 (2003).
9. Z. Li, "Manufacturing Technique of Lead-Acid Batteries," *Handbook of Physical Chemistry*, 116 (2003).
10. D. W. G. Lambert et al., "Advances in Gelled Electrolyte Technology for Valve-Regulated Lead-Acid Batteries," *J. Power Sources*, 107 (2002), 173–179.
11. R. C. Weast, *CRC Handbook of Chemistry and Physics*, 58th ed., CRC, Boca Raton, FL, 1977–1978, B-254.
12. K. R. Bullock, *J. Power Sources*, 35 (1991), 197.
13. K. R. Bullock, *J. Electrochem. Soc.*, 126 (1979), 360.
14. K. R. Bullock, *J. Electrochem. Soc.*, 126 (1979), 1848.
15. V. Danel and V. Plichon, *Electrochim. Acta*, 27 (1982), 771.
16. G. W. Vinal and D. N. Crag, *J. Res. Natl. Bur. Stand.*, 22 (1939), 55.
17. D. Polov, *Lead-Acid Batteries, Technology and Operation*, Hangzhou, China, 2000, KLT-13.
18. Z. Li, *Lecture Course on VRLA*, China, 2003.

6 Current Collectors, Battery Grids, and Lead-Acid Batteries

R. David Prengaman

CONTENTS

6.1 INTRODUCTION

The current collectors of lead-acid batteries consist of the grid, which holds the active material; the strap, which connects all the positive or negative grids in a cell and joins it to the next cell; and the posts and terminals, which connect the interior of the battery to the exterior of the battery. The grid of a lead-acid battery consists of a lead or lead-alloy material arranged in a mesh or lattice shape. The grid is designed to hold the positive or negative active material within the grid network, carrying the discharge current out of the active material and the recharge current back into the active material. The grid must hold the active material securely and resist the expansion forces produced when the active material PbO_2 is converted to $PbSO_4$ in the positive grid and Pb to $PbSO_4$ in the negative grid. The positive grid corrodes during use and must minimize corrosion, retain its shape, and retain a good bond between it and the active material to retain capacity and prevent degradation of the battery. The grids may be as small as 3 cm or as large as 1.8 m.

6.2 PLANTÉ BATTERY GRIDS

The original lead-acid battery was developed by Gaston Planté in 1859. The grid or current collector utilized a lead sheet with perforations, slits, or lattices in a variety of shapes to form both the positive and negative electrodes. The active material was produced in a thin layer on the grids by corroding the grids during successive charge and discharge cycles. This produced a thin layer of PbO_2 on the positive grid and spongy lead on the negative grid. Planté grids are still produced by a few manufacturers. The modern Planté grid is seen in Figure 6.1. It consists of a pure lead casting that contains an outer border for strength, very thin lead sections closely spaced, and larger thickness strips to carry the current to the top of the grid and a connector outside the battery. The positive grid will be corroded and PbO_2 will fill the small spaces between the thin sections, resulting in a robust electrode.

6.3 FAURE BATTERY GRIDS

The concept on which all modern batteries are based was developed by Faure in 1881. The concept incorporated the mechanical application of a lead paste of lead oxide active material onto a cast grid of lead antimony alloy to produce a battery plate similar to that of Planté without the need to cycle the battery to produce the active material. For the next 70 years, lead-acid battery grids retained much the same grid shape and alloy as the original Faure grids. Beginning in the late 1950s with the introduction of lead calcium alloy grids for standby power batteries, the conventional lead-acid battery grid changed markedly in composition, shape, manufacturing process, life, and ability to deliver and accept high currents.

FIGURE 6.1 Modern Planté grid. (Courtesy of Hoppecke.)

6.4 BOOK MOLD CAST LEAD ANTIMONY ALLOY GRIDS

Battery grids have been produced for many years in book molds. The shape of one-half of the grid was machined into a metal mold that was mated with the other half of a metal mold machined to match the shape of the other half of the grid. The mold was clamped together and molten lead antimony alloy was poured into the mold. The mold was kept closed until the metal solidified. Once the grid was solid, the mold was opened and the grid was extracted. Until the 1930s virtually all lead-acid battery grids were cast by hand with the molten metal ladled into the mold by hand. In the late 1930s, machines were developed that opened and closed the mold by mechanical or hydraulic pressure to contain the molten metal. The machines contained ladles that were tipped to pour a given amount of lead antimony alloy into the mold in a single pour to fully fill the mold and provide a more uniform grid. The molds were air cooled and the solidification was uneven.

As more batteries were required, some manufacturers designed and constructed their own mechanical battery grid casting equipment. Most grid casting equipment, however, was designed and supplied by specialists in lead-acid grid making such as Winkel, Farmer, Donath, Mac, Wirtz, TBS, CLIA, and Chloride.

Book mold cast lead antimony grids were used for virtually all lead-acid battery applications. Very large grids for submarine batteries, large grids for forklift trucks and stationary power, smaller sized grids for automobile batteries and electric vehicles, and small grids for applications such as miner's lamps all had the same basic shape. The grid consisted of a lug to carry the current into and out of the battery, a large thick rectangular frame to give mechanical strength, and smaller wires within the frame to hold the active material. A typical 1960s grid design is shown in Figure 6.2.

Initially most lead antimony grids were produced from a eutectic alloy of 11% antimony, which has a single freezing point at 273°C, making grid casting relatively simple. Antimony as an alloying element was very expensive and battery

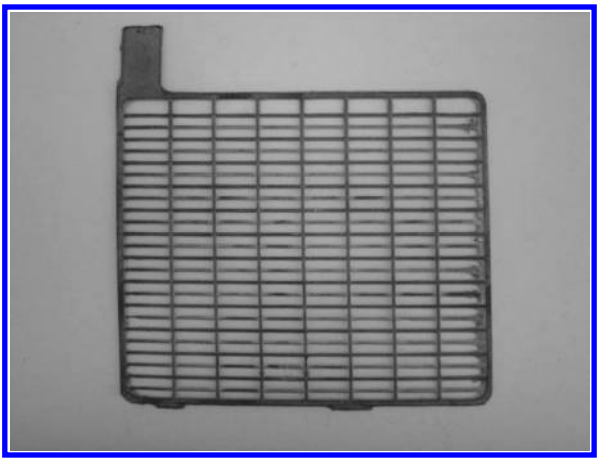

FIGURE 6.2 Book mold cast lead antimony grid.

manufacturers tried to reduce the antimony content of the grids. As antimony content was reduced, the alloy now had a freezing range rather than a single temperature, which made casting good-quality grids more difficult because the grids were subject to cracking.

Manufacturers of grid casting equipment developed many innovations to produce satisfactory grids from the lower antimony alloys. These included the development of a grid mold coating created from powdered cork and sodium silicate, which provided insulation to permit uniform filling and solidification of the cast grid as a replacement for smoking the mold to produce a layer of carbon on the mold. The book molds were electrically heated to control mold temperature, and cooled by recirculating fluid in internal cavities to control solidification. Despite the advances, casting grids with lead antimony contents below 5% without cracks was an art. Antimony plays an important role in the performance of the battery. During life, the positive grid is corroded and antimony from the grid is doped into the active material adjacent to the grid wire. The antimony doping permits the battery to be recharged easily from deep discharge.

6.4.1 Low-Antimony Book Mold Cast Grids

The lead antimony battery grids presented a problem. The high-antimony content grids corroded rapidly, and antimony was transferred from the positive grid to the negative causing gassing and loss of water. Batteries using grids containing antimony required frequent replacement of the lost water. The need to replace the water was responsible for the design of the lead antimony battery grid. The standard grid of many decades was a rectangular design with the lug placed at one end. This allowed the placement of the positive and negative grids at opposite sides of the cell to permit the addition of water at the top of the battery case between the positive and negative grids. The lug placement of these grids can be seen in Figure 6.2. Attempts to use lower antimony alloys to reduce water loss were unsuccessful due to severe cracking of book mold cast grids due to a wide freezing range.

Prengaman developed a low-antimony alloy containing copper and sulfur as nucleating agents, which controlled the grain structure and permitted casting of low-antimony alloys without cracks. The addition of nucleants permitted casting of any antimony content without cracks. Low antimony grids combined with the innovations in grid casting equipment allowed the production of thin grids for low maintenance batteries.

6.4.2 Evolution of Battery Grid Designs

Until the early 1970s lead-acid battery grids were relatively heavy at 2 to 3 mm thick. The grid wires were offset to permit better adhesion of the active material. The grid contained thicker wires in the vertical direction to enhance current flow. In the 1970s, with the introduction of low-antimony battery grids, the battery industry developed thinner and more powerful grid designs to produce more powerful cranking batteries for automobiles. This required the modification of the standard grid design to produce more conductive and lighter battery grids using lead antimony

alloys. The first modification merely involved the machining of several diagonal wires into the standard grid design. This is seen in Figure 6.3. The complete redesign to enhance cranking performance of low antimony battery grids is seen in Figure 6.4 where all the wires were set at a diagonal to the lug to enhance conductivity. The grid is cast in a double panel for ease of handling and subsequent processing on an automatic pasting machine. The top part of the casting contains the gate to provide a head of metal to provide pressure on the lead alloy to fill the grid mold. The bottom part of the grid provides an area of extra lead to ensure complete filling of the mold. The gate and bottom of the raw casting are removed in a trimming press to obtain the final grid dimensions.

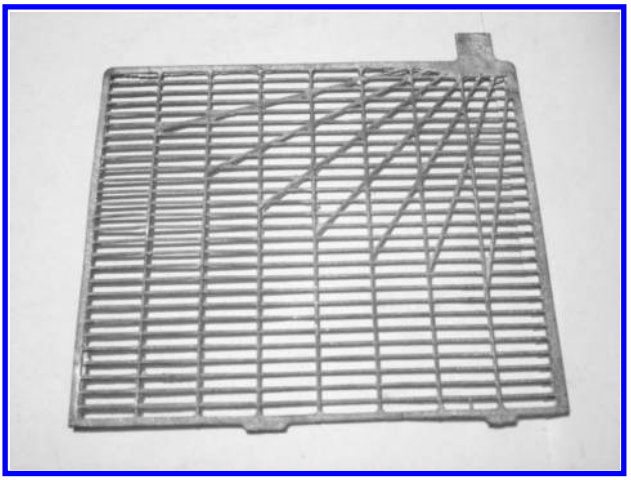

FIGURE 6.3 Book mold cast lead antimony diagonal current collectors.

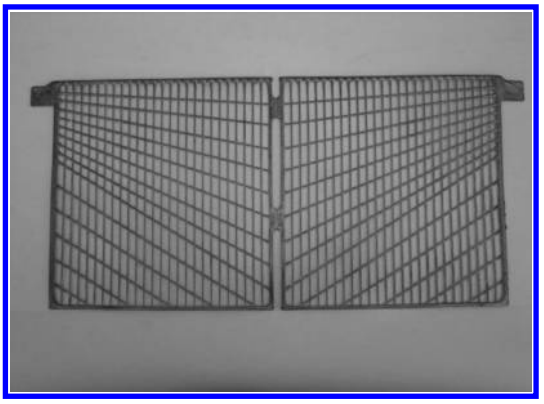

FIGURE 6.4 Book mold cast diagonal high-cranking current collectors.

6.4.3 Lead Calcium Book Mold Grids

The introduction of lead calcium alloy grids in the late 1970s and early 1980s caused a significant change in the grid design. Lead calcium-based grids did not cause gassing at the negative electrodes and thus batteries constructed from lead calcium-based grids could be sealed and no water needed to be added. The traditional grid design with the lug at one end of a rectangular grid could be modified to bring the lug into a much more central position (Figure 6.5) and, combined with the radial grid wire position, gave significantly higher performance and efficiency of the active material. Although the grid gave improved performance, it was difficult to cast. The molten metal entering the mold from the top was directed by the grid wires toward the lug and then back into the body of the grid, leaving the bottom right and left of the casting difficult to completely fill. The grid wires were also tapered from the top border to the lower part of the grid to enhance conductivity.

In book mold casting, the cork layer is gradually worn away and the grids gradually increase in thickness. The mold coating must be removed and replaced to maintain reasonable thickness and weight control. In lead calcium tin alloy grids for valve-regulated lead-acid (VRLA) batteries, the grids must be all the same thickness to maintain proper compression. In book mold cast grids, the normal thickness variation of 0.1 mm is too much for VRLA batteries. To reduce the variation, the grids are deformed slightly by squeezing or squashing in the press used to trim the gates from the grid to a set thickness. Planishing can reduce the thickness variation to 0.01 mm.

6.5 CONTINUOUS GRID PRODUCTION

The difficulty of book mold casting lead antimony grids without cracks led Delco Remy in the late 1960s to explore alternate automobile grid production methods. Prengaman developed a rolled lead calcium tin alloy strip that could be transformed into battery grids by expanding the strip in a continuous process. The process increased the rate of grid production by a factor of 10 and reduced the labor content of a grid, and the lead calcium alloy grid permitted the batteries to be maintenance

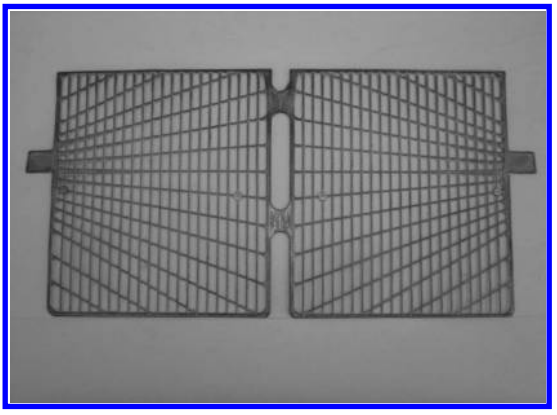

FIGURE 6.5 Lead calcium double grid central current collectors.

free in that no water needed to be added. The strip, expanded metal, and grid are shown in Figure 6.6. The expanded metal had better conductivity than the book mold antimony alloys, leading to the improved grid designs seen in Figures 6.4 and 6.5. The rolled lead calcium tin expanded metal was used for both positive and negative grids.

In the mid-1980s Cominco (now Battery Technology Solutions [BTS]) introduced a continuous strip caster that cast a thin lead calcium alloy strip that did not need to be rolled to be expanded into a strip for expansion into grids. The very low freezing range of the lead calcium alloys permits the rapid cooling to produce the thin strip. The strip and expanded grid can be seen in Figure 6.7. The cast material was softer than the rolled strip and a rotary expander was developed to process the strip into grids. The rotary expander was faster than the progressive die expander and production of grids at rates of more than 600 per minute became possible. The expanded

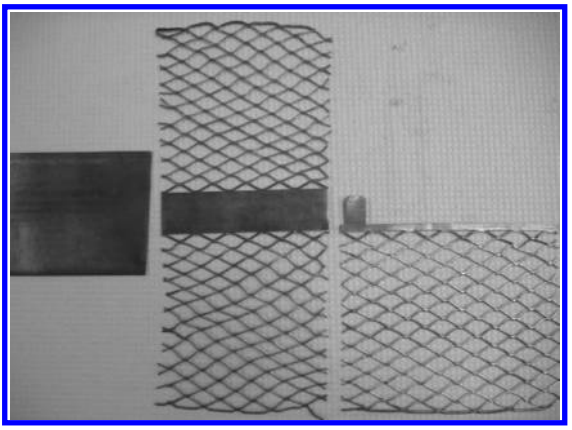

FIGURE 6.6 Rolled lead calcium tin strip, expanded metal, and grid.

FIGURE 6.7 BTS cast strip—rotary expanded metal grid.

metal grid wires are slightly offset so that the grid holds the active material more readily.

BTS has also developed a continuous grid strip extrusion process. The process produces a continuous profiled strip that can be expanded or punched to produce battery grids that have a thicker lug for improved processing and thinner grid body for reduced grid weight. The process has produced expanded negative grids for automobile batteries with a weight of 18 g, which is 40% lighter than normal negative grids. The process has been used to produce thicker grids for high-rate charge and discharge batteries. The grid is shown in Figure 6.8. The grid has a large, thicker lead strip extending from the lug area along the side of the grid. The lead strip is twice the thickness of the expanded metal portion of the grid. The design allows the current to flow to the bottom of the grid along the lead strip to more effectively utilize the active material throughout the grid. Such a grid has produced an 80% improvement in cranking performance compared to a conventional grid without the large side border.

In the early 1990s Wirtz Manufacturing introduced a continuous grid casting called Concast. Instead of casting a strip, this process casts a continuous coil of double panel grids to a final shape. The process is used extensively to produce thin negative lead calcium alloy automobile battery grids at speeds of up to 400 grids per minute, but has not yet been employed to produce positive grids. The continuously cast strip of grids is shown in Figure 6.9.

More recently Wirtz introduced a process called Conroll in which the Concast grids were cast in a thicker cross section and then rolled to produce a uniform grain structure and improved mechanical properties. The rolling adds additional speed to the grid production process and rates of more than 500 grids per minute are achieved.

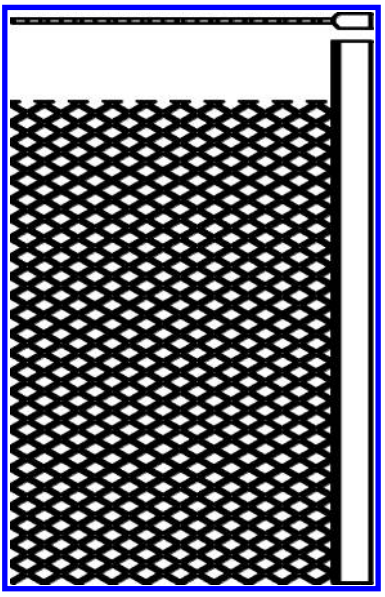

FIGURE 6.8 BTS dual-thickness grid for high-rate batteries.

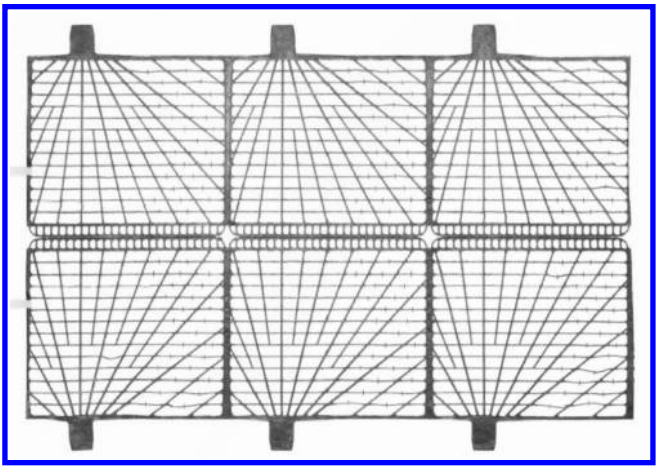

FIGURE 6.9 Wirtz continuously cast grids.

The Conroll process can also produce a wide cast rolled sheet that can be used for producing grids by punching.

6.6 NOVEL BATTERY GRID DESIGNS

In the past 10 years, there has been a tremendous increase in the demands placed on lead-acid batteries as the electrification of the automobile has increased dramatically. Conventional grid designs left areas of the grid inactive due to the inability to conduct high electrical currents into and out of the battery. The Advanced Lead Acid Battery Consortium initiated and funded research and battery design projects to evaluate novel battery current collector designs to enhance the performance of batteries through improved battery grids. Such designs have enhanced current collectors so that they distribute current more evenly over the grid surface to improve the capacity of the battery and improve battery life. Such a design is shown in Figure 6.10.

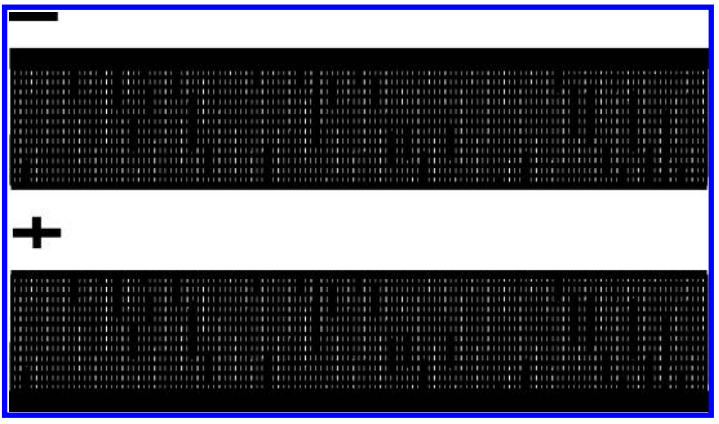

FIGURE 6.10 Grid configuration with most uniform current distribution.

The grid has a large top frame for easy conduction of the current into and out of the grid. This design also has positive and negative grids at opposite sides of the battery to better improve current flow into the battery. These designs and other similar designs are currently being used to produce higher performance batteries. As the grid length increases, and the dimensions of the grid mesh portion decrease, the grid can accept higher discharge and recharge currents. These designs are not produced by conventional book mold casting, but by production of wide rolled or BTS cast strip, which is punched to produce the final grid shape.

6.6.1 Punched Grids

In the past 10 years, as demands on batteries for improved performance has increased and the under-the-hood temperatures of automobiles have increased, the conventional rolled expanded metal positive grid was not able to give adequate life and performance. The grids suffered from corrosion and grew in length, causing the positive grid to contact the negative strap and introducing a short circuit, which in turn caused premature failure of the battery. The main cause of the problem was the lack of a side border on the expanded metal grid, which would have prevented the growth, as seen earlier in Figure 6.8. Book mold grids of special lead calcium tin silver alloys could perform well because they had a side border (see Figure 6.5). The book mold grids could not be produced continuously and thus a rolled lead calcium tin alloy wide strip was developed that could be continuously punched in a coil for pasting. The punching process could produce any grid shape desired with optimum design of grid wires for current collection. The rolled lead calcium strip was stronger than the expanded metal grids and thus lighter grids of the same power and capacity could be produced. An example of a rolled punched grid is shown in Figure 6.11. The BTS cast strip could be utilized for the punched grids, but required the addition of silver to the alloy similar to that of the book mold cast grid alloy to produce similar performance in automobile applications.

A BTS continuously cast strip in pure lead, lead tin, and lead tin silver alloys has been used to produce punched grids for VRLA batteries used in telecommunications,

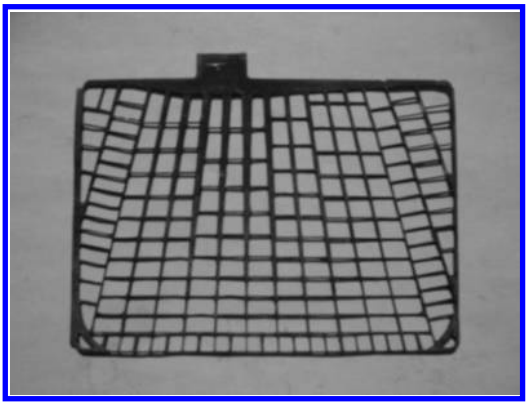

FIGURE 6.11 Rolled lead calcium tin punched grip.

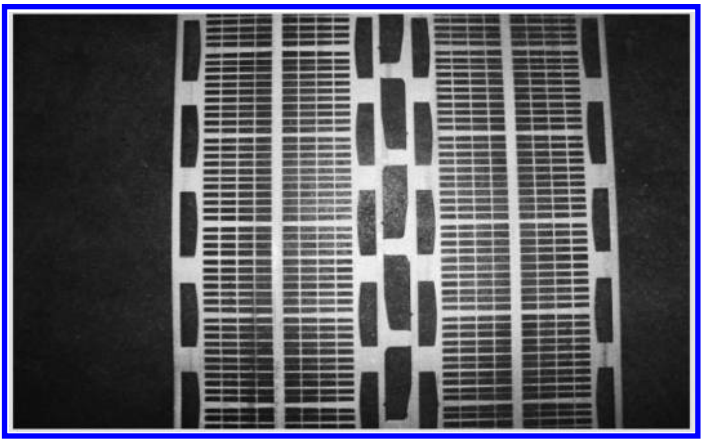

FIGURE 6.12 Coil of punched grids before pasting.

uninterruptible power supplies (UPSs), and standby power batteries. A number of manufacturers around the world have begun to produce high-power thin grid batteries using these alloys for punched grids. The punching process allows continuous production of grids in coils. The continuous process allows handling of very soft materials in a thin grid format for improved battery performance, which would not be possible with book mold cast grids. A strip of punched grids from Oak Press is shown in Figure 6.12.

6.6.2 Spiral-Wound Grids

In the early 1990s, spiral-wound batteries were produced by Gates manufacturing using a BTS continuously cast strip in lead tin or pure lead that was punched to produce the final grid shape. The punched grid can have a complete border, which can prevent some of the problems of grid growth resulting from expanded metal. The grid of a spiral-wound battery can be seen in Figure 6.13. The grid lugs are spaced at intervals so that they will align with each other. Being in alignment allows them to be welded together at the top of the grid to allow the current to be carried out of the grid in a uniform fashion. The spiral construction allows the active material to be compressed into the grid for better adhesion. The grid design permits higher discharge and recharge currents due to the multiple grid lug locations. The spiral-wound construction allows a large grid surface to be utilized that cannot be utilized in long straight lengths. Exide, Optima, and Enersys produce spiral-wound batteries.

Modification of the spiral-wound grid concept is seen in the grid design from Batteck shown in Figure 6.14. The grid has a large continuous strip at the top and a long length. The grid also has a very short grid mesh area so that the active material has improved utilization throughout the grid. The long strip is wound with the negative grid and separator in the same manner as the spiral-wound grids described earlier. The grids are designed for optimum current-carrying capacity and grid utilization because the grid current collectors are located at opposite ends of the battery, further increasing active material utilization.

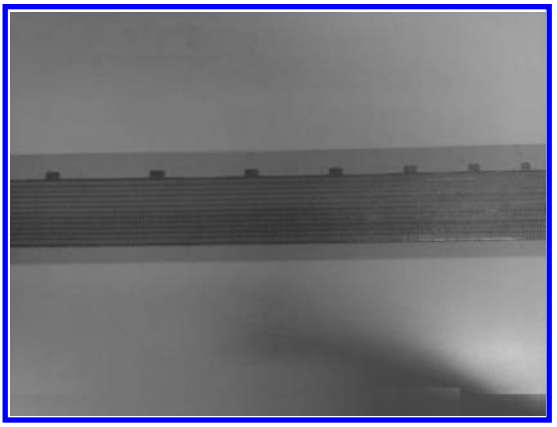

FIGURE 6.13 Punched grid for spiral-wound battery. (Courtesy of Exide.)

FIGURE 6.14 Long punched grid for spiral-wound high-rate battery.

6.6.3 Tubular Grids

Tubular battery grids consist of a large top bar and a series of long spines extending downward from the bar. Tubular grids get their name because the long spines are encased in glass or fiber tubes, which hold the active material within the annular space between the tube and the spine. The spines can be as long as 1 m in length and have small protrusions periodically along the length to keep the spine centered in the tube. The grids are cast in a special book mold that is nearly horizontal instead of vertical. The lead is injected into the bottom of the mold, displacing the air as

the mold is filled. To cast this grid, the lead alloy must flow a long distance to fill the spines and the top bar without freezing. To allow filling of the spines, the alloys used for many years consisted of eutectic or near eutectic lead antimony alloys of 9% to 11% antimony. The single freezing point or very low freezing range allowed the metal to flow long distances under pressure to ensure complete filling of the mold without significant porosity in the spines. Some casters employed vacuum as well as pressure to fill the molds. The tubular batteries are used for traction and deep-discharge applications where long life is important. Because the batteries are produced from high-antimony alloys, high water usage occurs. In the past 15 years, the antimony content of the tubular grids has been able to be reduced with the introduction of new pressure casters from HADI. Tubular grids with antimony contents as low as 1.8% can be cast on the new equipment, producing low water usage batteries. Tubular grids can now be produced from lead calcium tin alloys for sealed VRLA batteries used in telecommunications, UPSs, and cycling applications. The gauntlet around the grid spines keeps the active material in good contact with the spines, which is needed in VRLA batteries. A typical tubular battery grid is shown in Figure 6.15.

6.6.4 Composite Grids

Most lead-acid battery grids are produced from pure lead or lead alloys. Some batteries have utilized composite grids, which contain a core of copper that is coated with a layer of electroplated lead and tin. Large grids for submarines or traction batteries have utilized lead-coated copper composite materials for negative grids. The copper is almost an order of magnitude more conductive than the lead that it replaces. Copper inserts coated with tin and lead are used for the top terminals for large high-ampere-hour batteries to reduce the resistance of the terminals and prevent melting of the lead alloys under high-rate discharge conditions. Recently lead-coated copper grids have been produced in a continuous grid manufacturing process developed by DSL Dresden Material Innovation GmbH. The grids are electroformed by first plating a layer of copper onto a wheel matching the desired grid shape. The continuous copper foil is formed into a lead-acid battery grid by electrodepositing lead or lead alloys onto the copper foil. Multiple passes electrodeposit the lead alloys to the proper thickness and produce a continuous coil of grids that can be pasted like

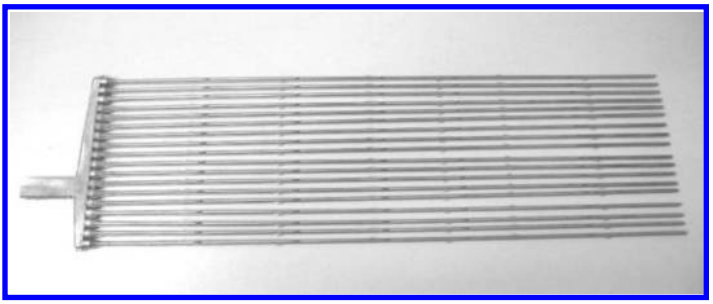

FIGURE 6.15 Tubular battery grid. (Courtesy of Exide.)

other continuous grid manufacturing processes. The cross section of a lead-coated copper grid is shown in Figure 6.16.

Bipolar batteries utilize composite grids. Atraverda utilizes a base grid material of conductive Ti_4O_7 ceramic material for the base grid material. The ceramic is coated on both sides with lead to provide the base for the positive active material on one side and the negative active material on the other. A bipolar battery increases the voltage by about 2 V for each grid added to the battery. A conventional battery increases the ampere-hour capacity of the battery for each grid that is added. The bipolar battery is positive on one side of the grid and negative on the other side. The current does not flow out of the grid to a lug and strap, but instead flows through the grid to the other side and the terminals are on each side of the grid rather than on the top or bottom. The ceramic grid allows the battery to be sealed at the edges of the grid with epoxy. The Atraverda ceramic grid is shown in Figure 6.17.

Novel grids for lead-acid batteries containing no lead have been developed in the past few years. The Firefly battery negative grid consists of carbon foam. The foam is graphitized to make it conductive. Two pieces of foam are bonded together using a polymer layer to form the base for the grid. The carbon grid has the normal shape of a lead-acid battery grid. The top surface of the foam is formed into a lug, which is

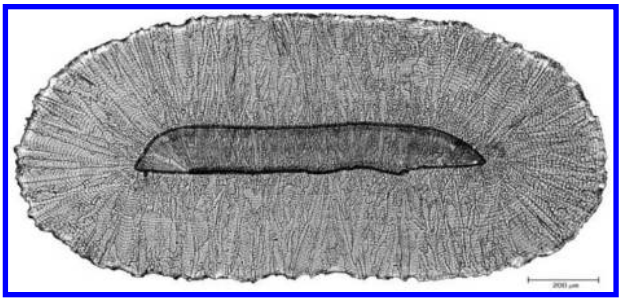

FIGURE 6.16 Composite copper-cored lead grid.

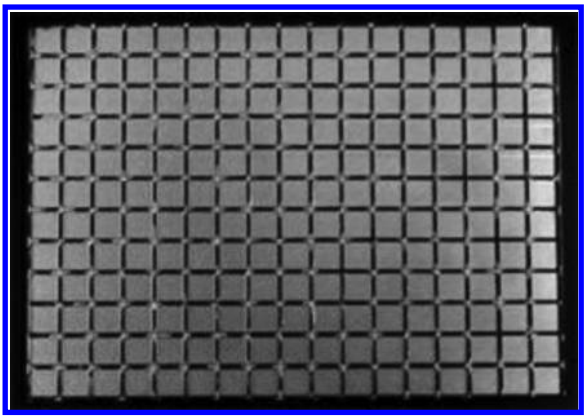

FIGURE 6.17 Atraverda bipolar grid.

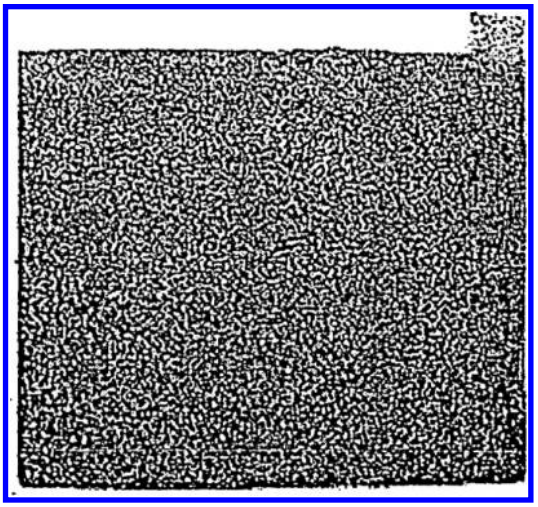

FIGURE 6.18 Firefly carbon foam 3D grid.

then coated with lead to form a current collector to conduct the current into and out of the battery. The very high surface area of the carbon foam is coated with a thin layer of lead active material. The grid is very lightweight and has a very high power due to the high surface area. The carbon foam Firefly grid is shown in Figure 6.18.

A similar negative grid has been developed by Axion. The grid consists of a flat copper foil sheet coated with lead and then pasted with activated carbon. The grid contains no lead-based active material. The negative grid acts as a superconductor and, combined with a conventional lead alloy book mold positive grid, creates a battery that can produce higher rates of discharge and recharge compared to traditional lead-acid batteries. The carbon negative grid gives the battery excellent cycling performance, but with lower capacity and with very little capacity fade over many cycles.

The Ultrabattery developed by CSIRO and Furukawa has a negative grid that is half conventional lead negative grid and half activated carbon-based grid. The combination gives the good capacity found with conventional grids and provides the high-rate recharge and discharge performance of a supercapacitor negative grid material.

6.7 SUMMARY

Grids for lead-acid batteries have evolved from thick, heavy, book mold cast high-antimony grids with short lives and high water loss to thin lead calcium-based continuously produced grids that allow the batteries to be sealed with no water loss. Newer grid designs produced from continuously cast strip or rolled strip and punched grids have placed the grid lugs and internal current collectors at optimum locations for full use of the active material pasted onto the grids. New lead alloys have enabled the grids to be more corrosion resistant, more conductive, and better able to retain the active material during use. The use of spiral-wound grids can allow for an optimum

grid geometry as well as maximum compression of the active material for long life. Composite grids of copper-lead, ceramic-lead, and carbon can dramatically improve the weight and power of lead-acid batteries and may lead to a new generation of battery grids. Modern continuous processing has increased battery grid production rates by a factor of 20 or more, and new calcium-based grid alloys have allowed a 50% reduction in grid weight over older high lead antimony book mold battery grids with significant improvement in battery life.

FURTHER READING

Chen, Y. L., "Battery Grid," U.S. Patent 6,953,641 B2 (October 11, 2005).

Ishikawa, T., "A Punched Grid Production Process for Automobile Batteries," *Proc. Seventh Int. Lead Conf. Pb-80*, Madrid, Lead Development Association, London (1980), 56.

McCartney C. P. and N. L. Williams, "General Motors," U.S. 3 891 459 (1975).

Prengaman, R. D., "Low Antimony Alloys," *The Battery Man*, 10 (1983), 29.

Prengaman, R. D., "Alloy for Thin Positive Grids for Lead Acid Batteries," U.S. Patent 6,649,306 B2 (November 18, 2003).

Prengaman, R. D., "Lead Alloys for Valve Regulated Batteries," Chap. 2 in *Valve Regulated Batteries*, P. Moseley, J. Garche, C. D. Parker, and D. A. J. Rand, Eds., Elsevier, New York (2004).

Rao, P., "Calcium Tin Silver Lead Based Alloys and Battery Grids and Lead Acid Batteries," U.S. Patent 5,298,350 (March 29, 1994).

Vince, A. M., "New Technology for High Performance SLI Batteries," *Proc. Int. Lead Conf. Pb83*, The Hague, Lead Development Association, London (1983), 37.

Wirtz, J. W., "New Development in Continuous Cast Grids," *Proc. Seventh Int. Lead Conf. Pb-80*, Madrid, Lead Development Association, London (1980), 54.

Zeman R. W. and J. B. Barclay, "Wrought Maintenance Free Battery Grids Progressive Dye Expansion Technology," *Proc. Int. Lead Conf. Pb-80*, Madrid, Lead Development Association, London (1980), 60.

7 Lead-Acid Battery Manufacturing Equipment

Joey Jung

CONTENTS

The manufacturing processes used to produce various types of lead-acid battery including starting, lighting, and ignition (SLI) batteries, traction batteries, and stationary batteries are similar. The lead-acid battery manufacturing process can be separated into eight major stages as follows:

1. *Grid casting*. Lead alloys are used for casting of the positive and negative grids as well as for small components (post, terminal posts, connectors, etc.). Highly automated and efficient casting machines are employed.
2. *Lead oxide production*. Pure lead ingots are simultaneously subjected to surface oxidation and grinding into powder or are melted, pulverized, and oxidized in air atmosphere. A 60% to 90% oxidized lead oxide is obtained with an adequate grain size distribution.
3. *Paste preparation*. The lead oxide is fed into a mixing machine and then water and H_2SO_4 solution are added under continuous stirring. Basic lead sulfates are formed during this stage. After a defined period of mixing, the paste is used for production of positive plates. The paste for negative battery plates is prepared in a similar way, but expanders are also added to the mixture. To ensure that the manufacturing process proceeds properly, the paste must have a definite consistency and density.
4. *Grid pasting*. Grids are pasted using specially designed pasting machines. The pasted plates are then dried in a tunnel oven and arranged in pallets.
5. *Plate curing*. Pallets with plates are placed in chambers with 100% humidity and 30°C to 95°C for 24 to 72 h. During this curing period, the lead in the paste is oxidized, the basic lead sulfates recrytallize, the grids corrode, and the paste changes in phase composition.
6. *Plate formation*. The dried plates are arranged in large tanks containing H_2SO_4 solution, and electric current is passed through the tanks. Spongy lead is formed on the negative electrode, and plates are washed with water and dried. The negative plates are treated in the same way, but drying is carried out in an oxygen-free atmosphere.
7. *Production of containers, covers, vents, etc*. Plastic components are manufactured by extrusion in appropriate molds.
8. *Battery assembly*. Dried plates with separators in between are assembled in active blocks. Similar polarity plates are soldered into semiblocks through the post straps. The active blocks are introduced into containers, which are then covered with lids. The cells are connected and tested to ensure airtightness, the vents are closed to eliminate access by air, and the battery is packed and ready for delivery.

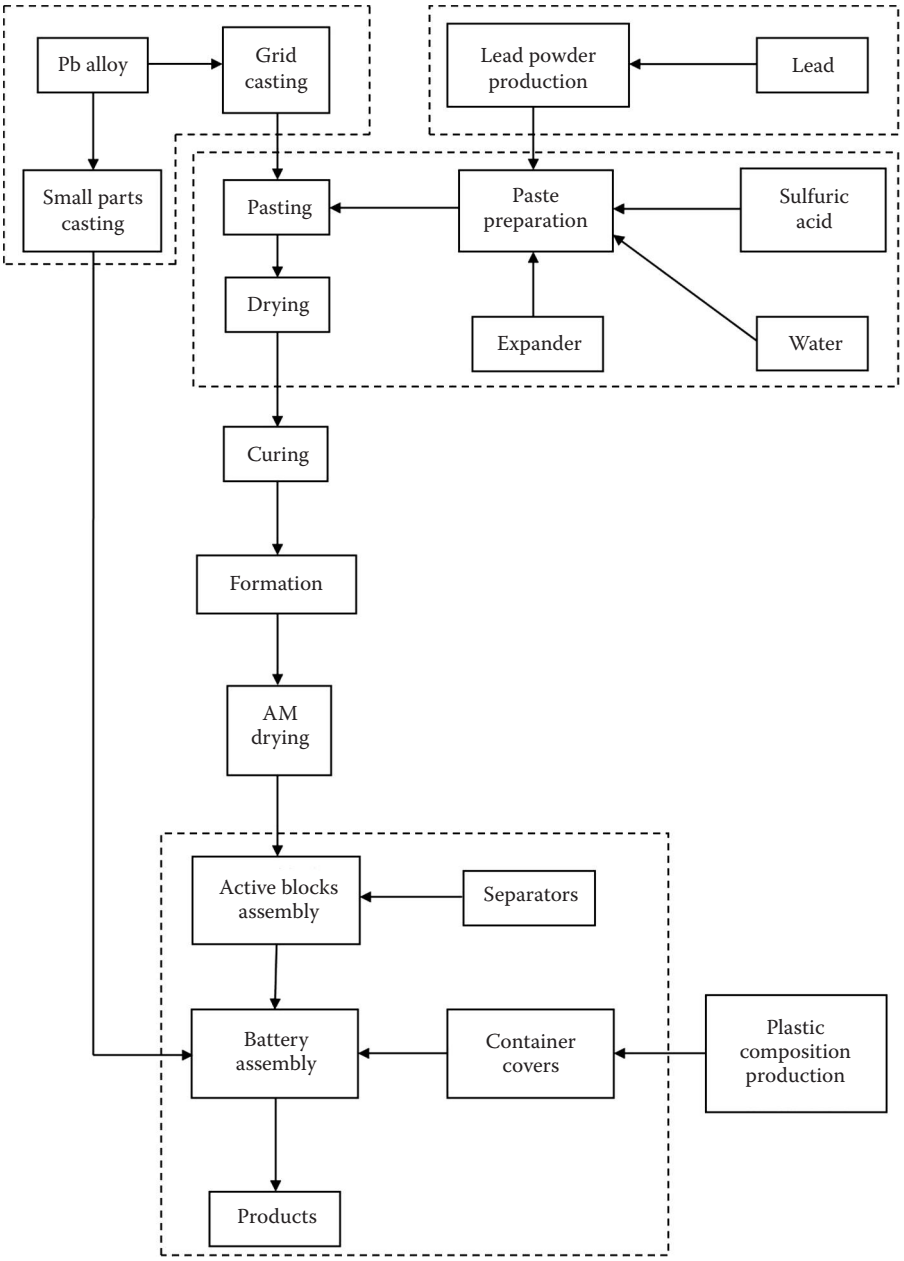

FIGURE 7.1 Battery manufacturing process. (From International Thermal Systems. Available at http://internationalthermalsystems.com/batterymanufacturing.)

This technological scheme is employed for the production of dry charged batteries. When filled with H_2SO_4 solution, the batteries are ready for use and do not need preliminary charging. The shelf-life of such batteries is about 1 year.

The classical technological scheme for the manufacture of batteries with flat pasted plates and tubular plates is presented in Figure 7.1 [1].

7.1 GRID CASTING

The function of a battery grid is to act as a current collector, which is used to hold the active material and conduct electricity between the active material and the cell terminals. A battery grid is often made of a lead alloy because pure lead is too soft.

In modern maintenance-free batteries, the lead alloy often contains calcium or other alkaline earth elements to make the lead stiffer. Calcium is added to the lead in the range of 0.03 to 0.20 wt% depending on the different battery manufacturers. The current trend is to lower the calcium level to 0.03% to 0.05% for better corrosion resistance. Tin has been added to the lead-calcium alloy to enhance the mechanical and corrosion-resistance properties in the range of 0.25 to 2 wt%. Some battery manufacturers have substituted strontium for calcium. The other type of lead alloy is a quaternary alloy that contains lead, calcium, tin, and aluminum. Aluminum is used to stabilize the drossing loss of calcium while molten.

In a flooded-type lead-acid battery, the most common lead alloy is lead antimony. The amount of antimony has varied between 5% and 12 wt% pending on the battery applications and the cost of antimony. The presence of antimony in the grids will dissolve during battery operation and migrate to the negative plates where it redeposits and promotes water splitting to hydrogen and oxygen. This results in the battery having a high-antimony content grid that requires the regular addition of water. As the antimony content goes below 4%, the addition of small amounts of other elements such as cadmium, sulfur, copper, arsenic, selenium, tellurium, and various combinations is necessary to prevent grid fabrication defects and grid brittleness. These added metal elements act as grain refiners to decrease the lead grain size. Another lead alloy is lead antimony cadmium. Antimony and cadmium will react to form an intermetallic compound, SbCd. During charge, the positive grid undergoes corrosion and produces antimony in the corrosion layer. The antimony and cadmium provide excellent conductivity through the corrosion layer. Although small amounts of cadmium and antimony are leached as a result of grid corrosion, which will deposit on the negative grid. Research has indicated that the cadmium will plate over the antimony and raise the potential of the negative plate, which diminishes the water loss.

Battery grids can be produced by two different methods: batch processes, such as book mold gravity casting, and continuous processes, such as strip expansion, strip stamping, continuous casting, and continuous casting followed by rolling. Grids made from these processes have unique features characteristic of the process and behave differently in lead-acid batteries, especially with respect to the pasting process.

7.1.1 Grid Caster

Book mold casting is a batch process. In the book mold casting process, molten lead is poured into a grid mold and cooled to form a grid. The surface of the grid made from a book mold casting is somewhat rough and the geometric shape of the cross section of the grid wires is usually oval with a sharp angle formed at the plane where the book mold closes. Figure 7.2 shows a battery grid mold [2].

The battery grid mold can be installed in a high-speed grid caster to enable continuous operation. A grid caster is designed to handle different book caster molds to produce various sizes of battery grids. Figure 7.3 shows a grid caster made by Wirtz Manufacturing.

A high-speed book mold grid caster can produce up to 18 panels per minute with minimum operator requirement. With proper setup, one operator can operate three machines to produce up to 35,000 grids per 8-h shift.

7.1.2 Strip Expansion Grid

In the strip expansion process, a cast or wrought lead strip is pierced, stretched above and below the strip plane, and then pulled or expanded to form a grid with a diamond

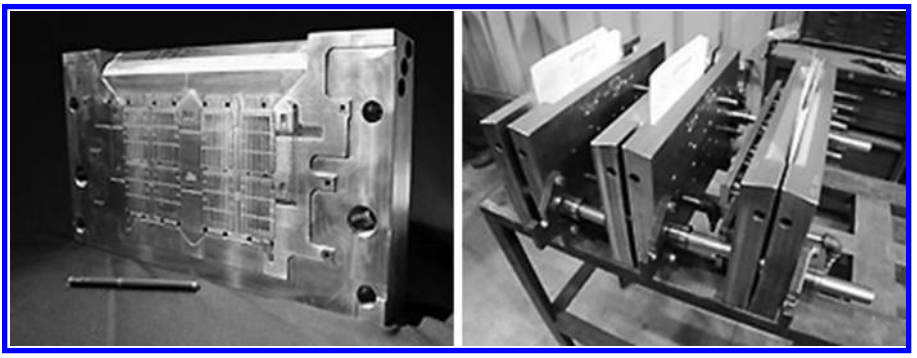

FIGURE 7.2 Battery grid casting mold (book mold). (From Wirtz Manufacturing. Available at http://www.wirtzusa.com.)

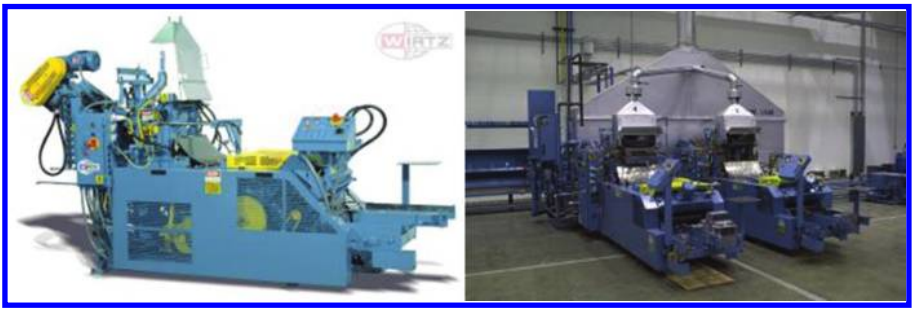

FIGURE 7.3 Book mold grid caster. (From Wirtz Manufacturing. Available at http://www.wirtzusa.com.)

pattern. The surface of the wires perpendicular to the plane of the strip is smooth and the cross section of the wires is rectangular. Stamped grids also have smooth surfaces and a rectangular cross section in the wires. The strip expansion process can produce thin and lightweight grids when compared to book mold grids. The strip expansion grid is produced with the equipment listed in Figure 7.4 [3,4], and an expanded grid is shown in Figure 7.5.

The strip expansion process can produce up to 200,000 SLI-type grids per 8-h shift. The strip expansion process is currently used to produce 40% of the world's SLI batteries.

7.1.3 Continuous Grid Caster

For continuous casting, the surface of the grid can be rough on the mold side and smooth on the belt/air side. The geometry of the cross section of the wires produced by continuous casting can be a triangle, a trapezoid, a section of an arc, or a

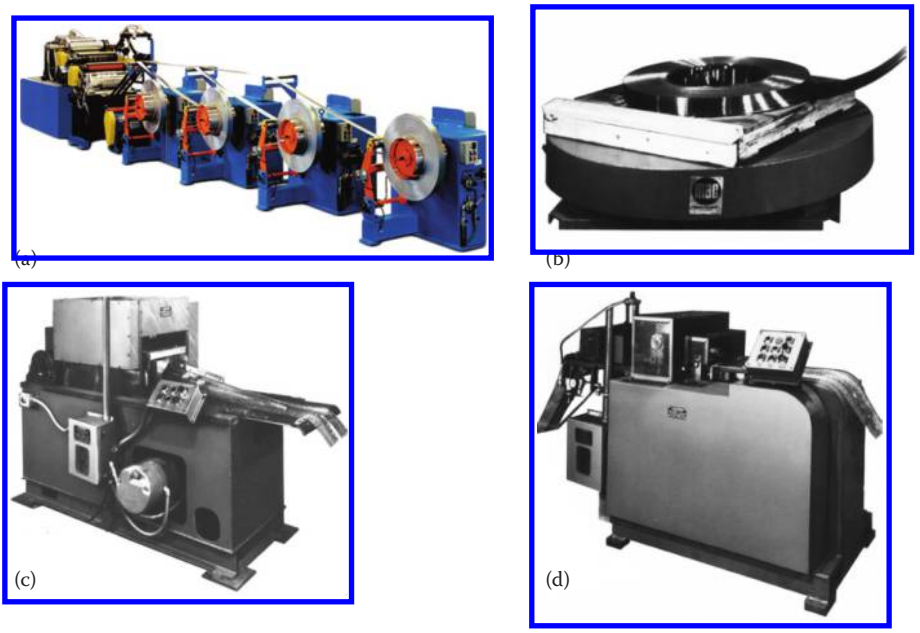

FIGURE 7.4 Strip expansion process equipment. (a) Lead-alloy strip caster: Multialloy caster produces fully edge-trimmed lead alloy strips; (b) Coil feeder: This machine feeds the coiled lead from the horizontal position; (c) Expander: Using a die, the expander produces controlled expansion, which results in the grid's diamond pattern and height; (d) Shaper: The shaper forms the lugs and accurately sizes the grid for height and thickness. A positive feed mechanism aligns and positions the expanded strip and a punch-and-die knocks out clean, reclaimable lead from the unexpanded center portion of the strip. (From MAC Engineering. Available at http://www.mac-eng.com; Battery Technology Solutions Inc. Available at http://www.batechsol.com.)

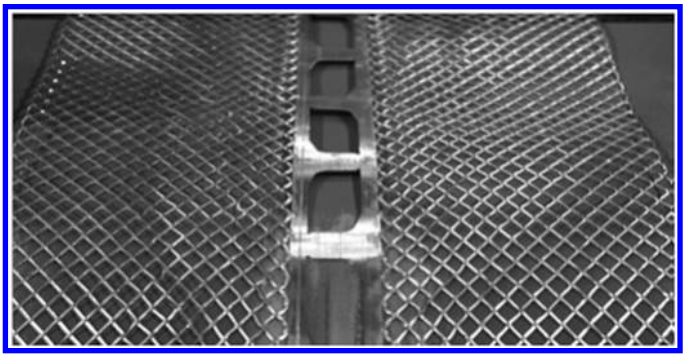

FIGURE 7.5 Expanded grid. (From MAC Engineering. Available at http://www.mac-eng.com.)

semicircle, depending on the mold design. If the grids are rolled after casting, the surfaces become smooth and the cross section of the grid wires becomes rectangular.

The automatic casting process begins with an operator loading copper inserts into the fixture and initiating the automatic process. The inserts are transferred to the preheating station, and then moved to the fluxing station. The inverted fixture is then moved to the tinning station, after which encapsulation of the part by the two mold halves makes them ready for lead pouring. Lead is then dispensed into the system. The extra gates from the casting are sheared off after cooling and ejected for reprocessing by the lead furnace. The finished parts are moved to the unloading station. Figure 7.6 shows a continuous grid caster made by Wirtz Manufacturing Inc.

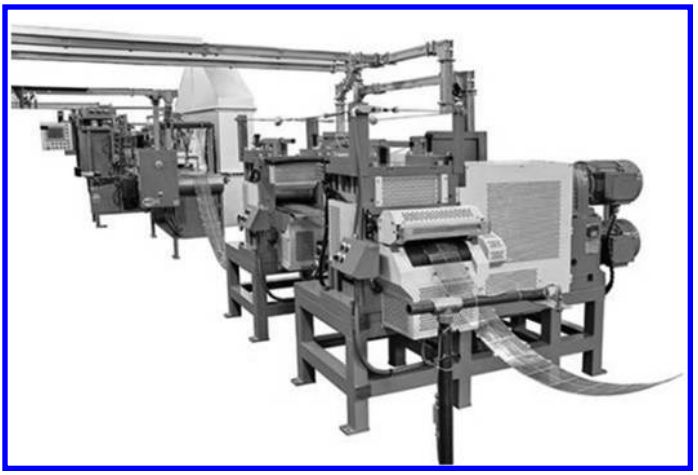

FIGURE 7.6 Continuous grid caster. (From Wirtz Manufacturing. Available at http://www.wirtzusa.com.)

7.2 LEAD OXIDE PRODUCTION

Lead oxide is the main component of the active material for both positive and negative electrodes. Lead oxide is made by oxidizing lead using either the Barton pot process or the Ball mill process.

7.2.1 Barton Pot Process

The Barton pot process (also called the Barton-like process) is a process that melts lead ingots and feeds them into a vessel or pot. The molten lead is rapidly stirred and atomized into very small droplets via a rotating paddle in proximity to the bottom of the vessel. The droplets of molten lead are then oxidized by oxygen in the air to produce an oxide coating around the droplet. Figure 7.7 shows a flowchart for the Barton pot process.

The lead oxidation process is exothermic and the generated heat is essential for sustaining a continuous reaction as more lead is introduced. The process temperature is critical for determining the degree of oxidation and crystal morphology of the lead oxide. The Barton pot process typically produces a product containing lead oxide with 15% to 30% free lead, which exists as the core of the lead oxide spherically shaped particles. Figure 7.8 shows a Barton pot.

7.2.2 Ball Mill Process

In the Ball mill process, as shown in Figure 7.9, lead pieces are fed into a rotating mill and the attrition of the lead pieces produces fine metallic lead flakes. The friction of lead flakes tumbling against each other inside the mill chamber creates sufficient heat to oxidize the lead flakes' surfaces. The degree of lead oxidation is impacted by the airflow through the system. The airflow also moves the lead oxide particles to be collected in a baghouse. The product of the Ball mill process contains 15% to 30% free lead in the shape of a flattened platelet core surrounded by an oxide coating. Figure 7.10 shows a Ball mill [3,5].

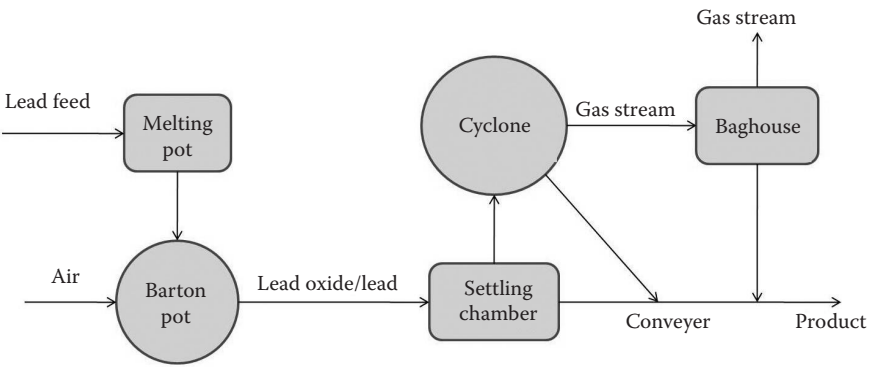

FIGURE 7.7 Flowchart of the Barton pot process.

FIGURE 7.8 Barton pot. (From Wirtz Manufacturing. Available at http://www.wirtzusa.com.)

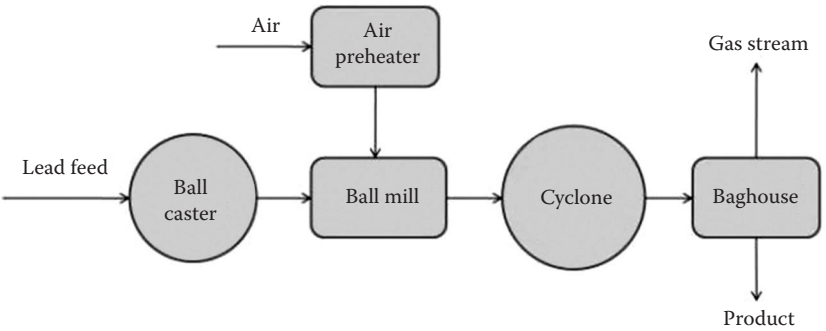

FIGURE 7.9 Flowchart of Ball mill process.

FIGURE 7.10 Ball mill. (From MAC Engineering. Available at http://www.mac-eng.com; Leader Tech United. Available at http://www.ltucompany.com.)

TABLE 7.1
Lead Oxide Characteristics of the Products of the Barton Pot and Ball Mill Processes

Characteristic	Barton Pot	Ball Mill
Particle size	3–4 mm in diameter	2–3 mm in diameter
Stability/reactivity in air	Stable	High reactivity in air
Oxide crystal structures (wt%)	5–30% β-PbO, remaining balance α-PbO	100% α-PbO
Acid adsorption (mg H_2SO_4/g oxide)	160–200	240
Surface area (m^2/g)	0.7	2.0–3.0
Free lead content (wt%)	18–28	25–35
Paste mixing characteristics	Softer paste	Stiffer paste
Paste curing	Average curing rate	Faster curing rate
Battery performance	Better battery life, low capacity	Good capacity, shorter life
Deep-cycle ability	Usually good	Sometimes good
Process control	More difficult	Easier
Production rate (kg/h)	300–900	1000
Operating costs	Low operating and maintenance costs	Higher operating and maintenance costs
Facility requirement	Smaller footprint	Bigger footprint
Energy consumption (kWh/ton)	Up to 100	100–300

Table 7.1 lists the lead oxide characteristics produced by the Barton pot and Ball mill processes.

7.3 PASTE MIXING

During the paste mixing process, both the positive and negative pastes are prepared as a dough-like material by blending lead oxide, water, acid, and other chemical additives using a mechanical mixer and the following steps:

1. Add lead oxide into the mixer.
2. Add the required additives.
3. Add water.
4. Add sulfuric acid.

Paste mixing is one of the most important processes in battery manufacturing and greatly affects the quality and life of a battery. The paste mixing machine is fully automatic and programmable logic controller (PLC) controlled. The machine comprises the main parts discussed next.

7.3.1 Batch Paste Mixer

Conventional mechanical mixers are batch type. The major types of mechanical mixers are the pony mixer, the muller, or the vertical muller (Figure 7.11). The batch paste mixer contains three major components: the paste tank, mixing system, and cooling system.

1. *Paste tank*. The paste tank is a closed cylindrical steel tank. The upper part of the tank has inspection doors and hoses for cooling air inlet and outlet. There are also pipes for the inlet of acid and water. The sides of the tank have two discharging doors that are used to dump the final prepared paste into the cone feeder.
2. *Mixing system*. The mixing system contains rotating paddles, which provide a complete mixing action of the various components (lead, acid, water, and additives/expanders) to obtain a uniform and easily pasted paste.

FIGURE 7.11 Vertical muller mixer. (From MAC Engineering. Available at http://www.mac-eng.com.)

3. *Cooling system*. In the mixing cycle, cooling is essential because heat is generated by the exothermic reaction between H_2SO_4 and lead oxide. Failure to maintain proper paste temperature causes hardening of the paste before it can be used. The temperature of the paste needs to be controlled, and this is often achieved by either cooling the mixer or evaporating the extra volume of water in the paste mixture. It is important to maintain the mixing temperature to ensure a good-quality paste results. Often, two types of cooling systems are used in the paste mixing system. The first cooling system, an air-conditioning (AC) system, uses a fan blowing over the paste surface for cooling. The second cooling system uses circulating water that runs through the bottom and surrounding area of the tank to maintain the desired temperature/cooling. The peak temperature limit for the pasting cycle is 60°C, whereas the final paste or dumping paste temperature should be less than 50°C.

The paste viscosity will rise in the beginning of paste mixing, but then gradually decreases. The ratio of lead oxide, water, and sulfuric acid varies depending on the type of battery applications. For example, plates for SLI application are generally made at a low $PbO:H_2SO_4$ ratio, whereas plates for deep-cycle applications are made at a high $PbO:H_2SO_4$ ratio. On the other hand, the amount of sulfuric acid affects the plate density because the more acid used, the lower the plate density. Paste density is measured by using a cup with a hemispherical cavity and by the measurement of paste consistency (viscosity) with a penetrometer.

7.3.2 Continuous Paste Mixer

A continuous paste mixer produces lead-acid battery paste over a broad output and chemistry range. The continuous mixer uses a gravimetric feeder for dry material and a positive displacement pump for liquid material to control the dosage of ingredients. Figure 7.12 shows a continuous mixer that has a clamshell with 127-mm-diameter twin co-rotating shafts. The continuous mixer has paddle and screw mechanisms to mix and drive material through the chamber. With the co-rotating shafts and the close clearances between the paddles and between the mixing chamber wall and the paddles, a continuous mixer can produce a homogenous paste in about 35 sec.

A continuous paste mixer provides the following benefits:

a. Requires minimum startup time
b. Provides a homogeneous paste in 35 seconds of mixing time
c. Fully enclosed and environmentally sealed
d. No bag house or cooling ventilation required
e. Ability to mix high carbon concentrations
f. More uniform additive dispersion of fiber and carbon additives
g. Minimal fiber clumping
h. Ability to generate tetrabasic crystals of variable size and concentration
i. Ability to regulate paste temperature
j. Small footprint

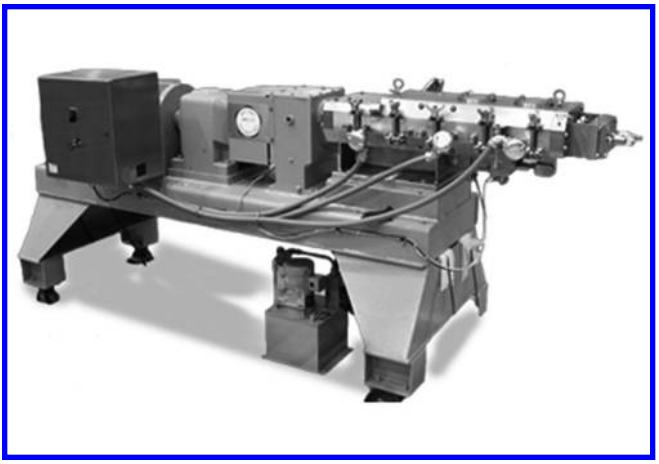

FIGURE 7.12 Continuous paste mixer. (From Battery Technology Solutions Inc. Available at http://www.batechsol.com.)

7.4 PASTING

Pasting is a process in which prepared paste is integrated with the grid to produce a battery plate. This process is carried out through extrusion, and the paste is pressed by a scraper or by machine into the grid interstices. Two types of pasting machines are used by manufacturers, a belt paster or a fixed-orifice paster. A belt paster presses the paste into the open side of a grid that is being conveyed past a paste hopper on a porous belt, and an orifice paster pushes paste into both sides of the plate simultaneously. Figure 7.13 shows a continuous belt paster and Figure 7.14 shows a continuous orifice paster.

The pasting machine consists mainly of a grid feeding system, hopper system, pasting belt system, after-hopper conveying system, and a PLC/main controller.

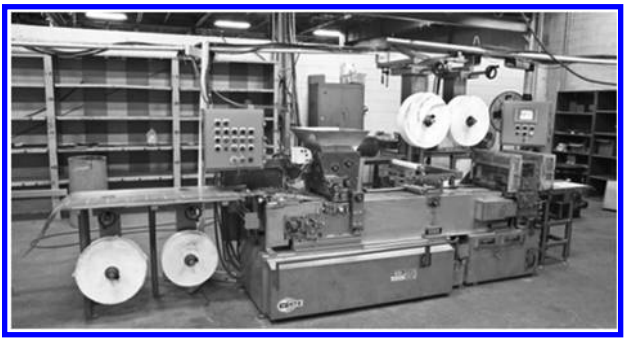

FIGURE 7.13 Continuous belt paster. (From Wirtz Manufacturing. Available at http://www.wirtzusa.com.)

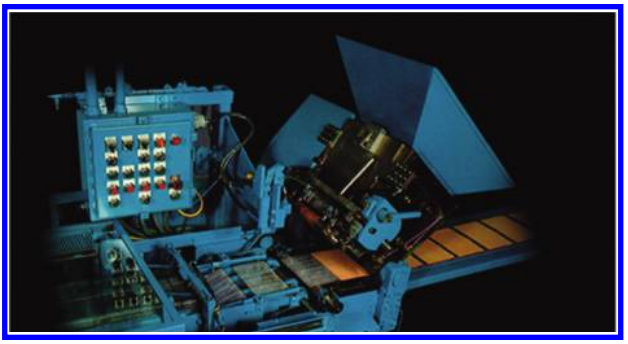

FIGURE 7.14 Continuous orifice paster. (From Wirtz Manufacturing. Available at http://www.wirtzusa.com.)

1. *Grid feeding system*. In a grid feeding system, panels are placed manually on two parallel conveyor chains. The gap between the two chains is adjusted according to the desired grid width. Two vacuum suction feeders pick panels from lugs automatically and place them on the feeding conveyor, which feeds panels directly into the hopper, through a feeder roller. Figure 7.15 shows a grid feeder.
2. *Hopper function and operating mechanism*. The hopper is main part/components of the pasting machine. The paste is dropped into the hopper's form cone feeder and by the combined action of rotating paddles and roller,

FIGURE 7.15 Grid feeder. (From MAC Engineering. Available at http://www.mac-eng.com.)

paste is continuously applied on the panels. The main parts of the hopper and their functions are as follows:

a. *Main pasting roller.* The main pasting roller is made of stainless steel with a lining on its surface. The lining is used to compact the pasted plate.
b. *Feeding roller.* Grids are automatically or manually placed onto the transfer belt of the pasting machine before being moved under the paste hopper. The feeding roller is fixed at the front of the hopper. It can easily control up and down movements to avoid grid blocking and provide safe grid transfer into the hopper bottom even during fast operation. Most smaller-sized plates are made as a double panel that is joined at the bottom or at the top edge, or as multiple panels. Larger industrial stationary or traction battery plates are pasted lengthwise individually.
c. *Trowel roller or squeegee.* The trowel roller is used by a cloth belt paster in an attempt to redistribute the paste that was not applied correctly up front because the amount of paste that is applied via the pasting machine is regulated by the spacing of the hopper above the grid. The trowel roller or squeegee controls paste weight and homogeneity. The trowel roller is adjusted according to the particular panel's weight and thickness and can pack the paste thicker and denser than a squeegee machine. Fixed-orifice pasters and steel belt pasters do not have a trowel roller; rather, the machine and the tooling apply the paste where needed.
d. *Hopper.* The hopper is driven by a separate motor and reduced gear system. The rpm/cycles is controlled through the hopper's control panel. The hopper is connected to a pneumatic cylinder, which safely lifts and lowers the hopper. Lifting is required either when grids are jammed inside the hopper or for cleaning of the machine. Figure 7.16 shows a paster hopper.

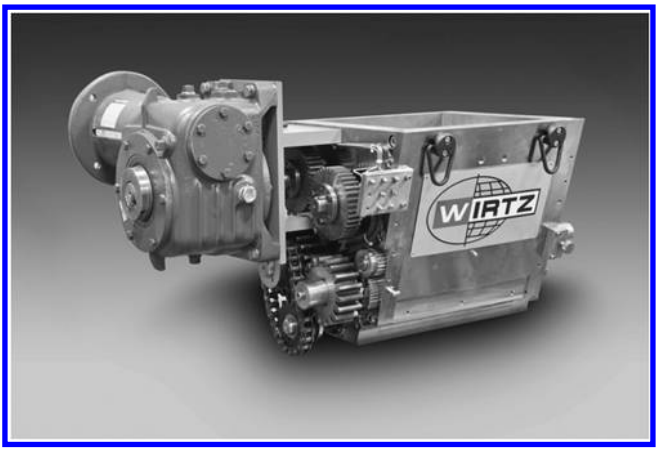

FIGURE 7.16 Paster hopper. (From Wirtz Manufacturing. Available at http://www.wirtzusa.com.)

e. *Hopper paddles.* Paddles are designed so that appropriate paste and required conditions within the hopper are achieved. These paddles mix the paste in the hopper and also create thrust/pressure in a downward direction.
f. *Pasting belt and operating mechanism.* The pasting belt is driven by a separate motor and reducing gear transmission system. The driving motor has a separate electronic driver for better operational adjustment. A seamless pasting belt is suggested to achieve better pasting results. Additionally, belt tensioning, roller belt squeezing (used to remove/extract moisture from pasting belt), and belt scraping are provided by the machine and work pneumatically.

3. *Conveying system.* After the hopper but before the flash-drying oven is a conveying system. It consists of a small rubber roller, one pair of compact or press rollers, and one pair of acid-showering rollers. The plate conveying system is designed to ensure safe plate transfer to the flash-drying oven.
   a. *Compacting roller.* This steel roller, which is wrapped with rubber and cotton, is used to ensure the pasted plates are the proper thickness and compactness.
   b. *Lug washing system.* This is used to remove extra/undesirable paste from the sides of the plates (lugs) and the gap in between two plates that may be left after the hopper step. The combined action of a stream of water and pressurized air is used for this purpose.
   c. *Safety control.* The machine has an emergency stop bar, enabling the operator to intervene immediately during machine operation. Such a machine is equipped with all of the necessary guards to provide for safe operation.
4. *Flash-drying oven.* After pasting, the plates are racked or stacked for curing. Stacked plates contain enough moisture that the plates stick together. Furthermore, the moisture content of the plate impacts the curing process. So to remove extra moisture and to attain the desired moisture content, the plates are usually passed through a flash-drying oven (FDO) to dry the plate surface prior to stacking in a so-called *flash-drying process.* The moisture content should be 8% to 11%, which can be controlled by the speed of the conveyor and the temperature of the FDO. Figure 7.17 shows a flash-drying oven.

   It has been found that if the oven is powered by a combustion process, some of the carbon dioxide that is generated in such a process might be absorbed on the plate surface such that the surface becomes harder. The elevated temperature of the flash-drying process also helps start the curing reactions. Small plates are usually stacked horizontally on pallets and thicker, larger plates are usually placed with the long edge upward in racks.
5. *Collection end.* At the exit end of the FDO is a link chain conveyor and three rollers. The speed of the chain conveyor is set in such a way as to achieve better overlapping or stacking of the panels. Figure 7.18 shows a stacker.

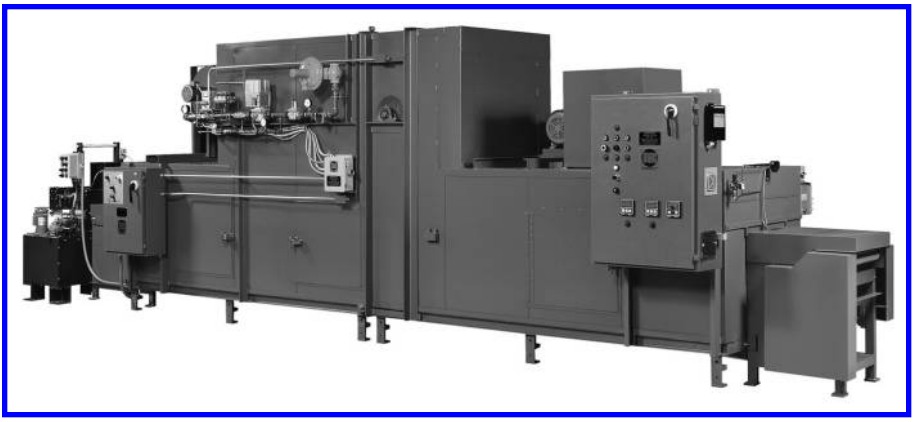

FIGURE 7.17 Flash-drying oven.

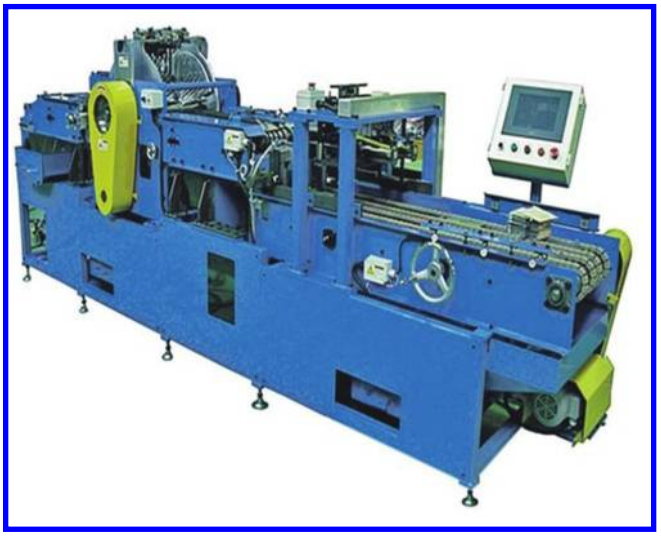

FIGURE 7.18 Stacker. (From International Thermal Systems. Available at http://internationalthermalsystems.com/batterymanufacturing.)

A pasting machine has the capacity to paste more than 50,000 panels per shift per day.

7.5 CURING

The curing process is designed to make the paste bond with the current collector and also make the paste into a cohesive, porous material. The curing process is often done at elevated temperature and humidity to ensure the PbO reacts with sulfuric acid to form lead sulfate salts, and to oxidize the lead core of the lead oxide to PbO to form additional lead sulfate salts. Generally, the higher the temperature employed

during curing, the better the adhesive bond produced. Curing is an important and time-consuming aspect of the manufacture of lead-acid batteries as the wet active paste material precursor is cured and converted to a dry porous mass.

The battery paste, which has an alkaline pH, reacts with lead alloy in the grid to partially convert the lead-alloy compounds and ultimately the tetrabasic lead sulfate, $4PbOPbSO_4$ (4BS) and tribasic lead sulfate, $3PbOPbSO_4H_2O$ (3BS). The 4BS typically forms at higher temperature (>70°C) and higher humidity, whereas the 3BS typically forms at low temperature and low humidity. The production of 4BS generally requires a controlled temperature profile and humidity during the curing process. Premature dryout or cooling of the plates could inhibit the formation of 4BS. The addition of red lead (Pb_3O_4) can promote the production of 4BS over a larger range of temperature and relative humidity. One of the reasons the curing process usually takes a long time is because the production of 4BS entails nucleation and growth. Nucleation is carried out at about 70°C or a higher temperature at high humidity. Nucleation during the curing process can have an induction period of about 10 h since 4BS forms as molecules that slowly coalesce by diffusion into seeds. The seeds react with nearby material to grow into crystals. When curing is adjusted to preclude nucleation and growth of 4BS, a predominance of 3BS is produced. The 3BS has a uniform crystal shape and size of $3 \times 0.5 \times 0.5$ μm. When a plate is pasted with 3BS, the plate has a uniform porosity and high cranking performance.

The discharge capacity of a battery is affected by the porosity and surface area of the porous battery electrode. The 3BS forms as small needle-like crystals that measure about 3 μm long and less than about 1 μm each in width and thickness. The 4BS crystals are larger and grow in length from several microns to several hundred microns. The longer 4BS crystals have width and thickness in proportion to length. A 300-μm-long 4BS might have a width of 60 μm and a thickness of 50 μm, which will have a surface area of 72,000 μm^2 and a volume of 900,000 μm^3. The 4BS crystal when packed with 3BS crystals would hold about 10^7 3BS, which corresponds to a total surface area of about 7.2×10^6 μm^2 and represents 1000 times greater surface area. In high-discharge-rate batteries such as SLI batteries, 3BS is the preferred active material precursor. In deep-cycle and long-life stationary batteries, 4BS is the preferred active material precursor. 4BS is also the preferred precursor for use in nonantimony grid batteries because 4BS can help prevent premature capacity loss, which causes shorter battery life.

Lead oxides are yellowish to brownish. The color of 3BS is white and the color of 4BS is orange. When 3BS is present in cured plates, the 3BS has a pale peach color. The presence of 4BS is revealed by a deep orange color. Sometimes, 4BS in cured pasted plates has a dark greenish color due to the presence of unoxidized free lead. Unoxidized free lead is undesirable because it reacts with sulfuric acid to form lead sulfate during the soak and formation process. Lead sulfate is difficult to convert to lead dioxide on the positive plate, which reduces plate capacity. Unoxidized free lead should not be higher than 2 wt% because it will lead to shedding and spalling failure of the positive plates and high self-discharge of formed lead dioxide plates [6].

The conditions for the curing process vary pending on the paste formulation and the battery applications. The curing process is often carried out using curing chambers, as shown in Figure 7.19, with controlled temperature and humidity to ensure

FIGURE 7.19 Curing chamber. (From International Thermal Systems. Available at http://internationalthermalsystems.com/batterymanufacturing.)

sufficient moisture and heat are available to oxidize free lead in the paste. The curing temperature ranges from 65°C to 90°C and the curing oven humidity is maintained above 95%.

Curing the paste at higher temperature for extended hours will produce a high percentage of tetrabasic lead sulfate and result in a plate with lower energy density. At the end of curing, the free lead content of the paste should be lower than 2%. Table 7.2 lists the typical curing profiles.

A conventional curing process for SLI plates is the *hydroset* process, which is conducted at low temperature and low humidity for 24 to 72 h. The curing temperature ranges from 25°C to 40°C and the humidity ranges from 8% to 20% of water. The plates are usually covered by canvas, plastic, or paper to retain the moisture. Hydroset is usually carried out in an enclosed room where the temperature and humidity can be controlled by the required climatic conditions. During the hydroset curing process, the plates are under an exothermic reaction and reach a peak temperature as the plates cure and temperature and humidity decrease. Plates produced with the hydroset curing process will have tribasic lead sulfate, which gives more energy density.

TABLE 7.2
Typical Curing Profile

No.	Item	Description
1	Loading cycle	Ramp up to 54°C and 95% relative humidity (RH) and hold until all plates are loaded.
2	Curing cycle	Ramp up to 80°C and 95% RH and hold for 72 h.
3	Drying cycle	Ramp up to 90°C and 75% RH and hold for 24 h.

Paste with insufficient curing is easily broken. The uncured paste is pale in color and soft. If the plate is insufficiently cured, it can be rewetted and reheated to force the paste to cure. Another way is to dip the partially cured paste into dilute sulfuric acid, which is called *pickling*. The pickling curing process is also used for curing powder-filled tubular positive plates.

Once the plates are cured, they can be stored with a long shelf-life.

7.6 FORMATION

After curing, the plates need to be electrically formed or charged to become functional positive and negative electrodes. During formation, the positive paste is converted to brownish black lead dioxide, and the negative paste is converted to a soft gray lead.

Before switching on the current for the formation of the active masses, cured plates are left in H_2SO_4 solution on open circuit for a certain period of time. This process is called *soaking*. PbO and basic lead sulfates are unstable in H_2SO_4 solution and, hence, chemical sulfation reactions proceed. It has been established that soaking in H_2SO_4 of 1.05 relative density results in formation of 3BS, 1BS, and, after 4 h, small amounts of $PbSO_4$. In more concentrated H_2SO_4 solutions, $PbSO_4$ dominates. Capacity, cold cranking, and cycle life tests have been performed with batteries soaked in the three acid solutions for different periods of time. It has been established that, depending on acid concentration and duration of soaking, the battery capacity may increase by 10% and the time of high-rate discharge at –18°C may be prolonged by about 1 min. Battery life may also be improved. As such, soaking has been introduced as a separate technological procedure with continuously controlled parameters in order to ensure stable battery performance characteristics [7–11].

7.6.1 Formation of Positive Plates

The two major formation methods for positive plates that convert the lead monoxide paste to lead dioxide are the two-stage formation process (used for stationary and traction batteries) and the one-stage formation process (used for SLI batteries).

In the two-stage formation process, the electrolyte is dumped to remove the low-density initial formation electrolyte and refilled with more concentrated electrolyte. The refilled concentrated electrolyte is mixed with the dilute initial acid residue, which is absorbed in the plates or trapped in the case. During the first formation stage, H_2SO_4 and H_2O penetrate from the bulk of the solution into the plate. As a result of chemical and electrochemical reactions, lead oxide (PbO) and basic lead sulfates are converted into α-PbO_2 and $PbSO_4$. These compounds form zones that advance into the paste interior. During the second stage of formation, the $PbSO_4$ is oxidized to β-PbO_2. H_2SO_4 is formed and diffuses into the volume of electrolyte. Ion diffusion and migration are considered to be the rate-limiting steps of the processes.

During the first formation stage, the conversion of PbO to PbO_2 + $PbSO_4$ is affected by the degree of paste sulfation, formation current, temperature, and phase composition of cured paste. These parameters influence the capacity and cycle life

performance of the battery. It has been established that the capacity of the positive plate is determined by the structure of PAM and the β/α-PbO_2 ratio.

7.6.2 Formation of Negative Plates

The formation method for negative plates for converting the lead monoxide paste to lead is also a two-stage formation process.

During the first stage, electrochemical reduction of PbO and basic lead sulfates ($PbSO_4$) occurs and a lead skeleton (network) is formed. Besides converting PbO to lead, chemical reactions of $PbSO_4$ formation also proceed. During the first stage, $PbSO_4$ crystals remain incorporated in the lead skeleton, and $PbSO_4$ + Pb zones are formed on both plate surfaces and advance into the interior of the plate.

During the second stage, reduction of $PbSO_4$ to Pb occurs and the lead crystals obtained are deposited on the lead skeleton surface in strongly acidic solution.

During formation, both the pore radii and the porosity of the active mass increase. The formation can be carried out either through tank formation (prior battery assembly) or case formation (after battery assembly).

7.6.3 Tank Formation

Tank formation is conducted by passing electric current through cured plates placed in tanks filled with sulfuric acid. The formation tanks are often made of PVC, polyethylene, or lead with slots. The cured plates are placed in the formation tank as doubles, with two to five plates stacked together and facing the counterelectrode in adjacent slots spaced 1 inch or less away. In tank formation, all of the positive plates are placed on the same side and all of the negative plates are placed on the other side. All plates with the same polarity are connected by welding a heavy lead bar, and the two bars are connected to a low-voltage, constant-current power supply. Besides forming the positive plates together with the negatives plates, the plates also can form against dummy pasted plates or bar grids. The tanks are arranged so that the acid can be drained and refilled because formation increases the electrolyte acid concentration (Figure 7.20) [12].

The tank formation conditions depend on the eventual battery applications. A variety of formation conditions are used, with variables like electrolyte density, charging rate, and temperature. The sulfuric acid used for charging is typically dilute, with a specific gravity in the range of 1.05 to 1.15. The charging current is fixed by battery manufacturers; some use a sequence of two to three charging rates for different periods of time. Tank-formed plates are unstable because the negatives will spontaneously be oxidized when contacting air, which requires dry charging before use.

7.6.4 Case Formation

The more usual method of formation is to completely assemble the battery, fill the electrolyte, and then apply the formation charge. Figure 7.21 shows the assembled batteries under formation charge.

FIGURE 7.20 Lead-acid battery formation tank. (From http://www.flickr.com/photos/flexpro/sets/72157616389278240/detail.)

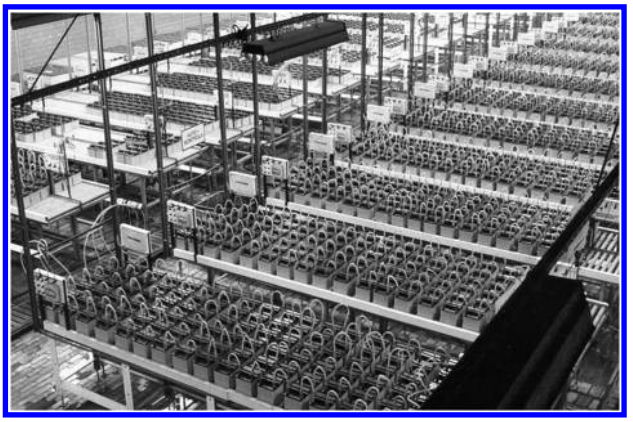

FIGURE 7.21 Case formation.

7.7 BATTERY ASSEMBLY

A 2-V lead-acid battery cell consists of at least one positive plate, one negative plate, and a separator between them. Normally, a 2-V cell contains about 3 to 30 plates with separators in between.

The battery assembly process includes the following steps: group stacking, alignment, group burning, group alignment, group insertion, inspection and terminal alignment, internal short circuit testing check, intercell welding, shear testing, case cover sealing, leak testing, aluminum foil sealing, acid filling, and packing.

7.7.1 Group Stacking

In the group stacking process, positive plates, negative plates, and separators are stacked into a group by a stacking machine or manually. The stacking procedure

FIGURE 7.22 Stacker. (From Wirtz Manufacturing. Available at http://www.wirtzusa.com.)

involves placing alternate negative and positive plates with separators placed in between the two. When using absorbed glass mat (AGM) separators, the AGM separators are placed so that their glass mat side is always toward the positive plate. This is to minimize the shedding of positive active mass during operation. Depending on the type of battery, the type and number of plates in a cell is determined during this activity. Figure 7.22 shows a stacker.

7.7.2 Alignment

The stacked groups are aligned in a box to facilitate the group welding procedure. The box allows for the alignment of six groups at a time (i.e., one battery at a time). Now this aligned box is ready for group burning.

7.7.3 Group Burning

Those groups which are aligned in a box are burned in such a way that the negative plates' lugs are burned with a strap or a pole, which becomes a negative terminal/strap, and vice versa for the positive plates.

The stacked plates are then staged on roller conveyors or carts to the interplate welding operations, where the positive plates and negative plates are welded into individual groups. Two general methods of welding are used. The first is done with the lugs of the plates facing upward, and the other is done by immersion of the lugs of the plates into a pool of molten lead alloy. The first method is the traditional method for assembling lead-acid batteries and is called *comb mold welding*. In comb mold welding, the plate lugs fit up through slots in a comb mold as shown in Figure 7.23. The shape and the size of the group strap are delineated by the dam and back iron portion of the tooling. A method for increasing comb mold welding efficiency is to premade slotted crowfoot posts that fit over the plate lugs.

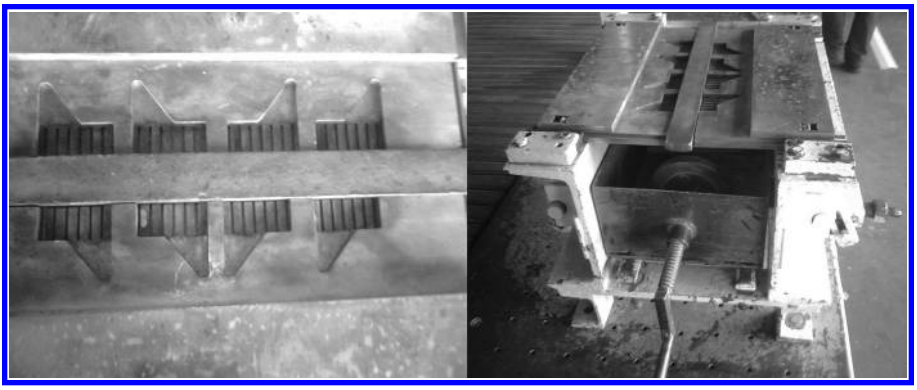

FIGURE 7.23 Comb mold for group burning.

The second type of welding process, which welds the plates with the plate lugs facing downward, is called *cast-on strap (COS) welding.* Most of the SLI batteries are using COS as the standard welding process. In COS, the stacked plates are loaded into the slots of the cast-on machine. The cast-on machine will place the stacked plates upside down so that the plate lugs are facing downward. A mold that has corresponding cutouts to the desired straps and posts is preheated and filled with molten lead alloy. The upside down stacked plates are immersed into the mold to be welded. External cooling in the cast-on machine then solidifies the strap onto and around each lug. It is important to note that the lead alloy used in the welding process should match with the plate alloy. Lead or lead calcium alloy should not join with lead antimony alloys. Comb mold welded plate straps are thicker and smoother than cast-on straps. Cast-on straps often show a convex meniscus of metal between the adjacent plate lugs on the underside of the strap if the lug is properly cleaned of paste. Figure 7.24 shows a COS machine.

Visual examination is important as the first quality check for the weld. A good weld is required between each plate lug and the strap so that it will have minimum voltage drop during high-rate-discharge performance. Electrical testing for short circuits is the second quality check before further assembly.

7.7.4 Group Alignment

Group alignment deals with aligning the separators in a group accurately so that no short circuit is observed within the group when those groups are inserted in the container. A worker checks the groups visually so that if there are any problems with the group it can be removed before the insertion.

7.7.5 Group Insertion

Once the group alignment check has been conducted, the aligned groups are inserted in the container in such a way that there should not be any mistake in the polarity of the group. Spacers are also inserted as they are subjected to the number of plates.

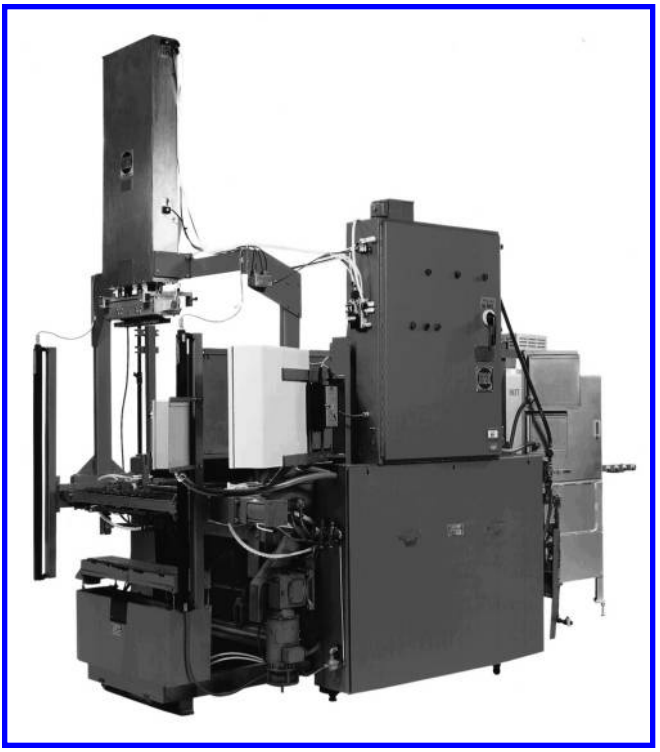

FIGURE 7.24 Cast-on strap machine. (From MAC Engineering. Available at http://www.mac-eng.com.)

7.7.6 Inspection and Terminal Alignment

Manual inspection will be conducted to check whether the terminals are aligned or not. Workers can also do the short circuit testing of the groups manually as the checking is provided alongside.

7.7.7 Short Circuit Testing

The battery will then be tested for short circuits. A short testing machine checks the battery to determine if the polarity is correct or not. If the battery is short circuited, then it is removed from the line. Figure 7.25 shows a short circuit testing machine.

7.7.8 Intercell Welding

After short circuit and polarity testing, the groups of the battery will be welded together. A 12-V lead-acid battery consists of six cells. These cells are connected through either a loop over the partition or through the partition wall. The loop-over partition requires long intercell connections to be used, where the cell-to-cell connections travel over the intercell partition wall and are seated in a slot. When connecting the cells through the partition wall, the tabs on the ends of the cast straps

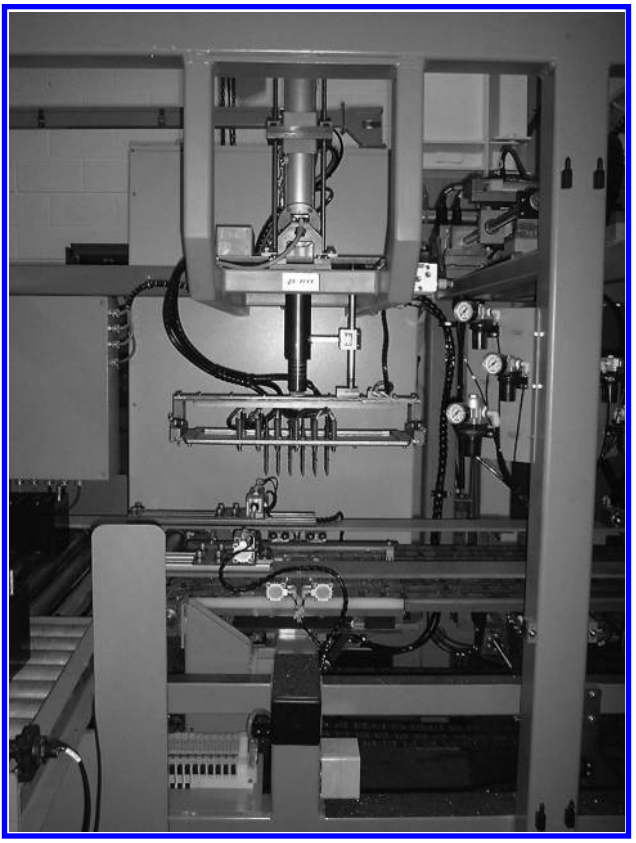

FIGURE 7.25 Short circuit test equipment. (From Wirtz Manufacturing. Available at http://www.wirtzusa.com.)

are positioned over holes that have been prepunched into the intercell partitions of the battery case and welded together manually using a torch or automatically by a resistance welding machine. This second method also squeezes the tabs and the intercell partition to provide a leak-proof seal. Figure 7.26 shows an intercell welding machine.

7.7.9 Shear Testing

After welding, the battery is again tested for short circuiting. It will also be tested for shear to check whether the weld is strong enough or not. This activity is performed by a worker through a shear testing device that runs on pneumatic pressure.

7.7.10 Case Cover Sealing

After shear testing, the battery cover will be sealed on the battery case. Enclosed cells are important to minimize safety hazards such as internal short circuits from

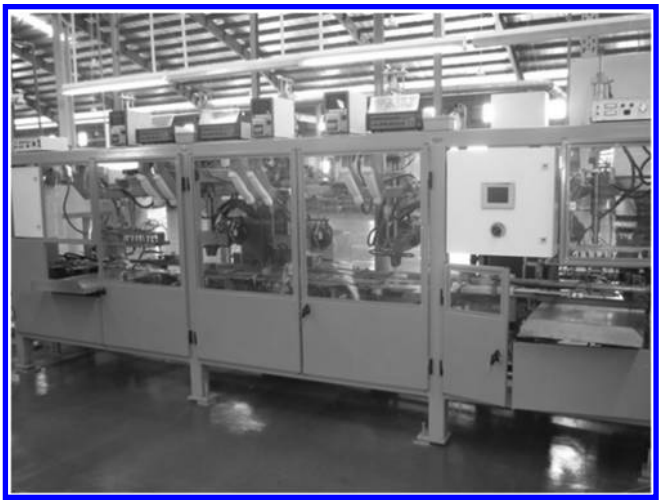

FIGURE 7.26 Intercell welding machine. (From Wirtz Manufacturing. Available at http://www.wirtzusa.com.)

electrolyte mist. Four different types of processes are used to seal the case to the cover.

1. *Heat (fusion) sealing.* Heat sealing is done by preheating both the case and the cover on a plate, then forcing the two together mechanically, or by ultrasonic welding of the case and cover. Once the battery case and cover have been heat sealed, it is almost impossible to repair. If the battery is found damaged, the cover and the case are discarded and replaced with a chance that the grouped plates can be salvaged. Figure 7.27 shows a heat sealing machine.
2. *Epoxy cement sealing.* Epoxy cement sealing is done by filling a groove in the cover with epoxy cement. The battery is inserted and positioned so the

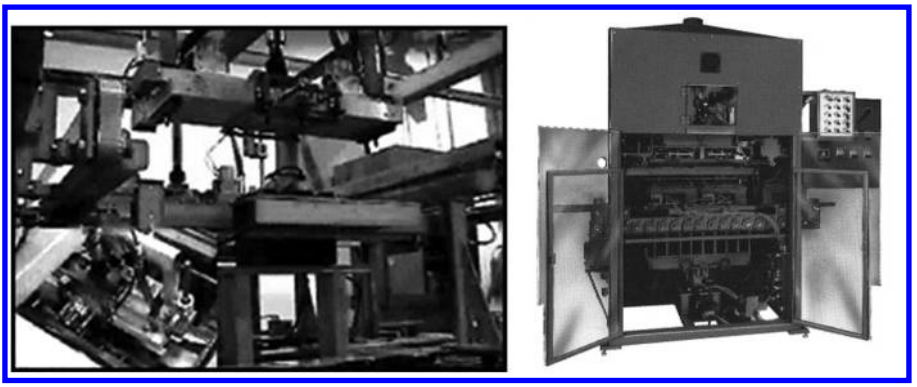

FIGURE 7.27 Heat sealing machine. (From MAC Engineering. Available at http://www.mac-eng.com.)

FIGURE 7.28 Epoxy sealing system.

case and intercell partition lips fit into the epoxy-filled groove. To activate the epoxy cement, the batteries are often passed through a continuous oven.

3. *Tar (asphalt) sealing.* Traditionally, lead-acid batteries have been sealed using tar. Molten tar is dispensed from a heated kettle to fill a groove between the case and the cover. The tar must be hot enough to flow easily but cool and viscous enough to solidify. Tar sealing allows for easy repair of a battery.
4. *Epoxy glue sealing.* The epoxy glue sealing process employs either solvent cement or a thermal seal. An epoxy glue seal is often used for stationary batteries and traction cells so that coolant can be circulated through the terminals. Figure 7.28 shows an epoxy seal system.

7.7.11 Leak Testing

After heat sealing, leak testing of the battery is done. A leak testing machine checks the batteries for leakage between the cells by applying and maintaining air pressure. The machine also checks the container's outer walls for leakage. The machine also stamps the lids with coding for the batteries. Figure 7.29 shows a leak testing machine.

7.7.12 Terminal (Post) Burning

Cell connectors and terminal post burning must be done in such a manner that there is complete fusion of the post strap top and the cover lead bushing with the connector ring or terminal post. The terminal burning machine places the battery under the

FIGURE 7.29 Leak testing machine. (From MAC Engineering. Available at http://www.mac-eng.com.)

working station and ignites the welding torches automatically. The welding torches rotate and descend onto the battery to burn the terminal posts within the bushing according to a preselected time. Once this operation has been completed, the torches are lifted away while rotating at a preselected speed to ensure a good finish (meniscus). Figure 7.30 shows a terminal post burning machine.

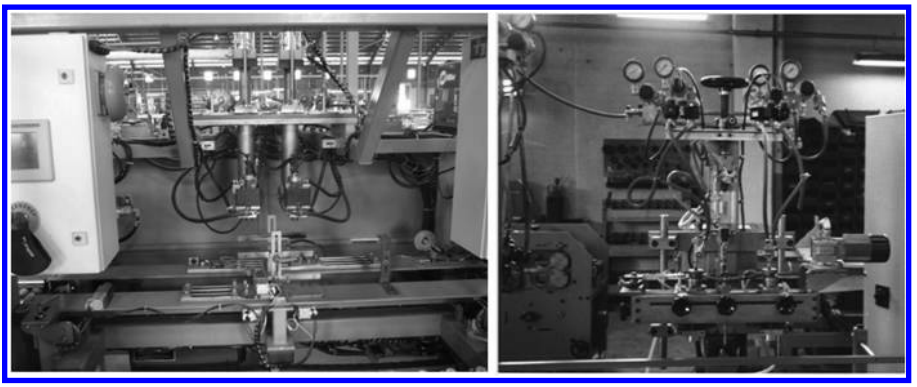

FIGURE 7.30 Terminal post burning machine. (From Wirtz Manufacturing. Available at http://www.wirtzusa.com; G. Mayer, US Patent Application, US 2006/0093912 A1, 2006.)

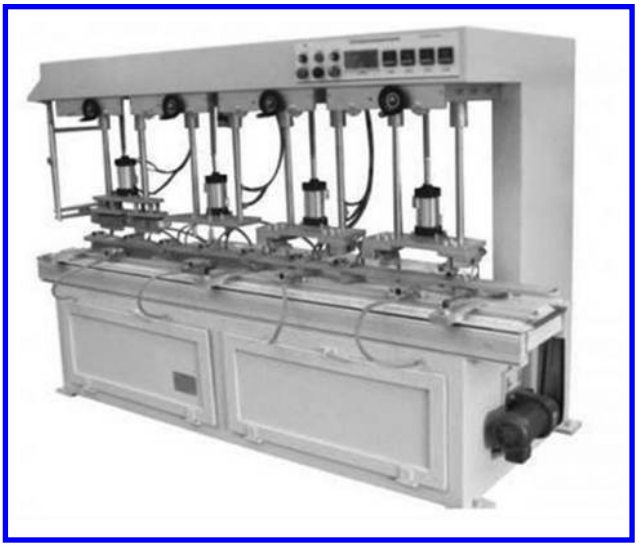

FIGURE 7.31 Aluminum foil sealing machine. (From Leader Tech United. Available at http://www.ltucompany.com.)

7.7.13 Aluminum Foil Sealing

Aluminum foil sealing is done on the vent plug holes where the foiling is included in the design of the battery. Aluminum foil sealing can prevent the battery plate from experiencing oxidation and self-discharge before the battery is filled with acid. Figure 7.31 shows an automated aluminum foil sealing machine.

7.7.14 Acid Filling

The electrolyte used in lead-acid batteries is sulfuric acid. The properties of sulfuric acid with different specific gravities are shown in Tables 7.3 and 7.4.

After the battery has been filled with acid, short circuit testing and leak testing will be conducted to ensure the battery has no short circuits and no leaks. Figure 7.32 shows the acid-filling machine.

7.7.15 Packing

The finished battery will be cleaned and packed in a carton for shipping. Plastic caps will be placed on both the positive and negative terminals to prevent a short circuit during shipping.

7.8 QUALITY ASSURANCE AND CONTROL

Quality assurance and control are very important to the high-volume production process of lead-acid batteries. Quality assurance refers to the process of verifying or determining whether the lead-acid battery meets the product specifications. Quality

TABLE 7.3
Chemical Properties of Sulfuric Acid

Specific Gravity		Temperature	H_2SO_4			Freezing	Electrochemical Equivalent per
@ 15°C	@ 25°C	Coefficient α	wt%	vol%	mol/L	Point (°C)	Liter (Ah)
1.000	1.000	–	0	0	0	0	0
1.050	1.049	33	7.3	4.2	0.82	–3.3	22
1.100	1.097	48	14.3	8.5	1.65	–7.7	44
1.150	1.146	60	20.9	13.0	2.51	–15	67
1.200	1.196	68	27.2	17.7	3.39	–27	90
1.250	1.245	72	33.2	22.6	4.31	–52	115
1.300	1.295	75	39.1	27.6	5.26	–70	141
1.350	1.345	77	44.7	32.8	6.23	–49	167
1.400	1.395	79	50.0	38.0	7.21	–36	
1.450	1.445	82	55.0	43.3	8.20	–29	
1.500	1.495	85	59.7	48.7	9.20	–29	

TABLE 7.4
Electrolyte Specific Gravity for Various Battery Applications

	Specific Gravity	
Type of Battery	Moderate Environment	Tropical Environment
SLI	1.260–1.290	1.210–1.230
Heavy-duty	1.260–1.290	1.210–1.240
Golf cart	1.260–1.290	1.240–1.260
Electric vehicle	1.275–1.325	1.240–1.275
Traction	1.275–1.325	1.240–1.275
Stationary	1.210–1.225	1.200–1.220
Railroad	1.250	1.250
Aircraft	1.260–1.285	1.260–1.285

control refers to the implementation of proper manufacturing techniques and ensuring that adequate raw material is used for the manufacturing process.

To achieve quality assurance and control, it is critical to ensure the following checks are implemented throughout the raw material and manufacture process:

1. Inspection of incoming raw material
2. Inspection of grid weight and appearance
3. Lead oxide composition check
4. Paste density and paste temperature monitoring
5. Pasted plate weight and paste moisture content check
6. Cured plate inspection
7. Finished electrode inspection

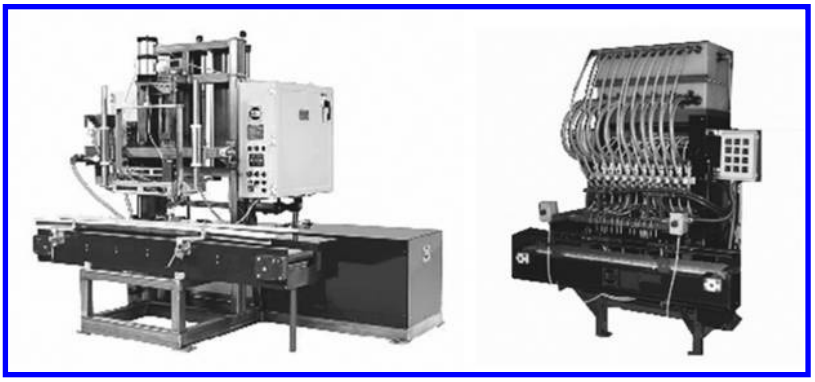

FIGURE 7.32 Acid filling machine. (From Leader Tech United. Available at http://www.ltucompany.com; G. Mayer, US Patent Application, US 2006/0093912 A1, 2006.)

8. Inspection of container, cover, vent plug, separator, packing material, and accessories
9. Electrical tests for short circuit
10. Final inspection of finished product

7.9 SUMMARY

Lead-acid technology is the most widely used electrochemical system. It is used in numerous applications from automobile SLI batteries to backup for UPSs and grid energy storage and for traction in battery electric vehicles. During the past 150 years, three major battery technologies were developed: flooded lead-acid batteries, valve-regulated lead-acid batteries, and absorbed glass mat lead-acid batteries.

Several manufacturing processes have been developed over the years from batching to continuous, with equipment getting more efficient and less labor intensive and products getting better and providing higher quality and higher performance. During the past decade, the demand for better battery performance and innovation has driven the lead-acid battery industry to develop new and innovative equipment. It is believed that lead-acid battery technology will continue to play an important role in energy storage and that innovative lead-acid technology research will provide new products for years to come.

REFERENCES

1. International Thermal Systems. Available at http://internationalthermalsystems.com/batterymanufacturing.
2. Wirtz Manufacturing. Available at http://www.wirtzusa.com.
3. MAC Engineering. Available at http://www.mac-eng.com.
4. Battery Technology Solutions Inc. Available at http://www.batechsol.com.
5. Leader Tech United. Available at http://www.ltucompany.com.
6. G. Mayer, US Patent Application, US 2006/0093912 A1, 2006.
7. Available at http://www.labatscience.com/2_1_2_4.html.

8. D. Pavlov, S. Ruevski, and T. Rogachev, "Processes in Positive Lead/Acid Battery Plates during Soaking Prior to Formation," *J. Power Sources*, 46 (1993), 337–348.
9. D. Pavlov, S. Ruevski, and T. Rogachev, "The Processes in the Positive Plates during Pickling before Formation," in *Proc. Int. Cong. LABAT '93*, June 7–11, 1993, Varna, Bulgaria, 152.
10. D. Pavlov, "Mechanism of the Processes of Formation of Lead-Acid Batteries Positive and Negative Plates," in *Proc. Symp. on Batteries for Traction and Propulsion*, 1972, Columbus Section of the Electrochemical Society, 135.
11. M. Dimitrov, D. Pavlov, T. Rogachev, M. Matrakova, and L. Bogdanova, "Processes Taking Place in the Paste of Lead-Acid Battery Plates during Soaking Prior to Formation and Their Influence on the Battery Performance," *J. Power Sources*, 140 (2004), 168.
12. Available at http://www.flickr.com/photos/flexpro/sets/72157616389278240/detail.

8 Battery Testing and Diagnostic Instrumentation

Isidor Buchmann

CONTENTS

8.1 INTRODUCTION

Batteries need more than just charging and then being used—proper care is instrumental to delivering good performance and achieving a long service life. Care begins by storing and operating batteries at cool temperatures, and charging and discharging them at moderate currents. There is some truth to why well-cared batteries outperform neglected ones; studies can back this up.

Device manufacturers measure battery runtime with a perfect pack, a condition that exists only for a short time. Capacity fade begins as soon as the battery leaves the factory. Unlike a mechanical device that displays wear and tear with use, a battery does not change physical shape whether fully charged or empty, nor does it disclose its age. A car tire, on the other hand, distorts when low on air; it shows signs of wear and indicates that it is reaching the end of its life when the treads are worn down.

In the absence of visible change and a lack of test methods, routine battery maintenance is often ignored or omitted as impractical and the battery is labeled "uncontrollable." Most users do not know when to replace a battery; it is installed and forgotten. Although everything may work well when a system is new, problems arise when some packs start failing and are replaced. In time, the battery fleet becomes a jumble of good and bad batteries. Operators say that half of all system failures are caused by faded batteries.

FIGURE 8.1 The "ready" light lies. The READY light indicates that the battery is fully charged. This does not mean "able." There is no link between "ready" and battery performance.

Battery charging is well understood, but the *ready light* can be misconstrued (Figure 8.1). Ready does not mean "able." There is no link to battery performance, nor does the green light promise full runtime; it simply states that the battery is full. With age, the ability to hold charge shrinks and the charge time shortens. This causes weak batteries to gravitate to the top, disguised as combat ready. System collapse is imminent when workers scramble for freshly charged batteries in an emergency. (The charge time of a partially charged battery can also be brief.)

The amount of energy a battery can hold is called *capacity*. Capacity is the leading health indicator that governs runtime and predicts when the battery should be retired. A new battery is rated at 100%, but few packs in service deliver the full amount. A workable capacity bandwidth is 80% to 100%. As a simple guideline, a battery with a capacity of 100% may provide a runtime of 10 h, 80% is 8 h, and 70% is 7 h.

8.2 CAPACITY MEASUREMENT BY DISCHARGE

Battery capacity is commonly measured by applying a discharge. The electrical energy a battery can hold is expressed in ampere-hours (Ah). Capacity is reflected in the elapsed time when discharging a fully charged battery at a constant current to the end-of-discharge voltage.

The discharge (and charge) rates are given in C-rate. Most portable batteries are serviced at 1 C, meaning that a 1-Ah battery would be discharged (and charged) at 1 A. If a fully charged battery discharges for 1 h at 1 C, then the capacity is 100%. If the discharge lasts only 30 min before reaching the end-of-discharge voltage, the battery has a capacity of 50%. A new battery can produce more than 100%, but many are underrated and may not reach the specified 100%, even with formatting. This is characteristic with lead-acid batteries. Each battery has a slightly different capacity when new and each fades at its own accord.

Applying a 2 C discharge should deliver the same capacity as 1 C since the identical amount of energy is dispensed, albeit in a shorter time. Capacity readings on a fast discharge are always lower than a more gentle discharge due to losses caused by internal resistance. Discharging the same battery at 0.5 C, or 0.5 A, over 2 h might give a slight increase in capacity as the internal losses become less evident.

To obtain a reasonably good capacity reading, manufacturers commonly rate lead-acid batteries at 0.05 C, or a 20-h discharge. Capacity offset provided by the

battery manufacturer offers correction if a battery is discharged at a higher C-rate. Figure 8.2 show examples of discharge times under different C-rates.

The efficiency factor of a discharging battery is expressed by the *Peukert's law*. W. Peukert, a German scientist (1897), devised a formula expressing loss at a given discharge rate in Peukert numbers. Because of the sluggish behavior of lead acid, Peukert numbers apply mostly to this chemistry. They help to calculate the capacity under various load conditions.

The Peukert law takes into account the internal resistance and recovery rate of a battery. A value close to 1 indicates a well-performing battery with good efficiency and minimal loss; a higher number reflects a less efficient battery. Figure 8.3 illustrates the available capacity as a function of ampere with different Peukert ratings.

Lead acid performs well under a momentary load; a continuous heavy discharge is less desirable. This is why lead acid performs so well in a starter application. The rest periods between cranking provide the needed recovery to regain composure. A slow recovery can be compared with a drying felt pen that works well for short markings but needs rest to replenish ink when in continuous use.

Starter batteries should not be deep discharged; they are designed for shallow discharges only. The lead is applied on thin plates in a sponge-like form that has the appearance of fine foam. This extends the surface area of the plates to achieve low resistance and maximum power, but this fragile structure is not suitable for deep discharges. Starter batteries are marked with CCA and ampere hour (Ah) or reserve capacity (RC). CCA refers to cold cranking amps, a measurement that represents the amount of current a battery can deliver at cold temperatures. (CCA and internal resistance are related.)

Deep-cycle batteries are built for maximum capacity and high cycle count. The manufacturer achieves this by making the lead plates thick. Although designed for cycling, full discharges still cause stress, and longevity correlates to cycle count and

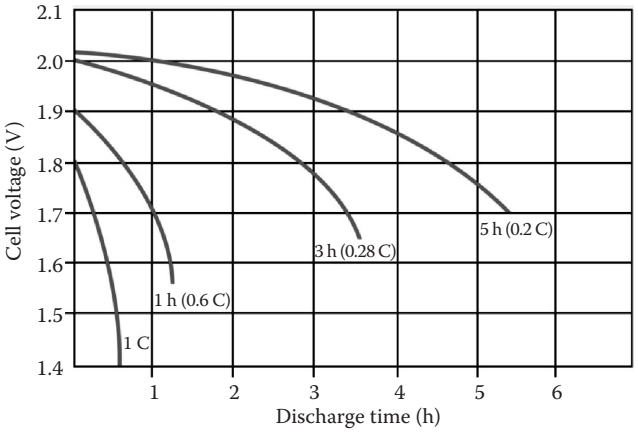

FIGURE 8.2 Typical discharge curves of lead acid as a function of C-rate. Smaller batteries are rated at a 1 C discharge rate. Due to sluggish behavior, lead acid is rated at 0.2 C (5 h) and 0.05 C (20 h).

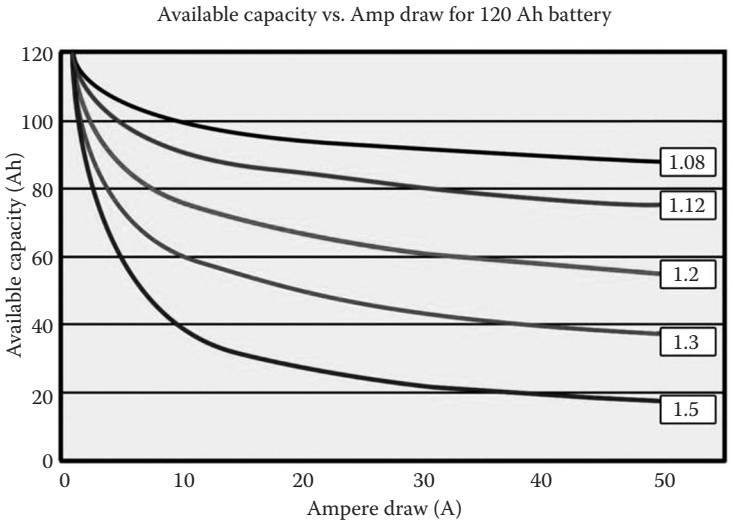

FIGURE 8.3 Available capacity of a lead-acid battery at Peukert numbers of 1.08 to 1.50. A value close to 1 has the smallest losses; higher numbers deliver lower capacities. (Source: von Wentzel [2008].)

depth of discharge. If at all possible, avoid full discharges and charge more often. Deep-cycle batteries are marked in Ah or minute of runtime at a specified discharge current. Table 8.1 compares the typical life of starter and deep-cycle batteries when cycled to various depths of discharge. With only 12 to 15 full cycles, the starter battery is a definite loser.

Large batteries are often discharged with a load bank. This may require temporarily removing the battery from service. A complete cycle can take a day or longer because a large amount of energy is dissipated for the purpose of measuring capacity. Unlike nickel and lithium-based batteries, lead-acid systems cannot be fast-charged, and a fully saturated charge can take up to 14 h. Figure 8.4 illustrates load banks for larger batteries.

Batteries rated at 20 Ah and smaller are commonly serviced with a programmable battery analyzer. Many come with multiple bays to allow simultaneous service of different battery types. Figure 8.5 shows an analyzer that uses configured battery

TABLE 8.1
Cycle Performance of Starter and Deep-Cycle Batteries

Depth of Discharge	Starter Battery	Deep-Cycle Battery
100%	12–15 cycles	150–200 cycles
50%	100–120 cycles	400–500 cycles
30%	130–150 cycles	1000+ cycles

Note: Starter batteries and deep-cycle batteries cannot be interchanged.

FIGURE 8.4 Load banks to discharge large battery systems for a performance check. The capacity of critical standby batteries is often measured by applying a full discharge. Such a test can take more than a day to perform.

FIGURE 8.5 Cadex C7400ER battery analyzer. Two- and four-station analyzers service batteries from 1.2 to 36 V, using unique algorithms for lead, nickel, and lithium-based chemistries. (Courtesy of Cadex.)

adapters; programmable smart cables are used to service packs for which no adapter is on hand. Most battery analyzers work in stand-alone mode; many interface with a PC.

Capacity measurements by discharge are most reliable and one would anticipate repeatable readings, but this is not always the case, especially with lead-acid batteries. Independent lab tests, including those at Cadex, have revealed differences in capacity readings of more than ±10% under identical test conditions. The reason for this discrepancy is not fully understood other than to realize that batteries are electrochemical devices that exhibit human-like qualities. (Our IQ [intelligence quotient] level also diverges depending on time of day and other conditions.) These tolerances

must be taken into account when comparing test results derived by discharge and rapid-test methods.

8.3 RAPID-TEST METHODS

The ultimate goal is to rapid-test a battery in a few seconds without removing it from service. Battery test devices are available that fulfill this requirement, but most identify deficiencies pertaining to voltage and resistance readings. Stating that a battery tester based on an internal resistance measurement can also estimate capacity is misleading. Advertising features that lie outside the equipment's capabilities confuses the industry into believing that multifaceted results are attainable with basic test functions. Manufacturers of these instruments are well aware of the complexity, but this does not prevent them from overpromising. An analogy can be made with a shampoo that promises to grow lush hair on a man's bald head.

Today's rapid-test methods range from the traditional DC load to AC conductance to advanced electrochemical impedance spectroscopy (EIS). Each has its advantages and limitations—and none fully satisfies all requirements. No single device can assess all battery characteristics on the fly. Much like a doctor examining a patient, or a weatherman forecasting the weather, several methods are needed to assess the overall condition.

The health of a battery cannot be "measured," but only estimated. A dead battery is easy to predict and most testers would recognize this with 100% accuracy. The challenge begins when measuring a battery in an operative capacity range of 70% to 100%. Besides capacity, other anomalies come into play and these include internal resistance, sulfation, and self-discharge.

Rechargeable batteries have improved in that modern lead and lithium-based systems retain low internal resistance through most of their life. Although resistance readings are quick and easy to take, they provide inconclusive results relating to battery health evaluation. To verify the connection between capacity and internal resistance, Cadex examined 175 aging starter batteries and found a correlation of 0.55. A perfect match would be 1.

In another test, Cadex measured the CCA and capacity of 20 aging but still functioning starter batteries. Figure 8.6 shows the relationship between CCA and capacity, sorted according to capacity. CCA drops somewhat with age, but not to a point where the cranking performance would be affected. Meanwhile, capacity demonstrates predictable losses on batteries 10 to 20 on the chart. Such performance degradation may not be noticeable until the motor won't crank on a cold morning due to insufficient capacity. Capacity is a more reliable state-of-health indicator than CCA (or internal resistance).

A battery is a reactive device, meaning that it behaves differently when applying a pure DC (direct current) load as opposed to an AC (alternating current) or pulsed load. A battery consists of resistive (R), capacitive (C), and *inductive* (L) resistance. The term *impedance* (Z) includes all three parameters in one, displayed in an ohmic value that varies with frequency.

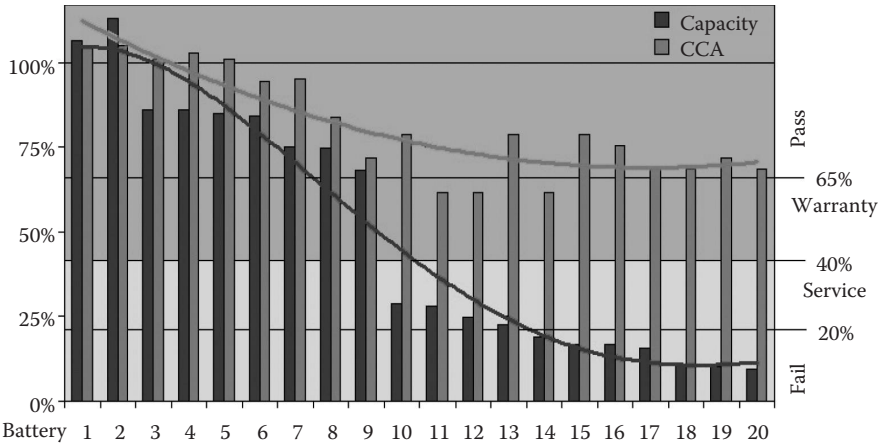

FIGURE 8.6 Capacity and CCA readings of 20 aging batteries. CCA tends to remain high while capacity drops steadily as part of aging. Low capacity goes mostly unnoticed by the motorist. CCA was estimated with the Spectro CA-12; capacity was measured with an Agilent load bank by a full discharge (BCI standard). (Courtesy of Cadex.)

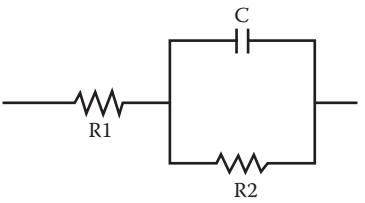

FIGURE 8.7 Randles model of a lead-acid battery. The overall battery resistance consists of ohmic resistance, as well as inductive and capacitive reactance. The values differ for each battery.

The impedance of a battery can best be represented with the Randles model. Figure 8.7 illustrates the basic model of a lead acid battery that includes resistors R1 and R2 and capacitor C. (Inductive reactance is commonly omitted because it plays a negligible role.) Resistive-based testers look mainly at R1, a value that increases with age but does not necessarily correlate with capacity.

8.3.1 DC Load Method

Ohmic measurement is one of the oldest and most reliable methods to measure internal battery resistance. The battery is discharged for a few seconds or minutes, a voltmeter measures the voltage drop, and Ohm's law calculates the resistance value (voltage divided by current equals resistance). The discharge current on a smaller

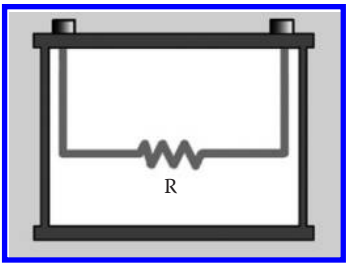

FIGURE 8.8 DC load method. Simplistic, but the true integrity of the Randles model cannot be seen. R1 and R2 appear as one ohmic value.

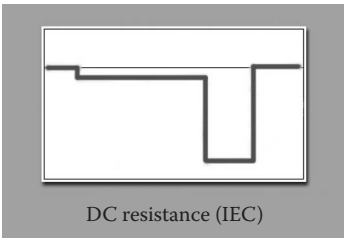

FIGURE 8.9 The two-tier DC load test method adheres to the IEC 61951-1:2005 standard. The load test is the preferred method for batteries powering DC loads.

battery may be 1 A or less; starter and uninterruptible power supply (UPS) batteries are often loaded with 50 A or more.

The DC load works well over a broad range of batteries and the ohmic readings are accurate and repeatable. Car garages have been using the carbon pile for many years to measure starter batteries, and an experienced technician can get a reasonably good assessment of a battery's condition.

The DC load has limitations in that it blends R1 and R2 of the Randles model into a combined resistor and ignores the capacitor C (see Figure 8.8). Capacitor C is an important component of a battery and represents 1.5 farads (F) per 100-Ah capacity. In essence, the DC method sees the battery as a resistor, providing only ohmic references. Capacity estimation is not possible.

The *two-tier DC load* test method applies two sequential discharge loads of different currents and time durations. IEC 61951-1:2005 specifies that the battery be first discharged at a low current for 10 sec, followed by a higher current for 3 sec (see Figure 8.9). This test protocol provides lifelike test conditions for many battery applications. The differences between the two load conditions provide additional battery information, but the values are strictly resistive and do not reveal capacity.

8.3.2 AC Conductance

Another method to measure resistance is to apply a 1000-Hz signal. (Other frequencies may be used.) The sinusoidal signal excites the battery and the resistance is calculated by looking at the phase shift and amplitude relationship between current

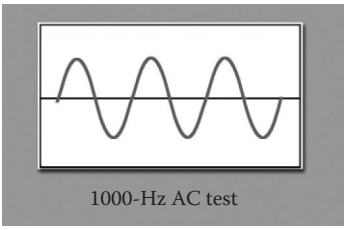

FIGURE 8.10 The IEC 1000-Hz method is the preferred method to take impedance snapshots of batteries powering digital devices.

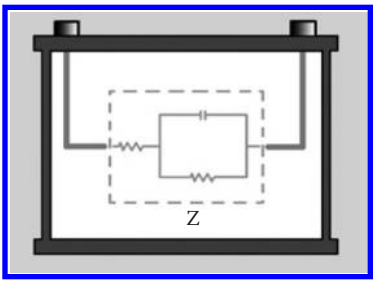

FIGURE 8.11 In the AC conductance method, the individual components of the Randles model are modeled together and cannot be distinguished.

and voltage. It is important to note that the AC method gives different resistive values than the DC load. Measuring a Li-ion packaged in an 18650 cell with a 1000-Hz signal results in a reading of about 36 mΩ; the same cell measured with a DC load is roughly 110 mΩ. Because both readings are correct, the user should identify the application. The 1000-Hz method works well for a digital load, such as a communications device, whereas the DC load provides the correct resistive references for pure resistive loading, such as a heating element. The 1000-Hz method as illustrated in Figure 8.10 only reads battery impedance relating to the applied frequency; different frequencies will result in unique readings and capacity estimation is not possible.

The AC conductance method injects an AC signal into the battery, and for simplicity this may be in a pulsed format. These testers are commonly used to check the CCA of starter batteries in car garages. Although small and easy to use, AC conductance only reveals resistive values that approximate a CCA reading. The single-frequency technology as illustrated in Figure 8.11 sees the components of the Randles model as one complex impedance called the *modulus of Z*; capacity estimation is not possible.

8.3.3 Electrochemical Impedance Spectroscopy

The EIS method scans a battery with a signal that typically ranges from 5 to 2000 Hz. The reflected signal produces a Nyquist plot that mirrors the individual components of the Randles model (Figure 8.12). Research laboratories have been using EIS for many years, but long test times and the need for trained professionals to decipher

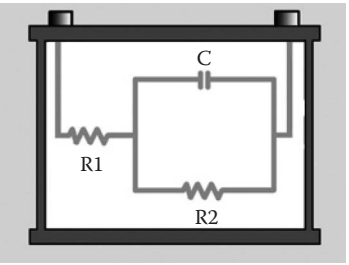

FIGURE 8.12 In the Spectro™ method, R1, R2, and C are measured separately, but these values alone do not disclose capacity and SOC information.

the results have limited the technology to laboratory environments. EIS can read the Randles components by extraction, but these measurements alone do not provide capacity information.

Testing by resistive methods requires that the batteries be sufficiently charged. A partial charge could manifest itself as a battery with faded capacity. Voltage can be used to measure state of charge (SOC; more on this later).

While none of the described methods provide capacity readings, resistance measurements are useful to find anomalies in manufacturing and to track resistive changes that occur during use, such as dry-outs in stationary batteries. The internal resistance can vary greatly. This is especially apparent with stationary lead-acid batteries that may diverge 8% to 10% between batches. With such wide tolerances, the resistance method is most effective when comparing resistive changes from birth to retirement. Service crews are asked to take a snapshot of each cell when installing stationary batteries and then observe the subtle changes as the cells age. All readings must be taken with the same type of instrument because different test methods will give dissimilar results.

8.3.4 Multimodel EIS (Spectro™)

Scientists believe that the future of battery diagnostics and monitoring lies in *electrochemical impedance spectroscopy.* Cadex Electronics has taken the bold move to advance EIS a step further by developing *multimodel electrochemical impedance spectroscopy* or Spectro™ for short. Spectro™ reads battery capacity, CCA, and SOC in a single, noninvasive 15-sec test. The tests can be done under a steady load, but not while charging. The battery must have a SOC of at least 60%.

Figure 8.13 illustrates the Spectro CA-12 handheld battery tester. Battery test devices using this technology are being deployed to test starter and deep-cycle batteries. Having the ability to make capacity estimations helps in more accurately evaluating a battery and determining its end of life.

Here is how the Spectro™ works. A sinusoidal signal ranging from 20 to 2000 Hz is injected into the battery at a few millivolts. After digital filtering, the extracted signal produces a Nyquist plot onto which Nyquist plots for various electrochemical models are superimposed. Applied algorithms find the best match within allotted margins; nonfitting models are rejected. Data fusion correlates the values of the

FIGURE 8.13 The Spectro CA-12 compact battery rapid tester displays capacity, CCA, and SOC in 15 sec. Capacity reflects the true state of health of a battery.

key parameters to derive at capacity and CCA estimations, a process that involves 40 million transactions. Figure 8.14 illustrates the patented process in a simplified way.

Measurement devices, such as the Spectro CA-12, using this technology are not universal instruments capable of estimating the capacity of any battery that may come along; they require battery specific matrices, also known as pattern recognition algorithms. A matrix is a multidimensional lookup table against which measured readings are compared. Text recognition, fingerprint identification, and visual imaging operate on a similar principle.

Matrices are primarily used to estimate battery capacity. CCA, and in part SOC, also require matrices, but these are easy to assemble and work over a wide battery population.

Spectro™ correctly predicts 8 out of 10 batteries on capacity, and 9 out of 10 on CCA. Combining these two classifications provides significant improvement in test accuracies over units measuring CCA alone. Many resistance-based testers deliver predictions that are not much better than 5 correct in 10. This is similar to the results of a coin toss. Most service personnel are unaware of the low precision

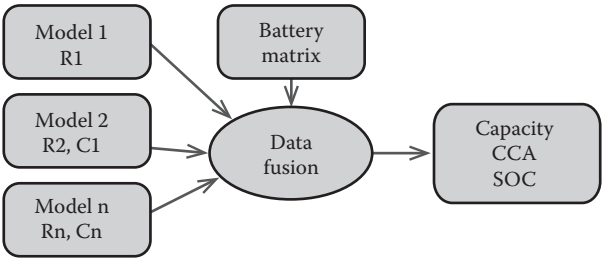

FIGURE 8.14 The Spectro™ tester combines EIS with complex modeling to estimate battery capacity and improve CCA measurements. A sinusoidal signal produces a Nyquist plot, and data fusion correlates the values of the key parameters to estimate capacity and CCA.

of resistance-based battery testers; lab verifications are seldom done. Low inaccuracies can result in replacing good batteries by error and passing low-capacity units as good, only to have them fail shortly after service.

Spectro-based technology has room to improve; however, the industry must understand that a battery can only be diagnosed if measurable indicators are present. The best results are achieved by dealing with a working battery pulled from the field. New batteries that have not been fully formatted or have been in storage provide less accurate results. Furthermore, a battery with low capacity or one with a partial charge produces similar pointers that must be identified and separated.

For unknown reasons, reversible (soft) sulfation does not display readable symptoms and the battery may receive a clean bill of health in spite of the anomaly. Only permanent (hard) sulfation that can no longer be corrected agrees with the state-of-health result. An analogy can be made with a person who is suffering from a unique illness that no medical instrument can diagnose. Measurable indicators must also be present here.

Creating a matrix involves scanning many batteries at different state-of-health levels. The more batteries that can be included in the mix of the same model but different capacity, the stronger the matrix will be. The population should include batteries from hot and cold climates with diverse user patterns.

Generic matrices are most practical but they have the limitation of giving the result in a pass/fail classification based on a capacity threshold. This is acceptable for most service personnel because the instrument makes the final decision, eliminating uncertainties and customer interference. A specific matrix will provide the capacity in number figures and slightly improved accuracy.

8.4 STATE-OF-CHARGE MEASUREMENT

Battery users perceive a battery as being an energy storage device like a tank that is dispensing liquid fuel. For simplicity reasons, a battery can indeed be seen as such; however, measuring stored energy from an electrochemical system is far more complex than drawing fluid from a fixed container.

Whereas a regular fuel gauge measures tangible liquid flowing from a tank of a known size, a battery fuel gauge must rely on a voltage that is affected by the environment and comes from a source that gradually diminishes in size. A full charge will provide a 100% SOC, but of what? With usage and age, the capacity will drop 50%, but the fuel gauge does not disclose this. There is no relationship between SOC and performance. Showing SOC while hiding the shrinking capacity is a major drawback with most battery fuel gauges. Considering these limitations, battery users will begin to understand why most battery fuel gauges are notoriously inaccurate and unreliable.

The most common and simplistic SOC measurement is by voltage. This method can be inaccurate due to the “rubber band effect,” which lifts the voltage during charge and drops it on discharge. Furthermore, different chemical compositions produce voltage variations. Calcium, an additive that makes lead-acid batteries maintenance free, raises the voltage by 5% to 8%. Surface charge further fools SOC estimations by showing an elevated reading immediately after charge; a brief

discharge neutralizes the voltage. Temperature also plays havoc. A warm battery raises the open circuit voltage (OCV) and a cold battery lowers it. Furthermore, absorbed glass mat (AGM) batteries have a slightly higher voltage than the flooded equivalent. Voltage polarization seen immediately after charge and discharge produces a further error with a voltage-based SOC readout. A charge raises the voltage artificially high for a while, whereas a discharge pushes it low before it reverts back to normal. The rest period to neutralize the battery is specified in hours; battery manufacturers recommend 24 h. When measuring SOC by voltage, the battery voltage must be "floating," meaning that no load or charge should be applied to the battery during SOC measurements.

In spite of the limitations, voltage-based SOC somehow works for applications such as golf carts, forklifts, scooters, and wheelchairs. Reasonably good accuracies are achieved by compensating for anomalies, and then taking some reserve energy into account. (No one knows the true accuracy unless a battery completely runs out of charge.) Alternative methods are more expensive, but not trouble free either.

Advanced systems are commonly based on *coulomb counting*. The theory goes back 250 years when Charles-Augustin de Coulomb first established the "Coulomb rule" on the principle of measuring inflowing and outflowing currents. Figure 8.15 illustrates the principle graphically.

Coulomb counting should be flawless, but it induces errors as well. If, for example, a battery was charged for 1 h at 1 A, the same amount of energy should be available on discharge, but this is never the case. Inefficiencies in charge acceptance, especially toward the end of charge, as well as losses during discharge and storage, reduce the total energy delivered and skew the readings. The available energy is always less than what has been fed into the battery.

A common error in fuel gauge design is assuming that the battery will always stay young. Aging evolves differently if a battery is used in a cool or hot environment. The type of charging and loading practices also affect the longevity. Batteries prefer gentle charging over an ultrafast charge and moderate loading over a high-energy discharge.

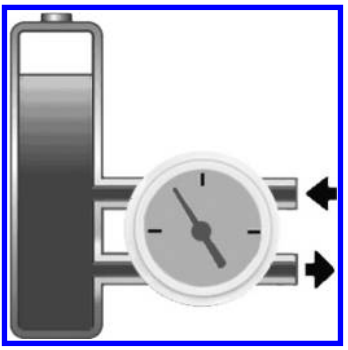

FIGURE 8.15 Principle of a fuel gauge based on coulomb counting. The stored energy represents the SOC; a circuit measures the inflowing and outflowing current. The outflowing energy is always less than what has been fed in.

Coulomb counting needs periodic calibration, also known as capacity relearning. This corrects the tracking error that develops between a chemical and digital battery with use. Applying one or several full-charge and full-discharge cycle solves this. This service can be omitted if the battery receives a periodic full discharge followed by a full charge.

Manual calibration is possible by running the battery down until "Low Battery" appears. This can be done in the equipment or externally on a battery analyzer. A full discharge sets the low-discharge flag and a full charge the high-charge flag. Establishing these two markers allows SOC calculation by tracking the distance between the flags. For best results, calibrate a device that is regularly used every 3 months or after 40 partial cycles. Every discharge is said to induce an error of about 1%. Figure 8.16 shows the full-discharge and full-charge flags.

What happens if the battery is not calibrated regularly? Can such a battery be used with confidence? Most chargers and devices obey the dictates of the *chemical battery* and not that of the parasitic digital battery. Most uncalibrated batteries function normally, but their readouts become a nuisance.

The SOC of flooded batteries can also be checked by measuring the specific gravity. The sulfuric acid gets heavier during charging, causing the specific gravity to increase. As the SOC decreases through discharge, the sulfuric acid removes itself from the electrolyte and binds to the plate, forming lead sulfate. The electrolyte density becomes lighter and more water-like; the specific gravity drops.

Temperature will affect the readings; the colder the temperature, the higher (denser) the specific gravity becomes. The offset between 0°C to 40°C (32°F to 104°F) is 2% to 3%. Errors also occur if the acid stratifies by developing a light concentration on top and heavy on the bottom. A shaking motion or tipping the battery on its side corrects the problem. The electrolyte must further be allowed to stabilize after charge and discharge before taking a specific gravity reading; neutralization times are specified in hours. Other inconsistencies occur when low on water or if the battery is overfilled.

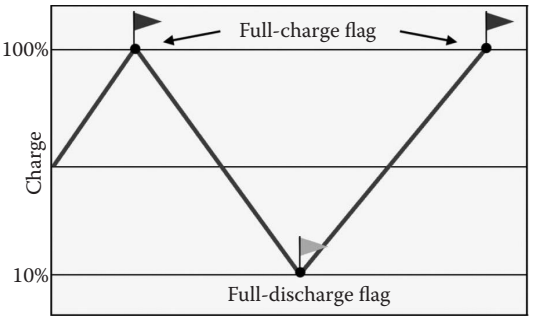

FIGURE 8.16 Full-discharge and full-charge flags are used to establish calibration markers. Calibration occurs by applying a full charge, discharge, and charge. This can be accomplished in the equipment or with a battery analyzer as part of battery maintenance.

8.5 BATTERY MONITORING

Many battery monitoring systems rely on *voltage*, *current*, and *temperature* measurements; advanced devices also include coulomb counting. Sensors provide SOC information and identify irregularities, but capacity estimations are beyond reach for most battery management systems (BMSs).

A common oversight by engineers when designing a BMS is ignoring battery aging. Tuned to a new battery, the accuracy is quite good, but it will drift after a few years of use. Aging is difficult to model because fading affects the battery differently in hot and cold climates; self-learning in advanced BMSs helps them adjust to the environmental conditions. Figure 8.17 illustrates a commercial sensor that mounts on the pole of a starter battery.

Adding capacity measurement converts a simple battery sensor into an advanced BMS. Figure 8.18 illustrates a system in which capacity becomes the leading component of a BMS. Developments are ongoing to also measure SOC by impedance. This will allow voltage-independent SOC measurements.

With SOC and capacity information on hand, a *tristate fuel gauge* can be built that shows the available energy, the empty portion that can be refilled, and the unusable part that is permanently lost. This information leads to the all-encompassing

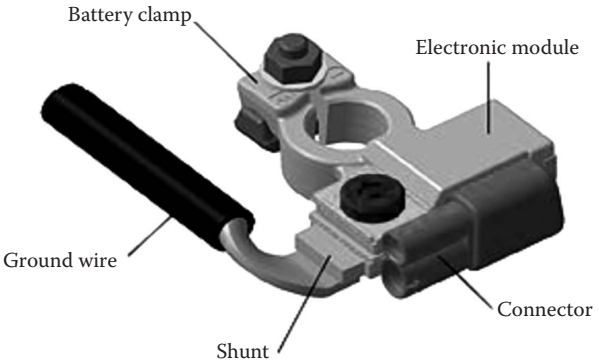

FIGURE 8.17 Battery sensor for starter battery. Sensor measures voltage, current, and temperature to estimate SOC. Such a device cannot estimate capacity.

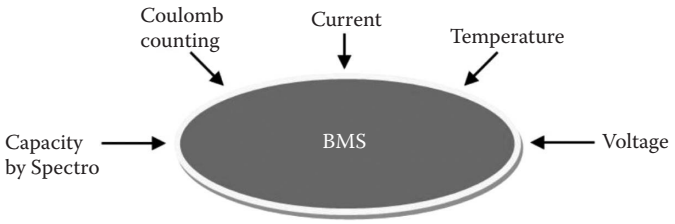

FIGURE 8.18 Spectro-BMS adds a capacity reading to voltage and temperature readings. Adding a capacity measurement converts a battery sensor into an advanced BMS.

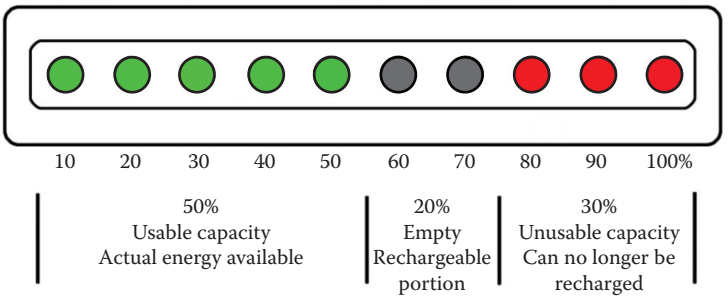

FIGURE 8.19 The tristate fuel gauge estimates the usable capacity, empty portion, and unusable part.

battery *state of function* (SOF) that reflects the immediate condition of a battery. Figure 8.19 graphically illustrates the concept of a tristate fuel gauge.

Knowing a battery's SOF will greatly improve the battery valuation, but device manufacturers may be hesitant to show the consumer a capacity that is less than 100%, especially during the warranty period. Access by a code could solve this. BMS will be moving toward capacity readings as a more reliable indicator for battery health and knowing when to retire a battery.

8.6 SUMMARY

More research is needed in the field of battery rapid-testing; the accomplishments do not rival those achieved in other technologies, such as microelectronics and medicine. It is as if the field of battery diagnostics and monitoring still dwells in medieval times. We don't even have a reliable method to measure SOC; the ability to assess capacity, the leading health indicator, still dwells far behind.

Professor Mark Orazem compares the complexity of testing batteries with the tale in which blind men touch an elephant to learn what it is like. Each one feels a different part, then compares notes, only to disagree at the end. Even for a sighted man, battery diagnostics is complex because no single measurement can quantify the state of health of a battery on the fly.

FURTHER READING

Buchmann, I., *Batteries in a Portable World: A Handbook on Rechargeable Batteries for Non-Engineers*, 3rd ed., Cadex Electronics, Vancouver, BC (2011).

Buchmann, I., Battery University website, http://www.BatteryUniversity.com (2010).

Orazem, M. E., University of California-Berkeley website, http://www.che.ufl.edu/faculty/orazem/ (1988).

von Wentzel, C., How lead acid batteries work. Comparing marine battery technologies. Available at http://www.vonwentzel.net/Battery/00.Glossary (2008).

Wikipedia, online encyclopedia containing information from various contributors.

9 Mathematical Modeling of Lead-Acid Batteries

Mikaël Cugnet and Bor Yann Liaw

CONTENTS

9.1 INTRODUCTION

Lead-acid battery (LAB) technology remains the most applied battery technology to date for electric energy storage and the auto industry. To facilitate its application, mathematical modeling is of great interest to researchers involved in developing battery technology. The modeling tool used, depending on its application, may need to provide different capabilities in its utility. It is only natural to select the best tool for a particular application. This chapter presents a brief overview of some notable modeling approaches available in the literature. These modeling efforts are aimed at simulating the behavior of electrodes, cells, and batteries in order to understand specific aspects such as corrosion, sulfation, or water loss by electrolysis known to occur in LABs. This allows researchers to predict such behavior during working conditions for an application.

For those interested in developing battery models, the choice of the modeling tool and approach for a given purpose depends on several considerations, many of which are resource limiting. First of all, the decision should be based on the application of the LAB. For instance, for energy storage applications, the calendar life and cycle life might be of great interest for cell selection and system performance considerations, whereas for hybrid vehicles the rate capability might be more critical than the calendar life. The differences in the emphases might determine the modeling framework and utility for the model design and implementation. Ultimately, one might want to have a universal model that can deliver all necessary capabilities in the simulation and prediction, but the person might soon realize that it would take a significant amount of effort and resources to make that happen. Often, the demanding requirements on resources can render modeling efforts impractical. To understand battery behavior, a battery designer may prefer an electrochemical model for incorporating materials and their properties into a cell design, whereas an engineer who needs to develop a real-time control system for a drivetrain may prefer an empirical or electrical model for convenience and ease of implementation. If a large amount of data is available for a specific application, a user may find that using artificial neural network or fuzzy logic-based models is a good choice for system control and management.

In this chapter we classify the modeling approaches into six categories, based on their flavor for applications in the design, management, or operation of LABs. These categories are (1) artificial neural network-based models that utilize an approach mimicking the operation of neurons in a human brain; (2) fuzzy logic models that offer robustness, fast development times, and high code efficiency; (3) empirical models that are easy to develop with sufficient accuracy; (4) electrical models that can meet most of the needs by offering the fastest development and the easiest parameter identification in the approach; (5) electrochemical models that are complex and probably dedicated to experts to assist with battery design; and (6) those that are not categorized as one of the preceding types but have unique capabilities to function as a tool in a specific application.

9.2 ARTIFICIAL NEURAL NETWORK-BASED MODELS

9.2.1 Introduction to Artificial Neural Networks

A typical battery is a complicated chemical system that pertains to energy conversion and storage via both chemical and electrochemical reactions, often with physical changes. Such a complicated nature makes battery modeling difficult to pursue by using simple algorithms to describe the complexity of the chemistry involved. An efficient way to solve complex problems is to follow the lemma "divide and conquer" (derived from the Latin saying "Divide et impera"). After all, a complex system can be divided into a group of simpler subsystems that we can understand individually. Neural networks (NNs), created in the 1940s, provide one way of achieving this. There are many types of networks, but they all are characterized by the following components: a set of nodes and connections between or among those nodes. The interactions of nodes through the connections lead to the global behavior of the network, which cannot be observed in the elements of the network. This global behavior is said to be *emergent*. This means that the abilities of the network supersede those of its elements, making networks a very powerful tool.

An artificial neural network (ANN) is a mathematical or computational model in which the nodes are seen as "artificial neurons." It mimics the operation of biological neurons in the human brain. The latter contains about 20 billion neurons. On average, each neuron is connected to other neurons through several thousand synapses. The network of neurons in a brain forms a massively parallel information processing system, in contrast to a conventional computer, in which a single processor executes a single series of instructions. However, if we consider the time taken for each elementary operation, then neurons typically operate at a maximum rate of about 100 Hz, whereas a conventional central processing unit (CPU) carries out more than several hundred million machine-level operations per second to date. Despite being built with very slow hardware, the brain has quite remarkable capabilities, among which is the fact that it can learn from experience (reorganize itself) and perform massively parallel computations extremely efficiently (complex visual perception). As a discipline of artificial intelligence, neural networks attempt to bring computers a little closer to the brain's capabilities by imitating certain aspects of information processing in the brain. The ANN is therefore highly simplified compared to the real brain, but it uses much faster hardware.

The two main categories of NN architectures are feedforward and feedback networks. Feedforward (or multilayer) networks consist of several interconnected layers l of neurons (Figure 9.1). The last layer L is called the output or visible layer, and the others are called the hidden layers. The number of neurons N_l per hidden layer depends on the problem considered and is usually specified by trial and error; that is, the more difficult the problem, the larger the required sizes of the hidden layers. Feedback networks consist of N neurons, with the output of each individual neuron being fed back to all others via weights w_{ij}. The operation of this network is given in terms of defined dynamics, which describes the time evolution of the neuron outputs.

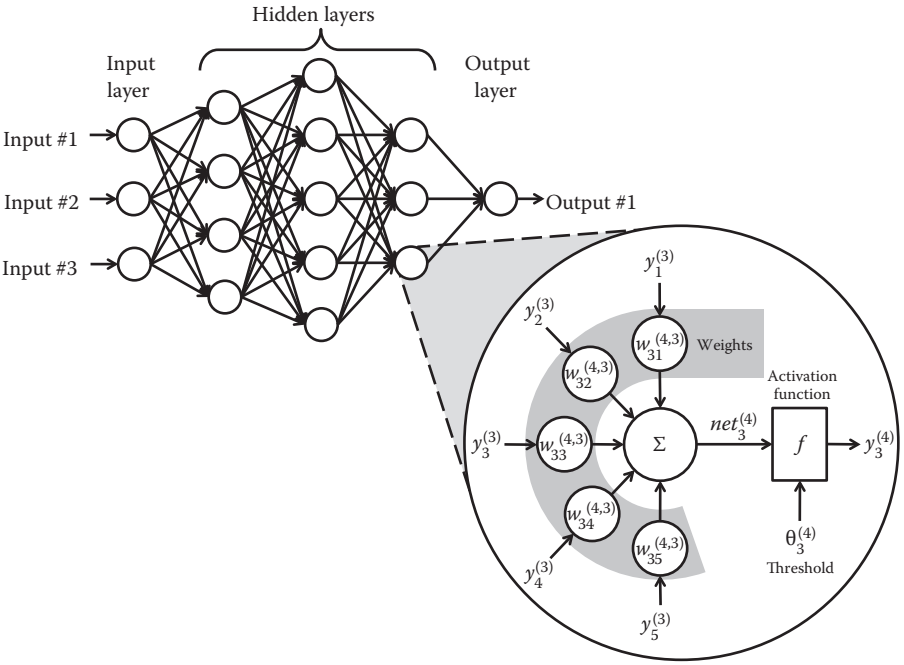

FIGURE 9.1 Example of an ANN with a focus on the composition of a specific neuron.

The basic computational element, or model neuron, can also be called a node or unit. It receives input from one or more other neurons, or perhaps from an external source. Each input has an associated weight $w_{ij}^{(l,l-1)}$, which refers to the weight from neuron j of layer $(l-1)$ to neuron i of layer l. The random initial value of the weight is modified by model synaptic learning. The neuron computes some activation function f of the weighted sum of its inputs y_j:

$$y_i^{(l)} = f\left(\sum_{j=1}^{N_{l-1}} w_{ij}^{(l,l-1)} y_j^{(l-1)} + \theta_i^{(l)}\right), \quad l = 1, ..., L, \quad i = 1, ..., N_l \tag{9.1}$$

where θ_i denotes the threshold of neuron i of layer l. The output y_i of the i'th neuron of layer l, in turn, serves as an input to other neurons, unless it belongs to the output layer of the ANN ($l = L$). The weighted sum is called the net input to neuron i, often written net_i. In the simplest case, called a linear unit, f is the identity function, and the neuron's output is just its net input. The higher the weight of an artificial neuron, the stronger its input and, hence, influence on the function will be. Weights can also be negative, so we can say that the signal is inhibited by the negative weighting. Depending on the weights, the computation of the neuron will be different. The desired output can then be obtained from specific inputs by adjusting the weights of an artificial neuron. Therefore, ANNs of hundreds or thousands of neurons require algorithms that can adjust the weights of the ANN in order to obtain the desired

output from the network. This process of adjusting the weights is called learning or training.

What has attracted the most interest in neural networks is the possibility of learning. The breakthrough for multilayer networks was the development of a method for learning by examples called the backpropagation (BP) learning algorithm. The BP algorithm has made it possible to design ANNs devoted to numerous applications, such as adaptive control, sonar, stock market prediction, and speech recognition. Training an ANN essentially means selecting one model from the set of allowed models that minimizes the cost criterion. The cost criterion, also called cost function, is an important concept in learning, because it is a measure of how far away a particular solution is from an optimal solution to the problem to be solved. Numerous algorithms are available for training ANNs. Most of them can be viewed as a straightforward application of optimization theory and statistical estimation. They often employ some form of gradient descent. This is done by simply taking the derivative of the cost function with respect to the network parameters and then changing those parameters in a gradient-related direction.

If the model, cost function, and learning algorithm are selected appropriately, the resulting ANN can be extremely robust. However, the main drawback of ANN is the strong dependence on the training data quality. If the training data set does not cover a significant portion of the operating conditions, or if the signal is noisy, then a substantial risk of errors might be inherited in the model. One way to resolve this issue is to design hybrid models (combining NNs and symbolic approaches). Intermixing of these two approaches can help the hybrid model provide more trustworthy output when it is tested with a new data set slightly different from the ones used for the training.

9.2.2 Applications of the ANN Approach

In 1996, Young et al. suggested the feasibility of a routine application of an ANN to LAB performance prediction as part of a maintenance strategy for long-string energy storage systems [1]. This study concerned a LAB manufactured by GNB, Inc. (Kankakee, IL) in June 1983. The 324-cell battery, fabricated according to Electric Power Research Institute specifications, is capable of delivering 1.2 MWh for a 5-h discharge (2080-Ah cell capacity). Routine battery maintenance data are evaluated for performance prediction, using the ANN as a pattern recognition tool. Those data include float voltages, specific gravities, water additions, electrolyte levels, and all the capacity tests performed on the cells. The architecture produces the best performing ANN, which consists of four layers (the input layer is not counted): 13 inputs, two first hidden layers of three nodes, a third single node-hidden layer, and three outputs (Figure 9.2). The ANN predictions are better than those obtained the *k*-nearest neighbor-based pattern recognition. It was possible to select 70% of the high-performing cells, without any false selections from the low-performing cells, and to identify nearly 96% of the poor-performance cells, with none of the high-performance cells misselected.

Three years later at Sandia National Laboratories, Urbina et al. investigated the reliability of LABs recharged from a renewable source that provides power in

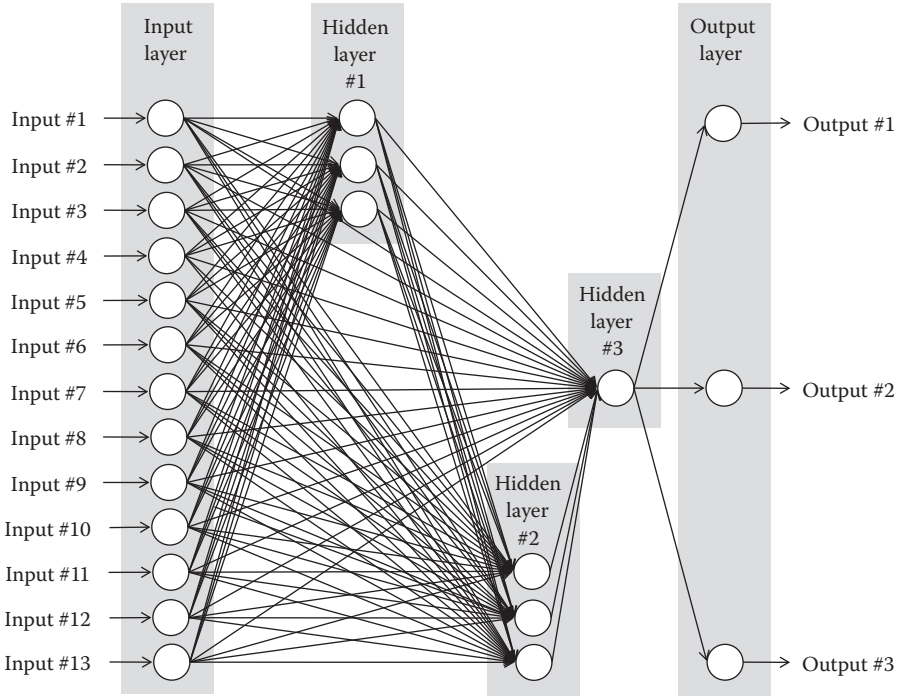

FIGURE 9.2 Architecture of the best performing ANN by Young et al. (From Young, R. E. et al., *Journal of Power Sources* 62, 121–134, 1996.)

random increments [2]. They narrowed their focus on the damage LABs accumulated when they were subjected to deep-discharge cycles. In particular, it is known that when those batteries were used at a low state of charge (SOC), their maximum capacity could be significantly diminished, eventually leading to battery failure. In view of this issue, they developed a framework to model battery SOC and maximum capacity as a function of time (where DOD is depth of discharge):

$$\mathrm{SOC}(t) = \frac{Q(t)}{Q_{\max}(t)} = 1 - \mathrm{DOD}(t) \tag{9.2}$$

with

$$Q(t) = \min\left(\int_{t_0}^{t} \eta(\tau)\, i(\tau)\, d\tau + Q(t_0), Q_{\max}(t) \right) \quad t \geq t_0, Q(t) \leq Q_{\max}(t) \tag{9.3}$$

The function $Q_{\max}(t)$ tracks the maximum battery capacity as a function of time. In photovoltaic (PV) applications, damage to a rechargeable LAB is assumed to be

caused by deep discharge, which is irreversible; therefore, $Q_{\max}(t)$ must be a monotonically decreasing function:

$$Q_{\max}(t) = \int_{t_0}^{t} \delta_Q(\tau)\, d\tau + Q(t_0) \quad t \geq t_0 \tag{9.4}$$

They introduced $\delta_Q(t)$, the damage effect that occurs during deep discharge, via a nonpositive function of DOD and deep-discharge duration. Because of the unknown nature of this function, they modeled it with an ANN method whose parameters were trained with experimental data.

In the same year, Peng et al. presented a novel design of a battery pack SOC estimator for electric vehicles (EVs) using a two-layer ANN (one single hidden layer) with four inputs (current, capacity, temperature, and minimum module voltage) and one output (estimated SOC) [3]. The N hidden neurons have a "sigmoid" activation function defined as

$$y_i^{(1)} = \text{sigmoid}\left(net_i^{(1)}\right) = \frac{1}{1 + e^{-net_i^{(1)}}}, \quad i = 1, ..., N \tag{9.5}$$

with $net_i^{(1)}$, the net input to neuron i, being a linear scalar function of the weight, which comprises a 1×4 vector $W_i^{(1,0)}$ multiplied with an input 4×1 vector $Y^{(0)}$ and a scalar bias $\theta^{(0)}$:

$$net_i^{(1)} = \sum_{j=1}^{4} w_{ij}^{(1,0)} y_j^{(0)} + \theta_i^{(0)} = W_i^{(1,0)} Y^{(0)} + \theta_i^{(0)} \tag{9.6}$$

The single output neuron has an identity activation function defined as

$$\text{SOC} = y^{(2)} = net^{(2)} = W^{(2,1)}\, \text{sigmoid}\left(W^{(1,0)}\left[\, I \;\; Q \;\; T \;\; U_{\min} \,\right]^{\mathrm{T}} + \Theta^{(0)}\right) + \theta^{(1)} \tag{9.7}$$

where $W^{(2,1)}$ is a $1 \times N$ weight vector from neurons of the hidden layer to the output neuron, $W^{(1,0)}$ an $N \times 4$ weight matrix from neurons of the input layer to neurons of the hidden layer, and $\Theta^{(0)}$ an $N \times 1$ bias vector. A large set of data under different driving cycles and operating conditions was used to train the ANN. Their results demonstrated performance with acceptable accuracy (5%) for most of the data recorded. The errors of the SOC estimates are well within the acceptable range compared to those obtained by using traditional mathematical models. Unfortunately, no life deterioration factor was included in this ANN; therefore, it may not perform well over time as a battery ages.

An ANN-based model of available capacity in a LAB for EV applications was developed by Chan et al. in 2000 with an ANN toolbox available in MATLAB® [4]. They compared their model with Peukert's equation (Equation 9.8), which describes the nonlinear relationship between the available capacity $Q_{\max}$ and discharge current I_{dch}:

$$Q_{\max} = K / I_{dch}^{n-1} \tag{9.8}$$

where the constants n and K depend on the temperature, concentration of the electrolyte, and the structure of the LAB. They used a simple two-layer ANN with one input (discharge current) and one output (available capacity). The four hidden neurons have "hyperbolic tangent" activation functions represented by the following expression:

$$y_i^{(1)} = \frac{2}{1 + e^{-2net_i^{(1)}}} - 1 = \tanh\left(W_i^{(1,0)} Y^{(0)} + \theta_i^{(0)}\right), \quad i = 1, ..., 4 \tag{9.9}$$

The single output neuron has an identity activation function defined as

$$Q_{\max} = y^{(2)} = net^{(2)} = W^{(2,1)} \tanh(W^{(1,0)} I_{dch} + \Theta^{(0)}) + \theta^{(1)} \tag{9.10}$$

This model is trained by adapting the connection weights in response to 10 training pairs (I_{dch}, $Q_{\max}$) with the BP algorithm. The aim is to arrive at a unique set of weights that is capable of correctly associating all of the discharge currents with their associated available capacities. The trained ANN provides a twice lower mean estimation error compared to the one estimated from the Peukert's equation. The accuracy of the ANN has been verified by using nine other measured pairs to be within 0.6%.

The influence of temperature on a battery's available capacity is highly nonlinear. Shen et al. improved the previous ANN by adding the battery temperature as a second input [5]. They also added two other neurons in the hidden layer and replaced the "hyperbolic tangent" activation function by a "sigmoid" one, as follows:

$$Q_{\max} = y^{(2)} = net^{(2)} = W^{(2,1)} \operatorname{sigmoid}\left(W^{(1,0)} [I_{dch} T]^{\mathrm{T}} + \Theta^{(0)}\right) + \theta^{(1)} \tag{9.11}$$

Experimental data come from a 24-V LAB pack consisting of two six-cell modules connected in series, whose rated capacity is 40 Ah at a 20-h discharge rate (C/20). For simulating battery operation in EVs, different discharge currents are selected to discharge the battery (i.e., C/5, C/4, C/3, C/2, C/1.3, and C/1). Also, different surface temperatures of the battery are considered (10°C, 15°C, 20°C, 25°C, 30°C, 35°C, and 40°C) to emulate the actual temperature inside the vehicle chassis. To train the ANN model using the BP algorithm effectively with the sigmoid function, the input and output should be normalized:

$$Y_{nor} = \frac{Y - Y_{\min}}{Y_{\max} - Y_{\min}} \tag{9.12}$$

After training, the ANN model can map the nonlinear relationship between the available capacity and the discharge current under different temperatures of the battery surface, with a maximum relative error of about 5% between 20°C and 30°C.

In another study by Abolhassani et al. [6], a two-layer ANN is used to determine the battery equivalent circuit parameters from a single input: the SOC. There are six outputs: three resistances, two capacitances, and one inductance (Figure 9.3). The ANN is trained with electrochemical impedance spectroscopy (EIS) data from 10 similar SABA 6SB6 sealed lead-acid maintenance-free batteries during their second discharge and at 20 different SOCs. For scaling ANN inputs and targets, the mean and standard deviation of the training set are normalized so that they will have zero mean and unity standard deviation. The BP algorithm is then used to estimate the optimal weight values. The cost function is the mean squared error (MSE) defined as

$$\mathrm{MSE}(k) = \frac{1}{N}\sum_{i=1}^{N}\left(\hat{y}_i^{(2)}(k) - y_i^{(2)}\right)^2 \tag{9.13}$$

where $y_i^{(2)}$ is the target and $\hat{y}_i^{(2)}(k)$ the estimator, which moves closer to the target at each step k. The weight at each step is defined by the "gradient descent" method as follows:

$$w_{ij}^{(l)}(k+1) = w_{ij}^{(l)}(k) - \gamma \frac{\partial \mathrm{MSE}(k)}{\partial w_{ij}^{(l)}(k)} \tag{9.14}$$

where γ is the learning rate, which is usually set between 0 and 1. This ANN works fast and the accuracy of this method has been validated with experimental data. It can be extended for other different equivalent circuit models, and can also be modified to simulate battery characteristics by entering other battery parameters.

Three ANNs made up of a single input and two layers have been designed in MATLAB by Karami et al. [7] in order to estimate critical points related to the cold

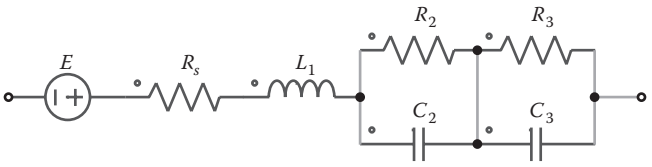

FIGURE 9.3 Equivalent circuit model of the lead-acid battery by Abolhassani et al. (From Abolhassani Monfared, N. et al., *Journal of Power Sources* 158, 932–935, 2006.)

cranking of LABs: time–voltage behavior of the batteries during a 10-s discharge (model 1), voltage values at discharge times of 30, 60 and 90 s (model 2), and time to reach a final voltage of 6 V (model 3). Cold cranking tests have been performed at −18°C on 17 sealed LABs (12 V, 50 Ah) with lead-calcium alloy grids. Nine discharge currents (1C, 3C, 5C, 7C, 9C, 11C, 12C, 14C, and 17C) are used for the training set, five discharge currents (2C, 6C, 8C, 13C, and 16C) for the prediction set, and three discharge currents (4C, 10C, and 15C) for the validation set. The prediction set is used as a tool for controlling the training. Maximum prediction errors in model 1 (seven hidden and ten output layers), model 2 (eight hidden and three output layers), and model 3 (three hidden and one output layers) are under 3.1%, 3.3%, and 3.5%, respectively. The results obtained show that the models can be used in the battery industry for the prediction of the cold cranking behavior of LABs at high discharge currents, based on experimental cold cranking data at low discharge currents, without the use of expensive and complex instruments.

The same authors also investigated the quantity of water loss in the life cycle of 72 LABs (12 V, 50 Ah) with a low antimony grid alloy at different end-of-charge (EOC) voltages (from 13 to 15 V in increments of 0.25 V) and temperatures (0°C, 30°C, 40°C, 50°C, 60°C, 70°C, 80°C, and 90°C), during a period of 10 days [8]. The behavior of batteries in different EOC conditions has been modeled by a three-layer ANN composed of three inputs (time, voltage, and temperature), two hidden layers of 10 neurons, and one output (water loss quantity), using MATLAB. Four temperatures are used in the training set, out of which three are used in the prediction set and one in the validation set. To achieve a better evaluation of the predictability of the approach, three models with different validation temperatures are used (model 1 = 50°C, model 2 = 60°C, and model 3 = 70°C). There is a good agreement between predicted and experimental results in both the prediction and validation sets for all models. Mean errors in predicting the water consumption from the EOC voltage–temperature–time relationship for models 1, 2, and 3 are below 0.99%, 0.03%, and 0.76%, respectively. The model can be used by inexperienced operators.

In 2007, Shen [9] extended the application of ANNs, which he contributed to develop in previous studies [4,5], to the SOC estimation in EVs. The LAB capacity changes noticeably, depending on the discharge profiles (Federal Urban Driving Schedule [FUDS], Federal Highway Driving Schedule [FHDS], etc.) even though the average discharge rate is the same. To account for this dependence, the first five inputs of its ANN are the capacities discharged at different rates (Figure 9.4). The activation function used is the regular "hyperbolic tangent." The ANN is trained by using the Levenberg–Marquardt algorithm, a variation of Newton's method designed for minimizing functions like MSE, defined in Equation 9.13. In this algorithm, the MSE is expressed as a function of the ANN parameters:

$$H = \left\{ w_{ij}^{(1,0)}, \theta_i^{(0)}, w_i^{(2,1)}, \theta^{(1)} \right\} \quad i = 1, ..., 11, \quad j = 1, ..., 7 \tag{9.15}$$

The optimum parameters are obtained through the following iterative process:

$$H(k+1) = H(k) - (\nabla^2 \mathrm{MSE}(H(k)))^{-1} \nabla \mathrm{MSE}(H(k)) \tag{9.16}$$

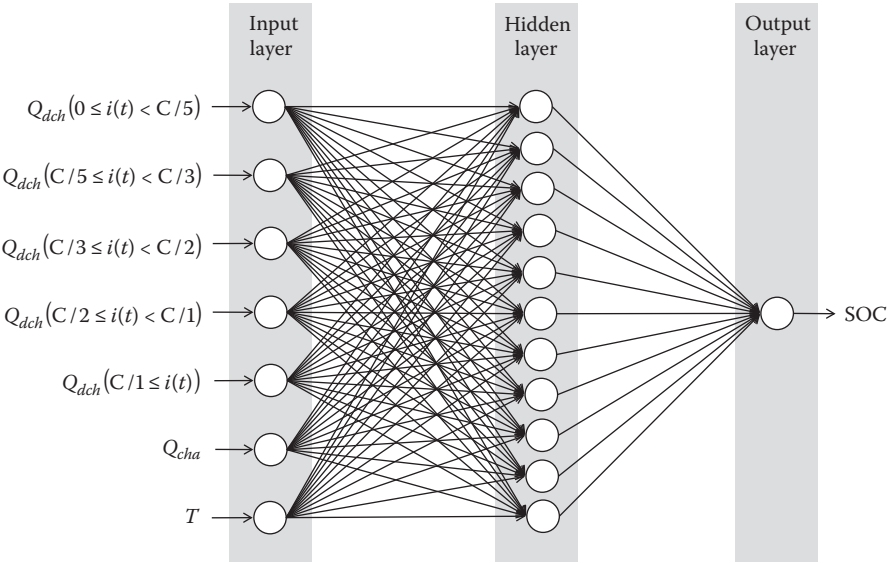

FIGURE 9.4 Architecture of the seven input, double layer ANN used by Shen. (From Shen, W. X., *Energy Conversion and Management* 48, 433–442, 2007.)

where $\nabla^2 \text{MSE}(H(k))$ and $\nabla \text{MSE}(H(k))$ are the Hessian matrix and the gradient vector of MSE at the k'th iteration, respectively. The proposed approach is effective and accurate, since it can estimate the SOC to better than 2% of error compared to the experimental data. Furthermore, it can easily be extended to the SOC estimation of other types of EV batteries.

Three years later, a novel approach was developed by Yanqing using an adaptive ANN-based model and a neurocontroller for online cell SOC determination [10]. A radial basis function (RBF) NN has been adopted to simulate the battery. It is a typical two-layer feedforward NN that allows for fast training and is capable of converging to a global optimum. Its hidden layer comes with a nonlinear RBF activation function given by

$$y_i^{(1)} = \sum_{j=1}^{N_0} w_{ij}^{(1,0)} \exp\left(-\beta \left\| y_j^{(0)} - c_j \right\|\right) + \theta_i^{(1)} \tag{9.17}$$

where β acts as a weight for the Euclidian distance between the input vector and the center c_j of neuron j. The SOC is described with a discrete-time approximate recurrence:

$$\text{SOC}(k) = \text{SOC}(k-1) + \frac{\eta(k)\, i(k)\, \Delta t}{Q_{\max}} \tag{9.18}$$

where Δt is the sampling period. The battery terminal voltage $u(k)$ is predicted with the following model, where U_0 is the open circuit voltage (OCV), and K_i a set of constants:

$$u(k) = U_0 + K_1 T(k) + Ri(k) - K_2 \mathrm{SOC}(k) - \frac{K_3}{1 - \mathrm{SOC}(k)} + K_4 \ln(\mathrm{SOC}(k)) + K_5 \ln(1 - \mathrm{SOC}(k)) \tag{9.19}$$

In addition, a neurocontroller based on a BP NN and modified proportional-integral-derivative (PID) controller was used to determine the cell SOC. This algorithm was applied for the SOC determination of a LAB and validated with tests performed on actual cells. Results showed that the ANN-based battery model can adaptively simulate a battery system with high accuracy, and the predicted SOC quickly converges to the real value within a relative error of ±1%.

9.3 FUZZY LOGIC-BASED MODELS

9.3.1 Introduction to Fuzzy Logic

Humans have a remarkable capability to reason and make decisions in an environment of uncertainty, imprecision, incompleteness of information, and partiality of knowledge, truth, and class membership. Misconceptions about fuzzy logic (FL) abound. To begin with, FL is not fuzzy. In large measure, FL is precise. Another source of confusion is the duality of meaning of FL. In a narrow sense, fuzzy logic is a logical system. But, in a much broader sense, as in its majority use today, FL is more than a logical system. The concepts of graduation and granulation form the core spirit of FL and are its most distinct features. More specifically, in FL everything is allowed to be graduated, that is, be a matter of degree that makes it "fuzzy." Furthermore, in FL everything is granulated, with a granule being a clump of attribute values drawn together by measuring distinguishability, similarity, proximity, or functionality. For example, the state of a LAB is granulated when its values are described as "deeply discharged," "normally discharged," or "shallowly discharged." A linguistic variable may be viewed as a granulated variable whose granular quantification is linguistic expressions of granules. In a qualitative way, graduation and granulation play pivotal roles in human cognition.

The principal objective of FL is the formalization/mechanization of this capability. The term *fuzzy logic* emerged during the development of the theory of fuzzy sets by Lotfi Zadeh (1965). A fuzzy subset A of a (crisp) set X is characterized by assigning to each element x of X the degree of membership of x in A (e.g., X is a group of batteries, A the fuzzy set of new batteries in X). Now, if X is a set of propositions, then its elements may be assigned their degree of truth, which may be "absolutely true," "absolutely false," or some intermediate degree of truth; that is, one proposition may be truer than another. This is obvious in the case of vague (imprecise) propositions like "this battery is new" (or "used," "dead," etc.). The standard set

of truth degrees is the real interval [0, 1] with its natural ordering ≤ (1 standing for absolute truth, 0 for absolute falsity); but one can work with different domains, finite or infinite, linearly or partially ordered.

To illustrate this, consider a LAB having an OCV value of 12.5 V, which is crisp data (i.e., expressed in a precise manner). In contrast, fuzzy data is depicted in an indefinite, often descriptive, way (e.g., the battery is "deeply discharged"). This linguistic description can cover a range of OCVs, and the degree to which a crisp data point falls into the fuzzy set of "deeply discharged" is indicated by a fit value (fuzzy unit) between 0 and 1. The fit value is sometimes called the *degree of membership*. Figure 9.5 shows an example of various fuzzy subsets or membership functions of OCV. Depicted is the degree of membership of various OCVs to the fuzzy subsets "deeply discharged," "normally discharged," and "shallowly discharged." The process of assigning membership functions to sets of data is referred to as "fuzzification." The membership functions and rule set may be prescribed by an expert or created by an ANN algorithm.

Fuzzy set theory explicitly depicts a method to categorize measured data using linguistic variables such as "deeply discharged," "normally discharged," and "shallowly discharged," as exemplified earlier. It accounts for the uncertainty, or fuzziness, inherent in such a linguistic description by using multivalued sets. This representation offers a qualitative rather than a numerical description of a system. This intuitive representation allows a relatively easy logical development of a model with a fuzzy algorithm compared to crisp numerical computations. This ease should not, however, undermine its powerful ability to solve complex control and modeling problems. FL usually uses "if–then" rules to perform the inference procedure describing the relationship between input and output variables. For example, in hybrid electric vehicles (HEVs), a simple battery management strategy might look like this:

- IF battery is shallowly discharged, THEN use only the electric motor.
- IF battery is normally discharged, THEN use the internal combustion engine (ICE), electric motor, and regenerative braking.
- IF battery is deeply discharged, THEN use only the ICE and regenerative braking.

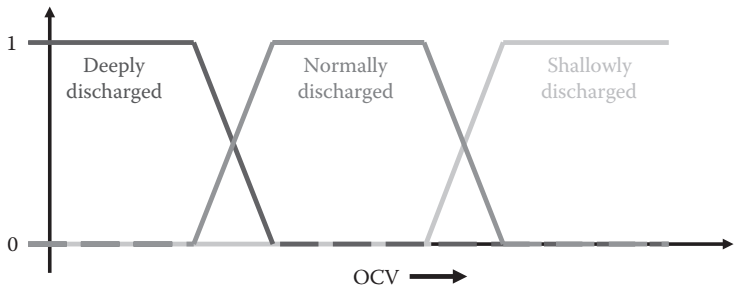

FIGURE 9.5 Example of membership functions for the battery OCV.

9.3.2 Applications of the Fuzzy Logic Approach

From 1998 to 2002, Singh and Reisner developed a patented FL method for estimating the SOC and state of health (SOH) of batteries [11]. The SOH of a battery may be defined in several ways. The precise definition depends on a particular application. For example, in a portable defibrillator application, the number of high-current discharge pulses that may be delivered by the battery is of paramount importance, whereas in an uninterruptible power supply (UPS) application, the available capacity of the battery is the parameter of concern. To make a low-cost, practical diagnostic system for automatic portable defibrillator batteries, the acquired EIS data at various SOCs and SOHs must be reduced to a form that can be easily manipulated by FL models. This involves finding one or more frequencies where the variation in the magnitude and/or phase angle of the impedance can provide "some discrimination" among different SOCs and SOHs. The FL model developed with the Fuzzy Logic Toolbox in MATLAB has three inputs: impedance magnitude at 160 Hz, phase angle at 16 Hz, and cycle number. When implemented in a low-cost microcontroller, it can provide an accurate, reliable, and low-cost LAB SOH.

Singh and Reisner also developed FL-based battery management systems (BMSs) dedicated to 42-V automotive applications in anticipation of the increasing use of electric and electronic devices in automobiles and the resulting demands of more electric power usage in the drive train and the cabin [12]. For this BMS application, not only EIS but also 15-min galvanostatic C/2.5 discharging data were used. In the FL model, the impedance at 10.3 and 103 Hz, respectively, the phase angle at 10.3 Hz of the EIS data, and the voltage of the battery system in the discharge are the inputs. The model output is the SOC. Singh and Reisner also applied this approach to other battery systems, including Li-SO_2 and Li-MnO_2 primary cells and Ni-MH secondary batteries. Clearly the combination of FL data analysis and a battery interrogation method, such as EIS or partial discharges, offers a powerful approach to battery SOC/SOH estimation if a data set is available. Even if the data set is new or still evolving, the FL model is adaptable and evolves as data are obtained.

Salkind et al. continued the study of the dynamic characteristics of LABs previously reported and adopted them into larger cells and batteries [13]. The same methodology combining EIS and discharge data with FL data analysis was used to characterize 6-V, 10-Ah valve-regulated lead-acid (VRLA) batteries and larger batteries used in tanks and other vehicles. The two batteries on which measurements were made are the Yuasa NP 10-6 and the Exide US6TMF military batteries. Two Hg-Hg_2SO_4 reference electrodes were inserted through the casing of the three-cell Yuasa battery in order to measure the potentials of the two external cells. The equivalent circuit model (ECM) used to fit the impedance data is shown in Figure 9.6. The bulk series resistance of the battery is modeled by the series resistance R_s and the two electrodes are modeled by a parallel resistor–capacitor circuit. A parallel inductor–resistor circuit is used to model the high-frequency part of the impedance characteristics. The authors use an additive FL model such as Takagi-Sugeno-Kang (TSK) or standard additive model (SAM). The latter basically consists of rules in the form of

$$\text{IF } i \text{ is } \mathbf{A}_i \text{ AND } T \text{ is } \mathbf{B}_j \text{ THEN } SOC \text{ is } \mathbf{C}_k \tag{9.20}$$

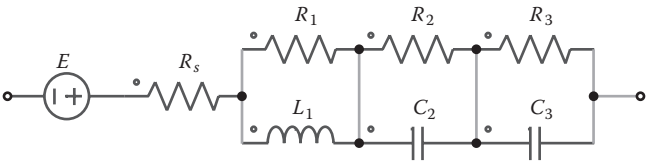

FIGURE 9.6 Equivalent circuit model of the lead-acid battery by Salkind et al. (From Salkind, A. J. et al., *Journal of Power Sources* 116, 174–184, 2003.)

A few years later, Malkhandi developed another kind of SOC estimator dedicated to LABs [14]. The proposed system works in two phases. In the first phase, the system estimates the SOC through Equations 9.2 and 9.3. The estimation of SOC is done by an improved coulomb metric method, which uses a correction parameter η supplied by a FL model from two inputs (current and temperature). The initial training of the FL model before the first-time use is performed with the following equation:

$$\eta(I,T) = \frac{1}{1 - K_I \log \dfrac{I}{I_{ref}} + K_T(T - 300)} \tag{9.21}$$

In the FL model, the ranges of current and temperature span from C/100 to C/2, and from 273 to 323 K, respectively; the output space is kept in the range from 0.1 to 5. The universes of discourse for the current, temperature, and output have 30, 6, and 150 fuzzy sets, respectively. In the second phase, when the battery is fully discharged, the learning process is carried out. The error in the SOC estimation is extracted and applied for the automatic generation of new rules in the FL model. At the end of the learning process the newly generated FL model replaces the old one and is used in the next estimation process. The validation is conducted in real time using the measured voltage, current, and temperature data of an 80-Ah, 12-V VRLA-type battery on an 8-bit microcontroller.

The energy management of a PV system can also be optimized by the fuzzy logic technique. In 2011, Chekired et al. proposed an "intelligent battery controller" based on a fuzzy algorithm and technique [15]. The two inputs are the battery voltage u and the change of the battery voltage Δu, which is defined by

$$\Delta u = u(kh) - u((k-1)h) \tag{9.22}$$

where k is the sample number and h the sampling time. The two output variables are the control signal of the switch K_1 located between the PV panel, and the battery and the control signal of the switch K_2 located between the battery and the load. The linguistic variables associated to u are BUD for underdischarged battery, BD for discharged, BIC for in charge, BC for charged, and BOC for overcharged. The linguistic variables associated with Δu are NC for negative change, ZC for zero change, and PC for positive change. The linguistic variables associated with the outputs are Off, Temporary Off, On, and Temporary On. The controller actions depending on

the inputs can be summarized in a table containing all possible combinations of u and Δu. The transition time between the charging and discharging modes using this technique is claimed to be very short compared to other techniques used in this field.

HEVs combine two or more energy sources (at least one electrical) to benefit from their different characteristics regarding autonomy, reversibility, and dynamic response. Therefore, there is also a need for an energy management system that meets different design requirements such as comfort or energy consumption minimization. Martinez et al. designed a fuzzy logic controller to manage the energy in a HEV equipped with three different energy sources: a lead-acid battery (540 V, 73 Ah), an ultracapacitor module, and a fuel cell [16]. They used human expertise to design the FL controller. A survey using linguistic labels was conducted among experts in HEVs. As each expert has defined different fuzzy sets and rules, they use type 2 fuzzy sets that permit the knowledge from the experts handling the uncertainty associated with the meaning of the words to be combined. Simulation results show that the type 2 FL-based energy management system satisfies the objectives.

9.4 EMPIRICAL MODELS

9.4.1 Introduction to Empirical Models

The empirical approach is usually chosen when we do not have all data required to develop a fundamental model of a complex process, the time to develop it, ease to perform experiments, or a need for a very accurate model. An empirical model is entirely based on data. Since any model has to be made to confront reality, it is through the data that the confrontation happens. By data, we mean measurements or observations collected in the real world. Interaction between data and models occurs in a couple of ways. Figure 9.7 presents the building procedure for a LAB empirical model. First, battery testing provides the data that are needed to design a model. Then, the test data are used to identify the model parameter values, during what we could call a calibration stage. The model is validated by comparing its simulation results to the experimental data. Finally, another dataset is used to check the model's robustness. Change can be made at different stages if the model does not meet the requirements.

A polynomial function is the first approach suggested by most of the curve-fitting tools available (e.g., Excel, graphing calculators, MATLAB). Usually, it is a univariate (single-variable) polynomial function with constant parameters given by

$$\forall n \in \mathbf{N}^*, x \in \mathbf{R} \quad y = f(x) = \sum_{i=0}^{n} a_i x^i \tag{9.23}$$

where n is an integer that defines the degree of the polynomial. A linear function ($n = 1$) is used very frequently when the plotted data points seem aligned. The slope of the line depends on the sign of a_1. If a_0 is sufficiently small, one should consider y as proportional to x. A quadratic function ($n = 2$) makes sense for fitting data with one minimum ($a_2 > 0$) or one maximum ($a_2 < 0$). A cubic function ($n = 3$) is appropriate

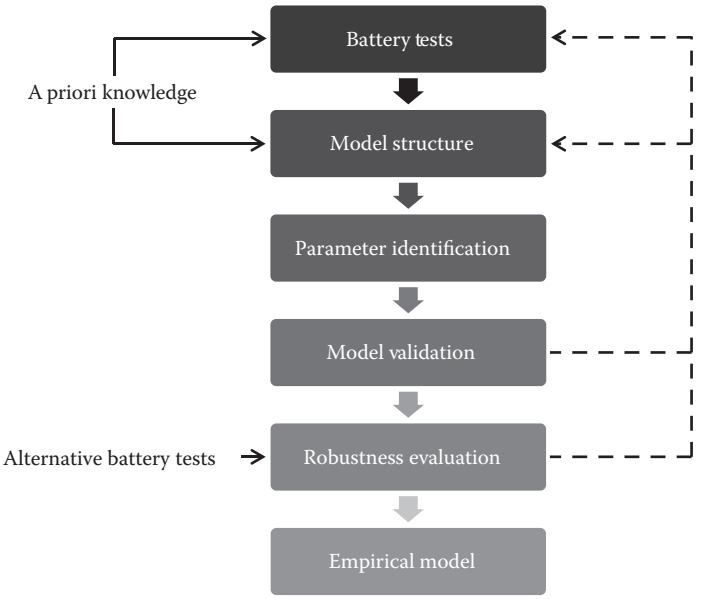

FIGURE 9.7 Building procedure for a lead-acid battery empirical model.

for fitting data with both a minimum and a maximum. A quartic function ($n = 4$) allows adding one more extremum and so on. Among the advantages of polynomial models are their simple form (computationally easy to use), well-known and understood properties, moderate flexibility of shapes, and independence on the underlying metric. The latter means that changes of location and scale in the raw data result in a polynomial model being mapped to a polynomial model. However, polynomial models also have the following limitations: poor interpolation (e.g., oscillations between two exact-fit values), poor extrapolation (e.g., rapid deterioration outside the range of the data), asymptotic properties, and a trade-off between shape and degree (a complicated structure may lead to a high-order unstable model).

A rational function can also be considered as an empirical model. It is an algebraic fraction such that both the numerator and the denominator are polynomials:

$$\forall (m,n) \in \mathbf{N}^{*2}, x \in \mathbf{R} \quad y = f(x) = \frac{\sum_{i=0}^{n} a_i x^i}{\sum_{j=0}^{m} b_j x^j} \tag{9.24}$$

A rational function has as many vertical asymptotes as real roots in the denominator, within the limits of m. Another asymptote comes from the limit of f as x approaches infinity, which can result in a horizontal ($n = m$), oblique ($n = m + 1$), parabolic ($n = m + 2$), or any other kind of asymptote defined by a polynomial.

Rational function models inherit the advantages of the polynomial family, despite a less simple form, and can take on an extremely wide range of shapes. They have better interpolation properties (typically smoother and less oscillatory) than polynomial models, and excellent extrapolation powers due to their asymptotic properties. Moreover, they can be used to model a complicated structure to a fairly low degree in both the numerator and denominator. On the other hand, because the properties of the rational function family are often not well understood, one might wonder which numerator and denominator degrees should be chosen. Unconstrained rational function fitting may also lead to undesired vertical asymptotes due to roots in the denominator polynomial.

Keeping in mind that a linear regression is the only one that can be relatively easily done "by hand," if the data do not seem to be linear, it is worth trying to plot one or both variables as logarithms. The idea is to get a graph that looks reasonably linear and then to get a linear model, which finally leads to three usual different cases:

- If y depends linearly on $\ln x$, a logarithmic function is then a suitable model.
- If $\ln y$ depends linearly on $\ln x$, a power function is then a suitable model.
- If $\ln y$ depends linearly on x, an exponential function is then a suitable model.

Some other functions can be considered if none of the preceding functions is appropriate. A sigmoid or logistic function (cf. the activation functions provided in Section 9.2.2) can be proposed if the data have an S shape. A trigonometric or circular function may also be useful if the data are periodic, since they can necessarily be decomposed in a Fourier series. Modeling with piecewise-defined functions might be a reasonable choice as well, recalling that such a function is defined by different formulas applied to specific intervals of the independent variable x. Indeed, it is sometimes better to model a given dataset using one piecewise-defined function than a single function.

Among the methods frequently used to obtain regression models and curve-fitting figures is the least squares criterion, previously put into practice through the MSE (Equation 9.13). This method is about estimating parameters by minimizing the squared discrepancies (residuals) between observed data, on the one hand, and their expected values on the other. In practice, the vertical offsets from a line (polynomial, surface, hyperplane, etc.) are almost always minimized, instead of the perpendicular offsets (Figure 9.8). This provides a fitting function estimating y for a given x, allowing uncertainties of the data points along the x- and y-axes to be incorporated simply, and also providing a much simpler analytic form for the fitting parameters than would be obtained using a fit based on perpendicular offsets. In addition, the fitting technique can be easily generalized from a best-fit line to a best-fit polynomial, when sums of vertical distances are used. In any case, for a reasonable number of noisy data points, the difference between vertical and perpendicular fits is quite small.

With logarithmic, power, or exponential models, one may modify the data by considering the logarithm of one or both of the variables instead of the original data, in order to reduce a nonlinear model to a linear one. This method is sometimes called the transformed least squares criterion. Another criterion, namely the Chebyshev

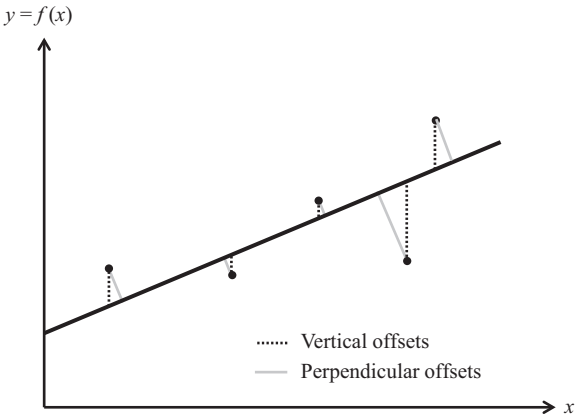

FIGURE 9.8 Illustration of the difference between vertical and perpendicular offsets.

approximation, is also available. It differs from the least squares criterion by minimizing the maximum of the absolute values of the residuals instead of the sum of their squares. Therefore, it provides some insight regarding the worst case scenario, which might help expose a possible weakness in the empirical model.

9.4.2 Applications of Empirical Models

The search for an equation giving an accurate description of the discharge of lead-acid cells and batteries over a wide range of conditions starts with Shepherd in the middle of the 1960s [17]. His equation gives the cell potential u during discharge as a function of discharge time t, current density i, and certain other factors:

$$u = E - R_i i + K_1 \exp\left(-K_2 \frac{it}{q_s}\right) - R_p \left(\frac{q_s}{q_s - it}\right) i \tag{9.25}$$

where E represents the electromotive force (V), R_p the polarization coefficient ($\Omega \cdot cm^2$), q_s the amount of available charges ($C \cdot cm^{-2}$), and R_i the internal resistance ($\Omega \cdot cm^2$). The first term on the right is the OCV. The second term considers the instantaneous voltage drop due to the internal resistance. The third term is added to account for the progressive voltage decrease due to the charge transfer. If the initial drop in voltage is too rapid in the observed experimental data, this term can be ignored ($K_1 = 0$). The fourth term expresses the fact that the polarization resistance is proportional to the amount of used active material. Shepherd's empirical model made possible a description of cell discharge characteristics using a minimal amount of experimental data, yet at the same time pinpointing experimental errors. This empirical equation can also be used to describe cell charges and power evolution and to predict capacity.

A number of empirical equations have been proposed to depict the dependence of capacity on the discharge current I and the discharge time t (Schröder [1894],

Liebenow [1897], Peukert [1897], Rabl [1936], Davtyan [1946], and Shepherd [1965]), as reported by Bode [18] and recently validated over a wide range of operating conditions [19]. Despite these attempts, only Peukert's equation has received wide acceptance:

$$I^n t = C \tag{9.26}$$

where n and C are empirical constants (typically $1.1 < n < 1.4$ and $C > 0$) that can be derived from tests at two different rates of discharge. The logarithmic Peukert's equation can be plotted as a straight line on a log-log chart. The reason why Peukert's law is the most widely used empirical equation to describe a battery's current and capacity relationship can be attributed to three merits. The first one is its ease of use since only two empirical parameters need to be determined from two test parameters: current and time. The second one is its accuracy, generally better than 90% from C/20 to 10C. The third one is its applicability over a variety of conditions, such as temperature (typically from –20°C to 60°C) or battery size (either aspect ratio or capacity).

Discharge or charge of a motive power cell (i.e., a cell with relatively tall and narrow plates) is accompanied by the development of a nonuniform current density and electrolyte distribution in the vertical direction y. Sunu and Burrows have used a variation of Shepherd's treatment to analyze their potential distribution data measured at C/5.5, C/2.5, and C/1 [20]. They assumed linear polarization, since the apparent current densities are relatively low, and that the current flow in the electrolyte is perpendicular to the electrodes, due to the small separation between the plates compared to their height. They defined the cell voltage drop Δu as a function of y:

$$\Delta u(y) = \left(R_s + R_n + R_p\right) i\, Q \coth Q \left(1 - \frac{y}{H}\right) \quad \text{with} \quad Q = H\sqrt{\frac{W\left(R_g^+ + R_g^-\right)}{R_s + R_n + R_p}} \tag{9.27}$$

where R_s, R_n, and R_p represent the resistance of the separator (including the electrolyte) and those due to the polarization of the two electrodes ($\Omega \cdot cm^2$); R_g is the resistance of two grids measured vertically ($\Omega \cdot cm^{-1}$); H is the electrode height (cm), and W is the electrode width (cm). Contrary to the Δu expressed by the three last terms on the right of Equation 9.25, this one does not account either for the voltage decrease due to charge transfer or for the polarization resistance dependence on the amount of used active material. Calculation shows that the overall current density nonuniformity is strongly dependent on the plate height.

In PV applications, an empirical model for a LAB derived from Shepherd's treatment was adopted by Facinelli to indicate SOH [21]. The model includes the charge efficiency (a key issue in PV) and temperature effects on battery performance. Experiments were conducted on a single cell of a C&D QP 75-5 battery, which has a nominal capacity of 161 Ah at a 10-h discharge rate. The equation relating u to I and T is a rearrangement of the four-parameter empirical formula of Shepherd [17]:

$$u(I,T)=\begin{cases} U_{cha}(T)+R_{cha}(T)\,I\left[1+\dfrac{K_{1,cha}\,Q(I)}{K_{2,cha}\,Q_{cha}(T)-Q(I)}\right], & I>0 \\ U_{dch}(T)+R_{dch}(T)\,I\left[1+\dfrac{K_{1,dch}\left(Q_{dch}(T)-Q(I)\right)}{K_{2,dch}\,Q_{dch}(T)+Q(I)}\right], & I<0 \end{cases} \tag{9.28}$$

These equations have been adapted to include the linear temperature dependence of the pseudo-OCVs:

$$\forall j=\{cha,\,dch\},\quad U_j(T)=K_{3,j}T+K_{4,j} \tag{9.29}$$

and the temperature dependence of the resistance as a function of capacity:

$$\forall j=\{cha,\,dch\},\quad R_j(T)=K_{5,j}+\frac{K_{6,j}}{Q_j(T)} \tag{9.30}$$

The charge that can be put into a LAB without causing heavy gassing is generally less than what the battery can provide when discharged at the same rate. The two categories of capacity are represented by Q_j (Ah):

$$\forall j=\{cha,\,dch\},\quad Q_j(T)=K_{7,j}T^2+K_{8,j}T+K_{9,j} \tag{9.31}$$

The best fit of these equations to the experimental data yields the values of the constants $K_{i,j}$, as given in Table 9.1.

TABLE 9.1
Constant Parameters Used in Facinelli's Empirical Model

$K_{i,j}$	j		
i	*cha*	*dch*	Units
1	3.643	2.456	
2	1.417	0.288	
3	–0.00127	0.000606	V K^{-1}
4	2.195	2.116	V
5	–0.00169	–0.000173	Ω
6	0.6987	0.3753	Ω Ah
7	–0.00757	0	Ah K^{-2}
8	1.953	1.292	Ah K^{-1}
9	111.9	141	Ah

Source: Facinelli, W. A., Modeling and simulation of lead-acid batteries for photovoltaic systems. In *Proc. 18th Intersociety Energy Conversion Engineering Conf.*, pp. 1582–1588. Orlando, FL, 1983.

The equation relating Q to I is the simplest ordinary differential equation:

$$\frac{dQ}{dt} = \begin{cases} I, & I \le I_m \\ I_m, & I > I_m \end{cases} \quad \text{with} \quad I_m = \begin{cases} 1.333\,(Q_{dch} - Q), & Q \le 0.9925\,Q_{dch} \\ 0.006\,Q_{dch}, & Q > 0.9925\,Q_{dch} \end{cases} \tag{9.32}$$

The main advantage of this model is its adaptability to a wide range of batteries.

In the early 1990s, an empirical model was developed by Roan and Raman [22] in order to provide a fast executing battery performance simulation model that could be used as a subroutine in HEV and EV simulation codes. The current effect on battery capacity has been modeled by Peukert's equation (Equation 9.26) and the temperature effect by Equation 9.31. Available cycle life data for LABs suggests that the cycle life depends strongly on DOD and has been modeled by the following equation:

$$N_{new}(\text{DOD}) = N_{new}(0)e^{a\,\text{DOD}} \tag{9.33}$$

where N_{new} is the cycle life (number of cycles) of a new battery at a given DOD and $a < 0$ is the slope of the natural logarithmic plot of $N_{new}(\text{DOD})/N_{new}(0)$, obtained experimentally. The effect of age A (year) on battery is modeled by considering a linear decrease in operational life as the battery gets older, typically 3% per year:

$$N(\text{DOD}, A) = N_{new}(\text{DOD})[1 - 0.03\,A] \tag{9.34}$$

The combined effect of age and DOD on the battery lifetime can therefore be reasonably modeled by introducing the age factor (N/N_{new}) as shown:

$$Q(T, \text{DOD}, A) = Q(T)\frac{N(\text{DOD}, A)}{N_{new}(\text{DOD})} \tag{9.35}$$

At high rates, the simulation shows that temperature and age do not result in any substantial effect on the capacity. At very low temperatures, age again does not have any significant effect on the capacity.

In the case of PV applications, Copetti et al. proposed a new empirical model of LABs from experiments carried out at various currents (C/100 to C/5) and temperatures (5°C to 45°C) with several references: Fulmen EF2050 (50 Ah), Varta Vb624 (100 Ah), and ATSA Tudor (180 Ah) [23]. A discharge voltage equation was developed for a single-cell (2 V) as follows:

$$u_{dch} = 2.085 - 0.12\,\text{DOD} + \frac{I}{Q_{ref}}\left(\frac{4}{1+|I|^{1.3}} + \frac{0.27}{\text{SOC}^{1.5}} + 0.02\right)(1 - 0.007\Delta T) \tag{9.36}$$

where the temperature variation ΔT is the difference between the battery temperature and an ambient temperature of 25°C, and the reference capacity Q_{ref} is obtained at C/10. The battery efficiency during discharge is assumed to be 100%; however, the total amount of useful charge is limited by the current and temperature given by the capacity equation:

$$Q_{nom} = \frac{1.67\, Q_{ref}(1 + 0.005\Delta T)}{1 + 0.67\left(I/I_{ref}\right)^{0.9}} \tag{9.37}$$

For the charging process up to overcharging, the parameter values differ from those used in discharging:

$$u_{cha} = 2 + 0.16\,\mathrm{SOC} + \frac{I}{Q_{ref}}\left(\frac{6}{1 + I^{0.86}} + \frac{0.48}{\mathrm{DOD}^{1.2}} + 0.036\right)(1 - 0.025\Delta T) \tag{9.38}$$

The charge efficiency η_{cha} variation with SOC and current is represented by the following relation, whose parameters fit the data measured on batteries with tubular positive plates and low-antimony alloys:

$$\eta_{cha} = 1 - \exp\left(-\frac{20.73\,\mathrm{DOD}}{I/I_{ref} + 0.55}\right) \tag{9.39}$$

The test results demonstrate that the final charge voltage u_{eoc} increases with the current intensity and with decreasing temperature:

$$u_{eoc} = \left[2.45 + 2.011 \ln\left(1 + \frac{I}{Q_{ref}}\right)\right](1 - 0.002\Delta T) \tag{9.40}$$

The same argument can be used to write a function for the gassing voltage u_{gas} with different parameter values:

$$u_{gas} = \left[2.24 + 1.97 \ln\left(1 + \frac{I}{Q_{ref}}\right)\right](1 - 0.002\Delta T) \tag{9.41}$$

The overcharge phenomenon (gas evolution) can be represented by an exponential function, such as

$$u_{ovc} = u_{gas} + (u_{eoc} - u_{gas})\left[1 - \exp\left(\frac{t - t_{gas}}{\tau_{gas}}\right)\right] \tag{9.42}$$

where t_{gas} is the start of the overvoltage, which is assumed by the authors to occur when 95% of the capacity is restored. The time constant of this phenomenon τ_{gas} is inversely proportional to the current intensity and, as an approximation, can be written

$$\tau_{gas} = \frac{1.73}{1 + 852\left(I/Q_{ref}\right)^{1.67}} \tag{9.43}$$

Therefore, the voltage evolution during the charge process is represented by Equation 9.38, up to the start of gassing ($u_{cha} \le u_{gas}$) and by Equation 9.42 for overcharging ($u_{cha} > u_{gas}$) until the end of charge voltage u_{eoc} is reached.

The change to the use of maintenance-free lead-acid starting, lighting, and ignition (SLI) batteries by the U.S. Army in the late 1990s has revitalized the interest in the gas evolution phenomenon that takes place in these batteries, since they do not permit access to the electrolyte. Therefore, Catherino et al. decided to model the charging process together with the overcharging associated with gassing [24]. The voltage u of a discharged battery is approximated in the following semiempirical form:

$$u = K_1 + K_2 \ln\left(\frac{Q_{nom}}{Q_{cha}} - 1\right) \quad \text{with} \quad Q_{cha} = \int_{t_0}^{t} i_{cha}(\tau)\, d\tau \tag{9.44}$$

The effect of gassing is then superimposed by adding a component that simulates the gassing process in the form of the Tafel equation:

$$u = K_3 + K_4 \ln(Q_{gas}) \quad \text{with} \quad Q_{gas} = \int_{t_0}^{t} i_{gas}(\tau)\, d\tau \tag{9.45}$$

Since the gassing and the charging are coupled, the sum of the two individual components is set equal to the total applied constant current $I = i_{cha} + i_{gas}$. Considerable data have been collected by Exide on the dependence of the steady-state current and the actual gas evolved as a function of temperature and applied voltage during overcharge. These data reveal the functional dependence of the model parameters by noting that the constant current used to recharge the battery actually fits the linear model:

$$\ln I = K_1 + K_2 u + K_3 T + K_4[\%\ \mathrm{Sb}] \tag{9.46}$$

with 13.2 V $\le u \le$ 15.6 V, 0°C $\le T \le$ 60°C, and 0% $\le$ Sb $\le$ 2.6% in the alloy composition.

Another gassing current calculation approach for PV applications was developed by Piller et al. [25]. Current is usually small in PV applications and gassing is the major loss during charging; therefore, the Butler-Volmer equation can be modified and normalized to define the gassing current:

$$i_{gas} = i_0 \exp\left(\frac{u - U_{nom}}{K_1} - K_2 \frac{T - T_{ref}}{T T_{ref}} \right) \tag{9.47}$$

where i_0 is the exchange current density and U_{nom} the nominal voltage. The knowledge of the gassing current value may increase the reliability of a SOC indicator based on the current that is effectively recharging the battery:

$$\mathrm{SOC}(t) = \mathrm{SOC}_0 + \frac{1}{Q_{nom}} \int_{t_0}^{t} i_{cha}(\tau)\, d\tau \quad \text{with} \quad i_{cha}(\tau) = i(\tau) - i_{gas}(\tau) \tag{9.48}$$

The same authors go beyond the well-known linear relationship between OCV and SOC (Figure 9.9) by describing the variation of SOC from a linear combination of the intermediate electrical measurements on the battery, and the previous SOC value, which in the discrete time domain of sampling period h can be written as

$$\Delta\mathrm{SOC}(t) = K_0 + K_1 u(t) + K_2 i(t) + K_3 \mathrm{SOC}(t - h) \tag{9.49}$$

with

$$\mathrm{SOC}(t) = \mathrm{SOC}(t - h) + \Delta\mathrm{SOC}(t) \tag{9.50}$$

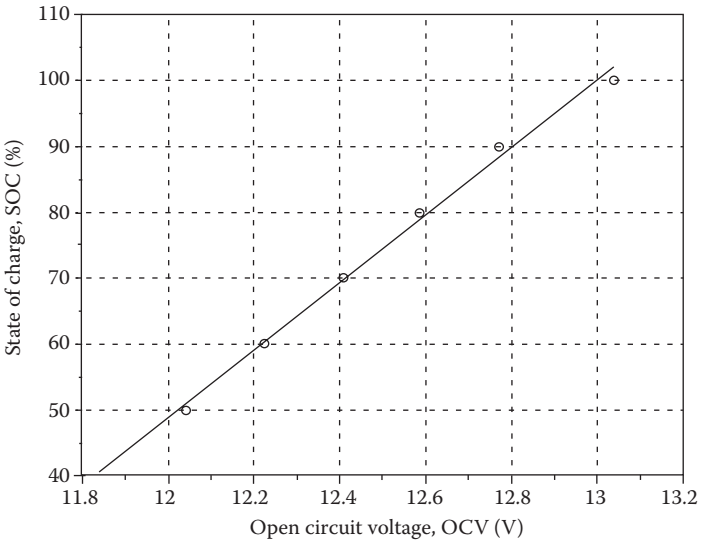

FIGURE 9.9 Dependence of the SOC on the OCV from a batch of VRLA batteries.

The model is developed for PV applications (i.e., for low currents and slow SOC changes) and is characterized by high robustness in relation to measurement errors and inaccurate initial conditions. It can be applied to various LAB types at different stages of their lives. However, the best results are achieved if reference data from the same battery type are used to calculate the K_i constants.

During the same period, Ross presented another LAB empirical model for PV applications, in which the battery current is normalized [26]:

$$I_{norm} = I_{sim}\frac{Q_{ref}}{Q_{sim}} \tag{9.51}$$

where I_{sim} is the simulated current, Q_{sim} the capacity of the simulated battery, and Q_{ref} the capacity of the reference battery used to develop the model. When the battery is discharging, its voltage is calculated from

$$\begin{aligned} u_{dch} = {} & E_{\max} + \frac{\partial E}{\partial T}(T-298) - \frac{\partial E}{\partial \mathrm{SOC}}(1-\mathrm{SOC}) \\ & + I_{norm}\frac{1-\dfrac{\partial R_i}{\partial T}(T-298)}{Q_{the}\left[1+\dfrac{\partial Q}{\partial T}(T-298)\right]}\left[\frac{K_{1,dch}}{1+(-I)^{K_{2,dch}}} + \frac{K_{3,dch}}{(\mathrm{SOC}+0.0001)^{K_{4,dch}}}\right] \end{aligned} \tag{9.52}$$

where $E_{\max}$ is the maximum OCV value obtained at 100% SOC and Q_{the} is the theoretical capacity of the battery obtained at an infinitesimal discharge current value. At rest, the voltage is equal to the OCV ($u_{rest} = E$) and calculated from a curve fit. When the battery is charging, its voltage is calculated from

$$\begin{aligned} u_{cha} = \min\Bigg\{ & U_{\max}, E_{\min} + \frac{\partial E}{\partial T}(T-298) + \frac{\partial E}{\partial \mathrm{SOC}}\mathrm{SOC} \\ & + \frac{I_{norm}}{Q_{nom}}\left[1+\frac{\partial R_i}{\partial T}(T-298)\right]\left[\frac{K_{1,cha}}{1+I^{K_{2,cha}}} + \frac{K_{3,cha}}{(1-\mathrm{SOC})^{K_{4,cha}}}\right]\Bigg\} \end{aligned} \tag{9.53}$$

where $U_{\max}$ is the maximum attainable voltage (i.e., the voltage reached when all the current is used in the gassing reaction), and $E_{\min}$ is the minimum OCV value obtained at 0% SOC. The gassing current I_{gas} is based solely on the voltage and the temperature through the Tafel equation, which is linearized at voltages just above the onset of gassing, U_{gas}. Between the latter and the voltage at which the linearization no longer applies, $U_{gas} + U_{Tafel}$, there is a smooth transition from the linear to the exponential curves, achieved by linearly weighting the two equations:

$$i_{gas} = \begin{cases} Q_{nom} K_5 \exp\left(\dfrac{u_{diff}}{K_6}\right), & u_{diff} \geq U_{Tafel}, \\ Q_{nom} K_5 \left[\dfrac{u_{diff}}{U_{Tafel}} \exp\left(\dfrac{U_{Tafel}}{K_6}\right)\left(1 - \dfrac{u_{diff}}{U_{Tafel}}\right) + \exp\left(\dfrac{u_{diff}}{K_6}\right)\right], & 0 \leq u_{diff} \leq U_{Tafel} \end{cases} \tag{9.54}$$

The gassing current is actually based on u_{diff}, the difference between u and U_{gas}:

$$u_{diff} = \max\left\{0, u - U_{gas}\left[1 - \frac{\partial U_{gas}}{\partial T}(T - 298)\right]\right\} \tag{9.55}$$

The self-discharge current is calculated from a monthly capacity loss Q_{self} at 298 K:

$$i_{self} = -\frac{Q_{nom}\,\mathrm{SOC}}{720} \ln\left[1 - Q_{self} \cdot 10^{0.027(T-298)}\right] \tag{9.56}$$

where 720 stands for the number of hours in 1 month (30 days) and 0.027 is a temperature dependence factor based on different sources. The LAB float life halves for every 8°C (for non- or low-antimonial grids) to 10°C (for antimonial grids) rise in temperature due to corrosion. Below 20°C, float aging is considered invariant with temperature, which leads to the following expression for the time rate of float life aging:

$$\frac{d\,\mathrm{SOH}_{float}}{dt} = \max\left[\frac{1}{8760\ A_{float}}, \frac{1}{8760\ A_{float} \cdot 10^{-K_7(T-293)}}\right] \tag{9.57}$$

where K_7 is estimated at 0.03 for antimonial grids and 0.038 for non- or low-antimonial grids. Aging and heat evolution are also taken into account in this model.

Cherif et al. [27] present a nonstationary empirical model for the aging of a LAB, which is based on Shepherd's model [17] with time-dependent parameters:

$$u(t) = E(t) + \frac{\partial U}{\partial \mathrm{DOD}}(t)\,\mathrm{DOD}(t) + R_p(t)\,I\left[1 + \frac{K_1(t)\,\mathrm{DOD}(t)}{K_2(t) - \mathrm{DOD}(t)}\right] \tag{9.58}$$

This model can simulate a discharge or a charge at a constant current. Its parameters are determined from experimental data obtained with several currents on a Tunisian battery ASSAD/TV90 (12 V, 90 Ah) dedicated to PV applications (Table 9.2). To take into account battery aging, the electromotive force E and the

TABLE 9.2
Effect of Aging on the Battery Parameters

		Battery Age in Months				
Regime	**Parameters**	**0**	**4**	**13**	**30**	**Units**
Discharge	E	2.175	2.150	2.120	2.100	V
	dU/dDOD	0.210	0.170	0.130	0.097	V
	R_p	0.005	0.008	0.014	0.025	Ω
	K_1	0.065	0.080	0.092	0.100	
	K_2	–0.005	–0.010	–0.020	–0.040	
Charge	E	2.205	2.167	2.130	2.115	V
	dU/dDOD	0.25	0.23	0.17	0.13	V
	R_p	0.011	0.014	0.019	0.030	Ω
	K_1	0.55	0.58	0.62	0.65	
	K_2	1.15	1.17	1.25	1.80	

Source: Cherif, A. et al., *Journal of Power Sources* 112, 9–53, 2002.

polarization resistance R_p are allowed to change according to measurements carried out when the battery was new and after 4, 13, and 30 months of operation, respectively.

In 2004, Pascoe and Anbuky presented a VRLA empirical model that allowed battery characteristics (e.g., capacity, SOH, number of cells, and number of strings) to be simulated under arbitrary operating conditions (including discharge–charge rate, end voltages, ambient temperature, and initial SOC) [28]. The model predicts the VRLA battery discharge and recharge behavior accurately, including the complex coup de fouet region. The functions that constitute this VRLA battery simulator have been developed as C dynamic link libraries (DLLs). The simulator's performance was assessed for variations in discharge rate, discharge ambient temperature, initial SOC, SOH degradation, and different cell types and battery configurations. The simulation model was found to reflect the behavior of the cell discharge and charge voltage, current, and temperature reliably. Further refinement is necessary if increased accuracy in the representation of the coup de fouet region is required. This includes taking into account additional influential parameters, such as charge duration and charge voltage, as well as the method of representation. For the latter, a simple linear relationship between the discharge conditions and the coup de fouet parameters was assumed. A more suitable representation may be provided by more advanced methods, such as fuzzy logic techniques.

9.5 ELECTRICAL MODELS

9.5.1 Introduction to Electrical Models

The simplest electrical model of a LAB is an ideal voltage source. The fact that a battery is modeled by an ideal voltage source, not an ideal current source, is a result of

thermodynamics. Any electrochemical cell has its voltage imposed by the potential resulting from the reaction occurring at each electrode. An ideal voltage source is a two-terminal device that imposes a fixed voltage to the electrical circuit to which it is connected, whatever the load impedance or the output current. However, neither a LAB nor a real-world voltage source can supply unlimited current under a constant voltage. That is why real-world sources of electrical energy, such as batteries, generators, and power systems, are usually modeled as a combination of an ideal voltage source and additional impedance elements.

The Thévenin equivalent circuit is the simplest combination, since it is the association of an ideal voltage source and a resistor connected in series. This is a much more realistic way of modeling a lead-acid battery. Indeed, the resistor illustrates the voltage drop due to the current passing through the components of the battery. In the case of LABs, this instantaneous voltage drop mainly results from the low electrical conductivity of electrolyte and is proportional to the current. But, such a simple combination does not account for the polarization of the electrodes happening later on, when the battery is operated.

Enter a second passive two-terminal electrical component: the capacitor. Originally known as a condenser, it is used to store energy electrostatically in an electric field. A capacitor consists of two conductors separated by a nonconductive region, called the dielectric. The analogy with a battery, and more precisely an electrochemical cell, is quite straightforward when you look at the two electrodes immersed in the electrolyte. The capacitor is especially representative of the electrical double layer appearing at the surface of each electrode. The first layer, called the *compact layer* (either positive or negative), comprises ions adsorbed onto the electrode of opposite charge. The second layer, called the *diffuse layer*, is composed of ions attracted to the compact layer via the electrostatic force described by Coulomb's law. This second layer is loosely associated with the electrode and made of free ions that move in the electrolyte under the influence of electric attraction and thermal motion.

However, a small capacitor such as the one equivalent to the electrical double layer cannot be connected in series to the ideal voltage source and the resistor. As soon as the circuit is closed with a load, a transient current would flow as the capacitor plates charge up and would decay exponentially to zero; the capacitor finally behaving like a break in the circuit. Thus, the interface between each electrode and the electrolyte has to be seen as a capacitor and a resistor connected in parallel, instead of a single capacitor. The association in parallel illustrates the fact that the current passing through the interface can either charge the double layer or transfer charge from the electrode to the electrolyte and reciprocally. The parallel resistor-capacitor (RC) circuit is generally of less interest than the series circuit. This is largely because the voltage of both components is equal—as a result, this circuit does not act as a filter. In the case of LABs, the double-layer equivalent capacitor of each electrode is fully charged in less than a second and then acts as an open circuit.

The diffusion of ions, inside the electrolyte contained in the pores, is the transport phenomenon responsible for the electrode response at low frequencies. Fick's second law predicts how diffusion D causes the concentration of sulfuric acid c to change with time and space in a LAB:

$$\frac{\partial c}{\partial t} = \nabla \cdot (D \nabla c) \tag{9.59}$$

The series RC circuit can play a role in describing this phenomenon, since it is a passive low-pass filter. More precisely, an RC transmission line or infinite RC delay line may be used to model the battery voltage relaxation after operation. Expressing the voltage change with respect to time through this line leads to a partial differential equation equivalent to Fick's second law (Equation 9.59).

The Warburg diffusion element is a common diffusion circuit element used to fit this line and is described by the following impedance:

$$Z_W(j\omega) = \frac{\sigma}{\sqrt{\omega}} - j\frac{\sigma}{\sqrt{\omega}} \tag{9.60}$$

where j is the imaginary number, ω the angular frequency, and σ the Warburg constant. Figure 9.10 shows on the left the RC transmission line used to model the diffusion and on the right the Randles ECM (including the Warburg impedance) designed to simulate the spectrum of rapid electrode reactions [29].

The Warburg diffusion element is a particular constant phase element (CPE) of 45°. The CPE is a nonintuitive element created to fit the Nyquist plot of real-world systems. In some systems (e.g., batteries or fuel cells), it was expected to be

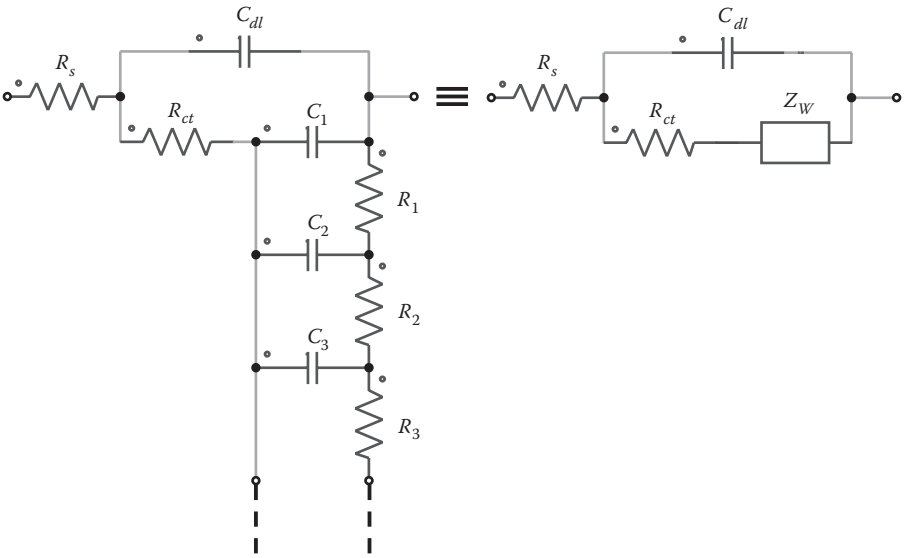

FIGURE 9.10 A Randles ECM (right) and the RC transmission line equivalent to the Warburg impedance (left).

a semicircle with the center on the *x*-axis followed by a straight line with an angle of 45° as the frequency decreases. However, the observed plot is indeed the arc of a circle, but with the center some distance below the *x*-axis, followed by a line with an angle different from 45°, in the low-frequency region. The CPE impedance is defined as

$$Z_{CPE}(j\omega) = \frac{1}{Y_1 \omega^n} \exp\left(-jn\frac{\pi}{2}\right) \tag{9.61}$$

where Y_1 is the admittance at ω =1 rad/s and n is a coefficient as such that the phase is equal to $n \times 90°$. The case $n = 1$ describes an ideal capacitor, whereas the case $n = 0$ describes a pure resistor.

A third passive two-terminal electrical component can also be seen in the LAB electrical models: the inductor. This component is connected in series to represent the battery behavior in high frequencies in order to fit EIS measurements. One has to keep in mind that such a component does not really describe the battery, but only the cables used to connect it to the load (or the charger). For EIS, the rule of thumb is approximately 10 nH per centimeter of cable. Otherwise, the self-inductance L (in nH) of a straight wire of length l, small diameter d, made of a metal having a relative permeability equal to 1 (like Cu or Al, but not Fe) can be calculated as follows [30]:

$$\forall d^2 f < 1\ \text{mm}^2\text{MHz} \ \text{ and } \ l > 100\ d, \quad L = 2l\left[\ln\left(\frac{4l}{d}\right) - \frac{3}{4}\right] \tag{9.62}$$

Most often, the battery behaves differently during charge and discharge. As a consequence, the model used in each case might not be exactly the same. It is possible to include both models in the same circuit by using another two-terminal electronic component: the diode. The most common function of a diode is to allow an electric current to pass in one direction (called the diode's forward direction), while blocking current in the opposite direction (the reverse direction). Thanks to this unidirectional behavior, the diode is the electronic equivalent of a one-way valve. Therefore, this component allows selection of a model suitable for the battery's operation, according to the current sign.

9.5.2 Applications of Electrical Models in the 1980s

In 1982, Appelbaum and Weiss proposed a piecewise-linear model with lumped elements for the LAB cell as outlined in Figure 9.11 [31]. This model is derived for a very low frequency range (processes take place in minutes and hours) and very low currents (from C/100 to C/50); therefore, self-inductance is not included. Temperature dependence is excluded from this model. The voltage source E_0 and the capacitance C_b represent the basic electrochemical process of charge storage. The

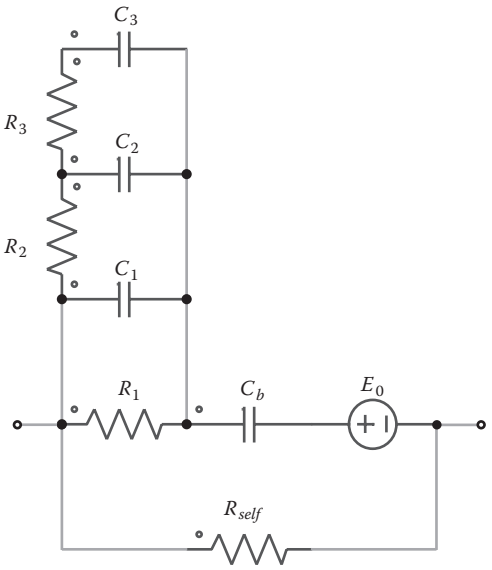

FIGURE 9.11 Equivalent circuit model of a LAB by Appelbaum and Weiss. (From Appelbaum, J., and Weiss, R., An electrical model of the lead-acid battery. In *Proc. Int. Telecommunications Energy Conf.*, pp. 304–307. Washington, DC, 1982.)

resistance R_{self} describes the self-discharge effect. These parameters are determined from measures performed at rest. The three resistances R_i and capacitances C_i (with $i \in \{1, 2, 3\}$) represent the battery cell overvoltage and are derived from the measured electrical response during operation. The battery nonlinearity in current and in SOC is expressed in different sets of element values of the same circuit model. Two sets of values are required for currents (charge and discharge) between 5% and 95% of the battery capacity, a third set of values is required for charging the battery between 95% and 100%, and a fourth set for discharging between 5% and 0% of the battery capacity.

Five years later, Buonarota et al. [32] criticized the increase of ECM complexity (the more comprehensive the forecasting is designed to be), claiming that it means greater difficulty in identifying the numerical values of the large number of parameters that are used to characterize the battery. Hence, they chose the Thévenin equivalent circuit with time-dependent parameters to model LAB discharge, using this analytical formulation:

$$u(t) = E(t) + R(t)i(t) \tag{9.63}$$

with

$$E(t) = E_0 + K_1 \ln\left[1 - \frac{Q(t)}{Q_{the}}\right] \tag{9.64}$$

$$R(t) = R_0 \left\{ 1 + K_2 \ln \left[\frac{1}{1 - K_3 Q(t)/Q_{nom}} \right] \right\} \tag{9.65}$$

$$\forall I_m(t) = \frac{Q(t)}{t}, \quad Q_{nom}(t) = \frac{Q_{the}}{1 + \left(Q_{the}/Q_{ref} - 1 \right) \left[I_m(t)/I_{ref} \right]^{K_5}}, \quad Q_{the} = \lim_{I_m \to 0} Q_{nom} \tag{9.66}$$

Based on experimental results and neglecting the influence of the temperature, the authors determined the values of the model parameters by performing simple tests and examining the battery response to the current step at various DODs. They admit that the model response with regard to voltage at the terminals is neither accurate during rapid transients on the order of milliseconds, nor for the rest periods occurring over a few minutes. The model has been used to forecast the performance of accumulators installed on an EV operating on an urban route, and shows substantial agreement with both the voltage and capacity supplied. A second application of the model is in assessing the SOC of a battery connected to a PV array by determining the electromotive force, which is univocally related to the extracted charge.

The electrical model proposed by Giglioli et al. [33] the following year, shown in Figure 9.12, simulates the voltage and the SOC when the battery charge or discharge is performed with constant current and neglecting the temperature and aging influence on the parameter values. The *p*-branch with the electromotive force E_p and resistance R_p schematizes the main and entire reversible reactions. The expression of E_p is given in Equation 9.64 and R_p as follows:

$$R_p(t) = R_{p0} \left\{ 1 + K_2 \ln \left[K_3 - \frac{Q(t)}{Q_{nom}} \right] + K_4 \left[\frac{Q_{the}}{Q(t)} \right]^{K_5} \right\} \tag{9.67}$$

Experimental data show that R_p is greater during charge than discharge at the same SOC. It seems to depend mainly on the SOC, but also on the current value. The last term inside the curly brackets of the R_p in Equation 9.67 has been added to take this fact into account. The definition of the nominal capacity is slightly simpler than that revealed in the relationship depicted by Equation 9.66:

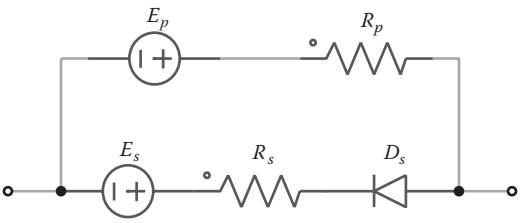

FIGURE 9.12 Equivalent circuit model of a LAB by Giglioli et al. (From Giglioli, R. et al., *L'Energia Elettrica* 1, 27–33, 1988.)

$$Q_{nom}(t) = \frac{Q_{the}}{1 + K_6\left[I_m(t)/I_{ref}\right]^{K_7}} \tag{9.68}$$

The s-branch with E_s and R_s schematizes the parasitic (gassing) and irreversible reactions. The electromotive force E_s refers to the minimum voltage value needed to have an appreciable effect of the gassing reaction, while R_s is the nonlinear voltage-controlled resistance that takes into account the gassing reaction behavior depending on the battery voltage. The equation describing R_s is obtained by an interpolation of experimental data:

$$R_s(t) = R_{s0} \exp[-K_8 u(t)] \tag{9.69}$$

In his book, Denno criticizes the Thévenin equivalent circuit by evoking the fact that at open circuit, the battery loses its charge as time goes on, and provides a still simple but more realistic battery ECM (Figure 9.13) [34]. It consists of a capacitance C in parallel with the leakage resistance R_L. The resistance R_E includes the wiring and the battery internal resistance, with R being the load resistance. The differential equation of the circuit is expressed as

$$\frac{dV}{dt} + \frac{V}{\tau} = 0 \quad \text{with} \quad \tau = \frac{CR_L(R_E + R)}{R_L + R_E + R} \tag{9.70}$$

From Equation 9.70, the voltage and current through the load resistance with discharge time t are given, respectively, by

$$V(t) = V_0 e^{-t/\tau} \quad \text{and} \quad I_R = \frac{V_0}{R_E + R} e^{-t/\tau} \tag{9.71}$$

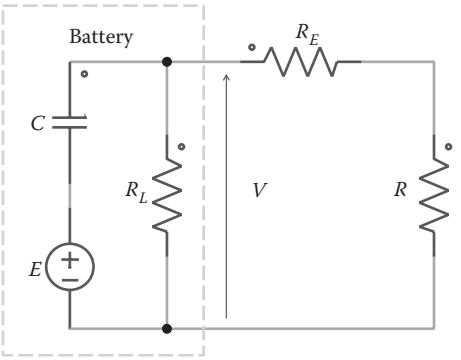

FIGURE 9.13 Equivalent circuit model of a LAB by Denno. (From Denno, K., *Power System Design and Applications for Alternative Energy Sources*. Prentice-Hall, Englewood Cliffs, NJ, 1989.)

where V_0 is the initial voltage. When $t = t_d$, the discharge time, the voltage reduces from V_0 to V_f, the final voltage. The load resistance R is a function of two independent parameters V_f and t_d:

$$R = \frac{(R_L + R_E)\, t_d - R_E R_L C \ln\left(V_0/V_f\right)}{R_L C \ln\left(V_0/V_f\right) - t_d} \tag{9.72}$$

Equation 9.72 shows that when

$$t_d = \frac{R_E R_L C}{R_L + R_E} \ln \frac{V_0}{V_f} \equiv t_{\min} \Rightarrow R = 0 \tag{9.73}$$

the battery is at short circuit. When

$$t_d = R_L C \ln \frac{V_0}{V_f} \equiv t_{\max} \Rightarrow R \to \infty \tag{9.74}$$

the battery is at open circuit. The load resistance R is always required to be a finite positive value, so the range of the discharge time t_d should be restricted by $t_{\min} < t_d < t_{\max}$.

9.5.3 Applications of Electrical Models in the 1990s

In 1990, Giglioli et al. proposed a model valid for charge and discharge processes, with time variable current, and taking into account the thermal behavior of the battery (Figure 9.14) [35]. The nominal capacity is defined by

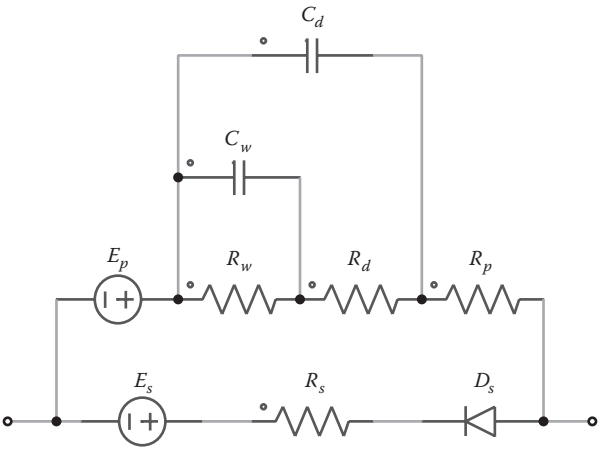

FIGURE 9.14 Equivalent circuit model of a LAB by Giglioli et al. (From Giglioli, R. et al., Charge and discharge fourth order dynamic model of the lead acid battery. In *Proc. Int. Electric Vehicle Symp.*, pp. 371–382. Hong Kong, China, 1990.)

$$\forall I_m(t) = \frac{Q(t)}{t}, \quad Q_{nom}(t) = \frac{Q_0 K_1 \left(1 - T/T_f\right)^{K_2}}{1 + (K_1 - 1)\left|I_m(t)/I_{ref}\right|^{K_3}} \tag{9.75}$$

where Q_0 is the reference capacity at 0°C, and T_f the electrolyte freezing temperature. The authors distinguish two different numbers to quantify the level of charge of the battery:

$$\mathrm{SOC}(t) = 1 - \mathrm{DOD}(t) = 1 + \frac{Q(t)}{Q_{the}} \neq 1 + \frac{Q(t)}{Q_{nom}} = \mathrm{DOC}(t) \tag{9.76}$$

While the SOC is an indicator of how full the battery is with reference to the maximum capacity available at a given temperature, the depth of charge (DOC) is an indicator of how full it is with reference to the actual discharge regime. The RC network represents the ohmic, polarization, and diffusion phenomena. Note that E_p is now temperature dependent:

$$E_p(t) = E_{p0} + K_4(273 + T)\ln[\mathrm{SOC}(t)] \tag{9.77}$$

For the resistances in the p-branch, experimental data and electrochemical theory suggest the following relationship:

$$R_p(t) = R_{p0}\{1 - K_5 T - K_6 \ln[\mathrm{SOC}(t)]\} \tag{9.78}$$

$$R_d(t) = R_{d0}\frac{K_7/\mathrm{DOD}(t) + \exp[K_8 \mathrm{SOC}(t)]}{1 + \exp\left|K_9 I_d(t)/I_{ref}\right|} \tag{9.79}$$

where I_d is the charge transfer current going through R_d, and

$$R_w(t) = -R_{p0}K_6 \ln\left[1 - \frac{\mathrm{DOD}(t)}{\mathrm{SOC}(t)}(K_1 - 1)\left|\frac{I_w(t)}{I_{ref}}\right|^{K_{10}}\right] \tag{9.80}$$

where I_w is the diffusion current going through R_w. The amplitude of i_s becomes a significant fraction of i_p only during gassing ($i_s \geq i_p$) and self-discharge ($i_s = i_p$). Note that E_s is still constant and R_s is voltage and temperature dependent as expressed by

$$R_s(t) = R_{s0}\frac{u(t)}{\exp[K_{11}u(t) + K_{12}(T - T_f)]} \tag{9.81}$$

Two years later, Salameh et al. proposed the ECM shown in Figure 9.15 after a series of experimental tests performed on a commercial LAB [36]. The mathematical

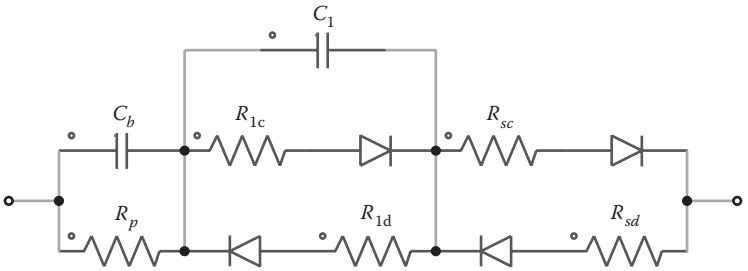

FIGURE 9.15 Equivalent circuit model of a LAB by Salameh et al. (From Salameh, Z. M. et al., *IEEE Transactions on Energy Conversion* 7, 93–97, 1992.)

functions of the model components are developed through examination of the graphic plots of the experimental data and manufacturer specifications. The model simulation is written in BASIC. The program numerically integrates the current into the capacitors using an iterative sequential solution method to generate the voltage waveforms of the capacitors. Ideal diodes, chosen strictly for directional purposes, are required to differentiate between the internal and overvoltage resistances for charge and discharge. Due to the nature of the battery chemical reactions, the elements can be modeled with a least squares approximation of the form:

$$\Theta = k \exp\{[wf(U_{mean} - E)]^{ff}\} \tag{9.82}$$

where Θ is a placeholder for the battery element, k the gain multiplier, wf the width factor, U_{mean} the mean voltage level, and ff the flatness factor. The temperature compensation results in a change in magnitude and width of the resistances (internal and overvoltage). The temperature compensation coefficient of the self-discharge resistance is found in the manufacturer's specifications. These coefficients are modeled as exponentials of the form

$$TC = \left(\frac{R}{R_{ref}}\right)^{\frac{T_{ref}-T}{T_{ref}}} \tag{9.83}$$

Bejan and Dan address the fundamental problem of determining the optimal history (regime of operation) of a battery so that the work output is maximal [37]. The battery is connected to an electric motor with finite winding resistance, which is equivalent to the circuit provided in Figure 9.13 with the load R replaced by the electromotive force E_M. At the end of the specified lifetime t_{eol}, the battery is dead and $U(t_{eol}) = 0$. The total work produced during the battery life is

$$W = \int_0^{t_{eol}} P dt \quad \text{with} \quad P = (V - R_E I_M) I_M \tag{9.84}$$

The motor current is

$$I_M = I - I_L = -C\frac{dV}{dt} - \frac{V}{R_L} \tag{9.85}$$

To locate the extremum of W, the authors solve the associated Euler equation, which yields the following equation for the optimal history of the battery voltage $V_{opt}(t)$:

$$\forall \dot{V} = \frac{dV}{dt}, \quad \frac{\partial P}{\partial V} - \frac{d}{dt}\left(\frac{\partial P}{\partial \dot{V}}\right) = R_L R_E C^2 \frac{d^2 V_{opt}}{dt} - \left(1 + \frac{R_E}{R_L}\right) V_{opt} = 0 \tag{9.86}$$

The solution to Equation 9.86, subject to the initial and final conditions of $V_{opt}(0) = E$ and $V_{opt}(t_{eol}) = 0$, respectively, is

$$V_{opt} = E\left[\cosh(at) - \frac{\cosh(at_{eol})}{\sinh(at_{eol})}\sinh(at)\right] \quad \text{with} \quad a = \frac{1}{R_L C}\sqrt{1 + \frac{R_L}{R_E}} \tag{9.87}$$

The corresponding optimal current history follows from Equation 9.87, leading to the optimal motor power output history. It shows that the maximized work output is smaller than the energy stored initially in the battery, as soon as the resistance of the external circuit is finite, no matter how small, and it decreases as the motor resistance increases.

Mauracher and Karden propose a model structure based on a Randles equivalent circuit (Figure 9.16) [38]. To reduce the numerical expense, the SOC dependence of all overvoltages is neglected in this modeling. Since the battery model is used for the simulation of EV driving only, the discharging operation is modeled. The equilibrium voltage depending on the molality m (mol/kg) at 25°C is defined by [18]

$$E(t) = 1.9228 + 0.147519x + 0.063552x^2 + 0.073772x^3 + 0.033612x^4 \tag{9.88}$$

with $x = \log[m(t)]$. A constant equivalent resistance R_i is used for modeling all conductive media of the battery and is obtained by measurements. The double-layer capacitance is a function of the voltage V_d:

$$C_d(t) = K_1 \cosh[K_2 V_d(t)] \tag{9.89}$$

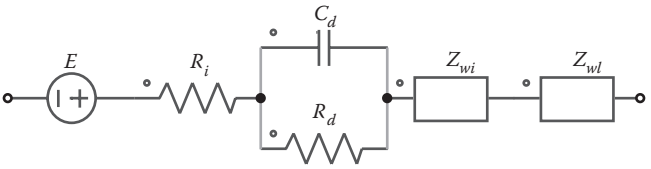

FIGURE 9.16 Equivalent circuit model of a LAB by Mauracher and Karden. (From Mauracher, P., and Karden, E., *Journal of Power Sources* 67, 69–84, 1997.)

where the constants K_i are experimentally obtained from EIS as a function of V_d. The charge-transfer resistance R_d is measured by EIS for some superimposed direct currents I_{DC}, which cause constant overvoltages V_d at the interface:

$$R_d(t) = \frac{1}{K_3\sqrt{K_4^2 + I_{DC}^2}} \tag{9.90}$$

Two different boundary conditions lead to two different Warburg impedances: (1) The electrolyte has the finite extension l and is limited by a reservoir of constant concentration:

$$Z_{wi}(j\omega) = \frac{RT}{cz^2F^2A_e\sqrt{j\omega D}}\tanh\left(l\sqrt{\frac{j\omega}{D}}\right) \tag{9.91}$$

where R is the gas constant, z the ion charge number, F the Faraday constant, and A_e the electrolyte surface, and (2) the electrolyte is limited by a nonpermeable wall:

$$Z_{wl}(j\omega) = \frac{RT}{cz^2F^2A_e\sqrt{j\omega D}}\coth\left(l\sqrt{\frac{j\omega}{D}}\right) \tag{9.92}$$

9.5.4 Applications of Electrical Models in the 2000s

After more than a decade of studies carried out by the University of Pisa on electrical models for LABs, in 2000 Ceraolo developed an implementation of the third-order model (Figure 9.17) [39], which shows a good compromise between complexity and precision. The assumed state variables are the currents i_w and i_p, the extracted charge Q, and electrolyte temperature T:

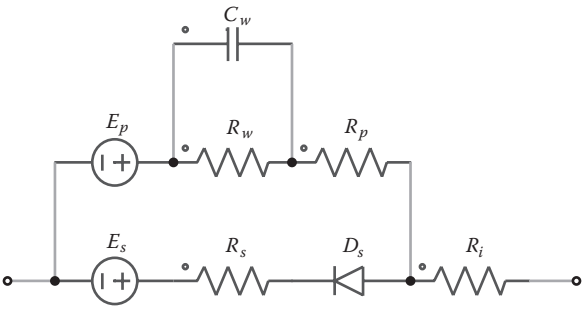

FIGURE 9.17 Equivalent circuit model of a LAB by Ceraolo. (From Ceraolo, M., *IEEE Transactions on Power Systems* 15, 1184–1190, 2000.)

$$\begin{cases} \dot{i}_w = \dfrac{i_p - i_w}{\tau_w} \\ \dot{Q} = i_p \qquad \text{with} \quad \tau_w = R_w C_w \\ \dot{T} = \dfrac{1}{C_p}\left(P_s - \dfrac{T - T_{amb}}{R_T}\right) \end{cases} \tag{9.93}$$

where C_p is the thermal capacity (J K^{-1}), R_T the thermal resistance (K W^{-1}), and P_s the source thermal power (W) (i.e., the heat internally generated by the battery). The assumed equations for E_p, R_i, R_w, and R_p are as follows:

$$E_p(t) = E_{p0} - K_1(273 + T)\mathrm{DOD}(t) \tag{9.94}$$

$$R_i(t) = R_{i0}[1 + K_2\mathrm{DOD}(t)] \tag{9.95}$$

$$R_w(t) = -R_{w0}\ln[\mathrm{DOC}(t)] \tag{9.96}$$

$$R_p(t) = R_{p0}\frac{\exp[K_3\mathrm{DOD}(t)]}{1+\exp\left[K_4 I_p(t)/I_{ref}\right]} \tag{9.97}$$

Here E_s is still constant and R_s is defined in Equation 9.81. Given the large number of parameters of the proposed model, the complete identification of all of them is particularly complex. For discharge modeling only, the whole *s*-branch as well as R_p can be omitted. The dimensional parameters used in the expressions of Q_{nom} and R_p vary a little among different batteries built with the same technology. When batteries of the same manufacturer in different models (and capacities) are considered, the parameters with the dimensions of a resistance can be taken in approximation as inversely proportional to the respective nominal capacities.

Two years later, the same team [40] presented the practical implications of the third-order model previously described [39]. Some simplified ways to identify the model parameters with a limited number of laboratory tests and limited computational effort have been proposed that still offer satisfactory model accuracy. Indeed, if $U_{exp}(t)$ indicates the measured voltage shape of a given test, $U_{sim}(t, \mathbf{p})$ the simulated voltage referring to the same input signals, and $\mathbf{p}$ a given set of parameters, the elements of vector $\mathbf{p}$, in principle, could be obtained by solving the following problem:

$$\min_{\mathbf{p}} \sqrt{\frac{1}{T}\int_{t_0}^{t_0+T} [U_{sim}(t,\mathbf{p}) - U_{\exp}(t)]^2\, dt} \tag{9.98}$$

In practice, however, because of the great number of elements of **p** and the high complexity of the relationships among them and the battery behavior, it is very unlikely that this process will converge to reasonable results if such general-purpose numerical algorithms are adopted. It is therefore advisable to simplify this task, by decomposing the problem into simpler subtasks for which the number of needed parameters is smaller and can be derived in a much easier manner. Four subtasks are described in details in this study concerning the identification of parameters related to the battery capacity, the *p*-branch, the *s*-branch, and finally the thermal behavior, from either laboratory tests or manufacturer data.

Karden et al. use EIS to obtain simulation models for the nonlinear, nonstationary dynamic behavior of LABs [41]. The ECM of the negative electrode under discharge–charge conditions consists of an inductance, the internal resistance, two ZARC (parallel connection of a resistor and a CPE) elements, and one pseudoinductive element characterized by negative R and C in parallel (Figure 9.18a). Although the CPE is considered to be a "fundamental" circuit element today, the earliest explanations of depressed semicircles modeled the semicircle directly as a system with a distribution of time constants:

$$Z_{ARC}(j\omega) = \frac{R_0}{1 + (j\omega\tau)^n} \tag{9.99}$$

where R_0 is the low-frequency real-axis intercept, τ the mean time constant, and $(1 - n)\pi/2$ the depression angle. It is called a ZARC or Cole-Cole circuit element and can also be obtained from the parallel combination of a resistor and a CPE. For the positive electrode, the capacitive branch of the electrode impedance deviates from depressed-semicircle behavior close to the real-axis intersection. This is interpreted as a porosity effect due to the limited penetration depth for high frequencies and is modeled with a transmission line instead of lumped elements. Figure 9.18b shows

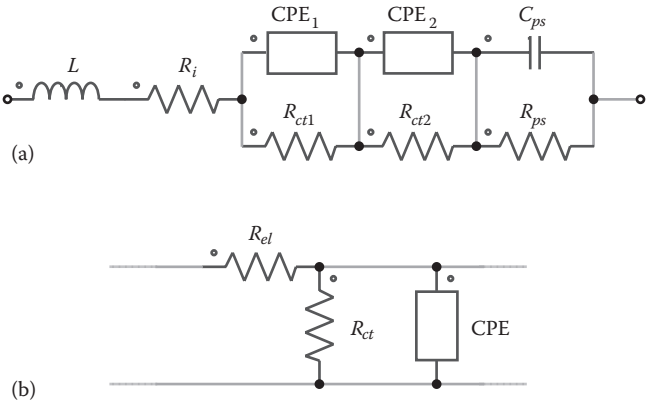

FIGURE 9.18 Simplified equivalent circuits of (a) negative and (b) positive electrodes for discharge–charge operation by Karden et al. (From Karden, E. et al., *Electrochimica Acta* 47, 2347–2356, 2002.)

its elementary components, consisting of a ZARC representing the pore wall and a resistance along the pore axis. De Levie's equations are used in their original form, not explicitly considering inhomogeneity along the pore axis (cf. Equation 9.92).

The maximum work from an electric battery in a finite time interval t_{eol} derived by Bejan and Dan [37] is considered unreasonable by Yan [42]. Indeed, they calculated a maximum work output that can be written in a more compact form as

$$W_{\max} = \frac{CE^2}{2}\left[1 + 2r - 2ar\frac{\cosh(at_{eol})}{\sinh(at_{eol})}\right] \quad \text{with} \quad r = \frac{R_E}{R_L} \tag{9.100}$$

but, it can become negative when

$$t_{eol} < \frac{R_L C}{a}\sinh^{-1}(2ar) \tag{9.101}$$

This comes from the fact that the power output of the motor P is negative when $V < R_E I_M$. According to the optimal history of the battery voltage (Equation 9.87) and the corresponding optimal current history,

$$I_{M,opt} = \frac{E}{R_L}\left[\frac{a\cosh(at_{eol})}{\sinh(at_{eol})} - 1\right]\cosh(at) + \left[\frac{\cosh(at_{eol})}{\sinh(at_{eol})} - a\right]\sinh(at) \tag{9.102}$$

One can show that when the operating time

$$t > \frac{R_L C}{a}\tanh^{-1}\left[\frac{a\tanh(at_{eol}) - 1}{a - \tanh(at_{eol})}\right] \equiv t_0 \tag{9.103}$$

$W_{\max}$ is negative. Here t_0 may be referred to as the critical operating time. That is, in the time interval $t_0 \rightarrow t_{eol}$, the power output of the battery is always negative. The total positive work produced during the time interval $0 \rightarrow t_0$ is

$$W_p(t_0) = \frac{CE^2}{2}\left[1 + 2r - 2ar\frac{\cosh(at_{eol})}{\sinh(at_{eol})} + \frac{r}{\sinh^2(at_{eol})}\right] \tag{9.104}$$

which can be derived from Equations 9.87 and 9.103. Obviously, $W_p(t_0)$ is larger than $W_{\max}$. However, $W_p(t_0)$ is still not the maximum mechanical work. To obtain the genuine maximum work output, the unsuitable final condition $V_{opt}(t_{eol}) = 0$ must be replaced by $V_{opt}(t_{eol}) = \varepsilon E$ ($\varepsilon < 1$), which leads to

$$W_{\max,g} = \frac{CE^2}{2}\left[\frac{1}{1 + 2r - 2ar\cosh(at_{eol})/\sinh(at_{eol})}\right] > W_p(t_0) > W_{\max} \tag{9.105}$$

If discharged as slowly as its self-discharge rate, the LAB does practically no work. On the opposite end, at short circuit, its work output is also equal to zero. To examine the maximum work question in the simplest possible form, Shi et al. [43] and Chen et al. [44] relied on the ECM established by Denno [34]. Using Equation 9.71, the work output obtained by the load resistance R is

$$W_R = \int_0^{t_d} RI_R^2\, dt = \frac{C\left(V_0^2 - V_f^2\right)}{2} \frac{\left[1 + \dfrac{R_E}{R_L} - \dfrac{R_E C}{t_d} \ln\left(V_0/V_f\right)\right]\left[\ln\left(V_0/V_f\right) - \dfrac{t_d}{R_L C}\right]}{\ln\left(V_0/V_f\right)} \tag{9.106}$$

and the total energy delivered from the battery is

$$W = \frac{1}{2} C\left(V_0^2 - V_f^2\right) \tag{9.107}$$

Then, the efficiency of the battery is

$$\eta = \frac{W_R}{W} = \frac{\left[1 + \dfrac{R_E}{R_L} - \dfrac{R_E C}{t_d} \ln\left(V_0/V_f\right)\right]\left[\ln\left(V_0/V_f\right) - \dfrac{t_d}{R_L C}\right]}{\ln\left(V_0/V_f\right)} \tag{9.108}$$

It is obvious, from Equations 9.73, 9.74, and 9.108, that when $t_d = t_{\min}$ or $t_{\max}$, the efficiency and thus the work output of the battery are equal to zero. Consequently, there exists a maximum for battery efficiency:

$$t_d = \frac{R_L C}{\sqrt{1 + R_L/R_E}} \ln \frac{V_0}{V_f} \equiv t_m \Rightarrow \eta = \max_{t_d} \eta = \left(\sqrt{1 + R_L/R_E} - \sqrt{R_L/R_E}\right)^2 \tag{9.109}$$

The value of the load resistance providing the maximum work output of the battery is obtained by replacing t_d by t_m in Equation 9.72, which gives

$$R_m = \sqrt{R_L R_E + R_E^2} \tag{9.110}$$

so that the Joule heating dissipated by R_L and R_E becomes minimal. To conclude, when t_d is smaller than t_m, the faster the discharge is, the lower the battery efficiency; the same applies when t_d is larger than t_m in that the discharge is slower.

Buller et al. presented a systematic approach to employ EIS for determining the structure and parameters of a VRLA battery model [45]. They focused on the interpretation of the impedance data in an ECM and described its MATLAB/Simulink

implementation and time-domain verification. The electric behavior of a battery half-cell can be described in a simplified way using the Randles ECM (Figure 9.10). The inductance L added in series is caused by the metallic connection (top lead) between the poles and the electrodes of the battery. When the two half-cell ECMs are merged into a complete battery cell model (as depicted in Figure 9.19), additional modification and simplifications are required. First, the two resistance values and inductance values of the half-cells are represented by one element each. Second, the DC voltage of the battery cell has to be added to the model. Third, for real electrochemical systems, the capacitances C_{dl} should be replaced by ZARC elements [41]. Because the influence of diffusion on the negative electrode is much smaller than on the positive electrode, only one diffusion element is employed for the battery cell. Finally, a parallel current path for the side reactions, which occur mainly during charging and overcharging, has to be realized.

In 2005, Jossen et al. used an ECM to simulate the battery in hybrid systems based on a LAB and a proton-exchange membrane fuel cell (PEMFC) [46]. The simple model presented in Figure 9.20 is applied to a 24-V, 150-Ah, vented-type battery, where $U_{00} = 2.078$ V is the equilibrium voltage in the discharged state (0% SOC), and the capacitance $C_a = 5.4 \times 10^6$ F describes the linear relationship between the equilibrium voltage and the SOC. In addition, C_d and R_p describe the polarization losses (mainly due to diffusion); R_0 describes the ohmic resistance plus the voltage drop resulting from charge transfer and is equal to 11 mΩ in charge and 5.8 mΩ in discharge. The resistance $R_{gas} = u/i_{gas}$ represents the loss by gassing (Equation 9.47), where $i_0 = 6$ mA, $U_{nom} = 2$ V per cell, $K_1 = 85$ mV, $K_2 = 6500$ K, and $T_{ref} = 298$ K. The polarization resistance depends on the SOC and is defined by

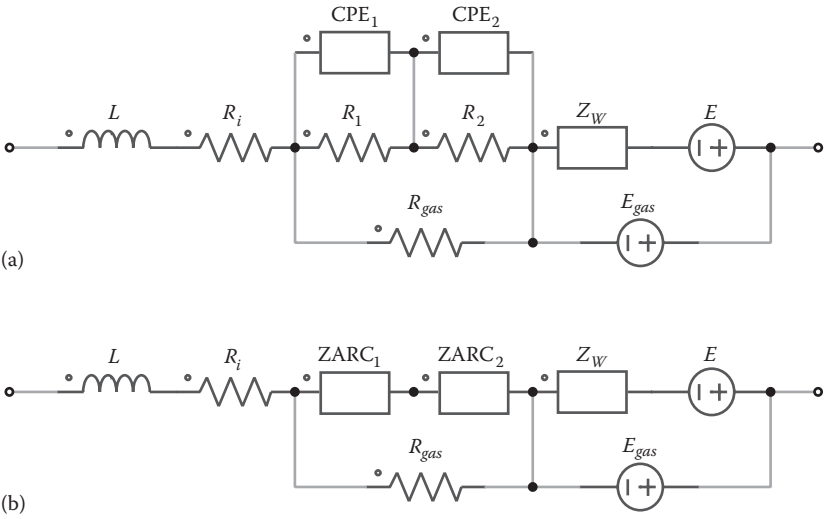

FIGURE 9.19 Two identical equivalent circuit models of a LAB by Buller et al.: (a) CPE elements; (b) ZARC elements. (From Buller, S. et al., *Journal of Power Sources* 113, 422–430, 2003.)

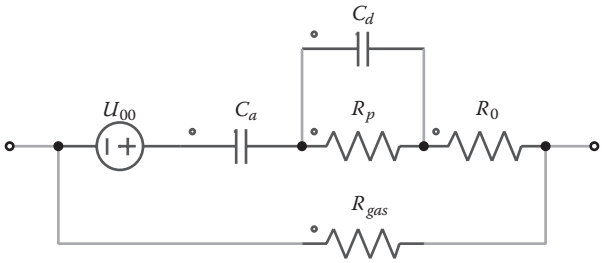

FIGURE 9.20 Equivalent circuit model of a LAB by Jossen et al. (From Jossen, A. et al., *Journal of Power Sources* 144, 395–401, 2005.)

$$R_p = \frac{K_3}{K_4 - \mathrm{SOC}} \tag{9.111}$$

during charge and

$$R_p = \frac{K_5}{K_4 - \mathrm{DOD}} \tag{9.112}$$

during discharge, where $K_3 = 2.6$ mΩ, $K_4 = 1.005$, and $K_5 = 1.3$ mΩ.

The parameterization of impedance-based models is difficult for operating profiles that have high ampere-hour throughput in short times. Such conditions result in non-steady-state conditions and do not allow precise measurements of impedance parameters. Therefore, Thele et al. extended the ECM presented in Figure 9.19 by means of an electrolyte transport model, which describes the generation and transport of sulfuric acid inside the porous electrodes [47]. They removed the Warburg impedance and expressed the OCV as the difference between the positive and negative standard potentials [18]:

$$E_{pos}(t) = 1.628194 + 0.073924x + 0.033120x^2 + 0.043220x^3 + 0.021567x^4 \tag{9.113}$$

$$E_{neg}(t) = -0.2946 - 0.073595x - 0.030531x^2 - 0.030552x^3 - 0.012045x^4 \tag{9.114}$$

with $x = \log[m(t)]$. The link between the OCV (a function of acid molality) and the electrolyte transport model (a function of acid concentration) is made by the following relation [18]:

$$m(t) = 1.00322 \times 10^3 c + 3.55 \times 10^4 c^2 + 2.17 \times 10^6 c^3 + 2.06 \times 10^8 c^4 \tag{9.115}$$

where the concentration c is expressed in mol cm^{-3}. A description of the MATLAB/Simulink implementation and its parameterization in the time domain is given.

Furthermore, the advantages and the limits of the improved model are discussed. The model allows for precise modeling of automotive batteries, both in conventional applications and in vehicles with electrically assisted propulsion. It is therefore an important tool for the design of automotive power nets.

The same team presented for the first time an impedance-based nonlinear ECM for LABs that is applicable in all operational modes (Figure 9.21) [47]. The electrodes are completely separated from each other. Their dynamic behavior is considered by RC elements with partly nonlinear resistors. An overcharging model describes the accumulation and depletion of the dissolved Pb^{2+} ions by employing two voltage sources. This physical model has been added to the earlier presented model (Figure 9.19) to expand its validity. To properly represent the charge acceptance during dynamic operation, a concept of "hardening crystals" has been introduced. Moreover, a detailed gassing and oxygen recombination model has been integrated considering the oxygen evolution at the positive electrode and the hydrogen evolution and oxygen reduction at the negative electrode. Grid corrosion has been neglected. Simplifications permit an efficient implementation and model parameterization in the time domain. A comparison between experimental data and simulation results demonstrates the achieved accuracy. The model enhancement is of major importance when analyzing charging strategies, especially in partial-cycling operation with limited charging time, as occurs with, for example, EVs, HEVs, and UPS systems.

The electrical model proposed by Dürr et al. the following year is based on the ECM shown in Figure 9.15, except for the fact that the capacitor C_b has been replaced by the OCV [48]. Indeed, the battery is not an ideal capacitor, which makes this previous model inaccurate for different discharge rates. Furthermore, the capacitance is defined by a mathematical function using various parameters, which complicates the battery model. In this new ECM, the OCV depends on the current, the temperature, and the energy drawn from the battery. All model parameters are nonlinear and described using mathematical functions. The model is implemented in MATLAB/Simulink and uses elements from the Power System Blockset. The authors developed a new, simple approach relating the calculated remaining energy of the battery to the OCV using a look-up table, which is based on discharge tests at low discharge rates.

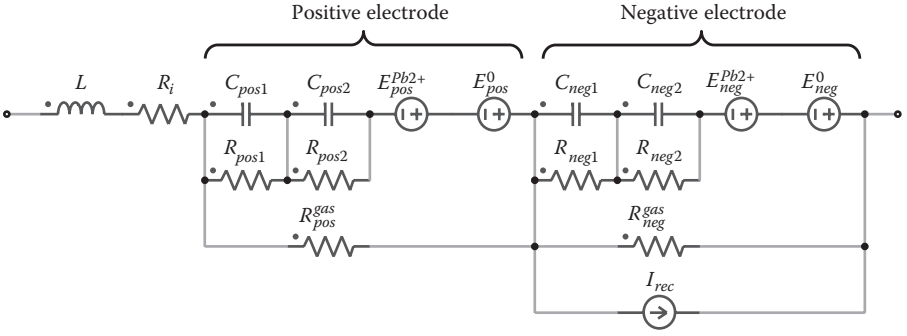

FIGURE 9.21 Equivalent circuit model of a LAB by Thele et al. (From Thele, M. et al., *Journal of Power Sources* 144, 461–466, 2005.)

This model uses the initial battery current, when connected to a load, to predict the maximum available energy at a given temperature. The energy being drawn from the battery is dynamically calculated and subtracted from the initial energy to give a value for the remaining energy and SOC.

In 2007, Thele et al. presented a model for flooded and VRLA batteries that is parameterized by EIS and includes overcharging effects to allow for charge-acceptance simulations (e.g., for regenerative-braking drive-cycle profiles) [49]. The full dynamic behavior and the short-term charge–discharge history are taken into account. This is achieved via detailed modeling of the sulfate crystal growth and the internal gas recombination cycle. The model is applicable in the full realistic temperature and current range conditions of automotive applications. For model validation, several load profiles (covering the dynamics and the current range found in EVs and HEVs) are examined and the charge-acceptance limiting effects are elaborately discussed. The validation measurements have been performed for different types of LABs (flooded and VRLA). The model is therefore an important tool for analyzing the different charging strategies and energy gains that can be achieved during regenerative braking. However, the conclusion that can be drawn about the electrical models jointly developed by Ford Research Center and Aachen University [45,47,49,50] is that they are located somewhere between the electrical and electrochemical models. What is certain is that they would definitely not be as efficient if they were not deeply inspired by the electrochemical models that we are going to review in the next section.

9.6 ELECTROCHEMICAL MODELS

9.6.1 Introduction to Electrochemical Models

An electrochemical model is constructed from a set of "first-principle" equations governing the physicochemical processes in the LAB. The framework of the volume-averaged porous electrode has been the standard approach in the electrochemical modeling of batteries, according to the most recent review by Ferguson and Bazant [51]. The seminal work of Newman and Tobias [52] in the 1960s was the first to introduce the effects of concentration variations on electrode kinetics and the mass and momentum conservation equations in porous electrodes to the modern modeling of battery behavior and performance. Extensive literature surveys conducted by Newman and coauthors for work up to the early 2000s are available [53,54].

An electrode in a LAB is supposed to comprise a porous matrix of electrochemically reactive and electrically conductive solids, which primarily consist of active materials, that is, PbO_2 (in the positive electrode) and Pb (in the negative electrode), and an electronically conductive network of grids. The electrolytic (sulfuric acid) solution fills the void of the porous matrix. In a typical porous electrode framework, the porous medium is regarded as a homogeneous body with a specific pore structure having a certain porosity and pore distribution. The mass transport within the pore structure is considered a function of tortuosity, governed by both electromigration (due to the presence of an electric field) and diffusion (due to the presence of a chemical concentration gradient introduced largely by the electrode reactions). The

electrode reactions are marked by the imposed current in the charge or discharge regime. From a macroscopic perspective, the overall reaction rate in the battery is depicted by the current. On a microscopic scale, the local reaction rate is governed by the physical microstructure and chemical environment, the conductivity of the solid matrix and that of the liquid electrolyte, and the parameters that dictate the electrode characteristics that are key to controlling the rate of the electrochemical processes at the electrode (the effective surface area, concentration of the acid along the electrode dimensions, temperature distribution, etc.). The electrochemical model is capable of simulating these phenomena at the electrode and in the cell. The complexity of the model could escalate quickly if some of the parameters become a function of external variables, such as time, temperature, dimensions, and locality. Many such dependencies are also coupled, making mathematical treatments difficult to apply. To enable a theoretical analysis of such a complex model, it is necessary to establish a framework that accounts for the essential features of an actual electrode with sufficient detail. Furthermore, the model should be described by variables that can be used to verify the simulation results by conducting suitable experimental measurements. Commonly, the properties of a porous electrode can be characterized by macroscopically averaged characteristics, such as porosity, average surface area per unit volume, and volume-averaged resistivity. Similarly, a volume-averaged resistivity can be used to describe the electrolytic phase in the voids. A typical electrochemical model would thus apply the concept and spirit of "averaged volume"-based approaches to a region of the electrode that is small with respect to the overall dimensions but large compared to the pore structure. In the model, rates of reaction and double-layer charging in the pores will have to be defined in terms of transferred current per unit volume. Typically, the parameters of interest as outputs in the model are local potentials in the electrode matrix of the cell and the associated concentration gradients throughout the same regions. These serve as the measurable parameters for validation or driving forces for mass transport.

Newman and Tiedemann define a potential Φ_1 in the solid, conducting matrix of the porous electrode and another Φ_2 in the pore-filling electrolyte [54]. These quantities, along with others to be defined shortly, are assumed to be continuous functions of time and space coordinates. In effect, the electrode is treated as the superposition of two continua, one representing the solution and the other representing the solid in the porous matrix. In the model, both are present at any point in space. Averaging is performed in each volume element within the electrode. The porosity is the void volume fraction ε within the element, filled with electrolytic solution. The element also contains representative volumes of the solid phases, which may be present. Let c_i be the solution-phase concentration of species i, averaged over the pores. The specific interfacial area a is the surface area of the pore walls per unit volume of the electrode. Let j_{in} be the pore-wall flux of species i averaged over this same interfacial area. The pore-wall flux to be averaged is the normal component of the flux of species i at the pore wall, relative to the velocity of the pore wall, and in the direction pointing into the solution. The pore wall may be moving slightly because of a dissolution process. Thus, aj_{in} represents the rate of transfer of the species from the solid phases to the pore solution (per unit volume of the total electrode).

Here a typical treatment in the model using a volume-averaging method is described to illustrate how this approach works and what sensible solutions in the computation can be derived from a model with temporal and spatial resolutions. Let $\mathbf{N}_i$ be the average flux of species i in the pore solution when averaged over the cross-sectional area of the electrode. Thus, for a plane surface, of normal unit vector $\mathbf{n}$ cutting the porous solid, $\mathbf{n}\cdot\mathbf{N}_i$ represents the amount of species i crossing this plane in the solution phase, but referred to the projected area of the entire plane rather than to the area of an individual phase. The superficial current density $\mathbf{i}_2$ in the pore phase is due to the movement of charged solutes:

$$\mathbf{i}_2 = F\sum_i z_i\mathbf{N}_i \tag{9.116}$$

Similarly, the current density $\mathbf{i}_1$ in the matrix phase is defined to refer to the superficial area and not to the area of an individual phase. Within a pore, in the absence of homogeneous chemical reactions, a differential material balance can be written for a species i:

$$\frac{\partial \varepsilon c_i}{\partial t} = aj_{in} - \nabla\cdot\mathbf{N}_i \tag{9.117}$$

This result applies to the solvent as well as the solutes.

A volume element within the porous electrode is, in essence, electrically neutral because it requires a large electric force to create an appreciable separation of charge over an appreciable distance. We shall also take each phase separately to be electrically neutral. For the solution phase, this takes the form

$$\sum_i z_i c_i = 0 \tag{9.118}$$

It is a consequence of the assumption of electroneutrality that the divergence of the total current density is zero. For the macroscopic model, this is expressed as

$$\nabla\cdot\mathbf{i}_1 + \nabla\cdot\mathbf{i}_2 = 0 \tag{9.119}$$

Charge that leaves the matrix phases must enter the pore solution. In fact, combining Equations 9.116, 9.117, and 9.118 gives

$$\nabla\cdot\mathbf{i}_2 = aF\sum_i z_i j_{in} = ai_n \tag{9.120}$$

where i_n is the average transfer current density (from the matrix phase to the solution phase).

For a single electrode reaction, represented as

$$\sum_i s_i M_i^{z_i} \rightarrow ne^- \tag{9.121}$$

Faraday's law is expressed as

$$aj_{in} = -\frac{as_i}{nF} i_n = -\frac{s_i}{nF} \nabla \cdot \mathbf{i}_2 \tag{9.122}$$

if the electrode is operating in a steady state or a pseudo steady state where double-layer charging is ignored. Equation 9.117 becomes

$$\frac{\partial \varepsilon c_i}{\partial t} = -\nabla \cdot \mathbf{N}_i - \frac{s_i}{nF} \nabla \cdot \mathbf{i}_2 \tag{9.123}$$

It is common to begin with a polarization equation of the form

$$\nabla \cdot \mathbf{i}_2 = ai_0 \left\{ \exp\left[\frac{(1-\alpha)nF}{RT} \eta_s \right] - \exp\left[-\frac{\alpha nF}{RT} \eta_s \right] \right\} \tag{9.124}$$

where α is the symmetry factor of the charge-transfer coefficients, and η_s is the local value of the surface overpotential. The surface overpotential is the potential difference between the electrode and a (perhaps imaginary) reference electrode of the same kind as the working electrode and positioned adjacent to it, just beyond the double layer. The potential difference $\Phi_1 - \Phi_2$ is equal to η_s, plus an additive term, which depends on the local solution composition. For a single electrode reaction, a material balance on the solid phases shows how the porosity changes with the extent of reaction at each location within the electrode:

$$\frac{\partial \varepsilon}{\partial t} = \sum_{\text{solid phases}} \left(\frac{s_i M_i}{\rho_i nF} \right) \nabla \cdot \mathbf{i}_2 \tag{9.125}$$

where M_i is the molecular weight and ρ_i the density of the solid phase (considered a homogeneous substance).

In addition to faradaic reactions, electrode processes can involve charging of the electric double layer at the interface between the pore solution and the conducting phases of the matrix. The surface charge density q_s on the electrode side of the double layer depends on the solution-phase composition

$$q_s = -F \sum_i z_i \Gamma_i \tag{9.126}$$

as represented by Γ_i, the surface concentration of a solute species *i*. The material balance for a solute species at the interface can be expressed as

$$\frac{\partial a\Gamma_i}{\partial t} = aj_{in,faradaic} - aj_{in} = -\frac{as_i}{nF} i_{in,faradaic} - aj_{in} \tag{9.127}$$

where the subscript *faradaic* refers to charge or mass that is actually transported through the interface or is involved in a charge transfer reaction. Addition of Equation 9.127 according to Equation 9.120 gives

$$\nabla \cdot \mathbf{i}_2 = ai_{in,faradaic} + \frac{\partial aq_s}{\partial t} \tag{9.128}$$

The current transferred from the matrix to the solution is involved either in double-layer charging or in faradaic electrode reactions. The differential double-layer capacity, defined by

$$C_{dl} = \left(\frac{\partial q_s}{\partial U'}\right)_{c_j} = -F\sum_i z_i \left(\frac{\partial \Gamma_i}{\partial U'}\right)_{c_j} \quad \text{with} \quad U' = \Phi_1 - \Phi_2 \tag{9.129}$$

leads to the following expression of the current transferred from the matrix to the solution:

$$\nabla \cdot \mathbf{i}_2 = ai_{in,faradaic} + aC_{dl}\left(\frac{\partial \Phi_1}{\partial t} - \frac{\partial \Phi_2}{\partial t}\right) \tag{9.130}$$

which is valid only in the absence of transient concentration variations and with a constant specific interfacial area.

In the matrix phase, the movement of electrons is governed by Ohm's law:

$$\mathbf{i}_1 = -\sigma \nabla \Phi_1 \tag{9.131}$$

where σ is the effective conductivity of the matrix. This quantity will be affected by the volume fraction of the conducting phase or phases, the inherent conductivity of each conducting solid phase, and the manner in which granules of conducting phases are connected. Many battery systems involve solutions of a single electrolyte. Consequently, it is desirable to develop the theory with all possible exactness, particularly since the equations used are not hopelessly complicated and the thermodynamic and transport data are frequently available for binary solutions. The binary electrolyte is simple because only two ionic species are present. The electroneutrality condition (Equation 9.118) then allows the electrolyte concentration to be defined as

$$c = c_+/\nu_+ = c_-/\nu_- \tag{9.132}$$

where ν_+ and ν_- are, respectively, the numbers of moles of cations and anions produced by the dissociation of a mole of electrolyte.

For a concentrated binary electrolyte, the superficial volume-average velocity $\mathbf{v}$ is defined as

$$\mathbf{v} = \bar{V}_0\mathbf{N}_0 + \bar{V}_+\mathbf{N}_+ + \bar{V}_-\mathbf{N}_- \tag{9.133}$$

where the partial molar volume of ions satisfies

$$\bar{V}_e = \nu_+\bar{V}_+ + \nu_-\bar{V}_- \tag{9.134}$$

This is not sufficient to determine the partial molar volumes of the ions separately. Consequently, we let

$$\nu_+\bar{V}_+ = t_-^0\,\bar{V}_e \quad \text{or} \quad t_+^0\,\nu_+\bar{V}_+ = t_-^0\,\nu_-\bar{V}_- \tag{9.135}$$

The transference numbers of the ions t_i^0 are assumed to be inversely proportional to their partial molar volumes. The cation flux can now be expressed as

$$\mathbf{N}_+ = c_+\mathbf{v} - \varepsilon(D + D_a)\nabla c_+ + \frac{t_+^0}{z_+F}\mathbf{i}_2 \tag{9.136}$$

with a similar expression for the anion flux, and the solvent flux is

$$\mathbf{N}_0 = c_0\mathbf{v} - \varepsilon(D + D_a)\nabla c_0 \tag{9.137}$$

where D_a is the dispersion coefficient. Substitution of these fluxes into the material balance (Equation 9.117) and rearrangement give two fundamental equations for porous electrodes involving a binary electrolyte:

$$\frac{\partial\varepsilon}{\partial t} + \nabla\cdot\mathbf{v} = a\left(\bar{V}_0 j_{0n} + \frac{\bar{V}_e t_-^0}{\nu_+}j_{+n} + \frac{\bar{V}_e t_+^0}{\nu_-}j_{-n}\right) - \bar{V}_e\frac{\mathbf{i}_2\cdot\nabla t_+^0}{z_+\nu_+F} - \varepsilon\frac{D + D_a}{c_0\bar{V}_0}\nabla c\cdot\nabla\bar{V}_e \tag{9.138}$$

and

$$\varepsilon\frac{\partial c}{\partial t} + \mathbf{v}\cdot\nabla c = \nabla\cdot[\varepsilon(D + D_a)\nabla c] - c_0\bar{V}_0\frac{\mathbf{i}_2\cdot\nabla t_+^0}{z_+\nu_+F} + ac_0\bar{V}_0\left(\frac{t_-^0}{\nu_+}j_{+n} + \frac{t_+^0}{\nu_-}j_{-n}\right) - ac\bar{V}_0 j_{0n} + c\varepsilon\frac{D + D_a}{c_0\bar{V}_0}\nabla c\cdot\nabla\bar{V} \tag{9.139}$$

Equation 9.138 is an overall conservation equation, expressing perhaps conservation of volume. It shows how the velocity **v** changes as a result of an electrode reaction and the changing composition of the solution. Equation 9.139 is a material balance for the electrolyte. Both equations simplify considerably with assumptions of constant transference numbers and partial molar volumes. Equations 9.122, 9.125, and 9.138 can then be combined and integrated to relate the velocity to the current density

$$\mathbf{v} = \left[-\sum_{\text{solid phases}} \left(\frac{s_i M_i}{\rho_i n F} \right) - \frac{\bar{V}_0 s_0}{nF} - \frac{\bar{V}_e}{nF} \left(\frac{t_-^0 s_+}{\nu_+} + \frac{t_+^0 s_-}{\nu_-} \right) \right] \mathbf{i}_2 \tag{9.140}$$

with the boundary condition that both **v** and $\mathbf{i}_2$ vanish at a plane of symmetry or the backing plate. The current density is finally expressed by the following Ohm's law in the solution phase:

$$\frac{\mathbf{i}_2}{\kappa} = -\nabla \Phi_2 - \left(\frac{s_+}{\nu_+ n} + \frac{t_+^0}{z_+ \nu_+} - \frac{s_0 c}{n c_0} \right) \frac{\nabla \mu_e}{F} \tag{9.141}$$

where κ is the effective conductivity of solution, Φ_2 is the potential in the pore solution measured with a reference electrode having the stoichiometric coefficients s_i and number n of electrons transferred, and μ_e is the chemical potential of the electrolyte.

9.6.2 Applications of Electrochemical Models in the 1970s

A theoretical model for the porous lead dioxide electrode was proposed by Simonsson on the basis of the macrohomogeneous model for porous electrodes, considering the following reaction [55]:

$$PbO_2 + 3H^+ + HSO_4^- + 2e^- \leftrightarrow PbSO_4 + 2H_2O \tag{9.142}$$

The kinetic expression (Equation 9.124) for the reaction rate is approximated by the Tafel equation:

$$\nabla \cdot \mathbf{i}_2 = j_{PbO_2} = -a i_0 \exp\left(-\frac{nF}{RT} \eta_s \right) \tag{9.143}$$

The plugging of the pores and gradual insulation of the active electrode surface by the lead sulfate are both considered by relating them to the local DOD:

$$\frac{\partial \text{DOD}}{\partial t} = -\frac{j_{PbO_2}}{q_{v,\max}} \tag{9.144}$$

where $q_{v,\max}$ is the theoretical capacity density per unit volume. The free active surface is then assumed to be linearly related to the DOD:

$$a = a_0 \left(1 - \frac{\text{DOD}}{\text{DOD}_{\max}} \right) \tag{9.145}$$

where a_0 is the initially available active surface in the fully charged electrode, and $\text{DOD}_{\max}$ is the maximum fraction of the electrode material that can be utilized at the actual current density. The numerical results show that, at high current densities, the discharge capacity is limited by both structural and transport restrictions. At the end of discharge, a layer of lead sulfate crystals blocks the electrode surface in the outer layers of the electrode. The current can then neither be transferred across this insulated surface nor reach remaining active material in the inner parts of the electrode because of acid depletion, which is further accelerated by the decreasing porosity.

A one-dimensional model describing the transient discharge behavior of a lead-acid cell was presented by Tiedemann and Newman [56] in 1979 (Figure 9.22), considering Reaction 9.142 at the positive electrode and

$$\text{Pb} + \text{HSO}_4^- \leftrightarrow \text{PbSO}_4 + \text{H}^+ + 2\text{e}^- \tag{9.146}$$

at the negative electrode. For constant transference numbers and partial molar volumes, with the use of Faraday's law (neglecting double layer charging), the material balance (Equation 9.139) becomes

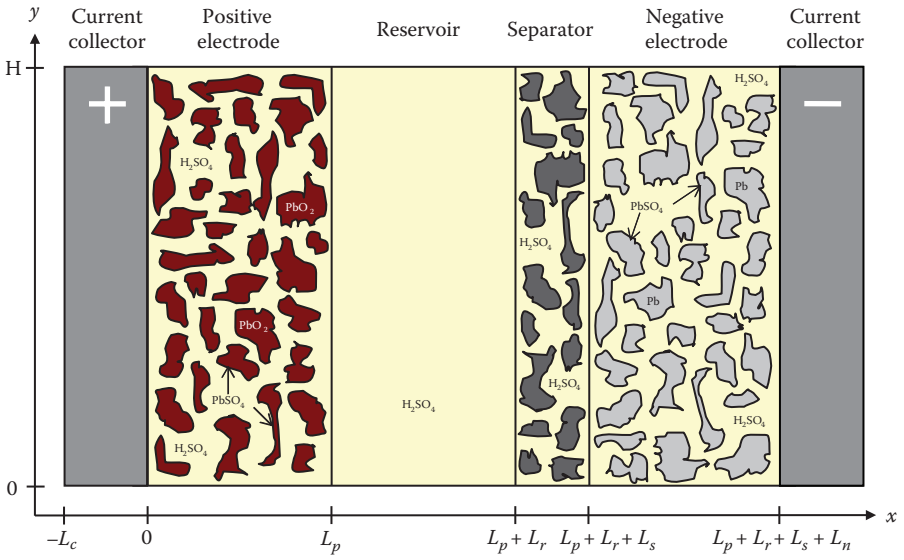

FIGURE 9.22 Schematic diagram of the electrochemical model of a lead-acid cell.

$$\varepsilon \frac{\partial c}{\partial t} + \mathbf{v} \cdot \nabla c = \nabla \cdot (\varepsilon^{ex} D \nabla c) + \left(\frac{3 - 2t_+^0}{2F} c_0 \bar{V}_0 + \frac{c \bar{V}_0}{F} \right) \nabla \cdot \mathbf{i}_2 \tag{9.147}$$

for the PbO_2 electrode, where *ex* is an exponent related to the geometry of the porous electrode (taken here to be 1.5),

$$\varepsilon \frac{\partial c}{\partial t} + \mathbf{v} \cdot \nabla c = \nabla \cdot (\varepsilon^{ex} D \nabla c) - \frac{\left(2t_+^0 - 1\right) c_0 \bar{V}_0}{2F} \nabla \cdot \mathbf{i}_2 \tag{9.148}$$

for the Pb electrode,

$$\varepsilon \frac{\partial c}{\partial t} + \mathbf{v} \cdot \nabla c = \nabla \cdot (\varepsilon^{ex} D \nabla c) \tag{9.149}$$

for the separator, and

$$\frac{V_r}{A_p} \frac{\partial c}{\partial t} = \varepsilon^{ex} D \nabla c \Big|_{separator} - \varepsilon^{ex} D \nabla c \Big|_{PbO_2} \tag{9.150}$$

for the reservoir. The kinetic expression for both electrodes is given by

$$\nabla \cdot \mathbf{i}_2 = a_0 i_0 \sqrt{\frac{c}{c_0}} \left(1 - \frac{\text{DOD}}{\text{DOD}_{\max}} \right) \left\{ \exp\left[\frac{(1-\alpha) nF}{RT} \eta_s \right] - \exp\left[-\frac{\alpha nF}{RT} \eta_s \right] \right\} \tag{9.151}$$

Treating the solution as a concentrated binary electrolyte and measuring the potential in solution with respect to a reference electrode of Pb, Ohm's law (Equation 9.141) becomes

$$\frac{\mathbf{i}_2}{\varepsilon^{ex} \kappa} = \nabla \eta_s + \frac{RT}{F} \left(3 - 2t_+^0 + \frac{2c \bar{V}_0}{1 - c \bar{V}_e} \right) \nabla \ln(cf) \tag{9.152}$$

for the PbO_2 electrode, where f is the activity coefficient of the electrolyte, and

$$\frac{\mathbf{i}_2}{\varepsilon^{ex} \kappa} = \nabla \eta_s + \frac{RT}{F} \left(1 - 2t_+^0 \right) \nabla \ln(cf) \tag{9.153}$$

for the Pb electrode and the separator. For the reservoir, the equation is the same, but simplified by a porosity of unity and the absence of a concentration gradient. This model shows reasonable agreement between predicted behavior and experimental results.

9.6.3 Applications of Electrochemical Models in the 1980s

The changes in structure and kinetics during charge of the porous PbO_2 electrode were studied by Ekdunge and Simonsson in 1985 [57]. It is commonly believed that the transformations between lead sulfate and lead dioxide occur via a dissolution precipitation mechanism involving dissolved Pb^{2+} ions. According to this mechanism, the oxidation reaction can be formally written as

$$PbSO_4 \rightarrow Pb^{2+} + SO_4^{2-} \tag{9.154}$$

$$Pb^{2+} + 2H_2O \rightarrow PbO_2 + 4H^+ + 2e^- \tag{9.155}$$

Assuming first-order, purely consecutive reactions, and constant concentration of sulfuric acid, the kinetic equation at high overvoltage for this scheme would be of the form

$$j_{PbO_2} = \frac{a_0 i_0 \exp\left[\dfrac{(1-\alpha)nF}{RT}\eta_s\right]}{1 + \dfrac{a_0 i_0}{2F}\left(\dfrac{1}{k_b a_b} + \dfrac{L_p}{D c_0 a_{a,b}}\right)\exp\left[\dfrac{(1-\alpha)nF}{RT}\eta_s\right]} \tag{9.156}$$

However, the polarization curves have a Tafel slope of about 60 mV decade^{-1} at overvoltages lower than 0.1 V and about 180 mV decade^{-1} at higher overvoltages. The authors explain this switch from a low to a high Tafel slope by a mechanism with two consecutive single-electron transfer reactions:

$$S_R \leftrightarrow S_M + e^- \tag{9.157}$$

$$S_M \leftrightarrow S_O + e^- \tag{9.158}$$

Writing down the rate equation for each step and eliminating the concentration of the intermediate S_M between the two equations give the following relation between current density and overvoltage:

$$j_{PbO_2} = 2a_0 i_{0,R} \exp\left[\frac{(1-\alpha_R)F}{RT}\eta_s\right] \frac{1 - \exp\left[-\dfrac{2F}{RT}\eta_s\right]}{1 + \dfrac{i_{0,R}}{i_{0,O}}\exp\left[-\dfrac{(1-\alpha_O+\alpha_R)F}{RT}\eta_s\right]} \tag{9.159}$$

At high anodic overvoltages, Equation 9.159 is simplified to

$$j_{PbO_2} = 2a_0 i_{0,R} \exp\left[\frac{(1-\alpha_R)F}{RT}\eta_s\right] \tag{9.160}$$

The anticipated linear decrease in current density with the increasing SOC indicated by the potentiostatic oxidations is tested by a rate equation of the form

$$j_{PbO_2} = 2a_0 \mathrm{SOC}\, i_{0,R} \exp\left[\frac{(1-\alpha_R)F}{RT}\eta_s\right] \frac{1-\exp\left[-\frac{2F}{RT}\eta_s\right]}{1+\frac{i_{0,R}}{i_{0,O}}\exp\left[-\frac{(1-\alpha_O+\alpha_R)F}{RT}\eta_s\right]} \tag{9.161}$$

Two years later, Gu et al. [58] extended the work of Tiedemann and Newman [56] by presenting a one-dimensional model of a lead-acid cell that is able to predict its dynamic behavior during discharge but also during charge and rest. Equation 9.125 describes the change in porosity with time due to the conversion of the active material in both electrode reactions. Ohm's law applied to the solid matrix is derived from Equation 9.131:

$$\nabla \cdot \mathbf{i}_2 - \nabla \cdot \left(\sigma\sqrt{\varepsilon}\nabla\Phi_1\right) = 0 \tag{9.162}$$

The Ohm's law in solution (Equation 9.153) becomes

$$\frac{\mathbf{i}_2}{\varepsilon^{ex}\kappa} + \nabla\Phi_2 - \frac{RT}{F}\left(1-2t_+^0\right)\nabla\ln(cf) = 0 \tag{9.163}$$

The material balance for each electrode is provided in Equations 9.147 and 9.148. The kinetic expression (Equation 9.124) is used assuming the concentration dependence of the exchange current density with $\gamma = 1.5$:

$$i_0 = i_{0,ref}\left(\frac{c}{c_0}\right)^{\gamma} \tag{9.164}$$

The charge dependence of the specific interfacial area is taken into account as follows:

$$a = a_{\max}\left(\frac{\varepsilon-\varepsilon_0}{\varepsilon_{\max}-\varepsilon_0}\right)^{\zeta} \tag{9.165}$$

during discharge and rest, and

$$a = a_{\max}\left(\frac{\varepsilon-\varepsilon_0}{\varepsilon_{\max}-\varepsilon_0}\right)^{\zeta}\left(\frac{\varepsilon_{\max}-\varepsilon}{\varepsilon_{\max}-\varepsilon_0}\right) \tag{9.166}$$

during charge, with $\zeta = 1$. Equation 9.166 accounts for the depletion of lead sulfate as lead dioxide is being formed. For convenience, the dependence of the overpotential on the acid concentration is neglected, and a concentration-independent lead electrode is used as a reference electrode. This model predicts profiles of acid concentration, overpotential, porosity, reaction rate, and electrode capacity as functions of time and temperature.

A two-dimensional mathematical model for a lead dioxide electrode has been presented by Dimpault-Darcy et al. [59] It contains all the features of the model by Gu et al. [58] According to Figure 9.22, its bounds are

$$-L_c \le x \le L_p \quad \text{and} \quad 0 \le y \le H \tag{9.167}$$

A concentration-independent lead dioxide electrode is used as a reference electrode. With $f = 1$, the Ohm's law in solution (Equation 9.163) becomes

$$\frac{\mathbf{i}_2}{\varepsilon^{ex}\kappa} + \nabla\Phi_2 - \frac{RT}{F}\left(\frac{3-2t_+^0}{c} + \frac{2V_0}{1-cV_e}\right)\nabla c = 0 \tag{9.168}$$

Convective flow of the electrolyte is considered negligible, which eliminates the velocity vector **v** from the governing equations. The material balance of Equation 9.117 simplifies to

$$\frac{\partial \varepsilon c}{\partial t} - \nabla\cdot(\varepsilon^{ex} D\nabla c) - \frac{3-2t_+^0}{2F}\nabla\cdot\mathbf{i}_2 = 0 \tag{9.169}$$

At the reservoir boundary, the potential in solution and the acid concentration are constant:

$$\forall x = L_p, \quad \Phi_2 = \Phi_{2,r}, \quad \text{and} \quad c = c_r \tag{9.170}$$

At the top of the electrode, a tab connector serves as a sink of current during discharge. For the part of the upper boundary in contact with the tab, the condition is

$$\forall y = H \text{ and } -L_c \le x \le 0, \quad \frac{\partial\Phi_1}{\partial y} = \frac{I}{\sigma HW} \tag{9.171}$$

Current enters the electrode matrix at the reservoir boundary in the electrolyte according to the condition

$$\forall x = L_p, \quad i_{2x} = \frac{I}{HW}, \quad \text{and} \quad i_{2y} = 0 \tag{9.172}$$

where H and W are the height and width of the electrode, respectively. At the center boundary, the current is parallel to the y-direction, resulting in

$$\forall x = -L_c, \quad i_{2x} = 0 \tag{9.173}$$

For the upper and lower boundaries

$$\forall y = 0 \text{ or } y = H, \quad i_{2y} = 0 \tag{9.174}$$

applies since the electrolyte is bounded there.

In 1989, Ekdunge and Simonsson published a model for the porous lead electrode in order to explain the limited discharge capacity at high rates of discharge [60]. They showed that the relationship between current and charge transfer overvoltage could be described by the kinetic expression

$$j_{Pb} = \frac{a_{\max} \mathrm{SOC}^{\xi} i_0 \left[1 - \exp\left(\dfrac{2F\eta_s}{RT} \right) \right]}{\dfrac{a_{\max} i_0}{j_{\lim}^{c}} - \exp\left(\dfrac{\alpha F \eta_s}{RT} \right)} \tag{9.175}$$

which takes into account the structural changes by means of the factor

$$\mathrm{SOC} = \mathrm{SOC}_0 + L_n (HW)^n I^{n-1} K^{-1} \int_0^t j_{Pb}(\tau)\, d\tau \tag{9.176}$$

where $j_{\lim}^{c}$ is the limiting current for the cathodic reaction. By comparison with experimental curves, the model predicts that the discharge process is ended by coverage of the electrode active surface of lead by lead sulfate, even at current densities around 1000 A m^{-2}. Only at concentrations lower than the normal (4 to 5 M) and very high current densities will depletion of sulfuric acid become a limitation. By using an expression that relates the local maximum utilization of the active material to the time integral of the local current density in a way that resembles the empirical Peukert's equation (Equation 9.8), final lead sulfate distributions can be predicted with a maximum in the center of the electrode, which is in agreement with measurements.

9.6.4 Applications of Electrochemical Models in the 1990s

A model of a porous lead dioxide electrode has been described and used to investigate lead-sulfate nucleation and growth during discharge by Bernardi [61]. A nucleation rate expression that is based on classical, heterogeneous nucleation theory is outlined:

$$\frac{\partial n_b}{\partial t} = \frac{\bar{V}_b}{4}\sqrt{\frac{2\gamma}{N_a RT}}\sqrt[3]{\frac{N_a^2}{c_A}}\,\nu c_B\left(n_b^0 - n_b\right)\exp\left[-\frac{8\pi\gamma^3\bar{V}_b^2 N_a}{3(RT)^3\ln^2\left(c_B/c_B^{eq}\right)}\right] \tag{9.177}$$

where n_b is the number of $PbSO_4$ nuclei per unit area, γ the surface tension, N_a the Avogadro's number, and ν the fundamental jump frequency. An electrochemical kinetic expression is derived based on a reaction mechanism involving two elementary steps:

$$PbO_2 + 4H^+ + 2e^- \rightarrow Pb^{2+} + 2H_2O \tag{9.178}$$

$$Pb^{2+} + HSO_4^- \rightarrow PbSO_4 + H^+ \tag{9.179}$$

The porosity variation

$$\frac{\partial \varepsilon}{\partial t} + \frac{\bar{V}_a}{nF}\nabla\cdot\mathbf{i}_2 + \bar{V}_b R_b \tag{9.180}$$

is a volume balance for the two solid phases, *a* and *b*, with

$$R_b = 5\varepsilon_b^{2/3}(n_b a)^{1/3} k_{ppt}\left(c_B - c_B^{eq}\right) \tag{9.181}$$

the volumetric production rate of $PbSO_4$ by precipitation reaction (Reaction 9.179). Concentrated ternary electrolyte theory is used in formulating material-transport equations for two electrolytes: H_2SO_4 (A) and $Pb(HSO_4)_2$ (B)

$$\frac{\partial \varepsilon c_A}{\partial t} + \nabla\cdot(c_A\mathbf{v}) - \nabla\cdot[\varepsilon^{ex}(D_{AA}\nabla c_A + D_{AB}\nabla c_B)] + \frac{2t_+^A - 4}{2F}\nabla\cdot\mathbf{i}_2 - R_b = 0 \tag{9.182}$$

$$\frac{\partial \varepsilon c_B}{\partial t} + \nabla\cdot(c_B\mathbf{v}) - \nabla\cdot[\varepsilon^{ex}(D_{BA}\nabla c_A + D_{BB}\nabla c_B)] + \frac{t_+^B + 1}{2F}\nabla\cdot\mathbf{i}_2 + R_b = 0 \tag{9.183}$$

An overall material balance on the solution phase electrolyte velocity

$$\frac{\partial \varepsilon}{\partial t} + \nabla\cdot\mathbf{v} + \frac{1}{2F}\left[\bar{V}_A\left(2t_+^A - 4\right) + \bar{V}_B\left(t_+^B + 1\right) + 2\bar{V}_0\right]\nabla\cdot\mathbf{i}_2 + R_b\left(\bar{V}_B - \bar{V}_A\right) = 0 \tag{9.184}$$

describes changes in the volume-average velocity. Ohm's law in solution

$$\frac{\mathbf{i}_2}{\varepsilon^{ex}\kappa}+\nabla\Phi_2+\frac{RT}{F}\left[\left(2t_+^A-4-\frac{2c_A}{c_0}\right)\nabla c_A+\left(\frac{3}{2}t_+^B+\frac{3}{2}-\frac{3c_B}{c_0}\right)\nabla c_B\right]=0 \quad (9.185)$$

relates gradients in solution potential and chemical potential of the electrolytes to local current density. The model simulates the "coup de fouet" and calculates the degree of lead-ion supersaturation, the number density of lead-sulfate particles, and the free energy of formation as well as the size of critical nuclei.

A mathematical model of a starved lead-acid cell was developed by Nguyen et al. [62] in 1990 to study its dynamic behavior during discharge. Most of the equations in this model derive from a previous work of this team [58]. A starved lead-acid cell does not have an acid reservoir as represented in Figure 9.22 ($L_r = 0$). Instead, a thicker and more porous separator is used with a porosity defined by

$$\varepsilon = f_{sat}\varepsilon_s \quad (9.186)$$

where f_{sat} is a constant used to specify the fraction of the separator that is filled with electrolyte—not occupied by oxygen. Convective flow of the electrolyte is neglected [59], which leads to the use of the material balance (Equation 9.169) for the positive electrode and

$$\frac{\partial\varepsilon c}{\partial t}-\nabla\cdot(\varepsilon^{ex}D\nabla c)-\frac{1-2t_+^0}{2F}\nabla\cdot\mathbf{i}_2=0 \quad (9.187)$$

for the negative electrode. The charge dependence of the specific interfacial area is taken into account as follows:

$$a=a_{\max}\left(\frac{q_v}{q_{v,\max}}\right)^{\zeta} \quad \text{with} \quad \frac{\partial q_v}{\partial t}=\begin{cases} j_{PbO_2}^{+} & \forall x\le L_p \\ -j_{Pb}^{-} & \forall x\ge L_p+L_s \end{cases} \quad (9.188)$$

The battery voltage is calculated based on six cells connected in series

$$u_{batt}=6\left(\Phi_{1,x=0}-\Phi_{1,x=L_p+L_s+L_n}\right)+i_{batt}\left(5R_{ic}+2R_t+\frac{12R_{grid}}{N_p-1}\right) \quad (9.189)$$

where R_{ic} and R_t are the measured resistance of the intercell connector and battery terminal, respectively; N_p is the total number of plates in each cell; and R_{grid} is the equivalent grid resistance due to both the positive and negative grids.

Three years later, Nguyen and White presented a model of a hermetically sealed lead-acid cell [63]. They studied the effect of having an excess negative electrode and the transport rate of oxygen across the separator on the oxygen evolution at the positive electrode

$$2H_2O \rightarrow O_2 + 4H^+ + 4e^- \quad (9.190)$$

and its reduction at the negative electrode

$$O_2 + 4H^+ + 4e^- \rightarrow 2H_2O \tag{9.191}$$

during charge and overcharge. At rest, oxygen reduction at the negative electrode continues to occur if oxygen is present in the system by the following corrosion reaction:

$$O_2 + 2Pb + 2H^+ + 2HSO_4^- \rightarrow 2PbSO_4 + 2H_2O \tag{9.192}$$

which is simply a combination of Reactions 9.146 and 9.191. The transfer current is

$$\nabla \cdot \mathbf{i}_2 = j_a + j_{O_2} = \begin{cases} j^+_{PbO_2} + j^+_{O_2} & \forall x \le L_p \\ j^-_{Pb} + j^-_{O_2} & \forall x \ge L_p + L_s \end{cases} \tag{9.193}$$

where the expressions for j_a come from Equations 9.124, 9.164, 9.165, and 9.166. The oxygen reaction leads to

$$j^k_{O_2} = a_{\max} i^k_{O_2,ref} \left(\frac{\varepsilon - \varepsilon_0}{\varepsilon_{\max} - \varepsilon_0} \right)^{\zeta} \left\{ \exp\left[\frac{(1-\alpha)nF}{RT} \eta_{O_2} \right] - \frac{c_{O_2}}{c_{O_2,ref}} \exp\left[-\frac{\alpha nF}{RT} \eta_{O_2} \right] \right\} \tag{9.194}$$

where c_{O_2} is the oxygen concentration, for which the material balance is

$$\frac{\partial \varepsilon c_{O_2}}{\partial t} - \nabla \cdot \left(\varepsilon^{ex} D_{O_2} \nabla c_{O_2} \right) - \frac{1}{4F} j^k_{O_2} = 0 \tag{9.195}$$

The material balance on electrolyte concentration is

$$\frac{\partial \varepsilon c}{\partial t} - \nabla \cdot (\varepsilon^{ex} D \nabla c) - \frac{3 - 2t^0_+}{2F} j^+_{PbO_2} - \frac{1 - t^0_+}{F} j^+_{O_2} = 0 \tag{9.196}$$

for the positive electrode and

$$\frac{\partial \varepsilon c}{\partial t} - \nabla \cdot (\varepsilon^{ex} D \nabla c) - \frac{1 - 2t^0_+}{2F} j^-_{Pb} - \frac{1 - t^0_+}{F} j^-_{O_2} = 0 \tag{9.197}$$

for the negative electrode. The model shows that the exchange current densities of the oxygen reactions are important to the rechargeability of a sealed lead-acid cell, and also that once oxygen gets to the negative electrode it is quickly reduced and does not penetrate deeply inside the electrode.

A two-dimensional model that details nonuniformities along cell height as well as thickness was developed by Bernardi et al. in 1993 [64]. It is made up of six governing equations. The porosity variation is described by Equation 9.125. The Ohm's laws in solid and liquid phases come from Equations 9.162 and 9.163 with $f = 1$, respectively. The material balance on electrolyte concentration is defined by Equation 9.169 for the positive electrode and Equation 9.187 for the negative electrode. Equations 9.124, 9.164, and 9.188 are used for electrode kinetics. Contrary to the model of Dimpault-Darcy et al. [59], half of the current collectors are included in each half-electrode without distinction:

$$0 \le x \le L_p + L_r + L_s + L_n \quad \text{and} \quad 0 \le y \le H \tag{9.198}$$

The boundary conditions are formulated with the assumption that the bottom of the cell and the top of the reservoir and separator are impermeable to both ions and electrons:

$$\forall y = 0 \text{ or } y = H, \quad i_{2y} = 0 \tag{9.199}$$

At the top of the electrodes, current flows in and out and the solid-phase current density is taken to be uniform:

$$\forall y = H \text{ and } x \le L_p, \quad \frac{\partial \Phi_1}{\partial y} = -\frac{I}{\sigma_{PbO_2} HW} \tag{9.200}$$

$$\forall y = H \text{ and } x \ge L_p + L_r + L_s, \quad \frac{\partial \Phi_1}{\partial y} = \frac{I}{\sigma_{Pb} HW} \tag{9.201}$$

The model results show that the local electrochemical reaction rates are lowest at the bottom center of the electrodes and highest at the top. As discharge proceeds, the distributions in reaction rates and current density become more uniform from the top to the bottom of the cell.

A one-dimensional model of the oxygen recombination lead-acid cell was developed by Bernardi and Carpenter two years later [65]. The model is applied to investigate mechanisms associated with oxygen recombination and species transport during charge. The cell volume contains three distinct phases (solid, liquid, or gas):

$$\varepsilon_s + \varepsilon_l + \varepsilon_g = 1 \tag{9.202}$$

The overall solid-phase material balance is

$$-\frac{\partial \varepsilon_s}{\partial t} - \sum_{\text{solid phases}} \left(\frac{s_i M_i}{\rho_i n F} \right) j_a = 0 \tag{9.203}$$

The overall liquid-phase material balance is

$$\frac{\partial \varepsilon_l}{\partial t} + \left[\frac{\bar{V}_A}{2F}\left(2t_+^0 - 3\right) - \frac{\bar{V}_0}{F}\right] j_{PbO_2}^+ + \frac{\bar{V}_A - \bar{V}_0}{2F} j_{O_2}^+ = 0 \tag{9.204}$$

for the positive electrode and

$$\frac{\partial \varepsilon_l}{\partial t} - \frac{\bar{V}_A}{2F}\left(1 - 2t_+^0\right) j_{Pb}^- - \frac{\bar{V}_A - \bar{V}_0}{2F} j_{O_2}^- = 0 \tag{9.205}$$

for the negative electrode. Equations 9.196 and 9.197 describe the material balance for H_2SO_4 with $\varepsilon = \varepsilon_l$. The simple reaction (Reaction 9.190) characterizes the oxygen evolution reaction that occurs at the PbO_2 electrode and

$$O_2 + 4H^+ + 4e^- \rightarrow 2H_2O \tag{9.206}$$

is its recombination, which occurs at the Pb electrode during charge. The transfer current is calculated from Equations 9.124, 9.164, and 9.193 with

$$a = a_{\max}\left(1 - \frac{q_v}{q_{v,\max}}\right)^{\zeta}\left(\frac{q_v}{q_{v,\max}}\right)^{\zeta} \quad \text{with} \quad \frac{\partial q_v}{\partial t} = \begin{cases} j_{PbO_2}^+ & \forall x \le L_p \\ -j_{Pb}^- & \forall x \ge L_p + L_s \end{cases} \tag{9.207}$$

The oxygen reaction (Reaction 9.194) now becomes

$$j_{O_2}^k = a i_{O_2,ref}^k \left(\frac{c_A}{c_{A,ref}}\right)\left(\frac{p_{O_2}}{p_{O_2,ref}}\right)\left\{\exp\left[\frac{n_{O_2}^k F}{2RT}\eta_{O_2}\right] - \exp\left[-\frac{n_{O_2}^k F}{2RT}\eta_{O_2}\right]\right\} \tag{9.208}$$

where p_{O_2} is the partial pressure of oxygen in the gas phase given by

$$p_{O_2} = \frac{N_{O_2} RT}{V_g^{tot}} \tag{9.209}$$

where V_g^{tot} is the total volume of gas in the cell:

$$V_g^{tot} = \iiint_{V_{cell}} \varepsilon_g \, dx \, dy \, dz + V_g^{ext} \tag{9.210}$$

V_g^{ext} is the gas space outside the unit cell stack, and N_{O_2} is the total moles of oxygen in the gas phase:

$$\frac{\partial N_{O_2}}{\partial t} = \frac{1}{4F} \iiint_{V_{cell}} j_{O_2}\, dx\, dy\, dz \tag{9.211}$$

The total pressure p_{tot} can then be calculated from the number of moles of inert gas N^0_{inert} present within the cell initially:

$$p_{tot} = p_{O_2} + \frac{N^0_{inert} RT}{V_g^{tot}} \tag{9.212}$$

In 1997, a model was developed by Gu et al. to predict transient behaviors of EV LABs during discharge and charge processes [66]. The model not only accounts for the coupled processes of electrochemical kinetics and mass transport occurring in a battery cell, but also considers free convection resulting from density variations due to acid stratification. For the positive electrode, the material balance (Equation 9.169) becomes

$$\frac{\partial \varepsilon c}{\partial t} + \mathbf{v} \cdot \nabla c - \nabla \cdot (\varepsilon^{ex} D \nabla c) - \frac{3 - 2t_+^0}{2F} \nabla \cdot \mathbf{i}_2 = 0 \tag{9.213}$$

and the same applies for the negative electrode material balance (Equation 9.187):

$$\frac{\partial \varepsilon c}{\partial t} + \mathbf{v} \cdot \nabla c - \nabla \cdot (\varepsilon^{ex} D \nabla c) - \frac{1 - 2t_+^0}{2F} \nabla \cdot \mathbf{i}_2 = 0 \tag{9.214}$$

A single set of conservation equations valid for both porous electrodes and the free electrolyte region is derived and numerically solved using a computational fluid dynamics technique. This numerical methodology is capable of simulating a two-dimensional cell with the fluid flow taken into consideration. The motion of the liquid electrolyte is governed by the Navier-Stokes equation with the Boussinesq approximation and the continuity equation as follows:

$$\frac{\partial \mathbf{v}}{\partial t} + \mathbf{v} \cdot \nabla \mathbf{v} + \frac{1}{\rho} \nabla p - \nabla \cdot \left(\frac{\mu}{\rho} \nabla \mathbf{v} \right) - \mathbf{g}[1 + \beta(c - c_{ref})] - \frac{\mu \varepsilon \mathbf{v}}{\rho \boldsymbol{K}} = 0 \tag{9.215}$$

$$\nabla \cdot \mathbf{v} = 0 \tag{9.216}$$

where μ is the electrolyte viscosity, $\mathbf{g}$ the gravitational vector, and β the volume expansion coefficient of the electrolyte. The permeability of the electrodes K is determined by the Kozeny-Carman equation:

$$K = \frac{\varepsilon^3 d^2}{180\,(1 - \varepsilon)^2} \tag{9.217}$$

with d being the mean diameter of particles making up the electrode.

Modeling of recombinant lead-acid batteries is extended by Newman and Tiedemann [67]. The fast kinetics of oxygen recombination (Reaction 9.206) is expressed as

$$j_{O_2}^{-} = -a\frac{4F}{RT}k_{m,O_2}p_{O_2} \tag{9.218}$$

where a comes from Equation 9.188 and k_{m,O_2} is a potential-independent rate constant. The kinetics of oxygen generation (Reaction 9.190) is expressed as

$$j_{O_2}^{+} = ai_{O_2,ref}^{+}\left(\frac{c_A}{c_{A,ref}}\right)^{\gamma_{O_2}}\left\{\exp\left[\frac{\left(1-\alpha_{O_2}\right)4F}{RT}\eta_{O_2}\right]-\frac{p_{O_2}}{p_{O_2,ref}}\exp\left[-\frac{\alpha_{O_2}4F}{RT}\eta_{O_2}\right]\right\} \tag{9.219}$$

and the kinetics of hydrogen recombination

$$H_2 \rightarrow 2H^+ + 2e^- \tag{9.220}$$

is expressed as

$$j_{H_2}^{+} = a\frac{2F}{RT}k_{m,H_2}p_{H_2} \tag{9.221}$$

In analogy to Equation 9.219, the kinetics of hydrogen generation on the negative electrode

$$2H^+ + 2e^- \rightarrow H_2 \tag{9.222}$$

is expressed as

$$j_{H_2}^{-} = -ai_{H_2,ref}^{-}\exp\left(-\frac{\alpha_{H_2}n_{H_2}F}{RT}\eta_{H_2}\right) \tag{9.223}$$

If the rate of transport of Pb^{2+} ions from the lead sulfate crystallites to the reaction site on the negative electrode is limited by diffusion, then Reaction 9.146 proceeds by dissolution of $PbSO_4$ (Reaction 9.154) followed immediately by electrochemical reaction of the Pb^{2+} ions on the lead surface

$$Pb^{2+} + 2e^- \rightarrow Pb \tag{9.224}$$

Oxygen reacts directly with lead

$$O_2 + 2Pb \rightarrow 2PbO \tag{9.225}$$

to form PbO, which reacts spontaneously with sulfuric acid to form lead ions

$$PbO + 2H^+ \rightarrow Pb^{2+} + H_2O \tag{9.226}$$

The reaction rate at the negative electrode can thus be expressed as

$$j^- = \frac{a^-_{\max} i^-_{0,ref} \left(\frac{q^-_v}{q^-_{v,\max}} \right)^\zeta \left\{ \frac{j^-_{O_2}}{a^-_{\max}} + 2Fk^-_{PbSO_4} c^{sat}_{Pb^{2+}} \left(1 - \frac{q^-_v}{q^-_{v,\max}} \right)^\zeta \left[\exp\left(\frac{nF}{RT} \eta^-_s \right) - 1 \right] \right\}}{i^-_{0,ref} \left(\frac{q^-_v}{q^-_{v,\max}} \right)^\zeta + 2Fk^-_{PbSO_4} c^{sat}_{Pb^{2+}} \left(1 - \frac{q^-_v}{q^-_{v,\max}} \right)^\zeta \exp\left(\frac{\alpha^- nF}{RT} \eta^-_s \right)} \tag{9.227}$$

There is a parallel treatment at the positive electrode where Reaction 9.142 is replaced by dissolution of $PbSO_4$ (Reaction 9.154) and the side reaction

$$H_2 + PbO_2 + 2H^+ \rightarrow Pb^{2+} + 2H_2O \tag{9.228}$$

which leads to the electrochemical reaction (Reaction 9.155). The reaction rate can finally be expressed as

$$j^+ = -\frac{a^+_{\max} i^+_{0,ref} \left(\frac{q^+_v}{q^+_{v,\max}} \right)^\zeta \left\{ \frac{j^+_{H_2}}{a^-_{\max}} + 2Fk^+_{PbSO_4} c^{sat}_{Pb^{2+}} \left(1 - \frac{q^+_v}{q^+_{v,\max}} \right)^\zeta \left[\exp\left(\frac{nF}{RT} \eta^+_s \right) - 1 \right] \right\}}{i^+_{0,ref} \left(\frac{q^+_v}{q^+_{v,\max}} \right)^\zeta + 2Fk^+_{PbSO_4} c^{sat}_{Pb^{2+}} \left(1 - \frac{q^+_v}{q^+_{v,\max}} \right)^\zeta \exp\left(\frac{\alpha^+ nF}{RT} \eta^+_s \right)} \tag{9.229}$$

9.6.5 Applications of Electrochemical Models in the 2000s

In 2001, Tenno et al. provided some changes related to electrode kinetics in their model in order to predict the charge–discharge behavior of VRLA batteries [68]. The active surface area between solid and liquid phases depends on the utilization of electrodes. A constant surface area can be expected partially if the small variation in battery capacity is considered. In general, Equation 9.188 is used for the full-discharge process. The value for tortuosity exponent ζ is typically 1.5 [62,64] or 0.5 [60,66]. However, the measured voltage cannot be explained with large values of ζ under deep-discharge conditions. A rapid decrease in voltage at the end of discharge can be predicted with a small value of 0.5 only. The entire discharge curve can be predicted with small values quite well. Recovery from deep discharge is much more rapid than can be predicted by the power function of Equation 9.207. A good fit to the model with measured data can be obtained using the following exponential function:

$$a = a_{\max} K_1 \frac{\exp(-K_2 \mathrm{SOC}) - \exp(-K_2)}{1 - \exp(-K_2)} \approx a_{\max} K_1 \exp(-K_2 \mathrm{SOC}) \tag{9.230}$$

with

$$\frac{\partial \mathrm{SOC}}{\partial t} = \begin{cases} \dfrac{\eta_{cha}^{+}}{q_{v,\max}^{+}} \nabla \cdot \mathbf{i}_2 & \forall x \le L_p \\ -\dfrac{\eta_{cha}^{-}}{q_{v,\max}^{-}} \nabla \cdot \mathbf{i}_2 & \forall x \ge L_p + L_s \end{cases} \tag{9.231}$$

where η_{cha} is the charging efficiency. The exchange current density depends on temperature. The following formula can be used for correction of the exchange current density in a wide temperature range:

$$i_0(T) = i_0(T_{ref}) \exp\left[\frac{E_A(T - T_{ref})}{RTT_{ref}}\right] \tag{9.232}$$

The following year, the same authors applied their model to the evaluation of VRLA batteries under discharge, recharge, and overcharge conditions [69]. The transfer current is

$$\nabla \cdot \mathbf{i}_2 = j_a + j_{O_2} + j_{H_2} \Rightarrow j_a = \eta_{cha} \nabla \cdot \mathbf{i}_2 \tag{9.233}$$

In this model, the volumetric reaction rate for recombination is considered proportional to the evolution rate

$$j_{O_2}^{-} = -\eta^{ore} j_{O_2}^{+} \tag{9.234}$$

where η^{ore} is the oxygen recombination efficiency. The transfer current density for the recombination process is proportional to the transfer current density for the evolution process. The following steady-state reaction model is proposed for hydrogen evolution:

$$j_{H_2}^{-} = -\frac{1 - \eta^{ore}}{2} j_{H_2}^{+} \tag{9.235}$$

The evolution rate of hydrogen is proportional to the imbalance between oxygen evolution and recombination rates

$$2 j_{H_2}^{-} = j_{O_2}^{+} + j_{O_2}^{-} \tag{9.236}$$

or to the oxygen evolution rate

$$2j_{H_2}^{-} = (1-\eta^{ore})j_{O_2}^{+} \tag{9.237}$$

The hydrogen evolution transfer current density is proportional to the oxygen evolution transfer current density. The electrode volume fraction filled with electrolyte can be evaluated as

$$\frac{\partial \varepsilon}{\partial t} = \sum_{\text{solid phases}} \left(\frac{s_i M_i}{\rho_i n F} \right) \eta_{cha} \nabla \cdot \mathbf{i}_2 \tag{9.238}$$

The material balance on the electrolyte concentration (Equations 9.196 and 9.197) now becomes

$$\frac{\partial \varepsilon c}{\partial t} - \nabla \cdot (\varepsilon^{ex} D \nabla c) - \frac{3-2t_+^0}{2F} \eta_{cha}^{+} \nabla \cdot \mathbf{i}_2 - \frac{1}{2F}\left(j_{O_2}^{+} + j_{H_2}^{+} \right) = 0 \tag{9.239}$$

for the positive electrode and

$$\frac{\partial \varepsilon c}{\partial t} - \nabla \cdot (\varepsilon^{ex} D \nabla c) - \frac{1-2t_+^0}{2F} \eta_{cha}^{-} \nabla \cdot \mathbf{i}_2 + \frac{1}{2F}\left(j_{O_2}^{+} + j_{H_2}^{+} \right) = 0 \tag{9.240}$$

for the negative electrode, respectively. Current flow through the surface area of the electrode (interface between electrode and electrolyte) generates heat proportional to the voltage drop caused by reaction hindrance

$$\frac{\partial W_{Joule}}{\partial t} = \eta_s I \tag{9.241}$$

where Q_{Joule} is the heat generated by the Joule effect.

A three-phase electrochemical and thermal coupled model for the overcharge process of VRLA batteries was developed by Gu et al. the same year [70]. Physical phenomena important to the VRLA battery overcharge process, such as gas generation, transport, and recombination, electrolyte displacement and capillary flow, and the venting event during discharge, rest, and charge periods, are incorporated in the model. The interfacial evaporation rate of oxygen from the liquid to the gas phase is determined by

$$R_{O_2}^{\text{lg}} = \frac{a_{O_2}^{\text{lg}}}{l_{O_2}^{\text{lg}}} D_{O_2}^{l} \left(c_{O_2}^{l} - H' c_{O_2}^{g} \right) \tag{9.242}$$

where the superscript lg denotes the liquid/gas interface, $l_{O_2}^{\lg}$ the microscopic diffusion length, and H' the dimensionless Henry's constant. With this evaporation rate, the material balance on oxygen concentration (Equation 9.195) becomes

$$\frac{\partial \varepsilon_l c_{O_2}^l}{\partial t} + \mathbf{v} \cdot \nabla c_{O_2}^l - \nabla \cdot \left(\varepsilon_l^{ex} D_{O_2}^l \nabla c_{O_2}^l \right) - \frac{1}{4F} j_{O_2}^k + R_{O_2}^{\lg} = 0 \tag{9.243}$$

in liquid phase and

$$\frac{\partial \varepsilon_g c_{O_2}^g}{\partial t} - \nabla \cdot \left(\varepsilon_g^{ex} D_{O_2}^g \nabla c_{O_2}^g \right) - R_{O_2}^{\lg} = 0 \tag{9.244}$$

in gas phase. Conservation of mass over the liquid phase yields

$$\frac{\partial \varepsilon_l}{\partial t} + \nabla \cdot \mathbf{v} = S_l^V \tag{9.245}$$

with

$$2FS_l^V = \begin{cases} \left[\bar{V}_e \left(3 - 2t_+^0 \right) - 2\bar{V}_0 \right] j_{PbO_2}^+ + \left[\bar{V}_e \left(2 - 2t_+^0 \right) - \bar{V}_0 \right] j_{O_2}^+ & \forall x \le L_p \\ \bar{V}_e \left(1 - 2t_+^0 \right) j_{Pb}^- + \left[\bar{V}_e \left(2 - 2t_+^0 \right) - \bar{V}_0 \right] j_{O_2}^- + \bar{V}_e \left(2 - 2t_+^0 \right) j_{H_2}^- & \forall x \ge L_p + L_s \end{cases} \tag{9.246}$$

where the source term S_l^V represents electrolyte displacement during battery operation resulting from the change in partial molar volumes between the reactants and products. The electrolyte saturation is defined as

$$s = \frac{\varepsilon_l}{1 - \varepsilon_s} = \frac{\varepsilon_l}{\varepsilon_l + \varepsilon_g} = 1 - \frac{\varepsilon_g}{\varepsilon_l + \varepsilon_g} = 1 - \frac{\varepsilon_g}{1 - \varepsilon_s} \tag{9.247}$$

It is then used to calculate the flow of electrolyte in porous media by Darcy's law:

$$\mathbf{v} = \frac{K k_r}{\mu} \nabla p_c \quad \text{with} \quad k_r = s^n \quad (1 < n < 3) \tag{9.248}$$

where k_r is the relative permeability of the liquid phase and p_c the two-phase capillary pressure expressed in terms of a Leverett function $J(s)$:

$$p_c = \sigma \sqrt{\frac{\varepsilon}{K}} J(s) \Rightarrow \mathbf{v} = \frac{K k_r}{\mu} \sigma \left[\sqrt{\frac{\varepsilon}{K}} J'(s) \nabla s + J(s) \nabla \sqrt{\frac{\varepsilon}{K}} \right] \tag{9.249}$$

In 2003, Srinivasan et al. [71] incorporated the double-layer concept from Newman and Tiedemann's seminal work [54] to simulate the behavior of VRLA cells that are subjected to dynamic operation with charge, rest, and discharge periods on the order of seconds. The transfer current (Equation 9.233) now becomes

$$\nabla \cdot \mathbf{i}_2 = j_a + j_{O_2} + j_{H_2} + j_{dl} \quad \text{with} \quad j_{dl} = a\,C_{dl}\left(\frac{\partial \Phi_1}{\partial t} - \frac{\partial \Phi_2}{\partial t}\right) \tag{9.250}$$

However, Srinivasan et al. [71] use Equation 9.130 in their model despite the fact that they do not take the specific interfacial area as constant. They should use the following preferable expression instead:

$$j_{dl} = C_{dl}\left[a\left(\frac{\partial \Phi_1}{\partial t} - \frac{\partial \Phi_2}{\partial t}\right) + (\Phi_1 - \Phi_2)\frac{\partial a}{\partial t}\right] \tag{9.251}$$

or prove that the second term in the brackets is negligible such as

$$a\left(\frac{\partial \Phi_1}{\partial t} - \frac{\partial \Phi_2}{\partial t}\right) >> (\Phi_1 - \Phi_2)\frac{\partial a}{\partial t} \Rightarrow j_{dl} \approx a\,C_{dl}\left(\frac{\partial \Phi_1}{\partial t} - \frac{\partial \Phi_2}{\partial t}\right) \tag{9.252}$$

Bernardi et al. studied the charge kinetics in VRLA cells the following year [72]. Their model is made up of Equations 9.131, 9.163, 9.203, 9.204, 9.233, 9.239, and 9.240. The overall liquid-phase material balance (Equation 9.205) for the negative electrode now becomes

$$\frac{\partial \varepsilon_l}{\partial t} - \frac{\bar{V}_A}{2F}\left(1 - 2t_+^0\right) j_{Pb}^- - \frac{\bar{V}_A - \bar{V}_0}{2F} j_{O_2}^- - \frac{\bar{V}_A}{2F} j_{H_2}^- = 0 \tag{9.253}$$

The $PbSO_4$ dissolution-transport mechanism is used to derive the kinetic expression for Reaction 9.146: dissolution of $PbSO_4$ (Reaction 9.154), diffusion of Pb^{2+} to an electrochemical reaction site, and electrochemical conversion to active material (Reaction 9.224). The rate of this reaction may be generalized to both electrodes as

$$j_a = \frac{a_a i_0 \left\{\exp\left[\frac{(1-\alpha)nF}{RT}\eta_s\right] - \exp\left[-\frac{\alpha nF}{RT}\eta_s\right]\right\}}{1 + \left[\frac{l_{Pb^{2+}}}{D_{Pb^{2+}}} + \frac{a_a}{a_b k_b}\right] k_{0,a} \exp\left(-\frac{\alpha nF}{RT}\eta_s\right)} \tag{9.254}$$

where the diffusion length $l_{Pb^{2+}}$ is related to the characteristic dimensions of $PbSO_4$ particles with the expression

$$l_{Pb^{2+}} = \left[\frac{M_b(q_{v,\max} - q_{v,0})}{2F\rho_b N_{ppt}}\right]^{1/3} - \left[\frac{M_b(q_{v,\max} - q_v)}{2F\rho_b N_{ppt}}\right]^{1/3} \tag{9.255}$$

and

$$\frac{a_a}{a_{a,\max}} = \left(\frac{q_v}{q_{v,\max}}\right)^{2/3} - \frac{N_{ppt}^{1/3}}{a_{a,\max}}\left(\frac{M_b\, q_{v,\max}}{2F\rho_b}\right)^{2/3}\left(\frac{q_{v,\max} - q_v}{q_{v,\max}}\right)^{2/3} \tag{9.256}$$

The first term on the right side of Equation 9.256 represents the surface area of active material particles as a function of SOC. The second term subtracts from this surface area the area that is covered by cubic $PbSO_4$ particles. The expression for a_b

$$\frac{a_a}{a_b} = \frac{1}{5}\left[\frac{a_{a,\max}}{N_{ppt}^{1/3}}\left(\frac{M_b q_{v,\max}}{2F\rho_b}\right)^{2/3}\left(\frac{q_v}{q_{v,\max} - q_v}\right)^{3/2} - 1\right] \tag{9.257}$$

follows from the same arguments. The following solid-state mechanism is also proposed for Reaction 9.142: disassociation of water

$$H_2O \rightarrow 2H^+ + O^{2-} \tag{9.258}$$

diffusion of O^{2-} toward the oxidation site, and oxidation involving two one-electron steps (*i*) and (*ii*) giving rise to the overall reaction

$$PbSO_4 + 2O^{2-} \rightarrow PbO_2 + SO_4^{2-} + 2e^- \tag{9.259}$$

The rate of this reaction may be expressed as follows:

$$j_{PbO_2}^{+} = a^{+} i_{0,ref}^{ii,+}\left(\frac{c_A}{c_{A,ref}}\right)^{\gamma_{PbO_2}} \frac{\exp\left[\frac{(2-\alpha^{ii,+})nF}{RT}\eta_s^{+}\right] - \exp\left[-\frac{\alpha^{ii,+}nF}{RT}\eta_s^{+}\right]}{1 + \frac{i_{0,ref}^{ii,+}}{i_{0,ref}^{i,+}}\exp\left[\frac{(1-\alpha^{ii,+}+\alpha^{i,+})nF}{RT}\eta_s^{+}\right]} \tag{9.260}$$

The authors assume ideal gas and valve behaviors:

$$p_{vent} > p_{amb} \Rightarrow \begin{cases} p_g < p_{vent} \Rightarrow v_{flow} = 0 \\ p_g = p_{vent} \Rightarrow v_{flow} > 0 \end{cases} \tag{9.261}$$

where v_{flow} is the molar gas flow rate:

$$v_{flow} = \frac{1}{RT}\frac{\partial}{\partial t}\left(V_g^{tot} p_{vent}\right) + \frac{1}{2F}\iiint_{V_{cell}}\left(\frac{1}{2} j_{O_2} + j_{H_2}\right) dx\, dy\, dz \tag{9.262}$$

They also assume that the gas within the cell case is well mixed so that the composition within the cell case is the same as that in the vent gas stream. The material balance (Equation 9.211) on the gaseous O_2 thus becomes

$$\frac{\partial N_{O_2}}{\partial t} = \frac{1}{4F}\iiint_{V_{cell}} j_{O_2}\, dx\, dy\, dz - N_{O_2}\frac{v_{flow} RT}{V_g^{tot} p_{vent}} \tag{9.263}$$

The H_2 and inert gas compositions, respectively, are obtained from

$$\frac{\partial N_{H_2}}{\partial t} = \frac{1}{2F}\iiint_{V_{cell}} j_{H_2}\, dx\, dy\, dz - n_{H_2}\frac{v_{flow} RT}{V_g^{tot} p_{vent}} \tag{9.264}$$

and

$$\frac{\partial N_{inert}}{\partial t} = -N_{inert}\frac{v_{flow} RT}{V_g^{tot} p_{vent}} \tag{9.265}$$

Five years later, a mathematical model for a LAB was developed by Boovaragavan et al. with due consideration given to the corrosion process that occurs at the interface between the active material and grid material of the positive plate [73]. The relationship (Equation 9.207) between a and the amount of conductive material (Pb or PbO_2) available in the electrode is slightly modified:

$$a = a_{\max}\left(1 - \frac{q_v}{q_{v,\max}}\right)\left(\frac{q_v}{q_{v,\max}}\right)^{\zeta} \quad \text{with} \quad \frac{q_v}{q_{v,\max}} = \frac{\varepsilon - \varepsilon_0}{\varepsilon_{\max} - \varepsilon_0} \tag{9.266}$$

Three different modeling approaches are used to incorporate the effect of corrosion in the model and to examine the effects of corrosion during discharge, rest, and charge processes. First, the electronic conductivity of the positive plate is empirically expressed as a function of N_{cyc}, the number of cycles:

$$\sigma^{+}_{PbO_2} = KN^{n}_{cyc} \tag{9.267}$$

where K and n are empirical constants. Next, a current–resistance loss term to account for the increase in electronic resistance due to the formation and growth of a passive corrosion layer is considered:

$$\eta_s^+ = \Phi_1 - \Phi_2 - U_{PbO_2}^+ - R_c \frac{j_{PbO_2}^+}{a_{PbO_2}^+} \tag{9.268}$$

where R_c is the additional resistance to electron conduction due to the corrosion layer buildup. Finally, the corrosion phenomenon is incorporated as a side reaction occurring in the positive plate:

$$Pb + 2H_2O \rightarrow PbO_2 + 4H^+ + 4e^- \tag{9.269}$$

To incorporate the effect of the side reaction into the electrochemical kinetics of the main reactions, a modification to the Butler–Volmer electrochemical kinetic expression is introduced:

$$\nabla \cdot \mathbf{i}_2 = j_{PbO_2}^+ + j_c \quad \text{with} \quad j_c = a_{PbO_2}^+ i_{0,c}^+ \exp\left[\frac{(1-\alpha^+)\, n_c F}{RT}\eta_c\right] \tag{9.270}$$

In the same year as Boovaragavan et al.'s work, Cugnet et al. developed a model running under MATLAB on a laptop that is able to simulate new and aged automotive LABs [74]. The interfacial active area of both electrodes is defined by

$$a = a_{\max} \exp\left(\zeta \frac{\varepsilon_{\max} - \varepsilon_0}{\varepsilon - \varepsilon_{\max}}\right) \tag{9.271}$$

in the charge regime and

$$a = a_{\max}\left[1 - \exp\left(-\zeta \frac{\varepsilon - \varepsilon_0}{\varepsilon_{\max} - \varepsilon_0}\right)\right] \tag{9.272}$$

in the discharge and rest regimes. The model is used to investigate the limitation of the available capacity at high rates by looking at the acid concentration depletion in the positive electrode and simulating the battery performance in galvanostatic discharges from C/20 to 20C. The model simulations are in accordance with Peukert's law. Cugnet et al.'s work demonstrates that a fully charged used battery is definitely not equivalent to a partially discharged new one, and each aging is unique, even if it is possible to observe some similarity for those operating in the same conditions. The two main aging phenomena affecting automotive batteries (anodic corrosion and irreversible sulfation) are taken into account by changing two model parameter values (grid resistance and active surface area), respectively. These parameter value

changes can be used either to simulate the performances of various used batteries or to diagnose the battery SOH.

9.7 OTHER MODELS

9.7.1 Thermal Models

By thermal models, we refer here to models dealing only with thermal effects and nothing else, since we have previously presented many models where the thermal effects were already taken into account.

VRLA batteries employ oxygen recombination technology and they generate more heat than flooded batteries during overcharging. In a tightly packed arrangement, the battery temperature can be considerably higher than the ambient temperature. Operating at high temperature accelerates water loss and reduces battery life. One method of solving this problem is to use a temperature compensation device that regulates (lowers) the float voltage with increasing battery temperature. To verify the benefits of a temperature compensation device, a thermal model developed by Ng and Wolf is used to predict the battery temperatures of a tightly packed battery frame [75]. The frame shows two 48-V strings that are exposed to ambient air on three sides. Each battery in the frame consists of three modular cells connected in parallel. The model, as shown in Figure 9.23, determines the steady-state temperature of each battery in the frame by balancing the dissipated power of the battery with the heat transferred to the air, and by using the battery conduction thermal resistance. This model accounts for (1) the increase in power loss as the battery temperature rises, (2) the conduction

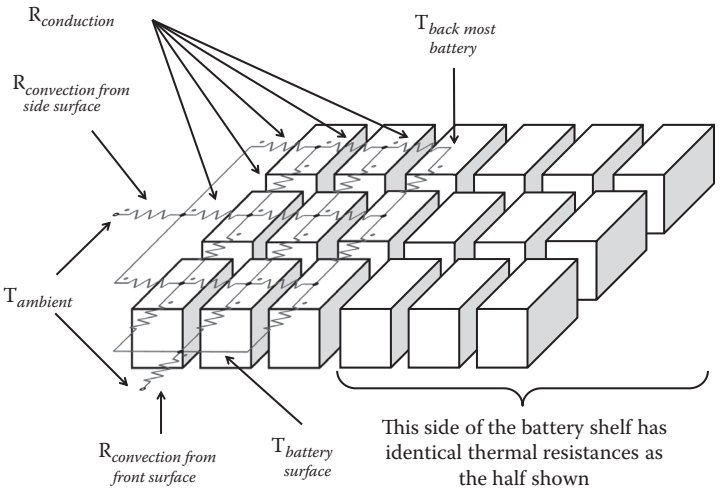

FIGURE 9.23 Schematic of the thermal resistances model of Ng and Wolf. (From Ng, P. K., and Wolf, K., Effect of temperature compensation on battery temperature as predicted by a thermal model. In *Proc. 18th IEEE Int. Telecommunications Energy Conf.*, pp. 33–38. Boston, 1996.)

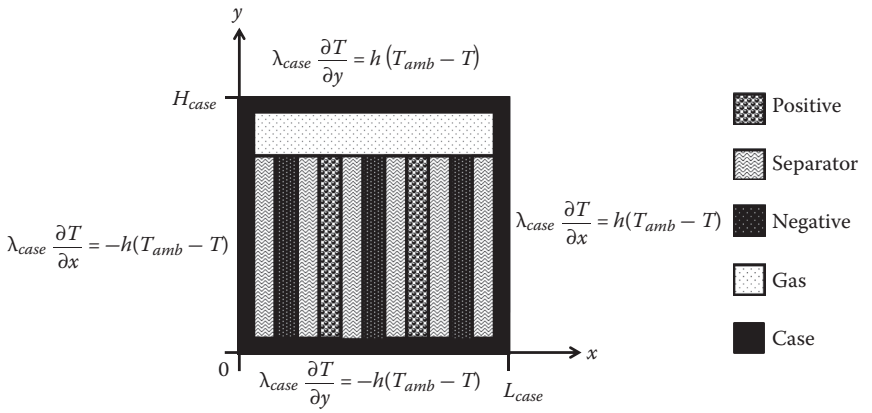

FIGURE 9.24 Schematic of the thermal model for a single cell by Huang and Nguyen. (From Huang, H., and Nguyen, T. V., *Journal of the Electrochemical Society* 144, 2062–2068, 1997.)

between the batteries on each shelf, (3) the convection from each shelf to the ambient air, and (4) the increase in local air temperature from shelf to shelf.

A two-dimensional time-dependent thermal model has been developed by Huang and Nguyen to predict the steady and transient behavior of VRLA batteries under overcharge conditions [76]. Figure 9.24 shows the 2D thermal model of a 2-V cell, which consists of several repeating units of electrode plates and separators, the case, and the gas volume. The thermal properties of both electrodes and the separator are defined as follows:

$$\lambda_p = \lambda_{PbO_2}(1-\varepsilon_p) + \lambda_e \varepsilon_p \tag{9.273}$$

$$\lambda_s = \lambda_{mat}(1-\varepsilon_s) + \lambda_{O_2}\varepsilon_s f_{wl} + \lambda_e \varepsilon_s (1-f_{wl}) \tag{9.274}$$

$$\lambda_n = \lambda_{Pb}(1-\varepsilon_n) + \lambda_e \varepsilon_n \tag{9.275}$$

$$(\rho C_p)_p = (\rho C_p)_{PbO_2}(1-\varepsilon_p) + (\rho C_p)_e \varepsilon_p \tag{9.276}$$

$$(\rho C_p)_s = (\rho C_p)_{mat}(1-\varepsilon_s) + (\rho C_p)_{O_2}\varepsilon_s f_{wl} + (\rho C_p)_e \varepsilon_s (1-f_{wl}) \tag{9.277}$$

$$(\rho C_p)_n = (\rho C_p)_{Pb}(1-\varepsilon_n) + (\rho C_p)_e \varepsilon_n \tag{9.278}$$

where ε_p, ε_s, and ε_n are the porosities of the positive electrode, separator, and negative electrode, respectively. The water loss fraction based on the total liquid volume of a new battery is denoted as f_{wl}. The model is governed by the heat equation

$$\forall_i = \{case, n, s, p, gas\}, \quad (\rho C_p)_i = \lambda_i \nabla^2 T + q_{h,i}(T) \tag{9.279}$$

and the boundary conditions provided in Figure 9.24. Neglecting potential drops in the separator (i.e., it has high conductivity with concentrated acid) and solid phase, the heat generation rate at the electrode is defined by

$$q_h = |j\eta_s| - |j| T \frac{\partial E}{\partial T} \tag{9.280}$$

The authors have found that thermal runaway is a consequence of inappropriate combinations of these parameters: number of cells packed together, case conductivity, heat-transfer coefficient, water-loss fraction, float current, and ambient temperature. The model could be used to help design more thermal-runaway-resistant VRLA batteries.

9.7.2 Hydraulic Models

A well-known hydraulic model of a LAB, the kinetic battery model (KBM), was developed by Manwell and McGowan [77] in the early 1990s and reported on later as a relevant model for stand-alone PV systems by Hansen et al. [78] and also submarines by McGuinness and Benjamin [79]. As illustrated schematically in Figure 9.25, it is made up of two tanks: one holding charge that is immediately available, $Q_1(t)$, and the other holding chemically bound charge, $Q_2(t)$, because the available battery capacity is a nonlinear function of the rate of discharge (as indicated by Peukert's law). Were there just one tank, at any rate of current, it should be possible to drain all of the battery capacity (i.e., the volume of the tank), and the available battery capacity would be a linear function of the rate of discharge, in contrast to what Peukert's law depicts. Therefore, adopting the two-tank model allows one to take into account the active material accessibility, in which $Q_1(t)$ and $Q_2(t)$ represent the electrode surface and bulk, respectively. Accordingly, at a high rate of discharge, the volume $Q_1(t)$

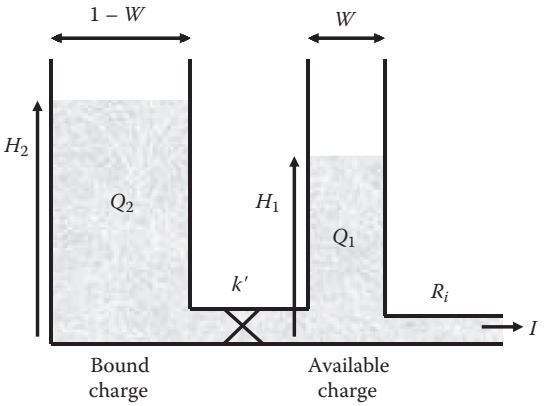

FIGURE 9.25 Schematic of the kinetic battery model of Manwell and McGowan. (From Manwell, J. F., and McGowan, J. G., *Solar Energy* 50, 399–405, 1993.)

decreases faster than $Q_2(t)$, because it is easier to access the surface active material than the bulk. The kinetics that governs the surface versus bulk is depicted by the conductance k' in concert with the experimental data.

The height $H_i(t)$ of both compartments is normalized and the battery SOC is defined by $H_1(t)$. The width of tank 1 ("available") is W, and that of tank 2 ("bound") is $1 - W$. The constant $W \in [0, 1]$ depicts the ratio of the capacity according to the amount of charge that is immediately available with respect to the total charge that could be retained in the battery. The maximum combined volume of the tanks, denoted by $Q_{\max}$, is then equal to the full head of the tanks $H_{\max}$, namely:

$$Q_{\max} = Q_{1,\max} + Q_{2,\max} = WH_{\max} + (1 - W)H_{\max} = H_{\max} \tag{9.281}$$

The equations describing the model are as follows:

$$\frac{dQ_1}{dt} = -I(t) - k'[H_1(t) - H_2(t)] \tag{9.282}$$

$$\frac{dQ_2}{dt} = k'[H_1(t) - H_2(t)] \tag{9.283}$$

where the current $I(t)$ is assumed constant during the time step of interest. The "head" that drives charge flow is $H_1(t) = Q_1(t)/W$ in the outer compartment and $H_2(t) = Q_2(t)/(1 - W)$ in the inner one. The internal resistance of the battery is represented by R_i. For mathematical simplicity, a new rate constant k is defined as

$$k = \frac{k'}{W(1-W)} \tag{9.284}$$

which leads to the following form for the governing equations of the model:

$$\frac{dQ_1}{dt} = -I(t) - k(1-W)Q_1(t) + kWQ_2(t) \tag{9.285}$$

$$\frac{dQ_2}{dt} = k(1-W)Q_1(t) - kWQ_2(t) \tag{9.286}$$

where the current drawn $I(t)$ is also found by simple rearrangement to be

$$I(t) = -\left(\frac{dQ_1}{dt} + \frac{dQ_2}{dt}\right) \tag{9.287}$$

The voltage $u(t)$ is given by

$$u(t) = U_{\min} + \frac{U_{\max} - U_{\min}}{Q_{1,\max}} Q_1(t) - R_i I(t) \tag{9.288}$$

Equations 9.285 and 9.286 can be solved with the help of Laplace transforms to give

$$Q_1(t) = 2W[Q_1(0) + Q_2(0)]\sinh\left(\frac{kt}{2}\right)\exp\left(-\frac{kt}{2}\right) + Q_1(0)\exp(-kt) - W\int_0^t I(\tau)\,d\tau - (1-W)\int_0^t I(\tau)\exp[k(\tau - t)]\,d\tau \tag{9.289}$$

and similarly for $Q_2(t)$.

Manwell and McGowan [77] suggest the problem could be reversed, so that instead of using a constant k to predict $u(t)$ given an $I(t)$, the voltage and currents are used to find $k(t)$. Once a dependable form for $k(t)$ is known, then this can be used to better predict future voltage and current values. From Equation 9.286 we have

$$k(t) = \frac{1}{Q_1(t) - W[Q_1(t) + Q_2(t)]}\frac{dQ_2}{dt} \tag{9.290}$$

and using Equation 9.287 this can be written as

$$k(t) = -\frac{I(t) + \dfrac{dQ_1}{dt}}{Q_1(t) + W\left[\displaystyle\int_0^t I(\tau)\,d\tau - Q_1(0) - Q_2(0)\right]} \tag{9.291}$$

Using Equation 9.288, the final expression is

$$k(t) = -\frac{\dfrac{dV}{dt} + R_i\dfrac{dI}{dt} + \dfrac{U_{\max} - U_{\min}}{Q_{1,\max}}I(t)}{u(t) - U_{\min} + R_i I(t) + W\dfrac{U_{\max} - U_{\min}}{Q_{1,\max}}\left[\displaystyle\int_0^t I(\tau)\,d\tau - Q_1(0) - Q_2(0)\right]} \tag{9.292}$$

Thus, theoretically, given data for $u(t)$ and $I(t)$ and the various parameters, $k(t)$ can be found. However, the data for $u(t)$ and $I(t)$ must be suitable for differentiation and integration, which will usually require the fitting of splines through the data. Care must be taken to make sure the approximation spline accurately represents the data, while still allowing relatively smooth and continuous derivatives. The KBM can be used by nonexperts who are looking for a simple LAB model for storage applications, where the fluctuations of rate are less of a concern. However, this kind of model is obviously too simple to offer sufficient accuracy under a dynamic situation.

9.7.3 Stochastic Models

Contrary to most of the models, which are deterministic (i.e., dealing with a solo possible "reality" of how the model might evolve with time), a stochastic model provides some indeterminacy in its future evolution, as described by a probability distribution. This means that even if the initial condition (or starting point) is known, there are many possibilities the model might go to, and some paths are more probable than others. A stochastic model is used to account for the uncontrollable aspects of LABs, even if they are from the same batch, and can also address the reproducibility issues for testing. The cell behavior is represented as a discrete time transient stochastic process that tracks the SOC. The smallest amount of capacity that may be discharged is a charge unit. Each fully charged cell is assumed to have a maximum available capacity of M charge units and a nominal capacity of N charge units ($N < M$).

The stochastic model developed by Panigrahi et al. focuses on the recovery effect that is observed when relaxation times are allowed in between discharges [80]. Figure 9.26 shows a graphical representation of the process. At each time unit, the SOC decreases from state i to the state $i - j$, if j charge units are demanded from the battery. Otherwise, if no charge units are demanded, the battery may recover from its current SOC (i) to a higher SOC (greater than i). The stochastic process starts from the state of full charge N, and terminates when the state 0 is reached, or the maximum available capacity M is exhausted. By allowing idle periods in between discharges, the battery can partially recover its charge during the idle times, and thus a number of charge units greater than N can be drained before reaching the state 0. In one time unit, called a slot, q_j is the probability that j charge units are demanded and q_0 the probability that an idle slot occurs (the cell recovers one charge unit or remains in the same state). The recovery effect is represented as a decreasing exponential function of the SOC. The model is fast and reasonably accurate but not sensitive enough to predict the experimental observations.

In 2005, Rao et al. modeled the battery discharge as a three-dimensional Markov process (i, j, t), which is a stochastic extension of the KBM (Figure 9.25) with certain refinements and additional parameters for accuracy [81]. Parameters i and j as explained earlier are the amount of charge stored in the available and bound charge

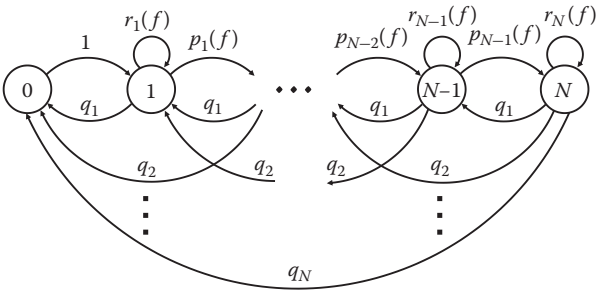

FIGURE 9.26 Stochastic process from Panigrahi et al. representing cell behavior. (From Panigrahi, D. et al., Battery life estimation of mobile embedded systems. In *Proc. 14th Int. Conf. on VLSI Design*, pp. 57–63. Bangalore, India, 2001.)

wells, respectively; t is the length of the current idle slot, that is, the time since some current was drawn from the battery previous to the current moment; and q_I is the probability that in one time slot, I charge units are demanded. This is modeled as follows: I charge units per unit time are drawn from the available charge well, while some charge J is being transferred or replenished by the bounded charge well, to the available charge well. The quanta (Q) of charge the battery may recover during a given idle slot depends on H_1, H_2, and the granularity of time. The value of Q is calculated as the charge recovered for an infinitely long idle slot leads to $H_1 = H_2$. If there is no recovery, then there will be no change in the values of parameters i and j, while t is incremented by one for the next successive idle slot. The transitions can be summarized as follows:

$$(i,j,t) \rightarrow \begin{cases} (i-Q, j-Q, t+1) \\ (i,j,t+1) \\ (i-I+J, j-J, 0) \end{cases} \quad \text{with} \quad J = k' H_2 (H_2 - H_1) \tag{9.293}$$

9.7.4 Bond Graph Models

An interesting alternative for battery modeling is the bond graph technique. A bond graph is a graphic representation of a dynamic physical system based on energy conservation principles. It depicts a bidirectional energy flow, based on continuity of power, among components in a dynamic system. The bond graph exhibits a number of advantages over conventional block diagram-based computer simulation techniques. It allows the development of a dynamic model from complicated physical domains, particularly when each of the domains has its own characteristics that cannot be easily merged with others in a simple mathematical framework. This is especially useful for HEV simulation, for which it is necessary to integrate a battery model with other more complex and multidisciplinary (mechanical, electrical, electromechanical, hydraulic, etc.) ones, such as those of engine, clutch, gearbox, chassis, and other powertrain components.

A bond graph model of a LAB has been developed by Esperilla et al. to predict how reproducible the behavior of electrochemical cells is during charging or discharging conditions [82]. The model considers each half-cell independently. For each half-cell the main electrode reaction and the electrolysis reaction of water are considered (i.e., the hydrogen evolution reaction in the negative electrode and the oxygen evolution reaction in the positive electrode). Electrochemical principles are considered to account for the main phenomena that appear in the battery, like the equilibrium potential, and the overpotential, modeled by means of the activation or charge transfer and the diffusion mechanisms. Each of these phenomena is modeled with bond graph elements and structures, showing the correspondence between the bond graph elements and its physical interpretation in this field. First, an isothermal model was developed in order to show the behavior of the main phenomena. A more complex model was then developed that includes thermal behavior. This model is very useful in the case of traction batteries in electrical and hybrid vehicles

where high current intensities appear. Some simulation results are also presented in Esperilla et al.'s work to show the accuracy of the proposed models and the impact of thermal effects on the battery behavior [82].

9.8 CONCLUSION

The LAB has a long history of success in commercial applications, often being considered as a matured battery technology. Nonetheless, the understanding of fundamental aspects of the electrochemistry remains incomplete for a reliable design and manufacturing. This assertion was evident from the observations on LAB modeling, where basic parameters for a successful electrochemical model remain empirical. Many approximations used in the modeling populate in the literature. No other battery technology has been modeled with so many diverse approaches mainly because none of them can claim complete success.

One underlying truth is that models and simulations are tools to assist us enhance our understanding of the system. Despite the fact that we still lack of detailed basic understanding of the electrochemical and engineering aspects with LAB, and therefore simple parameters can be determined unambiguously to plug into the models and get realistic results, we remain hopeful that through modeling and simulation, we can continue to transfer the most of the existing knowledge to assist those who are interested in using the knowledge to their applications. By applying LAB simulation, they can select the most appropriate modeling tool to increase the possibilities and success rates in their applications. Various types of models are summarized in Table 9.3 with the following criteria for consideration:

- Required experience in LAB design and knowledge of battery performance characteristics (in reference to the associated physics and electrochemistry);
- Packaging adaptability of the model for mobile and/or real-time applications;
- Ease in the model development (from its design to its parameter identification);
- Expectation in reliability and accuracy of the model and prediction;
- Amount of data necessary to build the model and obtain simulation results with the desired accuracy.

TABLE 9.3
Characteristics of Various Lead-Acid Battery Models

Models	LAB Experience	Adaptability for Inline Use	Ease of Development	Reliability and Accuracy	Data Requirement
ANN	Minimal	Difficult	Quite easy	Reasonable	High
FL	Lesser degree	Rather easy	Relatively easy	Reasonable	High
Empirical	Some	Very easy	Easy	Good	Demanding
Electrical	Sufficient	Easy	Very easy	Very good	Less demanding
Electrochemical	Significant	Very hard	Very hard	Reasonable	Significant

Most of the LAB models are mainly used in deriving solutions for SOC and SOH monitoring in response to present and future energy management needs. Therefore, most of the models are electrical or empirical in nature due to the expectations in applicability, reliability, and accuracy. In the last decade, a significant number of studies have been devoted to the effort of deriving solutions for SLI, EV, and HEV applications. To date, the latter represents a growing demand in the automotive industry. Although many think that the LAB technology might be unfit for HEV applications, LAB is still cost-competitive with room for improvements, as shown by the recent demonstration of the UltraBattery® and its kin. In the near future, LAB probably will remain as the most used system, while it continues to be a cost-effective power source for many applications including electrical energy storage.

NOMENCLATURE

A	age of battery (years) or surface area (m^2)
a	specific interfacial area (m^{-1})
C	electrical capacitance (F)
C_{dl}	specific capacitance of the electric double layer ($F \cdot m^{-2}$)
C_p	heat capacity or thermal capacity ($J \cdot K^{-1}$)
c_i	concentration of species i ($mol \cdot m^{-3}$)
D	diffusion coefficient of electrolyte ($m^2 \cdot s^{-1}$)
D_a	dispersion coefficient ($m^2 \cdot s^{-1}$)
d	mean diameter of the particles making up the electrode (m)
E	electromotive force or OCV (V)
E_A	activation energy ($J \cdot mol^{-1}$)
F	Faraday constant (96,485 $C \cdot mol^{-1}$)
f	frequency or ANN activation function or electrolyte activity coefficient
f_{sat}	fraction of the separator saturated with acid
f_{wl}	fraction of water lost based on the total liquid volume of a new battery
$\mathbf{g}$	gravitational vector (9.81 $m \cdot s^{-1}$)
H	height of the electrode (m)
H'	dimensionless Henry's constant for oxygen (3.181×10^{-2})
h	sampling time (s) or heat transfer coefficient ($W \cdot m^{-2} \cdot K^{-1}$)
I	constant current (A)
i	variable current (A) or species index or surface current density ($A \cdot m^{-2}$)
i_0	exchange current density ($A \cdot m^{-2}$)
$\mathbf{i}_1$	superficial current density in the solid phase ($A \cdot m^{-2}$)
$\mathbf{i}_2$	superficial current density in the liquid phase ($A \cdot m^{-2}$)
i_n	transfer current per unit of interfacial area ($A \cdot m^{-2}$)
j	imaginary unit ($j^2 = -1$) or volume current density ($A \cdot m^{-3}$)
j_{in}	pore-wall flux of species i ($mol \cdot m^{-2} \cdot s^{-1}$)
K	empirical constant or absolute permeability of the electrode (m^2)
k	sample number
$k_{0,a}$	electrochemical kinetic constant ($m \cdot s^{-1}$)
k_b	rate constant for the dissolution of $PbSO_4$ ($mol \cdot m^{-2} \cdot s^{-1}$)
k_{ppt}	rate constant for the precipitation of $PbSO_4$ ($m \cdot s^{-1}$)

k_r relative permeability
L number of layers of an ANN or inductance (H)
L_i thickness of half an electrode or the separator or the reservoir (m)
l layer of neurons in an ANN or microscopic diffusion length (m)
M_i symbol for the chemical formula or molecular weight of species i ($kg \cdot mol^{-1}$)
m molality ($mol \cdot kg^{-1}$)
N number of neurons in a layer of an ANN or cycles
N_i superficial flux of species i ($mol \cdot m^{-2} \cdot s^{-1}$)
N_a Avogadro's number ($6.0225 \times 10^{23}\ mol^{-1}$)
N_i number of mole of species i
N_p total number of plates in each cell of a battery
N_{ppt} number density of $PbSO_4$ particles (m^{-3})
$\mathbf{n}$ normal unit vector
n Peukert's empirical constant or number of electrons transferred in reaction
n_i surface number density of particles, nuclei, or sites i (m^{-2})
P power (W)
p pressure (Pa)
Q capacity (Ah)
q_h heat-generation rate ($W \cdot cm^{-3}$)
q_s charge per unit surface of an electrode ($C \cdot m^{-2}$)
q_v charge per unit volume of an electrode ($C \cdot m^{-3}$)
R electrical resistance (Ω) or universal gas constant ($8.3145\ J \cdot mol^{-1} \cdot K^{-1}$)
R_c resistance to electron conduction due to the corrosion layer buildup ($\Omega \cdot m^2$)
R_i volumetric production rate of species i by reaction ($mol \cdot m^{-3} \cdot s^{-1}$)
R_T thermal resistance ($K \cdot W^{-1}$)
S source term in conservation equations
s_i stoichiometric coefficient of species i in electrode reaction
T temperature (K) or period (sec)
t time (sec)
t_i^0 transference number of species i with respect to the solvent velocity
U constant voltage or equilibrium potential (V)
u variable voltage or battery voltage (V)
V volume (m^3)
$\overline{V}_i$ partial molar volume of species i ($m^3 \cdot mol^{-1}$)
$\mathbf{v}$ superficial volume-average velocity ($m \cdot s^{-1}$)
v_{flow} molar gas flow rate ($mol \cdot s^{-1}$)
W weight vector or matrix in an ANN or width of the electrode (m)
W_{Joule} heat generated by Joule effect (J)
w weight in an ANN
x normal distance from the center of the PbO_2 electrode (m)
Y output vector or matrix of a neuron layer in an ANN or admittance
y output of a neuron in an ANN
Z impedance
z_i valence or charge number of species i

GREEK LETTERS

α symmetry factor of the charge transfer coefficients
β volume expansion coefficient (m^3·mol)
Γ_i surface concentration of species *i* (mol·m^{-2})
γ learning rate of the BP algorithm or exponent for the concentration dependence of the exchange current density or surface tension (J·m^{-2})
δ capacity loss (Ah)
ε porosity
ε_i volume fraction of species *i*
ζ exponent for the charge dependence of the specific interfacial area
η efficiency
η_s surface overpotential (V)
Θ threshold/bias vector of a neuron layer in an ANN or placeholder for a variable
θ threshold/bias of a neuron in an ANN
κ electrical conductivity of the liquid phase (S·m^{-1})
λ thermal conductivity (W·m^{-1}·K^{-1})
μ viscosity of the electrolyte (Pa·s)
μ_i chemical potential of species *i* (J·mol^{-1})
ν fundamental jump frequency (s^{-1})
ν_i number of moles of ions produced by the dissociation of 1 mol of electrolyte
ρ_i density of species *i* (kg·m^{-3})
σ electrical conductivity of the solid phase (S·m^{-1})
τ time (sec)
Φ electric potential in liquid or solid phase (V)
ω angular frequency (rad·s^{-1})

SUBSCRIPTS AND SUPERSCRIPTS

A sulfuric acid: H_2SO_4
a active materials (Pb or PbO_2)
B lead bisulfate: $Pb(HSO_4)_2$
b $PbSO_4$
c corrosion
e electrolyte
eoc end of charge
eol end of life
ex exponent related to the geometry of the porous electrode
ic intercell connector
lg liquid/gas interface
M intermediate
n negative
O oxidized state
p positive
R reduced state

r	reservoir
rec	recombination
s	separator
t	terminal
the	theorotocal
0	initial value or solvent
+	cation
–	anion

REFERENCES

1. Young, R. E., Li, X., and Perone, S. P. (1996). Prediction of individual cell performance in a long-string lead/acid peak-shaving battery: Application of artificial neural networks. *Journal of Power Sources* **62**, 121–134.
2. Urbina, A., Paez, T. L., O'Gorman, C., Barney, P., Jungst, R. G., and Ingersoll, D. (1999). Reliability of rechargeable batteries in a photovoltaic power supply system. *Journal of Power Sources* **80**, 30–38.
3. Peng, J., Chen, Y., and Eberhart, R. (1999). Battery pack SOC estimator design using computational intelligence approaches. In *Proc. 15th Annual Battery Conf. on Applications and Advances*, pp. 173–177. Long Beach, CA.
4. Chan, C. C., Lo, E. W. C., and Weixiang, S. (2000). The available capacity computation model based on artificial neural network for lead-acid batteries in electric vehicles. *Journal of Power Sources* **87**, 201–204.
5. Shen, W. X., Chan, C. C., Lo, E. W. C., and Chau, K. T. (2002). A new battery available capacity indicator for electric vehicles using neural network. *Energy Conversion and Management* **43**, 817–826.
6. Abolhassani Monfared, N., Gharib, N., Moqtaderi, H., Hejabi, M., Amiri, M., Torabi, F., and Mosahebi, A. (2006). Prediction of state-of-charge effects on lead-acid battery characteristics using neural network parameter modifier. *Journal of Power Sources* **158**, 932–935.
7. Karami, H., Karimi, M. A., and Mahdipour, M. (2006). ANN modeling of cold cranking test for sealed lead-acid batteries. *Journal of Power Sources* **158**, 936–943.
8. Karimi, M. A., Karami, H., and Mahdipour, M. (2007). ANN modeling of water consumption in the lead-acid batteries. *Journal of Power Sources* **172**, 946–956.
9. Shen, W. X. (2007). State of available capacity estimation for lead-acid batteries in electric vehicles using neural network. *Energy Conversion and Management* **48**, 433–442.
10. Yanqing, S. (2010). Adaptive online state-of-charge determination based on neuro-controller and neural network. *Energy Conversion and Management* **51**, 1093–1098.
11. Singh, P., and Reisner, D. E. (2002). Fuzzy logic based state-of-health determination of lead-acid batteries. In *Proc. 24th Annual Int. Telecommunications Energy Conf.*, pp. 583–590. Montreal, QC.
12. Singh, P., and Reisner, D. E. (2002). Development of fuzzy logic-based lead acid battery management techniques with applications to 42V systems. Presented at Advanced Automotive Battery Conference (AABC 02), Las Vegas, NV.
13. Salkind, A. J., Singh, P., Cannone, A., Atwater, T., Wang, X., and Reisner, D. (2003). Impedance modeling of intermediate size lead-acid batteries. *Journal of Power Sources* **116**, 174–184.
14. Malkhandi, S. (2006). Fuzzy logic-based learning system and estimation of state-of-charge of lead-acid battery. *Engineering Applications of Artificial Intelligence* **19**, 479–485.

15. Chekired, F., Mahrane, A., Chikh, M., and Smara, Z. (2011). Optimization of energy management of a photovoltaic system by the fuzzy logic technique. *Energy Procedia* **6**, 513–521.
16. Martinez, J. S., John, R. I., Hissel, D., and Péra, M.-C. (2012). A survey-based type-2 fuzzy logic system for energy management in hybrid electrical vehicles. *Information Sciences* **190**, 192–207.
17. Shepherd, C. M. (1965). Design of primary and secondary cells—II. An equation describing battery discharge. *Journal of the Electrochemical Society* **112**, 657–664.
18. Bode, H. (1977). *Lead-Acid Batteries*. John Wiley & Sons, New York.
19. Cugnet, M., Dubarry, M., and Liaw, B. Y. (2010). Peukert's law of a lead-acid battery simulated by a mathematical model. *ECS Transactions* **25**, 223–233.
20. Sunu, W. G., and Burrows, B. W. (1981). Current density and electrolyte distribution in motive power lead-acid cells. *Journal of the Electrochemical Society* **128**, 1405–1411.
21. Facinelli, W. A. (1983). Modeling and simulation of lead-acid batteries for photovoltaic systems. In *Proc. 18th Intersociety Energy Conversion Engineering Conf.*, pp. 1582–1588. Orlando, FL.
22. Roan, V. P., and Raman, A. (1993). An approach to incorporating age and electrolyte temperature effects on performance simulation of electric/hybrid vehicle batteries. In *Proc. 27th Intersociety Energy Conversion Engineering Conf.*, pp. 2229–2237. San Diego, CA.
23. Copetti, J. B., Lorenzo, E., and Chenlo, F. (1993). A general battery model for PV system simulation. *Progress in Photovoltaics: Research and Applications* **1**, 283–292.
24. Catherino, H. A., Burgel, J. F., Rusek, A., and Feres, F. (1999). Modelling and simulation of lead-acid battery charging. *Journal of Power Sources* **80**, 17–20.
25. Piller, S., Perrin, M., and Jossen, A. (2001). Methods for state-of-charge and their applications. *Journal of Power Sources* **96**, 113–120.
26. Ross, M. M. D. (2001). A simple but comprehensive lead-acid battery model for hybrid system simulation. In *Proc. PV Horizon: Workshop on Photovoltaic Hybrid Systems*. Montreal, QC.
27. Cherif, A., Jraidi, M., and Dhouib, A. (2002). A battery aging model used in stand-alone PV systems. *Journal of Power Sources* **112**, 9–53.
28. Pascoe, P. E., and Anbuky, A. H. (2004). A VRLA battery simulation model. *Energy Conversion and Management* **45**, 1015–1041.
29. Randles, J. E. B. (1947). Kinetics of rapid electrode reactions. *Discussions of the Faraday Society* **1**, 11–19.
30. Rosa, E. B. (1908). The self and mutual inductances of linear conductors. *Bulletin of the Bureau of Standards* **4**(2), 301–344.
31. Appelbaum, J., and Weiss, R. (1982). An electrical model of the lead-acid battery. In *Proc. Int. Telecommunications Energy Conf.*, pp. 304–307. Washington, DC.
32. Buonarota, A., Menga, P., and Scarioni, V. (1987). An electrical model for discharge and recharge of lead-acid batteries, developed for industrial applications. *L'Energia Elettrica* **7–8**, 325–332.
33. Giglioli, R., Pelacchi, P., Raugi, M., and Zini, G. (1988). A state of charge observer for lead acid batteries. *L'Energia Elettrica* **1**, 27–33.
34. Denno, K. (1989). *Power System Design and Applications for Alternative Energy Sources*. Prentice-Hall, Englewood Cliffs, NJ.
35. Giglioli, R., Buonarota, A., Menga, P., and Ceraolo, M. (1990). Charge and discharge fourth order dynamic model of the lead acid battery. In *Proc. Int. Electric Vehicle Symp.*, pp. 371–382. Hong Kong, China.
36. Salameh, Z. M., Casacca, M. A., and Lynch, W. A. (1992). A mathematical model for lead-acid batteries. *IEEE Transactions on Energy Conversion* **7**, 93–97.

37. Bejan, A., and Dan, N. (1997). Maximum work from an electric battery model. *Energy* **22**, 93–102.
38. Mauracher, P., and Karden, E. (1997). Dynamic modelling of lead/acid batteries using impedance spectroscopy for parameter identification. *Journal of Power Sources* **67**, 69–84.
39. Ceraolo, M. (2000). New dynamical models of lead-acid batteries. *IEEE Transactions on Power Systems* **15**, 1184–1190.
40. Barsali, S., and Ceraolo, M. (2002). Dynamical models of lead-acid batteries: Implementation issues. *IEEE Transactions on Energy Conversion* **17**, 16–23.
41. Karden, E., Buller, S., and De Doncker, R. W. (2002). A frequency-domain approach to dynamical modeling of electrochemical power sources. *Electrochimica Acta* **47**, 2347–2356.
42. Yan, Z. (2002). A note on maximum work from an electric battery model. *Energy* **27**, 197–201.
43. Shi, Z., Chen, J., and Wu, C. (2002). Maximum work output of an electric battery and its load matching. *Energy Conversion and Management* **43**, 241–247.
44. Chen, J., Shi, Z., and Chen, X. (2002). The maximum work output of an electric battery in a given time. *Renewable Energy* **27**, 189–196.
45. Buller, S., Thele, M., Karden, E., and De Doncker, R. W. (2003). Impedance-based non-linear dynamic battery modeling for automotive applications. *Journal of Power Sources* **113**, 422–430.
46. Jossen, A., Garche, J., Doering, H., Goetz, M., Knaupp, W., and Joerissen, L. (2005). Hybrid systems with lead-acid battery and proton-exchange membrane fuel cell. *Journal of Power Sources* **144**, 395–401.
47. Thele, M., Buller, S., Sauer, D. U., De Doncker, R. W., and Karden, E. (2005). Hybrid modeling of lead-acid batteries in frequency and time domain. *Journal of Power Sources* **144**, 461–466.
48. Dürr, M., Cruden, A., Gair, S., and McDonald, J. R. (2006). Dynamic model of a lead acid battery for use in a domestic fuel cell system. *Journal of Power Sources* **161**, 1400–1411.
49. Thele, M., Schiffer, J., Karden, E., Surewaard, E., and Sauer, D. U. (2007). Modeling of the charge acceptance of lead-acid batteries. *Journal of Power Sources* **168**, 31–39.
50. Thele, M., Karden, E., Surewaard, E., and Sauer, D. U. (2006). Impedance-based over-charging and gassing model for VRLA/AGM batteries. *Journal of Power Sources* **158**, 953–963.
51. Ferguson, T. R., and Bazant, M. Z. (2012). Nonequilibrium thermodynamics of porous electrodes. *Journal of the Electrochemical Society* **159**, A1967–A1985.
52. Newman, J. S., and Tobias, C. W. (1962). Theoretical analysis of current distribution in porous electrodes. *Journal of the Electrochemical Society* **109**, 1183–1191.
53. Newman, J. S., and Thomas-Alyea, K. E. (2004). *Electrochemical Systems*, 3rd ed. John Wiley & Sons, Hoboken, NJ.
54. Newman, J. S., and Tiedemann, W. (1975). Porous-electrode theory with battery applications. *AIChE Journal* **21**, 25–41.
55. Simonsson, D. (1973). A mathematical model for the porous lead dioxide electrode. *Journal of Applied Electrochemistry* **3**, 261–270.
56. Tiedemann, W. H., and Newman, J. (1979). Mathematical modeling of the lead-acid cell. In *Battery Design and Optimization*, S. Gross, Ed., pp. 23–38. The Electrochemical Society Softbound Proceedings Series, Princeton, NJ.
57. Ekdunge, P., and Simonsson, D. (1985). Recharge kinetics of the porous lead dioxide electrode. I. The effect of structural changes. *Journal of the Electrochemical Society* **132**, 2521–2529.

58. Gu, H., Nguyen, T. V., and White, R. E. (1987). A mathematical model of a lead-acid cell. Discharge, rest and charge. *Journal of the Electrochemical Society* **134**, 2953–2960.
59. Dimpault-Darcy, E. C., Nguyen, T. V., and White, R. E. (1988). A two-dimensional mathematical model of a porous lead dioxide electrode in a lead-acid cell. *Journal of the Electrochemical Society* **135**, 278–285.
60. Ekdunge, P., and Simonsson, D. (1989). The discharge behaviour of the porous lead electrode in the lead-acid battery. II. Mathematical model. *Journal of Applied Electrochemistry* **19**, 136–141.
61. Bernardi, D. M. (1990). Nucleation of lead sulfate in porous lead-acid electrodes. *Journal of the Electrochemical Society* **137**, 1670–1681.
62. Nguyen, T. V., White, R. E., and Gu, H. (1990). The effects of separator design on the discharge performance of a starved lead-acid cell. *Journal of the Electrochemical Society* **137**, 2998–3004.
63. Nguyen, T. V., and White, R. E. (1993). A mathematical model of hermetically sealed lead-acid cell. *Electrochimica Acta* **38**, 935–945.
64. Bernardi, D. M., Gu, H., and Schoene, A. Y. (1993). Two-dimensional mathematical model of a lead-acid cell. *Journal of the Electrochemical Society* **140**, 2250–2257.
65. Bernardi, D. M., and Carpenter, M. K. (1995). A mathematical model of the oxygen-recombination lead-acid cell. *Journal of the Electrochemical Society* **142**, 2631–2641.
66. Gu, W. B., Wang, C. Y., and Liaw, B. Y. (1997). Numerical modeling of coupled electrochemical and transport processes in lead-acid batteries. *Journal of the Electrochemical Society* **144**, 2053–2061.
67. Newman, J., and Tiedemann, W. (1997). Simulation of recombinant lead-acid batteries. *Journal of the Electrochemical Society* **144**, 3081–3091.
68. Tenno, A., Tenno, R., and Suntio, T. (2001). Charge-discharge behaviour of VRLA batteries: Model calibration and application for state estimation and failure detection. *Journal of Power Sources* **103**, 42–53.
69. Tenno, A., Tenno, R., and Suntio, T. (2002). Evaluation of VRLA battery under overcharging: Model for battery testing. *Journal of Power Sources* **111**, 65–82.
70. Gu, W. B., Wang, G. Q., and Wang, C. Y. (2002). Modeling the overcharge process of VRLA batteries. *Journal of Power Sources* **108**, 174–184.
71. Srinivasan, V., Wang, G. Q., and Wang, C. Y. (2003). Mathematical modeling of current-interrupt and pulse operation of VRLA cells. *Journal of the Electrochemical Society* **150**, A316–A325.
72. Bernardi, D. M., Ying, R. Y., and Watson, P. (2004). Study of charge kinetics in valve-regulated lead-acid cells. *Journal of the Electrochemical Society* **151**, A85–A100.
73. Boovaragavan, V., Methakar, R. N., Ramagesigan, V., and Subramanian, V. R. (2009). A mathematical model of the lead-acid battery to address the effect of corrosion. *Journal of the Electrochemical Society* **156**, A854–A862.
74. Cugnet, M., Laruelle, S., Grugeon, S., Sahut, B., Sabatier, J., Tarascon, J.-M., and Oustaloup, A. (2009). A mathematical model for the simulation of new and aged automotive lead-acid batteries. *Journal of the Electrochemical Society* **156**, A974–A985.
75. Ng, P. K., and Wolf, K. (1996). Effect of temperature compensation on battery temperature as predicted by a thermal model. In *Proc. 18th IEEE Int. Telecommunications Energy Conf.*, pp. 33–38. Boston.
76. Huang, H., and Nguyen, T. V. (1997). A two-dimensional transient thermal model for VRLA batteries under overcharge. *Journal of the Electrochemical Society* **144**, 2062–2068.
77. Manwell, J. F., and McGowan, J. G. (1993). Lead acid battery storage model for hybrid energy systems. *Solar Energy* **50**, 399–405.
78. Hansen, A. D., Sørensen, P. E., Hansen, L. H., and Bindner, H. W. (2001). Models for a stand-alone PV system (Annual report). Risø National Laboratory, Roskilde, Denmark.

79. McGuinness, M., and Benjamin, B. (2003). Submarine lead-acid battery performance. In *Proc. Mathematics-in-Industry Study Group*. Adelaide, Australia.
80. Panigrahi, D., Chiasserini, C., Dey, S., Rao, R., Raghunathan, A., and Lahiri, K. (2001). Battery life estimation of mobile embedded systems. In *Proc. 14th Int. Conf. on VLSI Design*, pp. 57–63. Bangalore, India.
81. Rao, V., Singhal, G., Kumar, A., and Navet, N. (2005). Battery model for embedded systems. In *Proc. 18th Int. Conf. on VLSI Design*, pp. 105–110. Kolkata, India.
82. Esperilla, J. J., Félez, J., Romero, G., and Carretero, A. (2007). A model for simulating a lead-acid battery using bond graphs. *Simulation Modelling Practice and Theory* **15**, 82–97.

10 Applications of Lead-Acid Batteries

Zhongqi Li and Yufeng Zhang

CONTENTS

10.1 INTRODUCTION

The lead-acid battery has an application history of more than a century since it was invented. As a practical power source for many applications, great technological advances and breakthroughs have been achieved since its invention, and humans have benefited from its maturity, reliability, safety, and low cost. Today its use continues to expand into many new areas.

Regarding lead-acid batteries, their application fields are the widest among other kinds of batteries. The applications for lead-acid batteries are summarized in Figure 10.1 [1]. Note that the largest user of lead-acid batteries is the automotive industry. More than 600 million batteries are provided for a variety of vehicles, including automobiles, forklifts, golf carts, scooters, and so on. The other large user is the electricity storage industry, in which lead-acid batteries provide backup power for telecommunications, data storage, and emergencies.

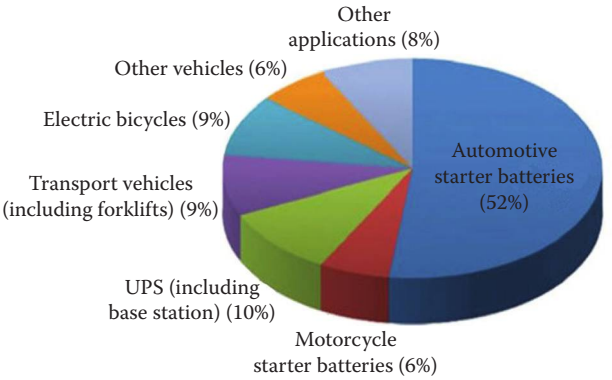

FIGURE 10.1 Lead-acid battery market application category ratio. (Available at http://www.systems-sunlight.com/blog/global-lead-acid-battery-market-development-status.)

Different applications require different energy ranges of the lead-acid batteries. Table 10.1 lists the possible application energy ranges of lead-acid batteries [2].

In industry, lead-acid battery applications can be cataloged into two major areas: stationary applications and automobile applications. These two application areas are discussed in detail in this chapter.

TABLE 10.1
Possible Application Energy Ranges of Lead-Acid Batteries

Type of Lead-Acid Battery	Energy Range	Application Area
Battery for portable equipment	2–100 Wh	Flashlights, toys, power tools, portable radios and TVs, mobile phones, camcorders, laptop computers, memory refreshing, instruments, cordless devices, wireless peripherals, and emergency beacons
Starting, lighting, and ignition batteries	100–600 Wh	Cars, trucks, buses, lawn mowers, wheelchairs, and robots
Vehicle traction battery	20–630 kWh	Electric vehicles (EVs), hybrid EVs (HEVs), plug in hybrid EVs (PHEVs), forklift trucks, milk floats, locomotives
Stationary battery	250 Wh–5 MWh	Emergency power, local energy storage, remote relay stations, communication base stations, and uninterruptible power supplies (UPS)
Military and aerospace battery	Wide range	Satellites, munitions, robots, emergency power, and communications
Special-purpose battery	3 MWh	Submarines and aircraft
Load-leveling battery	5–100 MWh	Spinning reserve, peak shaving, and load leveling

Source: Available at http://www.mpoweruk.com/applications.htm.

10.2 LEAD BATTERIES IN APPLICATIONS

10.2.1 Types of Lead-Acid Batteries

The many different types of lead-acid batteries on the market are used for various applications. The major types of lead-acid batteries can be described as follows [3]:

1. *Valve-regulated lead-acid (VRLA) batteries.* Also called *sealed lead-acid (SLA) batteries*, the VRLA batteries can prevent electrolyte evaporation loss, spillage, and gassing, which leads to a prolonged maintenance-free life span. The top of the battery has a capped vent that is used for the escape of gas. It also has some pressure valves that can open only under extreme conditions. This type of battery uses a specially designed electrolyte to reduce the release of gases such as oxygen and hydrogen generated by the side reactions that occur during charging. A recombinant system with a catalyst inside the battery is needed to facilitate the combination reaction between hydrogen and oxygen to recombine into water. This type of battery is normally safer than other types because the acid electrolyte spoilage is eliminated. This type of battery is used mainly in automobiles.
2. *Absorbed glass mat (AGM) batteries.* Also known as *absorptive glass microfiber (AGMF) batteries*, this type of battery belongs to the class of VRLA batteries, but it has a boron silicate fiber glass mat that acts as a separator between the electrodes, which can absorb the free electrolyte in much the same way a sponge absorbs water. This separator can promote recombination of the hydrogen and oxygen produced during the charging process. The fiber glass mat can absorb and immobilize the acid in the mat as a form of liquid rather than a gel form, therefore, there is no gel electrolyte in this type of battery. Furthermore, in the presence of such a mat separator, the acid electrolyte is more readily available to the plates, allowing for faster reactions between the acid and the plate material, resulting in higher charge–discharge rates as well as deep cycling. In addition, because the electrolyte is kept inside the mat separator, the battery is more robust and able to withstand severe shock and vibration without leakage even if the case is cracked. To realize this, the fiber glass mat separator is normally 95% saturated with sulfuric acid with excess electrolyte. For this reason, AGM batteries are also sometimes called “starved electrolyte” or “dry” batteries.
3. *Gel batteries.* This type of battery also belongs to the class of VRLA batteries. The acid electrolyte is in the form of a gel, however, rather than mobile liquid, which promotes oxygen recombination. In addition, batteries that use a gel as the electrolyte are more robust.
4. *Starting, lighting, and ignition (SLI) batteries.* SLI batteries are specially designed for automobile starting-lighting-ignition applications. The design does not allow the battery to be discharged below 50% depth of discharge (DOD) because discharging below these levels could damage the plates and shorten battery life. In general, automotive batteries are always fully charged before starting the car. After starting the vehicle, the lost charge,

typically 2% to 5% of the charge, is immediately replaced by the alternator and the battery returns to the fully charged state.

5. *Deep-cycle batteries.* Deep-cycle batteries are designed to be completely discharged before recharging. This is required by applications such as marine applications, golf carts, forklifts, and electric vehicles, where the batteries could be deeply cycled. In this deep-cycling process, excessive heat is produced, which can warp the plates. Therefore, thicker and stronger or solid plate grids are normally used for deep-cycle applications.

10.2.2 Typical Commercially Available Battery Units

Based on battery capacity, three types of lead-acid battery units are commercially available for different applications, as shown in Figure 10.2 [4–6]. The first type of unit is a large-sized battery with a capacity range of 100 to 3600 Ah (the open circuit voltage [OCV] is normally ~2.0 V), the second one is a medium-sized battery with a capacity range of 40 to 200 Ah (OCV is ~12.0 V), and the third one is a small-sized battery with a capacity range of 2 to 40 Ah (OCV is ~6.0 V). Depending on the power requirements of the application, different types of lead-acid batteries and/or their combinations can be used.

10.2.3 Use Pattern of Lead-Acid Batteries

As mentioned earlier, the battery products such as VRLAs can come in the form of a single cell, although this is rare and tends to exist in very small size. Most products on the market are 6- or 12-V batteries, which can be used directly or can be assembled into higher-voltage packages. Larger batteries can be built up using series, parallel, series-parallel, or matrixed connections among many small batteries, as shown in Figure 10.3 [7].

Note that one of the major performance issues for lead-acid batteries, particularly valve-regulated lead acid (VRLA) battery, is that the individual cells do not behave

FIGURE 10.2 (a) MSE lead-acid battery (MSE-1200AT [2 V, 1200 Ah]) (From Y. Onoda, *Journal of Power Sources*, 88 (1), 101–107, 2000.); (b) AGM battery (12 V, 120 Ah) (Available at http://it.made-in-china.com/co_sunbrightpower/product_12V120ah-Medium-Size-Maintenance-Free-AGM-Battery_eynnyogeg.html.); (c) ADT security batteries (6 V, 12 Ah). (Available at http://www.powerstridebattery.com/alarm-batteries/adt-security-batteries.)

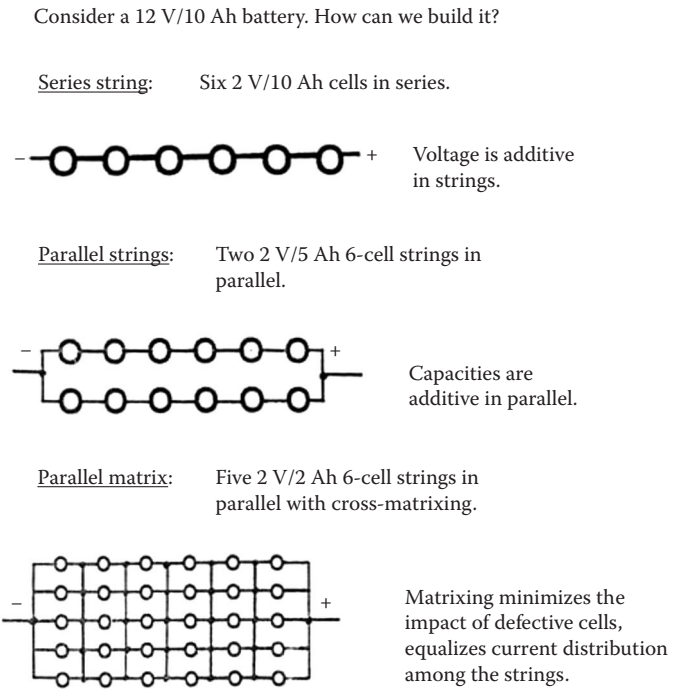

FIGURE 10.3 Battery configurations for charging. (From R. F. Nelson, *Lecture Course on VRLA*, Beijing, China, 2003.)

the same under either float or cyclic charging conditions. This cell-to-cell variance is largely due to the "almost starved/almost floated" knife edge, in which the separator plays a key role. Because of its random-mat nature, the structure of the separator may not be the same from one cell to another, and thus electrolyte movement and gas-channel formation will vary accordingly. Furthermore, because of the manufacturing tolerances, it is virtually impossible to build batteries with all cells having the same percentage of void space. As a result, some cells will behave more like a floated lead-acid entity and the others will recombine to beat the band—both in the same battery.

To address this challenge, the most likely solution will be to develop radically different charging methods that can overcome these cell-to-cell variances. For example, the VRLA batteries can be charged in a fairly aggressive manner on an intermittent schedule.

Because the separator is so critical to a uniform cell-to-cell performance, using the wrong type of separator can severely compromise performance. Normally, deep-cycling and large/tall batteries should use high-surface-area separators to minimize stratification. On the other hand, batteries should employ a low-surface-area glass as the separator, in order to provide more electrolytes for the negative plate, which is capacity limiting under these conditions. Batteries that operate for long lifetimes in hot environments (such as UPS and or telecommunications applications) may require a more acid-resistant glass fiber mix in order to maintain their integrity throughout

their design life. Therefore, different applications may need different batteries with targeted separators. For example, UPS batteries, which need to provide short, high-discharge-rate service, could be better served by a low-surface-area glass.

10.2.4 Charge–Discharge Procedures of Lead-Acid Batteries

In some applications such as automobile SLI processes, the lead-acid battery is charged intermittently between high-rated discharges. In some applications such as electric vehicles and in handheld home devices (e.g., vacuums, toothbrushes, cellphones, and razors), the battery is charged fairly regularly and then subjected to a deep-discharge duty cycle usually at low current drain rates. In other applications such as for backup power, the battery is not charged and discharged regularly; and in some applications such as hybrid electric vehicles and grid-scale electric storage, the battery is charged at a high rate with a partial state-of-charge operation (HRPSOC) [8]. Therefore, different applications have different charge–discharge procedures.

10.3 NONAUTOMOBILE APPLICATIONS OF LEAD-ACID BATTERIES

The three major types of nonautomobile applications in which lead-acid batteries play important and necessary roles are (1) stationary applications for large-scale electricity storage; (2) standby applications for UPS, telecommunications, and emergency lighting; and (3) backup power applications.

10.3.1 Stationary Applications of Lead-Acid Batteries [9–11]

In stationary applications of large-scale electricity storage, lead-acid batteries are the dominating devices, including both flooded and VRLA batteries. Normally, in such applications, the battery's size and weight as well as limited cycle life seem not to be the major concerns. Particularly, the limited cycle seems not to be a major issue because the batteries are almost never deeply discharged. Large-scale stationary flooded battery systems are the most mature systems that are both reliable and economic. However, they need regular maintenance in the form of checking the electrolyte level and adding water. VRLA batteries have also been used for large-scale electricity storage, and they are normally cost effective because of their maintenance-free qualities.

Regarding the application of stationary lead-acid batteries for grid electricity storage, the battery systems are mainly used for load leveling. In particular, the renewable energy sources such as wind and solar do not provide a steady stream of power, so large energy storage batteries such as lead-acid batteries are needed to provide seamless grid service. Currently, most of the energy storage batteries used in a grid are lead-acid batteries that can store more than 0.5 MW (0.5 to 20 MW; see Table 10.2) of electricity. In grid battery operation, the battery management system (BMS) can keep the battery system at 50% charge so that the system can absorb electricity from wind gusts and then deliver it to high load demands. Regarding the response time of the system, a modern BMS can switch from charge to discharge in less than a second, which can help stabilize the voltage on transmission lines.

TABLE 10.2
Examples of Installed Large-Scale Lead-Acid Batteries for Energy Storage

Name	Application	Operational Dates	Power	Energy	Battery Type	Cell Size and Configuration	Battery Manufacturer
Crescent Electric Membership Cooperative (now Energy United) BESS, Statesville, NC, USA	Peak shaving	1987–May 2002	500 kW	500 kWh	Flooded lead-acid	7080 cells in 12 parallel strings of 590 cells each; cell size: 1000 Ah	GNB Industrial Battery, now Exide Battery
Berliner Kraft-und Licht (BEWAG) Battery System, Berlin, Germany	Frequency regulation and spinning reserve	1987–1995	8.5 MW in 60 min of frequency regulation; 17 MW for 20 min of spinning reserve	14 MWh	Flooded lead-acid battery	8256 cells in 8 parallel strings of 1032 cells each; cell size: 2600 Ah	Hagen; OCSM cells
Southern California Edison Chino Battery Storage Project, Chino, CA, USA	Several "demo" modes including load leveling, transmission line stability, local VAR control, black start	1988–1997	Energy 14 MW	40 MWh	Flooded lead-acid battery	6000 cells in 6 parallel strings of 1000 cells each; cell size: 1600 Ah	Exide Batteries; GL-35 cells

(*Continued*)

TABLE 10.2 (CONTINUED)
Examples of Installed Large-Scale Lead-Acid Batteries for Energy Storage

Name	Application	Operational Dates	Power	Energy	Battery Type	Cell Size and Configuration	Battery Manufacturer
Puerto Rico Electric Power Authority (PREPA) Battery System, Puerto Rico	Frequency control and spinning reserve	November 1994–December 1999	20 MW	14 MWh	Flooded lead-acid battery	2000 low-maintenance, truck-starting batteries, 48 per 250-kW module, 8 modules per 2-MW PQ2000 system	C&D Battery
PQ2000 installation at the Brockway Standard Lithography Plant, Homerville, GA, USA	Power quality, UPS	1996–2001	2 MW	55 kWh	Lead-acid battery	1134 cells/378 each, 100A75 modules in one string	AC Battery, acquired by Omnion Power Engineering in 1997, in turn acquired by S&C Electric in 1999
Metlakatla Power and Light (MP&L) Battery System, Metlakatla, Alaska, USA	Voltage regulation and displacement of diesel generation	1997–?	1 MW	1.4 MWh	VRLA battery	Four strings of 3440 cells each, for a total of 13,760 cells	GNB Industrial Battery, now Exide Technologies, and General Electric

Source: D. H. Doughty et al., *The Electrochemical Society Interface*, 49–53, 2010.

In the energy storage industry, it is always desirable to develop lower maintenance and operating costs, deliver high efficiency, and ensure that large banks of batteries are controllable. Continued cost reductions and lifetime/state-of-charge improvements are always critical for lead-acid batteries used in grid applications.

10.3.2 Standby Applications of Lead-Acid Batteries

As shown in Figure 10.1, the total standby (UPS) application percentage in the entire lead-acid battery market is about 10%. A standby lead-acid battery system (see example in Figure 10.4) is designed to automatically provide electricity during a power outage [12]. The system is permanently installed at the home or business place. The battery system, which is always in standby mode, will constantly monitor the utility power 24 hours a day for 365 days. The automatic transfer switch (ATS) in the system can detect a power failure and send a signal that automatically disconnects from utility feed wires, and then connects generator feed wires to start the battery operating immediately. In this way, the home or business place will obtain power from the battery system smoothly and with minimal interruption, similar to operating from utility power. When utility power is restored, the ATS can switch back to utility feed wires and return itself to standby mode. The major standby application fields are as follows:

1. *Uninterruptible power supply* [13]. For standby UPS applications, including hospital operation and emergency lighting, the batteries normally require float charging to keep them at a full state of charge in the event of electricity outages. Discharge durations could be as short as 30 sec. Telecommunications, in particular, calls for a lifetime of 1 to 10 years and the batteries can be operated in hostile environments with poorly regulated charging.

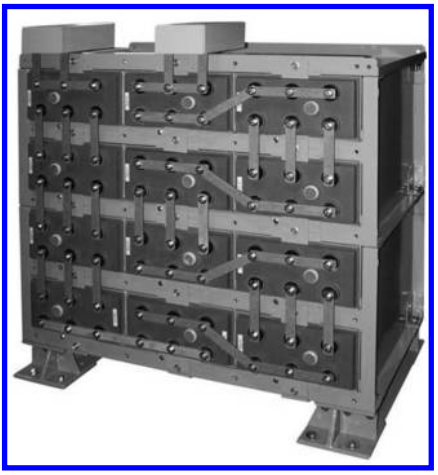

FIGURE 10.4 EnerSys PowerSafe mSeries battery (2000 Ah) for standby power. (Available at http://www.enersys.com/PowerSafe_m-Series_Batteries.aspx.)

2. *Telecommunications/data storage standby powers.* For telecommunications and data storage standby power applications, which are similar to UPS applications, the batteries normally require float charging to keep them at a full state of charge in the event of electricity outages. Regarding the lifetime of the lead-acid batteries, a lifetime of 1 to 10 years and the ability to operate in hostile environments with poorly regulated charging are required. Some of the telecommunications/data storage batteries are quite large (up to 3000 Ah), which requires specific design considerations.
3. *Aircraft emergency powers.* Backup batteries such as VRLA batteries in aircraft can keep essential instruments and devices running in the event of an engine power failure. This type of battery system should have enough power to allow operation of the radio equipment, emergency lighting, and emergency pressure/oxygen systems while running at altitude and also provide control to facilitate a safe landing. In general, the backup batteries should keep all necessary items running for between 30 min and 3 h.
4. *Power stations.* If a power failure occurs in a power station that produces electricity, a blackout situation would result, causing irreparable damage to equipment. To avoid equipment damage and to ensure the safety of power station employees during an unscheduled power outage at a power plant, a bank of large station backup batteries is normally used to power UPSs for up to 8 h while normal power is being restored to the power station.

10.3.3 Backup Power Applications of Lead-Acid Batteries

A backup lead-acid battery system, unlike a standby battery system, normally does not have the function of automatic outage detection. With a backup power system, when utility power fails, the user usually must start the battery system manually by connecting extension cords directly from the backup battery to the appliance to be powered. Note that all of the battery systems discussed in the standby power applications section can be used as backup systems. In addition, there are several other small-scale applications such as engine starting for portable generators, cable TV applications, cordless power tools, portable printers, battery-powered camping equipment, handheld home devices such as vacuums and razors, and medical equipment.

10.4 AUTOMOBILE APPLICATIONS OF LEAD-ACID BATTERIES

Many types of automobile vehicles (see examples in Figure 10.5) use lead-acid batteries either for SLI purposes or engine powering. The first type of application uses SLI batteries, and the second type uses deep-cycle batteries. Both SLI batteries and deep-cycle batteries use exactly the same chemistry for their operation. The difference between them is mainly their design.

A SLI battery is designed to provide a very large amount of current for a short period of time. This large current surge is needed to start the engine. Once the engine starts, the engine provides all necessary power to drive the car, while at the same time the engine-driven charging system charges the battery to its full-charge state. The amount of energy used for starting the engine is normally less than 20% of the

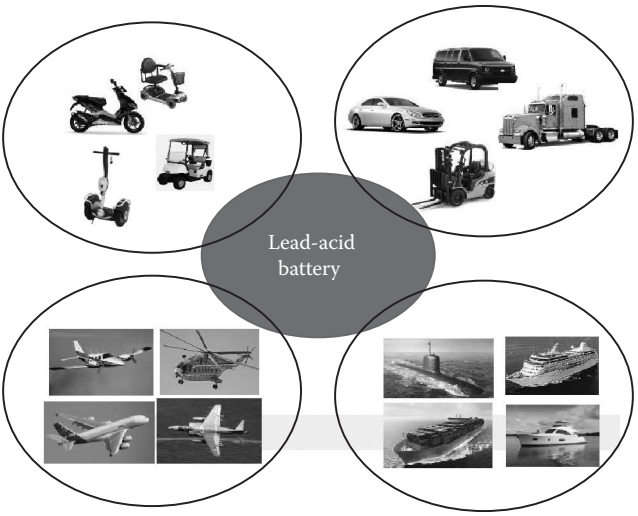

FIGURE 10.5 Possible applications of lead-acid batteries in automobile-type vehicles.

battery's total capacity. Due to this shallow charge–discharge situation, a car lead-acid battery can last a number of years. To achieve a large amount of current, SLI batteries are designed with thin plates that increase their surface area.

In contrast, deep-cycle batteries are designed to provide a steady amount of current over a long period of time for power electric and/or hybrid electric vehicles. Because a deep-cycle battery acts as an engine's power function, it should be designed to be deeply discharged over and over again. To accomplish this, a deep-cycle battery uses thicker plates than a SLI battery. One of the most important requirements for deep-cycle lead-acid batteries is cycle life.

10.4.1 Automobile Starting-Lighting-Ignition Applications

As mentioned earlier, the SLI battery is charged intermittently between high-rate discharges. For SLI batteries, the discharges are very short and at very high currents. To make this possible, the batteries' electrolytes and electrodes require special design considerations. For example, for a battery that is required to operate continuously in an engine compartment at high temperatures, the design and material selection for the glass separator should be given special attention. Commonly used batteries in automobile applications are the maintenance-free VRLA batteries, also called "sealed" batteries. The AGM-type of VRLA battery uses a glass mat separator and a gel sulfuric acid electrolyte.

10.4.2 Electric and Hybrid Electric Vehicle Applications of Lead-Acid Batteries

As discussed earlier, electric and hybrid electric vehicles use the deep-cycle type of lead-acid battery. These batteries are designed to provide continuous power for

long periods of time and it can be supplied as other small motors such as the trolling motor for a small boat, the auxiliary power for a recreational vehicle, the traction power for a golf cart, electric scooters, etc.). In general, deep-cycle batteries have fewer and thicker plates and are intended to have a greater DOD on each cycle and also a higher number of charge–discharge cycle. However, deep-cycle batteries will not provide a high current on heavy loads [14].

10.5 SUMMARY

In this chapter, applications for lead-acid batteries and their operational modules were reviewed. Due to the advantages of lead-acid batteries, such as high maturity, reliability, safety, and cost effectiveness, they have many applications in both human life and industry. In general, lead-acid batteries, including flooded and VRLA batteries, have been successfully used in many applications including in stationary, standby, and backup systems and as power for automobile-type vehicles. For stationary applications, lead-acid batteries can be used for large-scale electricity storage in grids. For standby/backup power applications, they can be used in UPSs, telecommunications/data storage, and to provide emergency power station and emergency lighting. We hope readers have found this chapter to be useful for their own research and development of applications for lead-acid batteries.

REFERENCES

1. Available at http://www.systems-sunlight.com/blog/global-lead-acid-battery-market-development-status.
2. Available at http://www.mpoweruk.com/applications.htm.
3. Available at http://www.systems-sunlight.com/blog/lead-acid-batteries-at-a-glance-advantages-applications-costs.
4. Y. Onoda, Development of a large-sized, long-life, valve-regulated lead-acid battery, *Journal of Power Sources*, 88 (1) (2000), 101–107.
5. Available at http://it.made-in-china.com/co_sunbrightpower/product_12V120ah-Medium-Size-Maintenance-Free-AGM-Battery_eynnyogeg.html.
6. Available at http://www.powerstridebattery.com/alarm-batteries/adt-security-batteries.
7. R. F. Nelson, *Lecture Course on VRLA*, Beijing, China, 2003.
8. Available at http://energy.gov/sites/prod/files/CELA.pdf.
9. Available at http://batteryuniversity.com/learn/article/batteries_for_stationary_grid_storage.
10. D. H. Doughty, P. C. Butler, A. A. Akhil, N. H. Clark, and J. D. Boyes, Batteries for large-scale stationary electrical energy storage, *The Electrochemical Society Interface*, (2010), 49–53.
11. M. Perrin, Y. M. Saint-Drenan, F. Mattera, and P. Malbranche, Lead-acid batteries in stationary applications: Competitors and new markets for large penetration of renewable energies, *Journal of Power Sources*, 144 (2005), 402–410.
12. Available at http://www.enersys.com/PowerSafe_m-Series_Batteries.aspx.
13. Available at http://www.eaton.com/pq/whitepapers.
14. D. Linden (Ed.), Chapter 23 in *Handbook of Batteries*, 3rd ed., McGraw Hill, New York (2002).

Index

Page numbers followed by f and t indicate figures and tables, respectively.

B

C

D

E

F

G

H

I

J

K

L

N

O

S

T

U

V

W

X

Y

Z